SIMULATION AND OPTIMIZATION OF NON-ISOTHERMAL COMPRESSIBLE FLOW THROUGH LARGE-BORE TWO-STROKE CYCLE NATURAL GAS TRANSMISSION ENGINES

by

DIANA KATHRYN GRAUER

B.S.M.E., Kansas State University, 2006

AN ABSTRACT OF A DISSERTATION

submitted in partial fulfillment of the requirements for the degree

DOCTOR OF PHILOSOPHY

Department of Mechanical and Nuclear Engineering
College of Engineering

KANSAS STATE UNIVERSITY
Manhattan, Kansas

2010

Abstract

This work includes a thermodynamic analysis of a large-bore two-stroke cycle engine air management system, resulting in the development of new software, for the purpose of analyzing: 1) the cylinder-to-cylinder distribution of charge air, 2) pollutant emission concentrations, and 3) energy availability to the turbocharger turbine. During the course of the thermodynamic analysis, four new algorithms were developed:

1. Charge Air Integrated Manifold Engine Numerical Simulation (CAIMENS),
2. Turbocharged-Reciprocating Engine Compressor Simulation (T-RECS) Nitrogen Oxide Kinetic Model,
3. T-RECS Carbon Monoxide Kinetic Model, and
4. Exhaust Manifold Design Software (EMDS).

The EMDS, which integrates the three previously developed algorithms, can forecast pulsation and possible unbalanced air delivery and interference within the intake system and simulates energy release and pollutant emission formation during and just after the combustion event. Specifically, the EMDS outputs a transient spatial and temporal distribution of pressure and temperature within the engine exhaust stream.

Beyond the development of the four engine characterization algorithms, an air flow balancer (AFB) was designed using data from the CAIMENS algorithm. This AFB as part of an overall Active Air Control system was used to balance the cylinder-to-cylinder distribution of air by the engine air management system and reduce total engine pollutant emission production.

SIMULATION AND OPTIMIZATION OF NON-ISOTHERMAL COMPRESSIBLE FLOW THROUGH LARGE-BORE TWO-STROKE CYCLE NATURAL GAS TRANSMISSION ENGINES

by

DIANA KATHRYN GRAUER

B.S.M.E., Kansas State University, 2006

A DISSERTATION

submitted in partial fulfillment of the requirements for the degree

DOCTOR OF PHILOSOPHY

Department of Mechanical and Nuclear Engineering
College of Engineering

KANSAS STATE UNIVERSITY
Manhattan, Kansas

2010

Approved by:

Major Professor
Kirby S. Chapman, PhD

Copyright

Abstract

This work includes a thermodynamic analysis of a large-bore two-stroke cycle engine air management system, resulting in the development of new software, for the purpose of analyzing: 1) the cylinder-to-cylinder distribution of charge air, 2) pollutant emission concentrations, and 3) energy availability to the turbocharger turbine. During the course of the thermodynamic analysis, four new algorithms were developed:

5. Charge Air Integrated Manifold Engine Numerical Simulation (CAIMENS),
6. Turbocharged-Reciprocating Engine Compressor Simulation (T-RECS) Nitrogen Oxide Kinetic Model,
7. T-RECS Carbon Monoxide Kinetic Model, and
8. Exhaust Manifold Design Software (EMDS).

The EMDS, which integrates the three previously developed algorithms, can forecast pulsation and possible unbalanced air delivery and interference within the intake system and simulates energy release and pollutant emission formation during and just after the combustion event. Specifically, the EMDS outputs a transient spatial and temporal distribution of pressure and temperature within the engine exhaust stream.

Beyond the development of the four engine characterization algorithms, an air flow balancer (AFB) was designed using data from the CAIMENS algorithm. This AFB as part of an overall Active Air Control system was used to balance the cylinder-to-cylinder distribution of air by the engine air management system and reduce total engine pollutant emission production.

Table of Contents

List of Figures

List of Tables

Nomenclature

A	Area
A_{cl}	Closed throttle area
A_E	Effective area
A_{th}	Throttle area
AV	Available energy
av	Specific available energy
B_1, B_2, b, c, d	Beattie-Bridgeman constants
C	Loss coefficient
C_D	Discharge coefficient
c	Speed of sound
c_p	Specific heat
D	Diameter
D_d	Throttle ratio
D_e	Equivalent diameter
d	Throttle shaft diameter
E	Energy
E_a	Activation energy
FA	Fuel-to-air ratio
f	Friction factor
g	Gravitational force
H	Height
h	Specific enthalpy
h_w	Water column pressure
k	Reaction rate
k_{co}	Collision frequency factor
k_r	Thermal resistance
L	Length
M	Molar mass
Ma	Mach number
$\dot{m}$	Mass flow rate
N	Engine speed (rpm)
n	Arrhenius form exponent
p	Pressure
PR	Pressure ratio
$\dot{Q}$	Heat transfer rate
$\hat{R}$	Universal gas constant
R	Mass specific gas constant
r	Radius
r_o	Rod offset
Re	Reynolds number
S	Entropy
s	Specific entropy
T	Temperature
t	Time
U	Internal energy
U_j	Experimental uncertainty
V	Velocity
V_w	Wave speed
$\forall$	Volume
v	Specific volume
$\bar{v}$	Molar specific volume
W	Width
$\dot{W}$	Power
wmg	Waste-gate margin
x	Horizontal location (distance)
x_b	Burn rate
Y_a	Adiabatic expansion factor (venturi)
y	Instantaneous stroke
Z	Compressibility factor
z	Vertical location (height)

Greek

$\boldsymbol{\alpha}$	Wiebe function constant	θ	Crank angle (from TDC)
β	Pipe angle (relative to horizontal)	κ	Scavenging coefficient
γ	Ratio of specific heats	$\mathit{\Lambda}$	Delivery ratio
Δ	Change	ν	Wiebe function exponent
δ	Separation factor (venturi)	ρ	Density
ϵ	Pipe roughness	ψ	Throttle angle
η	Efficiency	φ	Trapped equivalence ratio
η_{se}	Scavenging efficiency	$\mathit{\Omega}$	Heat transfer rate per length of pipe
η_{tc}	Turbocharger efficiency	ω	Momentum dissipation factor

Subscripts

a	Actual	fu	Fuel
amb	Ambient	h	Hydraulic (area or diameter)
b	Backward (reaction rate)	id	Ideal
c	Beginning of combustion	in	In
ca	Charge air	$inman$	Intake manifold
co	Collision (reaction rate)	max	Maximum
$comp$	Turbocharger compressor	R	Rod
cyl	Cylinder	re	Retained
e	Equilibrium	run	Runner (area)
eng	Engine	st	Stoichiometric
ex	Exit	T	Throat or restriction
$exman$	Exhaust manifold	t	Total or stagnation
f	Forward (reaction rate)	tr	Trapped
fl	Fluid	$turb$	Turbocharger turbine
$form$	Formation (reaction rate)	0	Dead state

Acronyms

AAC	Active Air Control	IPO	Intake port open
AFB	Air flow balancer	IT	Ignition timing
AMP	Air manifold pressure	N	Atomic Nitrogen
BDC	Bottom dead center	NAAQS	National Ambient Air Quality Standard
BTDC	Before top dead center	NESHAP	National Emission Standard for Hazardous Air Pollutants
CA	Crank angle	NGML	National Gas Machinery Laboratory
CAA	Clean Air Act	NMHC	Non-methane hydrocarbon
CH_4	Methane	NO	Nitrogen monoxide
CI	Compression ignition	NO_2	Nitrogen dioxide
CO	Carbon monoxide	NO_X	Oxides of nitrogen (NO and NO_2)
CO_2	Carbon dioxide	N_2	Nitrogen gas
ECC	Exhaust cylinder cavity	O	Atomic Oxygen
EM	Exhaust manifold	OH	Hydroxide
EMM	Exhaust manifold model	O_2	Oxygen gas
EMP	Exhaust manifold pressure	PRCI	Pipeline Research Council International, Inc.
EPC	Exhaust port closed	RICE	Reciprocating internal combustion engine
EPO	Exhaust port open	SI	Spark ignition
ERUN	Exhaust runner	TDC	Top dead center
H	Atomic Hydrogen	T-RECS	Turbocharged-Reciprocating Engine Compressor Simulation
HAP	Hazardous air pollutant	TTI	Turbocharger turbine inlet
HC	Hydrocarbon	VOC	Volatile organic compound
H_2	Hydrogen gas	2SC	Two-stroke cycle
IPC	Intake port closed	4SC	Four-stroke cycle

Acknowledgements

I thank all those who have encouraged me and contributed to the information included in this work. Thank you to Dr. Kirby S. Chapman, Professor and Director of the National Gas Machinery Laboratory for providing endless hours of professional and technical guidance, and for his continuous counseling and motivational support. Thank you to Sandy Chapman for her encouragement and limitless patience.

A special thanks to members of the PRCI Compressor and Pump Station Technical Committee and the NGML Advisory Council for their valuable guidance and expertise. I also thank my co-workers at NGML for their ongoing assistance and support.

I wish to thank members of my candidacy panel, Dr. Byron Jones, Dr. Sameer Madanshetty, Dr. Steven Eckels, and Dr. Dolores Takemoto for contributing their valuable time to the completion of this work.

In memoriam, Dr. Prakash Krishnaswami will always be remembered for his compassionate assistance and encouragement during my transition from undergraduate to graduate.

To my parents, Doug and Bette, for their infinite supply of patience and emotional support, thank you for keeping me focused and continually working to accomplish my goals. There are not enough words to describe my appreciation. Thank you for being my rock.

To my sister, Laura, for never letting me take myself too seriously, thank you for always being my best friend.

Dedication

To Grandpa Gene – large engine enthusiast and mentor.

Gene Fredrick Bohnenblust, P.E.

October 30, 1923 – September 25, 2008

B.S. Agricultural Engineering, Kansas State College, 1948

President, American Society of Agricultural Engineers, Kansas State College, 1948

Corporal, 3rd Platoon, Cannon Company, 263rd Regiment, 66th Infantry Division “Black Panthers,” U.S. Army, 1943-1946

Bronze Star Medal, World War II, Awarded January 2, 1998

Area Engineer, Soil Conservation Service, U.S. Department of Agriculture, 1949-1985

Preface

Information included in this work has been previously published in the form of technical reports submitted to the U.S. Department of Energy and the Pipeline Research Council International, Inc:

1. Chapman, K.S., Grauer, D.K., McFarland, J.J., and M. Toema. "Cost-Effective Reciprocating Engine Emissions Control and Monitoring for E&P Field and Gathering Engines." *U.S. Department of Energy*. DE-FC26-02NT15464. Quarterly Reports 28-30. Work completed July 2009 – March 2010.
2. Grauer, D.K. and K. S. Chapman. "Exhaust Manifold Design Guidelines to Optimize Scavenging and Turbocharger Performance: Final Report." *Pipeline Research Council International, Inc*. PR-266-08209. July 20, 2009.
3. Grauer, D.K. and K. S. Chapman. "Development of an Active Air Control System: Final Report." *Pipeline Research Council International, Inc*. PR-266-05208. July 1, 2008.

Technology developed during the course of the completion of this work is protected by:

1. U.S. Patent Application No. 61/101,957, "Active Air Control," Filed October 1, 2009. Available through Kansas State University Research Foundation.
2. Canadian Patent Application No. 2,640,077, "Active Air Control," Filed October 1, 2009. Available through Kansas State University Research Foundation.

In addition to previously published material, this work includes the development and validation of new kinetic mechanisms for pollutant emission formation and oxidation.
It also includes a parametric study of the impact of various operating conditions and component geometry on the large-bore two-stroke cycle turbocharged-engine system.

CHAPTER 1 - Introduction

The goal of this research is to develop a methodology for investigating techniques to enhance the flow of air into and exhaust products out of a large-bore two-stroke cycle natural gas transmission engine. This goal is achieved by developing a mathematical model of the thermodynamic and fluid flow phenomena within the air-delivery and exhaust-removal systems of the engine. Successful completion of this goal requires the development of individual models to quantify pulsating, non-isothermal, compressible, fluid flow, in addition to combustion kinetics, and thermodynamic availability of the engine charge air and combustion exhaust. In addition, models for equilibrium combustion products and kinetic formation of oxides of nitrogen (NO_X) and carbon monoxide (CO) are incorporated to provide a complete model of the in-cylinder combustion process.

A discussion of the US natural gas transmission industry and its employment of the large-bore two-stroke cycle engine are provided in the following paragraphs along with a summary of the factors motivating the present work. The chapter concludes with a discussion of the proposed method for defining engine performance and a list of the specific objectives required to complete the foregoing goal.

US Natural Gas Transmission Industry

In 2007, more than 68.4 trillion cubic feet of natural gas (Tcf) was transported by interstate and intrastate pipeline companies. The 30 largest interstate pipeline systems transported about 81 percent (29.8 Tcf) of the total. The interstate portion of the national natural gas pipeline network represents about 71 percent of the 305,954 miles of all natural gas mainline installed in the United States. The 30 largest interstate pipeline companies own about 77 percent of the 217,306 miles of interstate natural gas mainline and about 72 percent of the total capacity (183 billion cubic feet) available within the interstate natural gas pipeline network (EIA, 2010). Almost all of the 30 largest interstate pipeline companies are members of the Pipeline Research Council International, Inc. who provided the funding for this work.

The natural gas mainline is a wide-diameter, often-times long-distance, portion of a natural gas pipeline system located between the gathering system and the principal customer service area. Between the producing area or supply source, and the market area, over 1,200 compressor stations, with a total 16.9 million installed horsepower, and a throughput capacity of 881 billion cubic feet per day, are located along the transmission system as shown in Figure 1.1 (EIA, 2007). These stations contain one or more compressor units whose purpose is to receive the transmission flow – which has decreased in pressure since the previous compressor station – at an intake point, increase the pressure and actual volumetric flow rate, and thus, maintain the movement of natural gas along the pipeline. Compressor stations are usually situated between 50 and 100 miles apart along the length of the natural gas pipeline system and are designed to operate nonstop 24 hours per day, 365 days per year (EPA, 2010).

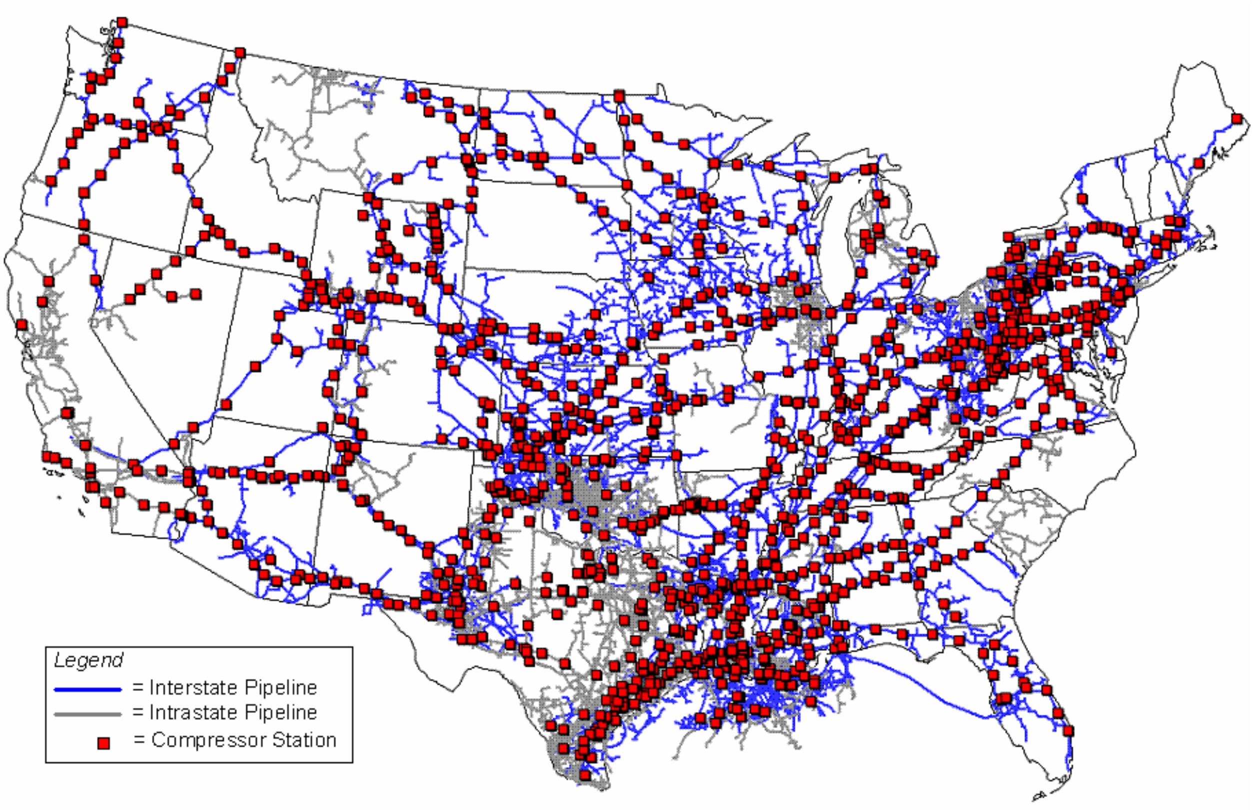

Figure 1.1: Interstate natural gas system mainline compressor stations (EIA, 2007)

Compressor units that are used on a natural gas mainline transmission system consist of an engine coupled to a compressor. The units are typically rated at 1,000 horsepower or more and are of the centrifugal (turbine) or reciprocating (piston) type. The larger compressor stations may have as many as 10-16 units with an overall horsepower rating of 50,000 to 80,000 brake horsepower (bhp) and a throughput capacity exceeding three billion cubic feet of natural gas per day. Most compressor units operate on natural gas which is extracted from the pipeline flow (EIA, 2007).

Large-Bore Two-Stroke Cycle Engines

The natural gas transmission industry relies heavily on reciprocating large-bore two-stroke cycle (2SC) engines to power the prime mover compressors used to move the product through the pipeline. The majority of natural-gas-fired reciprocating engine-compressor units are at least 30 years old, employing technology that originated in the first half of the 20th century, prompting the use of the term "legacy" when referring to this technology. Legacy units are periodically retrofitted to include the newest technology; not to increase throughput capacity per se, but rather to increase efficiency, safety, and reliability, with an emphasis on minimizing regulated pollutant emissions (EIA, 2007).

The industry's legacy engine population falls into four broad categories:

1. Purpose-designed low speed (250-400 rpm) 2SC and 4SC engines;
2. Diesel-derivative medium speed (360-630 rpm) engines converted to spark ignition natural gas operation by the original equipment manufacturer (OEM);
3. Various high speed (>720 rpm) rich- and lean-burn 4SC engines, generally <1,000 bhp; and
4. Various older and/or miscellaneous engines, generally <1,000 bhp.

The first two categories listed represent approximately 80% of the total fleet bhp with an average of 2,200 bhp per unit. Within the first two categories, five related makes and models account for approximately 70% of the total number of units, and total horsepower. These five makes and models are: (1) Cooper GMV, (2) Cooper GMW, (3) Cooper V-250/V-275/W-330, (4) Clark TCV, and (5) Clark TLA/BA (PRCI, 2005).

All of these engines are large-bore, lean-burn, 2SC, loop scavenged engines with various forms of aspiration ranging from reciprocating blowers to high pressure ratio turbochargers. Each of these engines uses a common air delivery system which transports air from a single source – reciprocating blower or turbocharger – to multiple cylinders as shown in Figure 1.2. The cylinders are positioned along one or two banks; each bank is connected to the air source by a manifold. This manifold is in essence a long run of 12-24 inch diameter steel pipe, prompting use of the term “log manifold”. The log manifold is connected to each cylinder by an individual runner that delivers air to the intake ports of each cylinder. The air flow rates to each cylinder of the engine, even under steady operating conditions, are not identical. This is due to the geometric details of the flow path to each cylinder, which change for each cylinder located on the manifold. Also, as each cylinders intake flow commences, air is drawn from the runner leading to the cylinder, the manifold, and the other runners leading to other cylinders. Thus the air flow to each individual cylinder is affected by its location on the manifold relative to the air source, its location relative to the other cylinders, and the firing order of the engine.

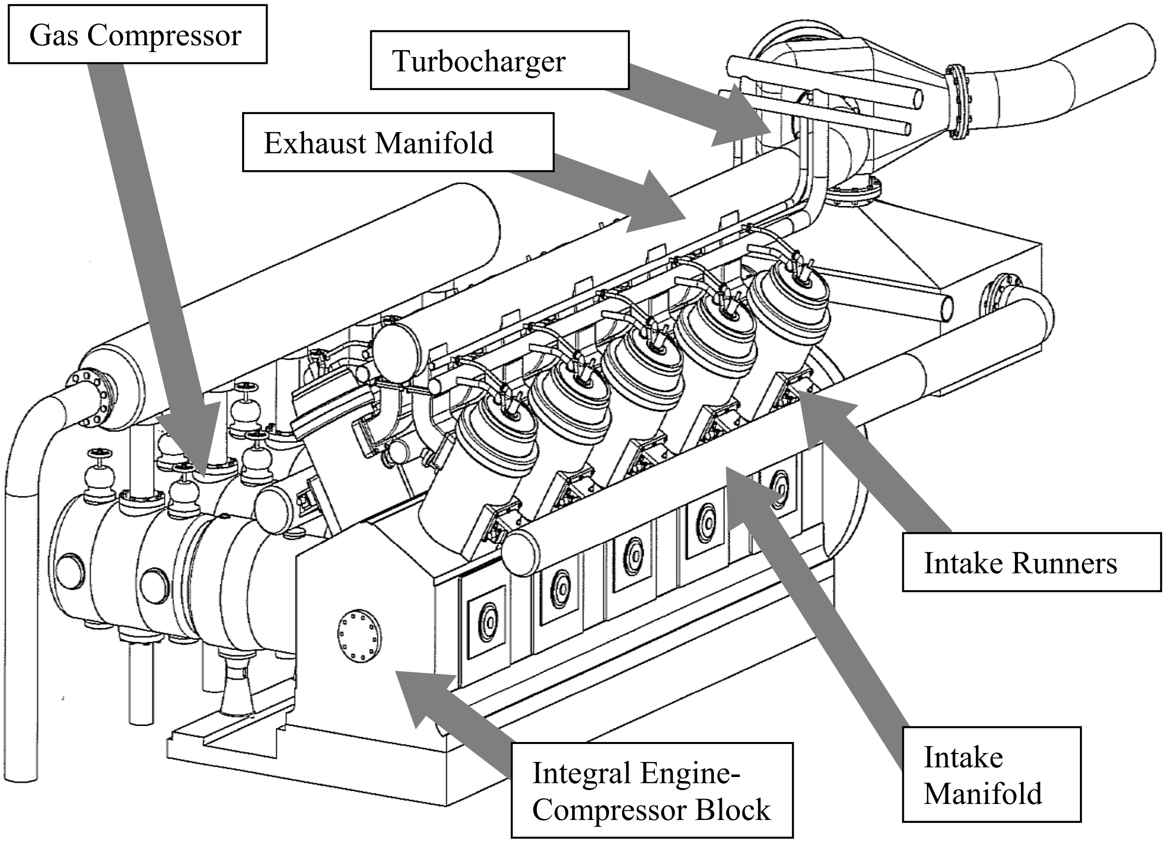

Figure 1.2: Integral 2SC engine-compressor configuration (AAC, 2009)

Air flow into the cylinders from the manifold occurs in a series of pulses. Each pulse is approximately sinusoidal in shape and creates a wave of pulsation within the intake system. Backflow also occurs early during the compression stroke, before the intake ports are covered, due to rising in-cylinder pressure.

The movement of the piston draws fresh charge air into the cylinder from the intake runner, scavenging the combustion residuals from the previous cycle. As the intake ports are covered, the in-cylinder mixture of air and fuel is compressed, is ignited, and combusts. As the piston moves down, the exhaust ports are uncovered, allowing burnt gases to exit the cylinder during the exhaust blow-down process.

Within the cylinder, following ignition, a turbulent flame develops, propagates through the mixture of air, fuel, and residual gas, until it reaches the combustion chamber walls, and then extinguishes. The flame development and subsequent propagation vary cycle-to-cycle and cylinder-to-cylinder due to variations in charge air flow as a result of the log manifold design and intake pulsation. These variations in burn rate result in variations in the engine exhaust pollutant emission concentrations. Spark-ignition engine exhaust gases contain oxides of nitrogen (NO and NO_2, collectively called NO_X), carbon monoxide (CO), and organic compounds which are unburned or partially burned hydrocarbons (HC). In general, the concentrations of NO_X and CO differ from values calculated assuming chemical equilibrium. Thus the detailed chemical mechanism of pollutant formation and the kinetics of these processes are important in determining cylinder-to-cylinder, cycle-to-cycle, and overall emission levels.

Regulatory Motivation

The Clean Air Act (CAA) is the comprehensive federal law that regulates air emissions from stationary and mobile sources. Among other things, this law authorizes EPA to establish

National Ambient Air Quality Standards (NAAQS) to protect public health and public welfare, and to regulate emissions of hazardous air pollutants. The CAA regulates the natural gas transmission industry via Class No. 4922 of Standard Industrial Classification or Class No. 48621 of the North American Industry Classification System.

One of the goals of the CAA was to set and achieve NAAQS in every state by 1975 in order to address the public health and welfare risks posed by certain widespread air pollutants. The setting of these pollutant standards was coupled with directing the states to develop state implementation plans, applicable to appropriate industrial sources in the state, in order to achieve these standards. The Act was amended in 1977 and 1990 primarily to set new dates for achieving attainment of NAAQS since many areas of the country had failed to meet the deadlines.

Section 112 of the CAA addresses emissions of hazardous air pollutants. Prior to 1990, the CAA established a risk-based program under which only a few standards were developed. The 1990 CAA Amendments revised Section 112 to first require issuance of technology-based standards for major sources and certain area sources. "Major sources" are defined as a stationary source or group of stationary sources that emit or have the potential to emit 10 tons per year or more of a hazardous air pollutant or 25 tons per year or more of a combination of hazardous air pollutants. An "area source" is any stationary source that is not a major source.

For major sources, Section 112 requires that EPA establish emission standards that require the maximum degree of reduction in emissions of hazardous air pollutants. These emission standards are commonly referred to as “maximum achievable control technology” or “MACT” standards. Eight years after the technology-based MACT standards are issued for a source category, the EPA is required to review those standards to determine whether any residual risk exists for that source category and, if necessary, revise the standards to address such risk (EPA, 2010).

As required by the Section 112 of the CAA, the EPA established Title 40 of the Code of Federal Regulations (CFR). Within 40 CFR, the EPA promulgated Part 50 – NAAQS, and Part 63 – National Emission Standards for Hazardous Area Pollutants (NESHAP) based on the MACT standards defined within the CAA literature.

In the presence of sunlight, NO_X reacts with other gases in the atmosphere to produce ozone. A geographical area with ambient ozone levels in excess of the NAAQS for ozone is termed non-attainment. The EPA establishes the ozone NAAQS, and requires regional, state, or local areas to take action to reduce emissions that contribute to ozone non-attainment. To date, NO_X control requirements have been triggered by non-attainment with the 1-hour ozone standard (the historical NAAQS is based on ambient ozone monitoring averaged over one hour), and ozone non-attainment has been most prevalent in urban areas. Thus, legacy engines were minimally impacted due to the rural location of most compressor stations. This approach changed after the 1990 CAA Amendments began to pursue NO_X reductions over broader regions in the eastern U.S. due to concerns that emissions transport from rural areas into urbanized non-attainment air basins.

In 2004, the first Federal standard, 40 CFR Part 63 – NESHAP for Reciprocating Internal Combustion Engines (RICE), was finalized requiring reduction of air toxic emissions from internal combustion (IC) engines. Air toxics are a category of pollutants that are believed to contribute to long term or acute public health impacts. The CAA identifies 188 hazardous air pollutants (HAP) that are to be controlled from sources. Stationary RICE is identified as a major source of four specific HAP: formaldehyde (CH_2O), acrolein, methanol, and acetaldehyde.

Since the publication of the 2004 NESHAP regulations, there have been two revisions to the rule: 1) 2008 Final Rule, published January 18, 2008, and 2) 2009 Proposed Rule, March 5, 2009. A summary of these rules as compared to the 2004 NESHAP is provided in Table 1.1. Table 1.1 briefly summarizes emission limits that define 2SC engine compliance, except during periods of startup or malfunction, during which the standards are more lenient.

The 2004 NESHAP took effect on August 16, 2004, at which time little was known about the population of stationary RICE with a site-rating of 500 brake horsepower (bhp) or less; therefore, decisions on regulation of these engines were deferred until more information could be obtained and analyzed. For standard operation of RICE with a site-rating of 500 bhp or more, the 2004 NESHAP required a 58% or more reduction in CO, and CH_2O must be limited to 12 parts per million volumetric dry (ppmvd) or less corrected to 15% oxygen (O_2).

On January 18, 2008, the EPA issued a combined rule updating the New Source Performance Standards (NSPS) for Stationary Spark Ignition IC Engines and NESHAP for RICE. Within the NSPS, all new, modified, and reconstructed stationary spark ignition engines, combusting any fuel, were covered, regardless of size. This Rule represented an abrupt change in direction for engine compliance; from previous regulation of CO to that of regulation of multiple criteria pollutants. Each engine was required to comply with corresponding limits for NO_X, CO, and volatile organic compounds (VOC). VOC limits were included in place of non-methane hydrocarbon (NMHC) limits as a surrogate for HAP control. The included 2008 NESHAP required compliance with the associated NSPS relative to engine size. For example, in order to comply with the 2008 NESHAP, a legacy 500 bhp 2SC engine would have to emit less than 540 ppmvd or 4.0 gm/hp-hr CO, 160 ppmvd or 2.0 gm/hp-hr NO_X, and 86 ppmvd or 1.0 gm/hp-hr

VOC, all corrected to 15% O_2. The 2008 NESHAP does not include emissions of CH_2O or ethane in the defined VOC limit.

With the 2009 NESHAP, proposed on March 5, 2009, the EPA again abruptly changed direction in the associated limits for engine compliance. The 2009 NESHAP proposed to limit HAP via limits for CO on 2SC engines, and suggests that the reduction in CO would also result in reduction of NO_X, VOC, and particulate matter (PM); therefore, these pollutants need not be regulated individually as in previously promulgated rulings. The CO emissions for 2SC engines rated 50 to 249 bhp were limited to 85 ppmvd, while engines rated 250 to 500 bhp were limited to 8 ppmvd CO or 90% reduction corrected to 15% O_2. It is important to note that the 2009 Proposed Rule reverted to the 2004 NESHAP limits for 2SC engines larger than 500 bhp.

Table 1.1: Summary of RICE NESHAP regulatory history

		Concentration in ppmvd @ 15% O_2			
Rule	**Manufacture Date**	**CO** (gm/hp-hr)	**CH_2O**	**NO_X** (gm/hp-hr)	**VOC** (gm/hp-hr)
2004 2SC >500 HP	--	58% or more reduction	12	--	--
2008 2SC 100≤HP<500	7/1/2008	540 (4.0)	--	160 (2.0)	86 (1.0)
	1/1/2011	270 (2.0)	--	82 (1.0)	60 (0.7)
2008 2SC 500≤HP<1350	1/1/2008	540 (4.0)	--	160 (2.0)	86 (1.0)
	7/1/2010	270 (2.0)	--	82 (1.0)	60 (0.7)
2008 2SC >1350 HP	7/1/2007	540 (4.0)	--	160 (2.0)	86 (1.0)
	7/1/2010	270 (2.0)	--	82 (1.0)	60 (0.7)
2009 2SC 50≤HP≤249	--	85	--	--	--
2009 2SC 250≤HP≤500	--	8 -or- 90% reduction	--	--	--
2009 2SC >500 HP	--	58% or more reduction	12	--	--

On February 9, 2010, the EPA announced 2010 NAAQS for nitrogen dioxide (NO_2). This was the first new standard for NO_2 in 35 years. The agency set the new one-hour standard for NO_2 at a level of 100 parts per billion (ppb). NO_2 is formed from vehicle, power plant, and other industrial emissions, and as a species of NO_X, is considered an ozone precursor, contributing to the formation of fine particle pollution and smog.

On January 7, 2010 the EPA announced that it is also proposing the strictest health standards to date for ground level ozone. The agency is proposing to set the Primary NAAQS to a level between 0.060 and 0.070 ppm measured over eight hours, and expects to issue final standards by August 31, 2010

In accordance with Section 126 of the CAA, numerous States have already filed petitions requesting that the EPA make findings and require decreases in NO_X emissions from stationary sources in upwind States that may contribute to NO_2 and ozone non-attainment problems in the petitioning state. The new NO_2 and ozone NAAQS, along with the filed petitions, will almost certainly result in further tightening of the NESHAP for RICE.

Industry Compliance

Current regulatory demands to reduce the environmental footprint of compressor stations have consistently increased the scale of station revitalization and retrofits with improved technology. In response to increasing regulatory demands via NAAQS and NESHAP implementations, the Pipeline Research Council International, Inc. (PRCI) developed a detailed technology roadmap. PRCI is a consortium of the world's leading pipeline companies, vendors, service providers, equipment manufacturers, and other organizations that support the natural gas transmission industry. Since 1952, PRCI has provided the natural gas transmission industry with the development and deployment of research solutions to the operation, maintenance, and regulatory challenges that face the industry.

The Roadmap defines a comprehensive, multi-year research plan to create options for pipelines to cost-effectively achieve 0.5 gm/hp-hr NO_X from legacy pipeline RICE, while meeting a cost-objective of 1/3 the installed cost of replacement horsepower, without increasing other pollutants or negatively affecting engine performance or reliability. Incorporating the accumulated knowledge of over 20 years of prior pipeline emissions control research and development, the roadmap defines a set of risk-controlled technology development pathways to achieve anticipated NO_X control requirements. Within the roadmap, technology options are defined that integrate the technical dimensions of engine design and operation. Specifically, the roadmap identifies air management, or effective distribution, use of the engine charge air, as one objective of the research plan (PRCI, 2005). PRCI has made funds available to complete a comprehensive investigation of the dynamics of the air delivery and exhaust removal system of large-bore 2SC natural gas transmission engines targeted by NAAQS and NESHAP.

Methods of Studying Engine Performance

Three different approaches are available to examine the air management of the large-bore 2SC natural gas transmission engine. The first is to build a full scale prototype of the engine, and perform a parametric study varying the design and operating parameters that affect the performance of the air delivery and exhaust removal system and assess the results. The second method is to instrument a field engine, and again perform a study of performance parameters. The third method is to mathematically model the engine and perform the parametric study via a variety of computer simulations.

The first two approaches are quite expensive. In addition, augmenting the flow path of a large IC engine, whether in a laboratory setting or in the field can be rather cumbersome, time-consuming, and dangerous. The second approach, field testing and engineering, requires the extensive cooperation of a pipeline company, including: supervised access to the station, security clearance, safety training and personal protective equipment, and multiple start-ups and shutdowns of the candidate engine. The third method, which involves numerical experiments, is much less expensive and invasive, and more flexible. Modeling activities can make major contributions to engine engineering by:

1. Developing a more complete understanding of the process under study from the discipline of formulating the model;
2. Identifying key controlling variables to provide guidelines for more rational and therefore less costly experimental development efforts;
3. Forecasting engine behavior over a wide range of design and operating variables to screen concepts prior to major hardware programs, to determine trends and trade-offs, and, if model is sufficiently accurate, to optimize design and control; and
4. Providing a rational basis for design innovation (Heywood, 1988).

The conservation equations for mass and energy, and momentum transfer are well defined, and routinely used in mathematical simulation. Methods have been developed to model equilibrium combustion products and chemical kinetics of pollutant formation. First and second law thermodynamic analysis of pulsating fluid flow are available, and can be applied to problems with moderately complex flow paths.

Objective

The specific objective of the research is to develop a mathematical model to predict fluid flow through the air delivery and exhaust removal systems of a large-bore 2SC engine and then use the model to develop a method to effectively and efficiently: 1) distribute charge air within the intake system, and 2) transfer exhaust products to the turbocharger turbine with minimal energy loss. This mathematical model will include procedures to predict pulsation and possible unbalanced air delivery and interference within the intake system. It will include sub-models to predict energy release and pollutant emission formation during and just after the combustion event. The model will also include a thermodynamic analysis of the exhaust stream to predict the availability of exhaust energy to the turbocharger turbine. The individual mathematical models were developed, tested, and tuned from field data, and then combined to form a comprehensive model of the engine air management system. Once the model development was complete, a parametric investigation was conducted to determine the effect of the following operating and design parameters on the engine air management system:

1. Intake manifold and runner design,
2. Intake manifold operating conditions,
3. Cylinder location and firing order,
4. Exhaust removal system design, and
5. Turbocharger location.

Chapter 2 contains the literature review of industry and academic work that has been previously documented to complete the above objectives. Chapter 3 presents the proposed mathematical models that were used to predict the non-isothermal compressible flow, in-cylinder phenomena, pollutant emission concentrations, and exhaust available energy. The solution method used in conjunction with the mathematical model is presented in Chapter 4 along with a description of the integration of the sub-models for distributing compressible fluid flow through a pipe matrix, in-cylinder combustion, chemical equilibrium and kinetics of formation for NO_X and CO, and thermodynamic availability. Chapter 5 describes an experimental investigation of charge air distribution and balance. Chapter 6 presents the simulated results for a typical large-bore 2SC RICE and the results of the parametric study. Chapter 7 presents the major conclusions of this work and recommendations for future investigations.

CHAPTER 2 - Literature Review

A thorough literature review of research and scholarly work that describe the 2SC turbocharged-engine system is presented. The author also researched past, current, and emerging active air control technologies that could, with some engineering effort, be scaled for application to large-bore 2SC pipeline engines. The literature in this chapter is arranged in a manner that reflects the path of air flow through the engine air management system. The review includes journal articles and texts that apply to:

1. Compressible flow and equations of state,
2. Manifold design and analysis,
3. Gas exchange processes and port flow,
4. Current and emerging technologies for air management in IC engines,
5. Emission production and reduction,
6. Exhaust system analysis, and
7. Available energy analysis.

Compressible flow in pipes and Equations of State

Compressible flow in the manifold and runners of the turbocharged-engine system can be modeled as one-dimensional flow through a pipe. Therefore, much of the literature reviewed in this section applies directly to flow within a pipeline.

Abbaspour et al. (2004) used the fully implicit finite difference method to solve the continuity, momentum, and energy equations for flow within a gas pipeline. The methodology: 1) incorporated the convective term in the conservation of momentum equation; 2) treated the compressibility factor as a function of temperature and pressure; and 3) considered the friction factor as a function of the Reynolds number. The fully implicit method representation of the equation offered the advantage of guaranteed stability for a large time step, which was very useful for the gas industry. The results showed that treating the gas in a non-isothermal manner was necessary for pipeline flow calculation accuracies, especially for rapid transient processes. The authors also indicated that the convective term played an important role in the gas flow analysis and must be included in the calculation.

Beattie and Bridgeman (1928) presented an algebraic equation of state whose constants were determined from pressure-volume-temperature data. This equation could be readily used for evaluating thermodynamic relations. The equation and corresponding constants for a variety of gases reproduced the data over a range of temperatures and pressures.

Benedict et al. (1940) presented an empirical equation for the isothermal variation with density of the work content of pure hydrocarbons in the gaseous or liquid state. The Benedict-Webb-Rubin (BWR) equation was derived from the Beatie-Bridgeman equation. The authors addressed the need of a more general equation of state for applications where other equations, including the van der Walls and Beatie-Bridgeman equations of state, fall short. From this fundamental equation were derived (a) an equation of state, (b) an equation for the fugacity, and (c) an equation for the isothermal variation of the enthalpy. These equations summarize properties of the gaseous or liquid phase, critical properties, vapor pressures, and latent heats of vaporization. A procedure was suggested for determining numerical values of the parameters in the equation. Such values were given for methane, ethane, propane, and n-butane. A comparison was made between observed properties of these hydrocarbons and those predicted by the equations.

Deen and Reintsema (1983) described gas flow in a natural gas transmission line by a set of three coupled partial differential equations (PDE) expressing conservation of mass, momentum and energy. Gas properties were described by a non-ideal equation of state. A technique was introduced that reduced the energy equation to a single parameter in the mass equation without the assumption of isothermal or isentropic flow. The remaining set of PDEs was solved by two different techniques. The first method was an accurate but time-consuming technique consisting of applying the method of characteristics to determine an improved representation of the friction term. The second way consisted of a finite-difference implementation with a second-order truncation error. Both the physical assumptions and the numerical approximations were compared to data obtained from experiments in the main transport system of Gasunie. Guidelines on the analog modeling of pipeline systems and the interpretation of simulation results concluded the paper.

Issa and Spalding (1972) described a numerical procedure for solving problems of one-dimensional, unsteady, compressible, frictional flows with heat transfer. The procedure was based on the Hartree hybrid method which combines the use of a rectangular grid with the use of the method of characteristics. The main features of the procedure were its applicability and ease of adaptability to complex unsteady-flow problems. Another feature was the simplicity of its programming for a computer. Computations for flows in shock tubes were presented.

Kiuchi (1994) developed a fully implicit finite-difference method for calculating unsteady gas flow in pipeline networks. The algorithm for solving the finite-difference equations of a pipe was based on the Newton-Raphson method. The Von Neumann stability analysis on the finite-difference equations of a pipe showed that the equations were unconditionally stable. An iterative convergence method was applied to the calculation of node pressure at junctions in the networks. The parameter study on convergence showed that stability depended on the convergence tolerance. Sample results were compared with those of the method of characteristics and the two-step Lax-Wendroff method.

Osiadacz and Chaczykowski (2001) advocated that the transient flow of gas in pipes can be adequately described by a one-dimensional approach. Basic equations describing the transient flow of gas in pipes were derived from the equation of motion (or momentum), continuity equation, energy equation and the state equation. In much of the literature, either an isothermal or an adiabatic approach to the description of thermodynamics of pipeline gas flow is adopted. However, for many dynamic gas applications this assumption of a process having a constant temperature or being adiabatic is not valid. In this case, the temperature of the gas is a function of distance and is calculated using a mathematical model, which includes the energy equation. In the paper, the PDEs describing the transient flow of gas were discretized using the method of lines. A non-isothermal pipeline gas flow model is presented. The discretized equations form a system of differential/algebraic equations which the authors used to compute both a steady-state and transient numerical solution.

Ouyang and Aziz (1996) presented a comprehensive review of general flow equations and developed new general flow equations to account for the pressure gradients due to friction, elevation and kinetic energy change. The authors presented simplified forms for new flow equations for gas flow in pipelines or wells where the kinetic energy term can be neglected. The general flow equations and their simplified forms were compared with the widely-used American Gas Association (AGA) equations and tested with field data. Results showed that the equations make excellent predictions of flow rates or pressure gradients, and that they were applicable over a much broader range of gas types and gas flow rates than the AGA equation and previously-used simplified flow equations. In addition, different empirical explicit correlations for the Fanning friction factor are compared. They found that different correlations give quite different values of the friction factor. For smooth pipes, many correlations were reviewed, but the modified 1/9th power law, Blasius, Drew et al., and Panhandle equations were recommended for different Reynolds number ranges. For rough pipes, Serghides (I) and (II), Zigrang-Sylvester (I) and (II), Chen, and Haaland equations can be employed with confidence. They recommend avoiding other friction factor correlations reported in the literature because they can result in large errors.

Price et al. (1996) presented a method to determine the effective friction factor and overall heat transfer coefficient for a high pressure, natural gas pipeline during fully transient flow conditions. Time varying Supervisory Control and Data Acquisition (SCADA) measurements at the pipeline boundaries (i.e., inlet and outlet) provided boundary conditions for a transient flow model as well as additional information used to determine these parameters. The resulting friction factor and overall heat transfer coefficient minimized the least-squared difference between the additional SCADA measurements at the pipeline outlet and the corresponding values predicted from the transient flow model. The concept was referred to as parameter estimation. The transient flow model was based on a numerical solution of the one-dimensional, unsteady flow equations (i.e., continuity, momentum and energy) which were discretized using a highly accurate and compact finite-difference scheme. The transient flow model and parameter estimation were incorporated into a computer program that was initially tested on a simple pipeline with steady flow conditions. Here, the predicted outlet pressure and temperature, using the estimated friction factor and overall heat transfer coefficient, exactly matched the corresponding prescribed values. Subsequently, a portion of the Foothills Pipe Line

Ltd. transmission system in Alberta was analyzed using time varying SCADA flow measurements. The resulting outlet pressure and temperature from the transient flow model were in good agreement with SCADA measurements at this location.

Thorley and Tiley (1987) mathematically modeled highly compressible unsteady flows. In order to obtain tractable solutions of the governing equations, the investigators made various simplifying assumptions such as presuming isothermal or isentropic flow of ideal gases, etc. This review, with dense phase gas transmission systems of particular interest, briefly developed the basic equations without such assumptions and included the effects of wall friction and heat transfer. After re-expressing the equations in terms of the measurable quantities of pressure, temperature and velocity, previously published work was reviewed for their solution.

As described by the information included in the science reviewed above, non-isothermal flow through the manifold and runners is governed by the time-dependant continuity (mass conservation), momentum, and energy equations. These are supplemented by an equation of state for homogeneous, one-dimensional, single-phase flow and a correlation for the friction factor, as a function of the Reynolds number and relative pipe roughness. By solving the resulting system of equations, the behavior of the fluid parameters can be obtained in the manifold-runner matrix. The following equations were developed by *Deen and Reintsema (1983)*, *Issa and Spalding (1972)*, *Price et al. (1996)*, and *Thorley and Tiley (1987)* for one-dimensional, unsteady, compressible flow, to include the effects of wall friction and heat transfer. The equations are presented in partial differential form.

Conservation of Mass:

$$\frac{\partial \rho}{\partial t} + \frac{\partial}{\partial x}(\rho V) = 0 \tag{2.1}$$

Conservation of Momentum:

$$\rho\frac{\partial V}{\partial t}+\rho V\frac{\partial V}{\partial x}+\frac{\partial p}{\partial x}=-\frac{\omega}{A}-\rho g\sin\theta \tag{2.2}$$

Where the dissipation of momentum is a function of the fanning friction factor (f) and the fluid velocity (ν):

$$\omega=\frac{fV|V|}{8}\pi D \tag{2.3}$$

Conservation of Energy:

$$\rho\frac{\partial h}{\partial t}+\rho V-\frac{\partial p}{\partial x}-V\frac{\partial p}{\partial x}=\frac{\Omega+\omega V}{A} \tag{2.4}$$

Heat flow into the pipe per unit length and per unit time (Ω) is identified by (Abbaspour, 2004):

$$\Omega=-\frac{4h_{amb}A(T-T_{amb})}{D} \tag{2.5}$$

The friction factor utilized by both the momentum and energy equations is calculated for turbulent flow in rough pipes using the modified Colebrook-White equation (Ouyang and Azziz, 1996):

$$f^{-0.5}=3.48-4\log\left(\frac{2\epsilon}{D}+\frac{9.35}{f^{0.5}\mathrm{Re}}\right) \tag{2.6}$$

To obtain the gas enthalpy (h) in terms of local pressure, temperature, and density, *Osiadacz and Chaczykowski (2001)* used the thermodynamic identity:

$$dh=c_p dT+\left[\frac{T}{\rho}\left(\frac{\partial\rho}{\partial T}\right)_p+1\right]\frac{dp}{\rho} \tag{2.7}$$

The following Equation of State is used to incorporate compressibility:

$$\frac{p}{\rho} = ZRT \tag{2.8}$$

The gas compressibility factor (Z) given by the Beattie-Bridgeman Equation of State is (Beattie and Bridgeman, 1928):

$$Z = 1 - \frac{\bar{v}d}{T^3} + \frac{B_2}{\bar{v}} - \frac{B_2 d}{T^3} - \frac{B_1}{\bar{v}\bar{R}T} \tag{2.9}$$

where B_1 and B_2 are defined as functions of the gas molar specific volume ($\bar{v}$). Constant values for air are included in Table 2.1.

$$B_1 = B_{11}\left(1 - \frac{b}{\bar{v}}\right) \tag{2.10}$$

$$B_2 = B_{22}\left(1 - \frac{c}{\bar{v}}\right) \tag{2.11}$$

Table 2.1: Beattie-Bridgeman constants for selected gases

Fluid	B_{11}	b	B_{22}	c	d
Air	1.3012	0.01931	0.04611	-0.0110	4.34×10^4
N_2	1.3445	0.02617	0.05046	-0.00691	4.20×10^4
O_2	1.4911	0.02562	0.04624	0.004208	4.80×10^4
CO_2	5.0065	0.07132	0.10476	0.07235	66.00×10^4
CH_4	2.2769	0.01855	0.05587	-0.01587	12.83×10^4

These equations and identities are combined to create a set of three equations in terms of local pressure, temperature, and density as functions of time, and thoroughly describe transient compressible gas flow. The equation set is (Abbaspour, 2004):

$$\left(\frac{\partial p}{\partial t}\right) + V\left(\frac{\partial p}{\partial x}\right) + \rho V_w^2\left(\frac{\partial V}{\partial x}\right) = \frac{V_w^2}{c_p T}\left[1 + \frac{T}{Z}\left(\frac{\partial Z}{\partial T}\right)_p\right]\frac{\Omega + \omega V}{A} \tag{2.12}$$

$$\left(\frac{\partial V}{\partial t}\right) + V\left(\frac{\partial V}{\partial x}\right) + \frac{1}{\rho}\left(\frac{\partial p}{\partial x}\right) = -\frac{\omega}{A\rho} - g\sin\theta \tag{2.13}$$

$$\left(\frac{\partial T}{\partial t}\right) + V\left(\frac{\partial T}{\partial x}\right) + \frac{V_w^2}{c_p}\left[1 + \frac{T}{Z}\left(\frac{\partial Z}{\partial T}\right)_p\right]\left(\frac{\partial V}{\partial x}\right) = \frac{V_w^2}{c_p p}\left[1 - \frac{p}{Z}\left(\frac{\partial Z}{\partial p}\right)_T\right]\frac{\Omega + \omega V}{A} \tag{2.14}$$

Where the wave speed (V_w) is:

$$V_w = \sqrt{\frac{ZRT}{\left\{1 - \frac{p}{Z}\left(\frac{\partial Z}{\partial p}\right)_T - \frac{p}{\rho c_p T}\left[1 + \frac{T}{Z}\left(\frac{\partial Z}{\partial T}\right)_p\right]\right\}}} \tag{2.15}$$

Manifold Design and Analysis

Bourn et al. (2005) described work conducted in a project to investigate two-stroke cycle engine air balance and manifold designs to improve the trapped air mass balance between cylinders. Field and laboratory measurements of dynamic cylinder pressure on several engine models showed significant variation in compression pressures between cylinders during the compression stroke. Flow variation due to manifold design and/or dynamic pulsations were assumed to cause the spread in compression pressure by creating deviations in the scavenging and resulting trapped mass. A spread in trapped air mass, and therefore trapped air/fuel ratio, would lead to undesirable results such as lower efficiency, higher NO_X production, increased crank shaft stress, increased vibration, and reduced operating margins from detonation and misfire. The authors focused on quantifying the root causes of the compression pressure spread and developed solutions to improve the air balance and reduce variations in trapped air/fuel ratio between cylinders. This project used a laboratory Cooper GMVH-6 turbocharged two-stroke cycle engine to allow for detailed measurements and testing flexibility. A computational model was developed for this engine to aid in the investigation of manifold dynamic flows and design.

Scherer et al. (1997) presented an analysis of manifold pressure pulsations, the influence of these pulsations on mean value throttle and manifold models, and a precise algorithm for the estimation of the in-cylinder air mass. The simulation results of the throttle and manifold model were discussed and compared with experimental results from a steady state flow test bench and engine experiments. By calculating the correct geometrical area of flow, at a constant discharge coefficient, the air mass error was less than 10% compared with steady flow experiments. But with manifold pressure pulsations, there was still a large difference between simulated and measured air mass flow which was compensated for when using mean value models. The nonlinear behavior of the throttle is analyzed and discussed. The air fuel ratio control, a nonlinear observer algorithm for the estimation of the in cylinder air mass was presented. The influence of the pressure pulsations was compensated by modeling the effective area of flow as a sound wave and combining its estimated state with the estimated mean value and the air mass flow at the throttle. Pressure and airflow pulsations were modeled as harmonic perturbations. The use of the redundant information contained in the different sensor signals (throttle air flow, throttle angle, manifold absolute pressure) resulted in a precise, reliable, and sensor fault tolerant operation of the outgoing algorithm.

Gas Exchange Processes and Port Flow

Annand and Roe (1974) described the flow of air and exhaust gases through the engine system as governed by fundamental laws of fluid dynamics, heat transfer, and thermodynamics. A mathematical model for gas flow through a restriction was derived from the mass flow equation for compressible ideal flow. Ideal flow was assumed to be frictionless, steady, adiabatic, and reversible. The development was dimensionless and well suited for experimental test due to the relative ease of measurement of the variables involved and its computational simplicity.

Chapman and Beshouri (2000) presented a short course highlighting the development of an algorithm to forecast air flow through large-bore internal combustion engines. The course included modeling schemes for the flow phenomena through engine components such as valves and ports as well as means to take into account the unsteady nature of the flow in computing the air flow rate. The algorithm was intended to improve turbocharger-engine matching processes, and enhance the existing knowledge base to improve the ability of design engineers to properly size turbochargers to existing and modified engines.

Heywood (1988) discussed in depth the importance of intake and exhaust systems as those systems that govern the air flow into the engines cylinders in Chapter 7 of his text. The objectives of any gas exchange model have an important bearing on its complexity and structure. The author outlined three types of models for calculating details of intake and exhaust flows: 1) quasi-steady models for flows through the restrictions which the valve or port provide, 2) filling and emptying models, which account for the finite volume of critical manifold components, and 3) gas dynamic models which describe the spatial variations in flow and pressure through manifolds.

Heywood and Sher (1999) examined how the mass flow rate through a scavenging or exhaust port depends on port geometry and flow parameters. Equations were presented for calculating the mass flow rate of a compressible gas through a restriction derived from a one-dimensional isentropic flow analysis. Real flow effects were included by using an experimentally determined discharge coefficient. The multiplication of this coefficient by the reference area gave the effective area of the restriction. The discharge coefficient was presented as the ratio between the actual mass flow rate through the port and the theoretical mass flow rate assuming isentropic expansion.

Li (2003) developed correlation and discharge coefficients that could be used to accurately determine air flow rates through large-bore engine ports at various pressure ratios. The data may be used by designers to better match turbochargers and aftercoolers to engines. The methodologies employed included experimental tests and numerical simulations. A flow bench was designed to experimentally determine the discharge coefficients of ports in three primary large-bore engines: Clark HBA, Cooper GMVA and Worthington UTC. The results showed that the Clark cylinder intake ports interfere with each other whereas the Cooper intake ports do not exhibit any interference with each other. The Clark intake ports discharge coefficients were approximately 38% higher than the Cooper intake port discharge coefficients. Hence, for a given flow area, the Clark ports were expected to transport more air than the Cooper intake ports. The Worthington UTC liner with a "dog-legged" port configuration had a higher intake port discharge coefficient of 0.8 compared to the intake port discharge coefficient of 0.65 for the Clark and of 0.4 for the Cooper engines. The data also showed the substantial difference between the discharge coefficients for large-bore engine ports and for small ports from the open literature. The validity of the numerical method was proven by a close match of the numerical results to the experimental results.

Miyasato (1997) presented the development of an algorithm to predict air flow through large-bore internal combustion engines. The author described modeling schemes for the flow phenomena through engine components such as valves and ports as well as the means to account for the unsteady nature of the flow in computing the mass flow rate. The algorithm was intended to improve the turbocharger-engine matching processes, and its study and development would enhance the existing knowledge base that will then improve the ability of design engineers to properly size turbochargers for existing and modified engines.

Reddy (1995) developed a 2SC RICE model for integration into the existing Turbocharger-Reciprocating Engine Compressor Simulation (T-RECS) algorithm developed at the National Gas Machinery Laboratory (NGML). The 2SC model predicted the mass flow rate and the performance characteristics of 2SC RICE and worked in conjunction with the other components of the T-RECS algorithm to define parameters for turbocharger component matching. The simulation predicted optimal performance parameters and exhaust concentrations of oxides of nitrogen for various operating conditions.

Information included in the prior art reviewed above allowed the author to model flow of the charge air into the cylinder via the intake ports and burned gases out of the cylinder via the exhaust ports is modeled as one-dimensional, quasi-steady, compressible flow through a restriction. Solving the above system of conservation equations results in a temporal and spatial distribution of the fluid parameters within the manifold-runner pipe network. The solution scheme uses the upstream pressure and gas temperature, or boundary conditions for quantifying flow through the intake and exhaust ports of the large-bore 2SC engine. The appropriate relationship is (Annand and Roe, 1974):

$$\dot{m} = \frac{C_D A_T p_0}{\sqrt{R T_0}} \left(\frac{p_T}{p_0}\right)^{\frac{1}{\gamma}} \left\{\frac{2\gamma}{\gamma - 1}\left[1 - \left(\frac{p_T}{p_0}\right)^{\frac{\gamma-1}{\gamma}}\right]\right\}^{\frac{1}{2}} \tag{2.16}$$

The values C_D and A_T represent the discharge coefficient and the minimum area of the restriction. The subscript ‘0’ refers to the upstream stagnation point of the restriction. For flow into the cylinder via the intake or air delivery system, the stagnation conditions refer to local time-dependant conditions in the intake manifold. For exhaust flow out of the cylinder, the stagnation conditions refer to conditions in the cylinder. Alternately, the subscript 'T' refers to values at the restriction, or port in this case. A thorough derivation of the final equation relating mass flow rate to pressure and temperature is in Appendix B -Compressible Flow through a Restriction.

To evaluate the management of fluid flow into or out of the cylinder, the discharge coefficient (C_D) must be determined experimentally or numerically. An experimental analysis and development of a method to optimize the discharge coefficient of large-bore 2SC engines is presented in Chapter 5 of this work.

The simplest variation of the 2SC engine design includes ports in the cylinder liner, uncovered and covered by the piston motion, which control the exhaust removal and intake flow. Replacement of the burned gases with fresh charge – broadly referred to as the gas exchange process – is identified as "scavenging" in 2SC engines. After combustion, the piston motion uncovers the exhaust ports and the high in-cylinder pressure ejects the burned gases into the exhaust removal system. This process, prior to intake port opening, is called blow-down. As the cylinder pressure decreases, and the piston continues toward bottom dead center (BDC), the intake ports are uncovered. When the cylinder pressure falls below the intake pressure, charge air enters the cylinder and scavenging begins. This flow continues as long as the intake ports are uncovered and the inlet pressure exceeds the pressure in the cylinder. As the piston begins to move back up, the fresh charge air replaces the burned gases. The scavenging process is complete when the exhaust ports are covered (Heywood, 1988).

The crank angle (CA) at which the ports open, the size, number, geometry, and location of the ports around the cylinder circumference, and the direction and velocity of the flow issuing from the ports into and out of the cylinder all affect the cylinder scavenging (Heywood, 1988). The quality of the gas exchange process is defined primarily by the scavenging efficiency (η_{se}):

$$\eta_{se} = \frac{m_{re}}{m_{tr}} \tag{2.17}$$

The scavenging efficiency indicates to what extent the residual gases in the cylinder have been replaced with fresh air, specifically, the mass of delivered air retained by the cylinder (m_{re}) divided by the mass of trapped cylinder charge (m_{tr}).

In real scavenging processes, mixing occurs as the fresh charge air displaces the burned gases and some of the fresh charge may be expelled. Two limiting ideal models have been defined: 1) perfect displacement, and 2) complete mixing. Perfect displacement would occur if the burned gases were replaced by fresh charge without mixing. Complete mixing occurs if the entering fresh charge mixes spontaneously and uniformly with the remaining burned gases. In order to take into account the imperfect nature of real scavenging processes, *Chapman and Beshouri (2000)* proposed a modified mixing model, to allow for tuning of the engine scavenging to the candidate engine air delivery system:

$$\eta_{se} = \kappa_2 (1 - \kappa_1 e^{-\Lambda}) \tag{2.18}$$

The delivery ratio (Λ) is defined by a ratio of the mass of delivered charge air (m_{ca}) to a reference mass, quantified by the displacement volume of the cylinder ($\forall_d$) and the gas density (ρ_{ca}):

$$\Lambda = \frac{m_{ca}}{\forall_d \rho_{ca}} \tag{2.19}$$

Technologies for Air Management

Azechi et al. (1992) outlined a throttle-valve-actuation system which can easily be installed in conventional stationary gas engines to improve the thermal efficiency under low-NO_X-emission conditions. The system was applied to a six-cylinder turbocharged and aftercooled engine, and implemented to control the intake-air throttle valve for a stationary natural gas engine. The throttle system consisted of an additional rotary valve provided with a variable timing device and a conventional butterfly valve. This throttle system could simultaneously control not only the mass flow rate of the air-fuel mixture by changing the intake duration, but also the compression ratio. The experimental results showed an improvement in thermal efficiency at part load and reduced NO_X emissions.

Benson et al. (1974) studied steady and non-steady flow through a carburetor. A model was presented in which the carburetor was represented by an adiabatic pressure loss at a discontinuity in the intake system of an engine. They showed that the simple model gives consistent predictions of the pressure-time development in the intake system except at small throttle openings where there was some error in the peak amplitude. Mass flow and trapped mass predictions were also presented.

Gad-el-Hak (2000) discussed the technological importance of actively or passively manipulating a flow field. The author provided an up-to-date review of the fundamentals of some basic flows and control practices that can be employed to produce needed effects. The literature covered ideas and methods for affecting such control to achieve transition delay, separation prevention, drag reduction, lift augmentation, turbulence suppression, noise abatement, and heat and mass transfer (including combustion) enhancement in both free-shear and wall-bounded flows.

Heywood (1988) presented the throttle as the minimum flow area in the entire intake system, except at or close to wide-open throttle in Chapter 14 of his text. In analyzing flow through the throttle plate, the author encouraged the consideration of: 1) throttle shaft size, 2) discharge coefficient as less than that of a smooth converging-diverging nozzle, 3) discharge coefficient variation with throttle angle, pressure ratio, and Reynolds number, and 4) minimum leakage area due to manufacturing tolerances even when the throttle plate is closed. An equation characterizing the throttle plate open area in terms of throttle angle was given. Mass flow rate through the throttle valve could be calculated from standard orifice equations for compressible fluid flow when the reference area was the calculated throttle open area and the discharge coefficient was determined experimentally.

Ingram et al. (2003) developed a robust feedback controller design procedure to regulate the mass air flow (MAF) into a 4.6L V8 spark ignition engine. A system level model of engine throttle to engine mass air flow was experimentally determined. The authors focused on lean burn technology and used a catalyst during lean combustion. Once the catalyst was full of NO_X the authors ran the automobile rich to purge the catalyst. This transfer from lean to rich burn was done using the mass air flow control system. The authors also acknowledged that the individual air charge per cylinder was directly related to torque and emissions. For the MAF feedback controller, the authors used a standard frequency response calculation. In addition, a controller was designed to control engine mass air flow with zero steady state error while addressing the nonlinear throttle characteristics and pure delay. The controller design methodology applied to the mass air flow control problem was discussed and an interpretation of the controller presented. Finally, engine dynamometer data demonstrated that the controller rejected noise and disturbances while meeting transient and steady state performance objectives.

Sullivan (1998) presented varying types of mass air flow meters currently utilized by the automotive industry. The mass air flow sensor converted the rate of air drawn into the engine into a voltage signal. The signal was used by the engine controller to calculate air volume and engine load. The air flow sensor in automotive applications was located directly in the intake air stream, between the air cleaner and throttle body where it could measure incoming air. The author outlined components, design, applications, and operation of the: 1) hot wire anemometer; 2) vane air flow meter; and 3) Karmen vortex air flow meter.

Woods and Goh (1979) reviewed various applications of butterfly throttle valves. The authors presented tests examining the flow characteristics of a butterfly throttle valve in relation to valve opening, pressure ratio and circumferential and axial location of the pressure tapping. They gave results of a comprehensive series of steady flow tests and, also, results of a limited number of unsteady flow tests. In the latter, the butterfly throttle valve was located in the intake system of a single cylinder diesel engine. The paper highlighted the importance of the position of pressure tapping when pressure measurements were used to estimate flow rates. The results of the study showed that when suitable precautions are taken, the quasi-steady flow method may be used to predict the flow rate under pulsating conditions.

Emission Production and Reduction

Adriani (2005) discussed emission control technologies applied to a two-stroke cycle natural gas-fueled engine. In this first phase, a one-cylinder Ajax DP-115 was used to assess a variety of low-emissions technologies. These technologies were targeted to the exploration and production oil and gas field engines to meet clean air requirements. The primary goal in this project was to determine a roadmap to apply successful NO_X reduction technologies for pipeline engines, to exploration and production engines, such as the Ajax. The paper described the battery of tests that demonstrated synergies between some technologies, as well as the impact and capabilities of new technologies, such as ion sensing. The end goal was a closed loop control, low cost NO_X retrofit package. The battery of tests included a range of fuel nozzles, pre-combustion chambers, in-cylinder sensors, the means to adjust the air-to fuel ratio, and electronic fuel injection. The battery of tests with these technologies showed the capability of optimizing the engine and reducing NO_X.

Beshouri (1999) describes the need to establish accurate emissions inventories for reciprocating engine-compressors to assess their contribution to overall emissions generation, and to provide data for increasing interest in trade-offs between emissions of NO_X versus CO, total HC and, in particular, HAP. These chemicals have contributed to heightened interest in real world engine emissions, and the associated trade-offs in lean burn engine performance. This interest has created a strong incentive to collect, collate, and characterize a reliable database which owner/operators can utilize to make informed, cost competitive emissions related decisions. Therefore, engine performance and emissions data from seven industry- and client-funded projects encompassing 26 engines of 18 different models typifying 2SC and four-stroke cycle (4SC) open and pre-combustion chamber engines in gas transmission service were compiled into a common database. Then, using the database, the trade-offs between NO_X and other engine pollutant emissions, in addition to engine performance was analyzed.

Borman and Ragland (1998) presented a general global rate reaction scheme for hydrocarbon fuels in Chapter 4 of their text. Because the elementary reaction schemes for hydrocarbons were so complex, it was not feasible to consider all the chemically reacting species and their reaction rates when analyzing practical combustion systems; therefore, it is useful to use an overall, simplified one- or two-step scheme. This simplification allowed for practical simulation for numerical fluid mechanical codes, but the authors warn that use of global sets of this sort should be limited to the regimes for which they have been tested. The authors presented a two-step reaction for the combustion of methane (CH_4) to CO, and then the oxidation of CO to form carbon dioxide (CO_2). The authors also discussed the application of kinetic models to lean burn, low temperature combustion to overcome the difference in concentration between chemical equilibrium CO and measured values. The authors finally suggested the use of implicit methods for solving "stiff" kinetic equations, rather than the use of standard methods such as Runge-Kutta, which can be unstable when radical species have much shorter time constants than the major combustion species.

Bowman (1975) reviewed previous investigations of the kinetics of formation and destruction of nitrogen oxides, carbon monoxide and organic pollutants and examines the coupling between the pollutant chemistry and the combustion process. There are five pollutant species created during the combustion process: NO_X, CO, unburned and partially burned HC, sulfur oxides, and particulates. Throughout the paper, the author analyzes the difference between exhaust values and calculated equilibrium values for each pollutant. The formation and oxidation of soot and the fate of sulfur compounds in combustion are not discussed.

Chapman (2008) developed a gas turbine combustor model applying first engineering principles to calculate the emission formation of NO_X and CO from a gas turbine engine. The model was based on a lean-premixed combustor with a main and pilot burner, including the function of a bleeding air valve. The model relied on ambient condition and load. The load was expressed as a percentage of the target speed of the gas producer turbine. Air flow and fuel flow for the main and pilot burners was calculated by the model based on the load through a set of measured input data for a specific gas turbine. To find the combustion temperature characteristics, the combustor was divided into several zones. The temperature for each zone was calculated by applying an energy balance. To calculate NO_X and CO, several correlations explored by various researchers were used and compared against each other, using the calculated temperatures, pressures and equivalence ratios. The calculated emissions were compared to emissions data collected from a gas turbine engine test cell at Solar Turbines Incorporated, San Diego, California. The comparison showed a highly accurate match for NO_X emissions at any load. Because of the high variation of CO at part load, the model calculations only matched the CO data set at full load.

Hughes et al. (2001) developed a comprehensive chemical mechanism to describe the oxidation of methane, consisting of 351 irreversible reactions of 37 species. The mechanism also accounted for the oxidation kinetics of hydrogen gas ($H_{2(g)}$), CO, ethane, and ethylene in flames and homogeneous ignition systems in a wide concentration range. The mechanism was tested against a variety of experimental measurements of laminar flame velocities, laminar flame species profiles, and ignition delay times. The highest sensitivity reactions of the mechanism were discussed in detail and compared with the same reactions in the GRI, Chevalier, and Konnov mechanisms. Similarities and differences of the four mechanisms were discussed.

Li et al. (2001) reported new experimental profiles of stable species concentrations for formaldehyde oxidation in a variable pressure flow reactor at initial temperatures of 850-950 K and at constant pressures ranging from 1.5 to 6.0 atm. The data, along with other data published in the literature and a previous comprehensive chemical kinetic model for methanol oxidation, were used to hierarchically develop an updated mechanism for $CO/H_2O/H_2/O_{2(g)}$, and CH_3OH oxidation. Important modifications include recent revisions to the hydrogen-oxygen sub-mechanism, an updated sub-mechanism for methanol reactions, and kinetic and thermo-chemical parameter modifications based upon recently published information. The presented C1/C2 mechanism compared favorably against a wide range of experimental conditions for laminar premixed flame speed, shock tube ignition delay, and flow reactor species time history data at each level of hierarchical development. Very good agreement between the model predictions and the experimental measurements was demonstrated.

PRCI (2005) presented a detailed technology development roadmap defining a comprehensive, multi-year plan for the PRCI Compressor and Pump Station research program to create options for pipelines to cost-effectively achieve 0.5 g/bhp-hr NO_X from legacy pipeline reciprocating engines. The options investigated do not increase other pollutants or have a negative effect on engine performance and reliability, and meet a cost-objective of 1⁄6 to 1⁄3 the installed cost of replacement horsepower. The roadmap incorporates the accumulated knowledge of 15 years of prior pipeline emissions control research and development, user experience with first and second generation control technologies, state NO_X control programs, current vendor products, and parallel reciprocating engine developments pursued under separate public and private initiatives. The premise of the technology development roadmap was that emissions control is a multi-faceted issue that crosscuts many engine subsystems and components, and that significant variations in legacy engine designs preclude a single solution. The roadmap concludes that this option should be carefully examined to determine its technical maturity and cost-effectiveness vis-à-vis conventional alternatives, as well as to rigorously identify application challenges that may preclude its wide use. The roadmap defined a set of risk-controlled technology development pathways to achieve the very aggressive NO_X control requirements anticipated for ~2010. It outlined development options that are rank-ordered using qualitative marginal benefit/cost and technical risk considerations, and identifies research and development decision points where alternative solutions should be considered.

Westbrook and Dryer (1984) reviewed chemical kinetic modeling of high temperature hydrocarbon oxidation in combustion. The authors discussed reaction mechanism for specific fuels with emphasis on the hierarchical structure of the mechanisms for complex fuels. A comprehensive mechanism was developed and validated by comparison with data from a wide range of experimental regimes. Fuels of increasing complexity from hydrogen to n-butane were described in detail, along with further extensions of the general approach to other fuels. Application of kinetic models, beginning with kinetic-thermodynamic application, where heat and mass can be neglected, to laminar flames and the coupling of diffusive transport and chemical kinetics, to practical combustion problems were included.

Zervas (2003) used a spark ignition engine to determine the influence of fuel composition and air/fuel equivalence ratio on the exhaust emissions of regulated pollutants. Two specific fuel matrices were used: the first contains eight HC and the second contains four oxygenated compounds. A specific experimental design was used for these tests. Fuel aromatics increased the exhaust CO, HC, and NO_X at stoichiometry, lean and rich conditions. Lambda was more important than fuel composition in the case of CO and HC. At stoichiometry, the addition of oxygenated compounds could decrease exhaust CO, HC, and NO_X up to 30%, 50%, and 60%, respectively. Under those conditions, the addition of 5% of 2-propanol was the most effective for the reduction of CO, the addition of 20% of ethanol for the reduction of HC, and that of 5% of methyl tributyl ester (MTBE) for the NO_X. The addition of oxygenated compounds could decrease CO by 30% at lean conditions, while no decrease was observed at rich ones; HC and

NO_X could decrease up to 30% and 80%, respectively, under lean conditions and 50% under rich ones. At all lambda tested, exhaust NO_X increased with the addition of 20% of 2-propanol.

The large-bore 2SC engine exhaust gases contain NO, NO_2, CO, and organic compounds which are unburned or partially burned HC. Hydrocarbons, or more appropriately organic emissions, are the consequence of incomplete combustion of the HC fuel. While the total HC emission is a useful measure of combustion efficiency, it is not necessarily a significant index of regulated pollutant emissions (Borman and Ragland, 1998). Thus, further discussion of pollutant emissions in this work will focus on the formation of NO_X and CO.

In general, the concentrations of these pollutants in 2SC engine exhaust differ from values calculated assuming chemical equilibrium. As such, the detailed chemical kinetics processes by which these pollutants are formed are important to determining emissions levels. The formation and destruction of CO is intimately coupled with the primary fuel combustion process; thus, an understanding of combustion chemistry is needed.

The combustion environment is primarily controlled by the corrected trapped equivalence ratio (φ_{se}), which compares the actual fuel to air ratio to the stoichiometric fuel to air ratio, corrected by the scavenging efficiency (η_{se}):

$$\varphi_{se} = \frac{1}{\eta_{se}}\left[\frac{\left(\frac{\dot{m}_{fu}}{\dot{m}_{ca}}\right)_a}{\left(\frac{\dot{m}_{fu}}{\dot{m}_{ca}}\right)_{stoich}}\right] \tag{2.20}$$

where the scavenging efficiency (η_{se}) was defined previously in equation (2.18). The corrected trapped equivalence ratio, coupled with the ignition timing (IT) of the engine controls the temperature of the primary combustion reaction and therefore the temperature of the environment created by the combustion event. For NO_X, the formation and destruction processes are not part of the fuel combustion, but the reactions that produce these species take place in an environment created by the combustion itself (Bowman, 1975). This correlation is written in the form:

$$\mathrm{NO_X}(\varphi_{se},\mathrm{IT}) \tag{2.21}$$

NO is the predominant oxide of nitrogen produced inside the engine cylinder. NO forms throughout the high-temperature burned gases both in the flame front and post-flame gases through chemical reactions involving nitrogen and oxygen atoms and molecules that do not attain chemical equilibrium. The mechanism of NO formation from atmospheric nitrogen has been studied extensively. It is generally accepted that in combustion of fuel-air mixtures the principal reaction governing formation and destruction of NO from molecular nitrogen are:

$$\mathrm{O + N_2 \overset{1}{\leftrightarrow} NO + N}$$

$$\mathrm{N + O_2 \overset{2}{\leftrightarrow} NO + O}$$

$$\mathrm{N + OH \overset{3}{\leftrightarrow} NO + H}$$

For modeling chemical kinetics, a uniform method for expressing the variation of reaction rates with temperature, called the Arrhenius form, has been adopted. The reaction rate (k) is a function of the temperature (T), the activation energy of the fuel (E_a), and a pre-exponential collision frequency factor (k_{co}):

$$k = k_{co}T^n e^{-\frac{E_a}{\hat{R}T}} \tag{2.22}$$

It is important to note that the pre-exponential collision frequency factor (k_{co}) is a function of the amount of fuel introduced to the combustion environment, or more generally, the corrected trapped equivalence ratio (φ_{se}), and should be experimentally determined as such.

The forward (k_f) and reverse (k_b) rate constants for the three reactions listed previously have been measured in numerous experimental studies. NO formation in the post flame gases almost always dominated any flame-front produced NO. Therefore, it is appropriate to assume that the combustion and NO formation processes are coupled. This assumption allows for the approximation of the concentrations of molecular oxygen (O), oxygen gas (O_2), hydroxide (OH), molecular hydrogen (H), and nitrogen gas (N_2) by their respective equilibrium values. From the above chemical reactions with rate constants defined by equation (2.22), the rate of formation of NO is given by:

$$\frac{d[\mathrm{NO}]}{dt} = k_{f1}[\mathrm{O}][\mathrm{N_2}] - k_{b1}[\mathrm{NO}][\mathrm{N}] + k_{f2}[\mathrm{N}][\mathrm{O_2}] - k_{b2}[\mathrm{NO}][\mathrm{O}] + k_{f3}[\mathrm{N}][\mathrm{OH}] - k_{b3}[\mathrm{NO}][\mathrm{H}] \tag{2.23}$$

Chemical equilibrium considerations indicate that for burned gases at typical flame temperatures, NO_2/NO ratios should be negligibly small. However, NO formed in the flame zone can be rapidly converted to NO_2 via simple reactions with hydroxide (OH) or oxygen (O_2) molecules (Bowman, 1975).

CO emission formation and destruction is primarily controlled by the corrected trapped equivalence ratio and the oxidation of a hydrocarbon fuel. Methane oxidation, the hydrocarbon of interest in this work, has been studied extensively. Data from a flow reactor for lean methane-air mixtures was used to generate concentration profiles for CH_4, CO_2, and six intermediate species. A kinetic model was developed from extensive experimentation which included 207 reactions with 40 species. The major trends are shown in Figure 2.1 (Borman and Ragland, 1998):

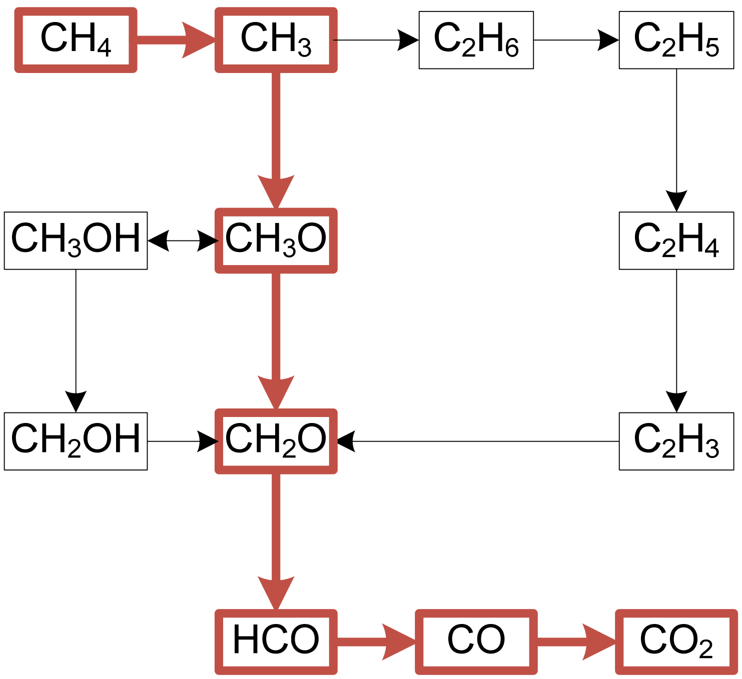

Figure 2.1: Primary reaction mechanisms for CH_4 oxidation

This complex combustion mechanism still does not completely describe CH_4 combustion. The use of every mechanism to quantify the oxidation event could require the solution of approximately 1000 coupled differential equations (Westbrook and Dryer, 1984). Furthermore, these equations must be solved at each time step in the numerical solution of the combustion problem.

The levels of CO observed in spark-ignition engine exhaust gases are lower than the maximum valued measured within the combustion chamber, but are significantly higher than the equilibrium values for the exhaust conditions. Thus the processes which govern CO exhaust levels are kinetically controlled; therefore, a cycle-resolved correlation for CO formation and oxidation in lean-burn 2SC engines must be defined. During combustion, CO values within the cylinder are contributed to a kinetic formation mechanism. Once the combustion event has been completed, and the expansion process begins, values of CO within the cylinder are then controlled by a kinetic oxidation mechanism.

In order to simplify calculations, a quasi-global model has been applied with some success to model the energy-release rates for combustion of several hydrocarbon fuels. Hence, it may be possible to model CO formation by a one-step reaction in which CH_4 reacts with O_2 to form CO and hydrogen gas (H_2) at some experimentally determined rate:

$$\mathrm{CH_4} + \tfrac{1}{2}\mathrm{O_2} \rightarrow \mathrm{CO} + 2\mathrm{H_2}$$

The formation rate of CO is then:

$$\frac{d[\mathrm{CO}]}{dt} = k_f[\mathrm{CH_4}][\mathrm{O_2}]^{\frac{1}{2}} \tag{2.24}$$

A few select previously published values for the kinetic formation of CO are summarized in Table 2.2 (Westbrook and Dryer, 1984). These values are for ideal, pre-mixed, laminar flames at constant pressure and temperature.

Table 2.2: Global constants for CO formation

Fuel	k_{co}	E_a (kcal/gmol)	Reference
CO	$10^{14.6}$	40.0	(Westbrook and Dryer, 1984)
CO	5.0×10^8	40.0	(Westbrook and Dryer, 1984)

This formation rate for CO can also be expressed as the negative rate of consumption or oxidation of the fuel, methane in this case:

$$\frac{d[\mathrm{CH_4}]}{dt} = -k_f[\mathrm{CH_4}][\mathrm{O_2}]^{\frac{1}{2}} \tag{2.25}$$

Previously published values for the kinetic oxidation of methane are summarized in Table 2.3 (Bowman, 1975).

Table 2.3: Global constants for CH_4 oxidation

Fuel	k_{co}	E_a (kcal/gmol)	Reference
CH_4	2.8×10^9	48.4	(Bowman, 1975)
CH_4	1.5×10^7	30.0	(Bowman, 1975)

As discussed previously, the reaction rate constant must be determined via comparison with experimental results. The concentration of methane ([CH_4]) and the oxygen gas concentration ([O_2]) may be found using the corrected trapped equivalence ratio and in-cylinder burn-rate.

The CO formed in the combustion process is oxidized to CO_2 during expansion at a rate which is relatively slow compared to the CO formation rate. CO may be formed via a series of rapid reactions, most notably:

$$\mathrm{CO} + \mathrm{OH} \leftrightarrow \mathrm{CO_2} + \mathrm{H}$$

In order to force the above model to agree with experimental values, the rate of the reaction must be reduced by a factor of ten below its known value. The magnitude of this disagreement indicates that the initial mechanism is inadequate and must be augmented to include reactions with hydroperoxyl (HO_2) and hydrogen peroxide (H_2O_2), which dramatically improved the model predictions. Therefore, several investigators have determined “overall” kinetics equations for CO oxidation by using a two-step global reaction (Westbrook and Dryer, 1984):

$$\mathrm{CH_4} + \tfrac{3}{2}\mathrm{O_2} \rightarrow \mathrm{CO} + 2\mathrm{H_2O}$$

$$\mathrm{CO} + \tfrac{1}{2}\mathrm{O_2} \rightarrow \mathrm{CO_2}$$

This two-step global reaction is for CO oxidation only, not to be confused with the above one-step reaction for CO formation. A reverse rate for the CO oxidation step can be introduced to account for the variation of extent of reaction and heat release with corrected trapped equivalence ratio and the effects of pressure variation. As with the CO formation reaction rate, the oxidation reaction rate (k_{ox}) must be determined via comparison to experimental results.

The oxidation rate of CO is then:

$$\frac{d[\mathrm{CO}]}{dt} = k_{ox}[\mathrm{CO}][H_2O]^{\frac{1}{2}}[\mathrm{O}_2]^{\frac{1}{2}} \tag{2.26}$$

This kinetic oxidation reaction continues throughout cylinder expansion and blow-down, until the intake ports are uncovered. At the initiation of scavenging, it can be assumed that the concentration of CO is frozen (Borman and Ragland, 1998). A final kinetic mechanism can be defined by combining equation (3.28) and equation (3.30) via the method included in Appendix D - Chemical Kinetic Reaction Mechanism Development:

$$\frac{d[\mathrm{CO}]}{dt} = k_{form}[\mathrm{CH}_4][\mathrm{O}_2]^{\frac{1}{2}} - k_{ox}[\mathrm{CO}][H_2O]^{\frac{1}{2}}[\mathrm{O}_2]^{\frac{1}{2}} \tag{2.27}$$

It is imperative that the optimization of the engine air management system, a primary objective of this work, does not adversely affect the exhaust pollutant emission concentrations of $\mathrm{NO_X}$ or CO.

Exhaust System Analysis

Analysis of the exhaust system includes physical geometry, gas exchange and blow-down processes, pulsation, and the relation between exhaust system performance and turbocharger operation.

Adair et al. (2006) performed computational modeling of the exhaust system of two types of large-bore, multi-cylinder, 2SC engine. The airflow performance of a four-cylinder V-bank Cooper GMV-4TF engine and a six-cylinder in-line Clark TLA engine was simulated. The simulation included the computation of pressure wave propagation in the exhaust manifold. Using a modified method of the steepest ascent numerical technique, tuned exhaust manifolds were designed for each engine with the objective of reduced NO_X emissions. The NO_X reduction was accomplished by increasing the trapped cylinder mass and correspondingly reducing the peak combustion temperature. The simulations predicted NO_X reductions in the range 10–30 percent as a result of exhaust tuning. However, a thorough review of industry resources and available literature proved tuning of the large "log" style manifolds to be impractical.

Macian (2004) examined the difficulty of measuring instantaneous exhaust pressure in internal combustion engines in a production environment. High temperatures of the exhaust manifold and its pulsating character made the application of exhaust gas recirculation control algorithms impossible. An alternative method for estimating the exhaust pressure pulsation was presented. A numerical model was built which enabled the exhaust pressure pulses to be forecasted from instantaneous turbocharger speed measurements. Although the model was data based, a theoretical description of the process was also provided. This combined approach made it possible to integrate the model at different engine operating points. Also, the compressor contribution in the turbocharger speed pulsation was discussed extensively. The compressor contribution was initially neglected, and an analysis of this simplified approach was included.

Sengupta et al. (2006) discussed the ejection of exhaust gases from the cylinder of both the two-stroke cycle and the four-stroke cycle internal combustion engine. This activity was termed 'blow-down.' In a 2SC engine the in-cylinder gases, which are at a pressure higher than the exhaust manifold pressure, burst out of the exhaust port into the manifold, resulting in a high-pressure wave propagating through the manifold. In a multi-cylinder engine where the exhaust ports of each cylinder are connected to the manifold, the high pressure pulses in the manifold will augment the in-cylinder performance of the cylinders downstream of the first cylinder. This impact was investigated using the T-RECS, a zero-dimensional cycle simulation tool developed at the NGML. Manifold pressure distributions were generated using the NGML developed Virtual Pipeline Simulation Tool, which was a one-dimensional pipe flow simulation software package. The analysis assumed that at any given instant the exhaust port of only one cylinder was open while the exhaust ports of all other cylinders remained closed. The results showed that the in-cylinder pressure distributions could be significantly altered under the influence of the exhaust manifold pressure pulses.

Available Energy Analysis

In this study, a second law thermodynamic analysis of the turbocharged-engine system is used to quantify the amount of available energy, mechanical and thermal, at the turbocharger turbine via the exhaust stream.

Lawland (2009) analyzed the use of turbocharger systems for spark-ignition engines due to the importance of fuel efficiency, and in some cases, increased performance. To better understand the tradeoffs and the fundamental aspects of a turbocharged engine, the authors investigated the energy and exergy quantities for a range of operating conditions for a spark-ignition engine.

Moran (1989) provided a comprehensive presentation of the availability method of analysis. Specifically, the author focused on the use of the availability equation as an important unifying concept, a thorough discussion of the meaning and use of second law efficiencies, exact and approximant methods for calculating the availabilities of pure fuels and fuel mixtures, means for the evaluation of combustion and other chemical processes, and an introduction to the use of availability analysis in the field of engineering economics.

Paulus (2001) proposed that consideration be given to an alternative, streamlined manner for mathematical modeling of the performance of energy conversion and transfer equipment. The authors make the case by application to compressors. Instead of using an expression for efficiency as one of the governing equations, performance could be accounted for directly, with entropy production. It was shown that: (1) the modeling is more straightforward, using fewer relations, and (2) compressor performance (e.g. maps) can be represented equally well.

Rakopoulos (2006) presented a survey of publications available concerning the application of the second-law of thermodynamics to internal combustion engines. The availability (exergy) balance equations of the engine cylinder and subsystems were reviewed in detail providing also relations concerning the definition of state properties, chemical availability, flow and fuel availability, and dead state. Special attention was given to identification and quantification of second-law efficiencies and the irreversibility of various processes and subsystems.

Sayin (2007) presented a comparative energy and exergy analysis of a four-cylinder, 4SC spark-ignition (SI) engine using gasoline fuels of three different research octane numbers, namely 91, 93 and 95.3. Each fuel test was performed by varying the engine speed between 1,200 and 2,400 rpm at an engine torque of 20 and 40 N-m. Then, using the steady-state data along with energy and exergy rate balance equations, various performance parameters of the engine were evaluated for each fuel case. It was found that the gasoline of 91-RON, the design octane rating of the test engine, yielded increased energetic and exergetic performance, while the exergetic performance parameters were slightly lower than the corresponding energetic ones. Furthermore, this study revealed that the combustion process was the most important contributor to the system inefficiency, and almost all performance parameters increased with increasing engine speed.

Sezer (2008) presents a study aimed at the theoretical exergetic evaluation of spark ignition engine operation. For this purpose, a two-zone quasi-dimensional cycle model was developed, excluding the complex calculation of fluid motions. The cycle simulation consisted of compression, combustion, and expansion cycles. The combustion phase was simulated as a turbulent flame propagation process. Intake and exhaust processes were also considered using a simple approximation method. The results of the model were compared with experimental data for validation. The results of the exergy analysis show that variations of operation parameters examined have considerable effect on the exergy transfers, irreversibility, and efficiency.

Yoshida (2005) evaluated the available energy losses, i.e. exergy losses, caused by irreversible processes in the theoretical cycle of 2SC and 4SC diesel engines. All exergy losses in these cycles were divided into three categories: (1) heat receiving processes, (2) scavenging processes in turbocharged diesel engines, and (3) heat loss dissipated by exhaust gas and cooling water. The quantity of each exergy loss was distinctly expressed via a temperature-entropy diagram. Thermal efficiency was improved by reducing exergy loss.

The maximum power that a given engine can deliver is limited by the amount of fuel that can be burned efficiently inside each cylinder. This is limited by the amount of air that is introduced into each cylinder each cycle. If the inducted air is compressed to a higher density than ambient, prior to entry into the cylinder, the maximum power an engine of fixed dimensions can deliver will be increased. This is the primary purpose of supercharging or turbocharging the engine. Over the last 20 years, most large-bore 2SC engines have been retrofitted with a typical mechanical turbocharging system shown in Figure 2.2.

A turbocharger – a compressor and turbine on a single shaft – is used to “boost” the density of the charge air introduced to the intake system. After combustion, energy available in the engines exhaust stream is used to drive the turbocharger turbine which drives the turbocharger compressor, raising the density of the inlet fluid prior to entry to each engine cylinder.

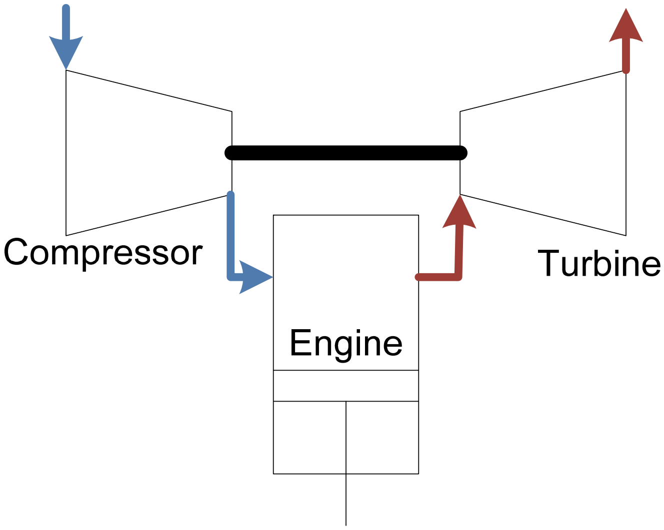

Figure 2.2: Turbocharged-Engine System

This cycle of fluid and mechanical energy transfer between the engine cylinder, turbocharger compressor, and turbocharger turbine is maintained by a delicate balance between the components operating parameters.

Of interest in engine performance analysis is the amount of useful work that can be extracted from the gases within the cylinder at each location in the air management system. Specifically, the quantification and optimization of the energy available to the turbocharger turbine via the engine exhaust removal system is of importance to this study. The first and second laws of thermodynamics together define this amount of useful work, which is expressed in terms of availability (AV). The amount of availability to the turbocharger turbine (AV_{TTI}) can be quantified by subtracting the availability lost due to thermal and mechanical losses within the fluid flow path (ΔAV_{EM}) from the amount of exhaust availability at the exhaust port opening (AV_{EPO}) (Heywood, 1988):

$$AV_{TTI} = AV_{EPO} - \Delta AV_{EM} \tag{2.28}$$

Availability at a given state is a function of the volume ($\forall$), entropy (S), and energy (E), referenced to a dead state, represented by the '0' subscript (Moran, 1989):

$$AV = (E - U_0) + p_0(\forall - \forall_0) - T_0(S - S_0) \tag{2.29}$$

Careful distinction should be made between availability losses and irreversibility within a component. Within the air management system, changes in the availability of the exhaust products can be divided into two categories: 1) thermo-mechanical or flow availability, and 2) thermal availability. Exhaust stream specific thermo-mechanical or flow availability can be determined by:

$$av_{fin} - av_{fex} = (h_{in} - h_{ex}) - T_0(s_{in} - s_{ex}) + \left(\frac{V_{in}^2 - V_{ex}^2}{2}\right) + g(z_{in} - z_{ex}) \tag{2.30}$$

Additionally, for a length of pipe, it is important to quantify the loss of availability and irreversibility due to radial heat transfer. For a length of pipe, the loss of availability due to radial heat transfer ($\dot{AV}_Q$) is:

$$\dot{AV}_Q = \left(1 - \frac{T_{amb}}{T_{fl}}\right)\dot{Q} \tag{2.31}$$

This loss of availability is a function of the local fluid temperature (T_{fl}) and the time rate of heat transfer from the pipe ($\dot{Q}$).

Summary

In summary, the literature presented in this chapter outlined current and previous investigations into the flow mechanics of the 2SC RICE charge air delivery and exhaust product removal systems. The review highlighted seven specific topics:

1. Compressible flow through the manifold and runners of large-bore 2SC RICE could be modeled as flow through a pipe.
2. There was a spread in trapped air mass due to manifold design and also pressure pulsations.
3. Flow through the ports of large-bore 2SC RICE could be modeled using quasi-steady calculations for the mass flow rate of a compressible gas through a restriction derived from a one-dimensional isentropic flow analysis.
4. Air flow was most readily managed in the automotive industry by way of a throttle plate, a technology that could readily be applied to large-bore 2SC RICE.
5. There was a need for technology to control the production of emissions, primarily NO_X and CO from the large-bore 2SC RICE.
6. Recently, there have been thorough investigations into the exhaust system including physical geometry, gas exchange and blow-down processes, pulsation, and the relation between exhaust system performance and turbocharger operation.
7. A second-law thermodynamic analysis of the turbocharged-engine system could be used to quantify the amount of available energy, mechanical and thermal, obtainable by the turbocharger turbine via the exhaust stream.

During the course of completing the presented review of prior art, the author found that the science lacked a system-based analysis of the large-bore 2SC engine. As a result, the author has completed a component focused design optimization of the large-bore 2SC engine using a system-based approach. The author completed a transient, open system, 1st and 2nd Law thermodynamic analysis, including validated chemical kinetic models for in-cylinder pollutant emission formation.

CHAPTER 3 - Mathematical Description

The literature review in Chapter 2 showed that modeling of the large-bore 2SC engine requires consideration of quasi-steady compressible fluid flow in addition to mass continuity, momentum transfer, and energy conservation. Supplementary mathematical models were required for prediction of pollutant emission formation. A second-law thermodynamic analysis of the 2SC engine could be used to quantify the amount of available energy, mechanical and thermal, obtainable by the turbocharger turbine via the engine exhaust stream.

This chapter includes only those equations solved by the author for the purpose of satisfying the objective of this work.

Continuity and Conservation in Pipe Matrices

In this study, the intake manifold is defined as a pipe with a finite diameter and length, termed in Chapter 1 as a “log” manifold. The intake ports of each cylinder of the large-bore 2SC engine are connected to this log manifold via individual runners. The runners are also modeled as pipe with a finite length and hydraulic diameter. This arrangement creates the pipe matrix shown in Figure 3.1. Each consecutive cylinder is positioned along the log manifold at an increasing plenum length – a summation of the hydraulic distance of the individual cylinder down the manifold, plus the hydraulic length of the intake runner – from the turbocharger compressor discharge; therefore, the charge air must travel a different length of conduit to each cylinder. This variation in plenum length translates to variations in average cycle-to-cycle charge air mass flow rate and instantaneous pressure upstream of the scavenging port.

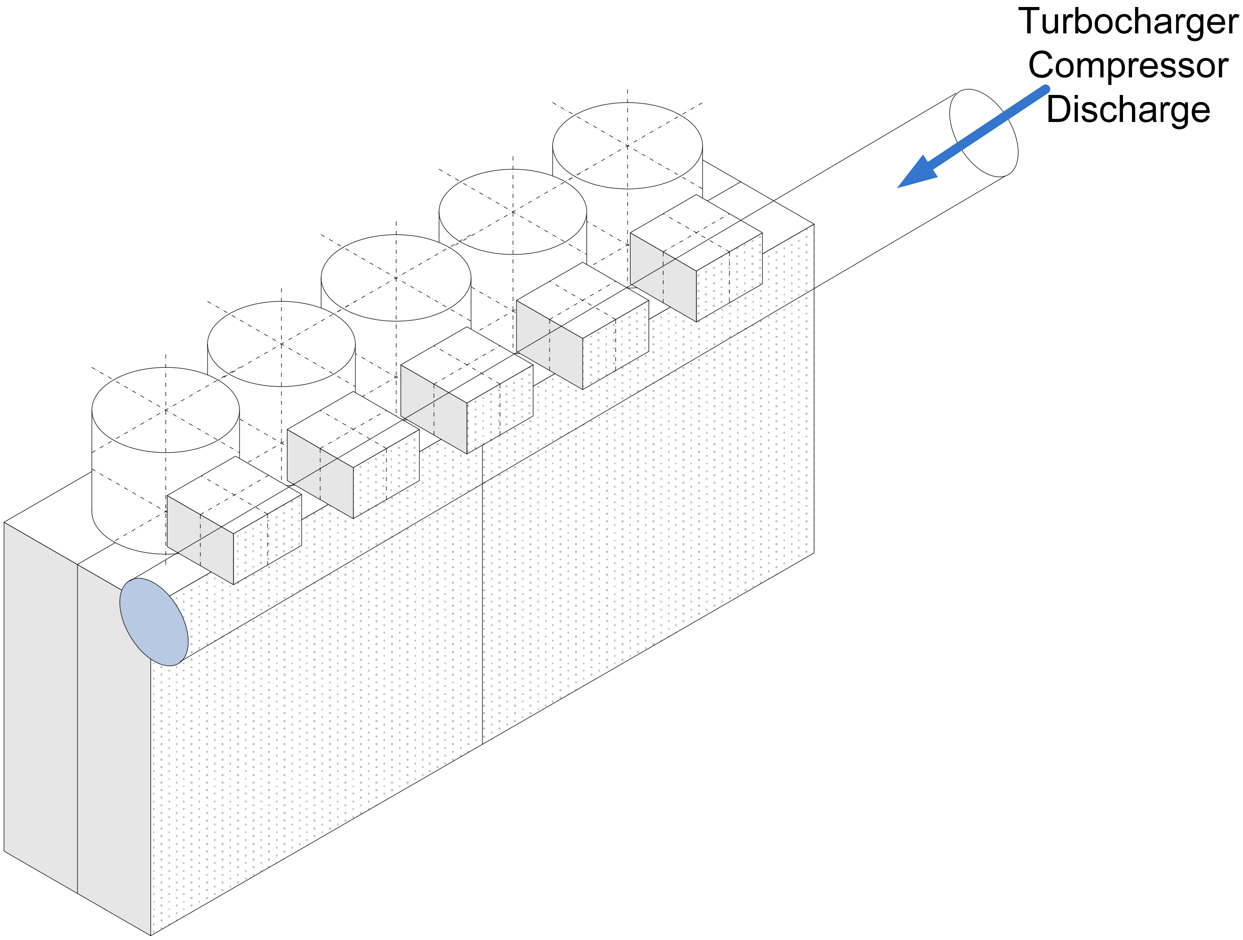

Figure 3.1: 2SC engine generic manifold-runner matrix

The equations and identities identified in Chapter 2 are combined to create a set of three equations in terms of local pressure, temperature, and density as functions of time, and thoroughly describe transient compressible gas flow. For convenience, the continuity, momentum, and energy equations are written in terms of the mass flow rate ($\dot{m}$), given that the primary interests of this work are the local charge air delivery pipe network pressure and mass flow rate as a function of time. Translating velocity into mass flow rate:

$$V = \frac{\dot{m}}{\rho A} = \frac{\dot{m} ZRT}{pA} \tag{3. 1}$$

Therefore (Abbaspour, 2004):

$$\left(\frac{\partial p}{\partial t}\right)+\frac{\dot{m}ZRT}{pA}\left\{1-\frac{V_w^2}{ZRT}\left[1-\frac{p}{Z}\left(\frac{\partial Z}{\partial p}\right)_T\right]\right\}\left(\frac{\partial p}{\partial x}\right)+\frac{\dot{m}V_w^2}{A}\left\{\frac{1}{\dot{m}}\frac{\partial \dot{m}}{\partial x}+\frac{1}{T}\left[1+\frac{T}{Z}\left(\frac{\partial Z}{\partial T}\right)_p\right]\frac{\partial T}{\partial x}\right\} = \frac{V_w^2}{c_pT}\left[1+\frac{T}{Z}\left(\frac{\partial Z}{\partial T}\right)_p\right]\left(\frac{\Omega}{A}+\frac{\dot{m}ZRT}{pA^2}\omega\right) \qquad \square 3.\ 2)$$

$$\frac{ZRT}{pA^2}\left\{p\left(\frac{\partial \dot{m}}{\partial t}+\frac{\dot{m}ZRT}{pA}\frac{\partial \dot{m}}{\partial x}\right)-\dot{m}\left[\left(1-\frac{p}{Z}\left(\frac{\partial Z}{\partial p}\right)_T\right)\times\left(\frac{\partial p}{\partial t}+\frac{\dot{m}ZRT}{pA}\frac{\partial p}{\partial x}\right)\right] +\frac{\dot{m}p}{T}\left[\left(1+\frac{T}{Z}\left(\frac{\partial Z}{\partial T}\right)_p\right)\times\left(\frac{\partial T}{\partial t}+\frac{\dot{m}ZRT}{pA}\frac{\partial T}{\partial x}\right)\right]\right\}+\frac{ZRT}{p}\frac{\partial p}{\partial x} = -\frac{\omega ZRT}{pA}-g\sin\theta \qquad (3.\ 3)$$

$$\left(\frac{\partial T}{\partial t}\right)+\frac{V_w^2}{c_p}\left[1+\frac{T}{Z}\left(\frac{\partial Z}{\partial T}\right)_p\right]\frac{ZRT}{p^2A}\left\{p\frac{\partial \dot{m}}{\partial x}-\dot{m}\left[1-\frac{p}{Z}\left(\frac{\partial Z}{\partial p}\right)_T\right]\frac{\partial p}{\partial x}\right\} +\frac{\dot{m}ZRT}{pA}\left\{1+\frac{V_w^2}{c_pT}\left[1+\frac{T}{Z}\left(\frac{\partial Z}{\partial T}\right)_p\right]^2\right\}\frac{\partial T}{\partial x} = \frac{V_w^2}{c_pp}\left[1-\frac{p}{Z}\left(\frac{\partial Z}{\partial p}\right)_T\right]\left(\frac{\Omega}{A}+\frac{\dot{m}ZRT}{pA^2}\omega\right) \qquad (3.\ 4)$$

The fully implicit method is used to numerically solve the continuity, momentum, and energy equations via the method documented by *Abbaspour (2004)*. The implicit method is unconditionally stable, and utilizes the Newton-Raphson technique to solve the set of nonlinear simultaneous equations at each time step (Kiuchi, 1994). A thorough investigation of one-dimensional gas flow in pipes was conducted by *Abbaspour (2004)*; including in-depth derivations of the conservation equations and their translation into the implicit solution scheme. Boundary conditions for the above equation scheme are provided by the operating conditions of the turbocharger compressor (p, T, and design $\dot{m}$). An abbreviation of the *Abbaspour* (2004) derivations and numerical formulation are included in Appendix A -Single-phase Flow Conservation Equations.

Gas Exchange in Large-bore 2SC Engines

The 2SC engine requires, for each engine cylinder, one crank-shaft revolution for each power stroke, as opposed to the 4SC engine, which require two crank-shaft revolutions. The 2SC engine was developed to obtain higher power output from a given engine size. The 2SC design is applicable to both SI and compression ignition (CI) engines; this work focuses solely on the SI variety of 2SC engine.

Flow of the charge air into the cylinder via the intake ports and burned gases out of the cylinder via the exhaust ports is modeled as one-dimensional, quasi-steady, compressible flow through a restriction. Solving the above system of conservation equations results in a temporal and spatial distribution of the fluid parameters within the manifold-runner pipe network. The solution scheme uses the upstream pressure and gas temperature, or boundary conditions for quantifying flow through the intake and exhaust ports of the large-bore 2SC engine. The appropriate relationship is (Annand and Roe, 1974):

$$\dot{m} = \frac{C_D A_T p_0}{\sqrt{R T_0}} \left(\frac{p_T}{p_0}\right)^{\frac{1}{\gamma}} \left\{ \frac{2\gamma}{\gamma - 1} \left[1 - \left(\frac{p_T}{p_0}\right)^{\frac{\gamma-1}{\gamma}} \right] \right\}^{\frac{1}{2}} \tag{3. 5}$$

The values C_D and A_T represent the discharge coefficient and the minimum area of the restriction. The subscript '0' refers to the upstream stagnation point of the restriction. For flow into the cylinder via the intake or air delivery system, the stagnation conditions refer to local time-dependant conditions in the intake manifold. For exhaust flow out of the cylinder, the stagnation conditions refer to conditions in the cylinder. Alternately, the subscript 'T' refers to values at the restriction, or port in this case. A thorough derivation of the final equation relating mass flow rate to pressure and temperature is in Appendix B -Compressible Flow through a Restriction.

Chemical Kinetics of Pollutant Emissions

The large-bore 2SC engine exhaust gases contain NO, NO_2, CO, and organic compounds which are unburned or partially burned HC. Hydrocarbons, or more appropriately organic emissions, are the consequence of incomplete combustion of the HC fuel. While the total HC emission is a useful measure of combustion efficiency, it is not necessarily a significant index of regulated pollutant emissions (Borman and Ragland, 1998). Thus, further discussion of pollutant emissions in this work will focus on the formation of NO_X and CO.

For modeling chemical kinetics, a uniform method for expressing the variation of reaction rates with temperature, called the Arrhenius form, has been adopted. The reaction rate (k) is a function of the temperature (T), the activation energy of the fuel (E_a), and a pre-exponential collision frequency factor (k_{co}):

$$k = k_{co} T^n e^{-\frac{E_a}{\hat{R}T}} \tag{3. 6}$$

It is important to note that the pre-exponential collision frequency factor (k_{co}) is a function of the amount of fuel introduced to the combustion environment, or more generally, the corrected trapped equivalence ratio (φ_{se}), and should be experimentally determined as such.

The forward (k_f) and reverse (k_b) rate constants for the three reactions listed previously have been measured in numerous experimental studies. NO formation in the post flame gases almost always dominated any flame-front produced NO. Therefore, it is appropriate to assume that the combustion and NO formation processes are coupled. This assumption allows for the approximation of the concentrations of molecular oxygen (O), oxygen gas (O_2), hydroxide (OH), molecular hydrogen (H), and nitrogen gas (N_2) by their respective equilibrium values. From the above chemical reactions with rate constants defined by equation (3.26), the rate of formation of NO is given by:

$$\frac{d[\mathrm{NO}]}{dt} = k_{f1}[\mathrm{O}][\mathrm{N_2}] - k_{b1}[\mathrm{NO}][\mathrm{N}] + k_{f2}[\mathrm{N}][\mathrm{O_2}] - k_{b2}[\mathrm{NO}][\mathrm{O}] + k_{f3}[\mathrm{N}][\mathrm{OH}] - k_{b3}[\mathrm{NO}][\mathrm{H}] \tag{3. 7}$$

Chemical equilibrium considerations indicate that for burned gases at typical flame temperatures, NO_2/NO ratios should be negligibly small. However, NO formed in the flame zone can be rapidly converted to NO_2 via simple reactions with hydroxide (OH) or oxygen (O_2) molecules (Bowman, 1975).

CO emission formation and destruction is primarily controlled by the corrected trapped equivalence ratio and the oxidation of a hydrocarbon fuel. This kinetic oxidation reaction continues throughout cylinder expansion and blow-down, until the intake ports are uncovered. At the initiation of scavenging, it can be assumed that the concentration of CO is frozen (Borman and Ragland, 1998). A final kinetic mechanism can be defined by combining equation (3.28) and equation (3.30) via the method included in Appendix D - Chemical Kinetic Reaction Mechanism Development:

$$\frac{d[\mathrm{CO}]}{dt} = k_{form}[\mathrm{CH_4}][\mathrm{O_2}]^{\frac{1}{2}} - k_{ox}[\mathrm{CO}][H_2O]^{\frac{1}{2}}[\mathrm{O_2}]^{\frac{1}{2}} \tag{3. 8}$$

It is imperative that the optimization of the engine air management system, a primary objective of this work, does not adversely affect the exhaust pollutant emission concentrations of NO_X or CO.

Exhaust Available Energy

Availability at a given state is a function of the volume ($\forall$), entropy (S), and energy (E), referenced to a dead state, represented by the '0' subscript (Moran, 1989):

$$AV = (E - U_0) + p_0(\forall - \forall_0) - T_0(S - S_0) \tag{3. 9}$$

Careful distinction should be made between availability losses and irreversibility within a component. Within the air management system, changes in the availability of the exhaust products can be divided into two categories: 1) thermo-mechanical or flow availability, and 2) thermal availability. Exhaust stream specific thermo-mechanical or flow availability can be determined by:

$$av_{fin} - av_{fex} = (h_{in} - h_{ex}) - T_0(s_{in} - s_{ex}) + \left(\frac{V_{in}^2 - V_{ex}^2}{2}\right) + g(z_{in} - z_{ex}) \tag{3. 10}$$

Additionally, for a length of pipe, it is important to quantify the loss of availability and irreversibility due to radial heat transfer. For a length of pipe, the loss of availability due to radial heat transfer ($\dot{AV}_Q$) is:

$$\dot{AV}_Q = \left(1 - \frac{T_{amb}}{T_{fl}}\right)\dot{Q} \tag{3. 11}$$

This loss of availability is a function of the local fluid temperature (T_{fl}) and the time rate of heat transfer from the pipe ($\dot{Q}$).

Summary

In summary, the mathematical description presented in this chapter to simulate the air management system of large-bore 2SC RICE is based on fundamental thermodynamic and fluidic principles. The analysis of the air management system can be decoupled into three individual analyses:

1. First law thermodynamic analysis of the air delivery or intake system, using one-dimensional unsteady compressible flow, to assess the cylinder-to-cylinder distribution of charge air;
2. Chemical kinetic analysis of in-cylinder pollutant emission formation to quantify exhaust concentrations of NO_X and CO; and
3. First and second law thermodynamic analysis of the exhaust removal system to quantify pulsation and effective delivery of available thermo-mechanical and thermal energy to the turbocharger turbine.

These individual quasi-steady models will be integrated into an existing single-cylinder thermodynamic-based cycle simulation to effectively simulate and provide parameters for optimization of the large-bore 2SC engine air management system.

CHAPTER 4 - Solution Method and Development of the Air Management Model

As discussed previously in Chapter 3, a thermodynamic analysis of the large-bore 2SC engine air management system can be developed to assess: 1) the cylinder-to-cylinder distribution of charge air, 2) pollutant emission concentrations, and 3) energy availability to the turbocharger turbine. In order to thoroughly analyze the complex system, that is the engine air management system, an effective research strategy must be followed. The author has chosen to the use the 5-step *Chapman Research Strategy* (2008) outlined below:

1. *Fundamental Model* – Build and exercise a simple fundamental model to create an understanding of the "process" being investigated. The simple model should be based on engineering fundamentals such as physics, thermodynamics, and fluid mechanics.
2. *Experimental Design and Execution* – Information provided by the simple engineering model should be used to design and conduct experiments. The experiments should be complete enough to fill in gaps in the fundamental model or expand the simple model to a more sophisticated engineering model of the process, not to understand the previously modeled process. Collected experimental data should bound the range of operation of the process, and should only be extensive enough to validate the engineering model.
3. *Expand and Validate Model* – The fundamental model developed in Step 1 should be expanded to a sophisticated engineering model of the process. The level of sophistication of the engineering model should be driven exclusively by the research needs. Data collected in Step 2 should be used to validate the model and verify its accuracy.

4. *Parametric Study* – The sophisticated model should then be used to conduct a parametric study and sensitivity analysis. A sophisticated, experimentally validated model can provide significantly more information at a much lower cost than continuous experimentation. The parametric study results can then be used to optimize selected design or operating parameters.
5. *Field Test* – A final experiment should be conducted using the optimized design or operating parameters. Once the sophisticated model and optimized parameters have been validated, a thorough understanding of the process can be affirmed.

Employment of this 5-step methodology will be the basis for Chapters 4 through 6 of this work. The continuation of Chapter 4 will include the development of a simple model for the air management system from the integration of the fundamental thermodynamic, chemical, and fluidic models described in Chapter 3. Chapter 5 includes the development of a multi-cylinder flow bench for collection of experimental data to validate and expand the simple model. Validation of the simplified model and expansion to a sophisticated engineering model, along with a parametric study for optimization of the air management system is included in Chapter 6.

Candidate Engine

Prior to the development of a simplified model, the author selected a candidate engine to supply a physical framework. As discussed in Chapter 1, purpose-designed low speed (250-400 rpm) 2SC and 4SC integral engines and diesel-derivative medium speed (360-630 rpm) engines represent approximately 80% of the total compression power of the natural gas transmission industry. The Cooper GMV, Cooper GMW, and Cooper V-250/V-275/W-330, along with the Clark TCV, and Clark TLA/BA account for approximately 70% of the total number of units, and total horsepower. Therefore, with the guidance of the PRCI Compressor and Pump Station

Technical Committee, and cooperation of both El Paso Corporation and Arrow Industries, the author selected the Cooper GMV, shown in Figure 4.1, as the candidate engine for the development of an integrated algorithm for simulation and optimization of the large-bore 2SC engine. Design parameters of the Cooper GMV are included in Table 4.1.

Table 4.1: Candidate engine – Cooper GMV design parameters

Geometry		**Operation**	
Cylinders	10	Rated HP	1700 HP
Bore	14 in	Rate Speed	300 RPM
Stroke	14 in	BMEP	100 psi
Rod Length	34.375 in	Effective Compression Ratio	7.72

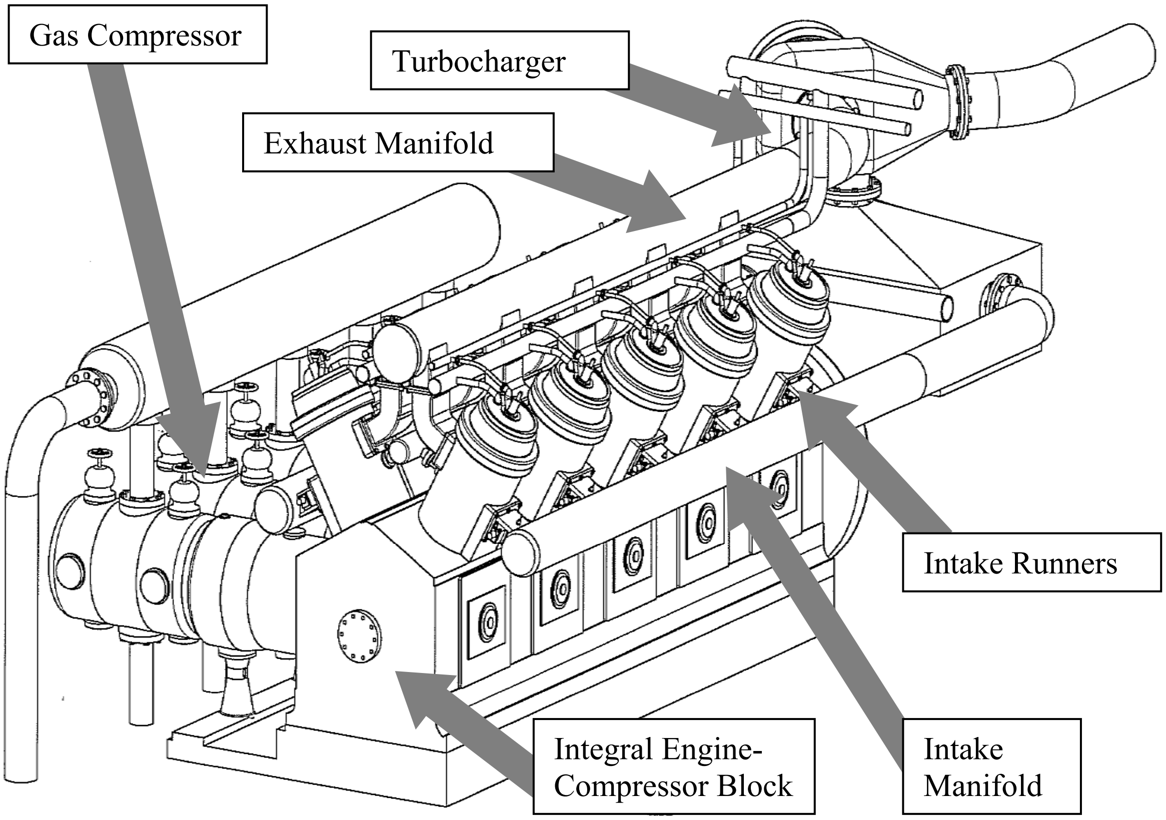

Figure 4.1: Candidate Cooper GMV engine (AAC, 2009)

Mathematical Model Integration

The integration of the fundamental mathematical models presented in Chapter 3 is done on a component basis. The components and analysis presented in this chapter follow the path of air and then exhaust flow through the air management system of a large-bore 2SC engine. The charge air and then exhaust products of a 2SC engine follows the simplified flow path described by the block diagram in Figure 4.2. This simplified flow path provides the framework for the integration of the fundamental mathematical models outlined in Chapter 3.

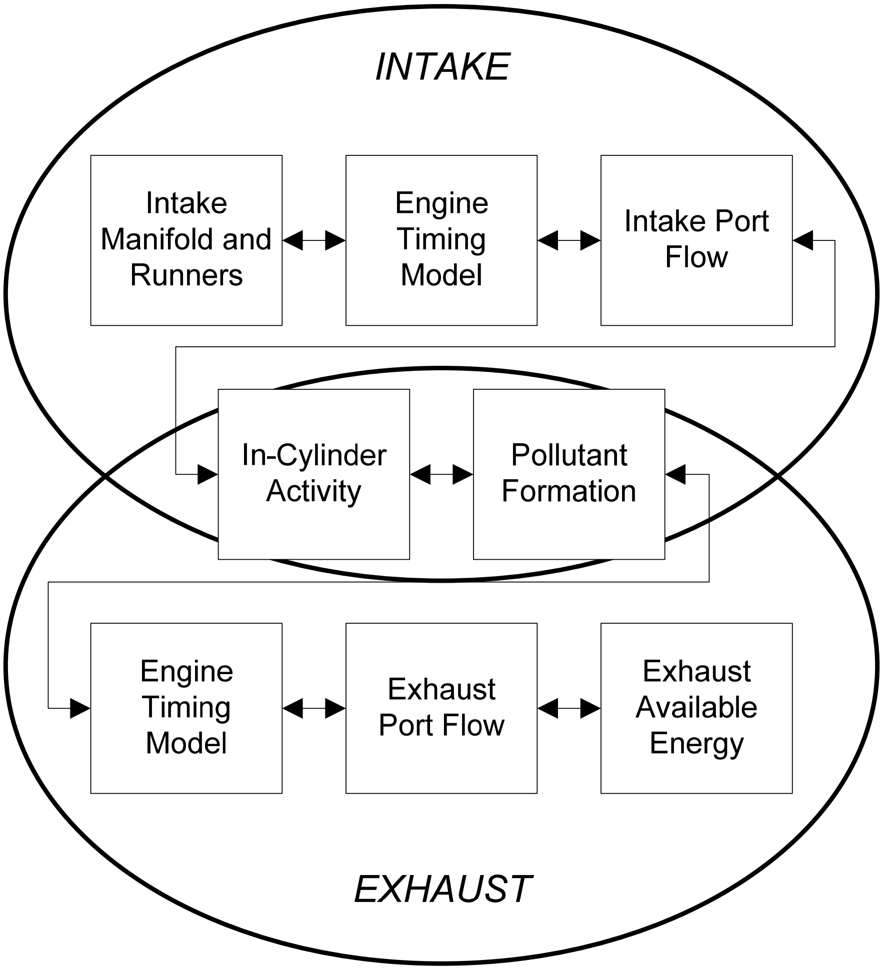

Figure 4.2: Fundamental model integration

Charge air is delivered to the intake manifold by the turbocharger compressor. This relatively low energy air flows down the log manifold and into each individual intake runner. As the piston uncovers the intake ports, air is drawn from the runner leading to the cylinder, the manifold, and the other cylinder runners, through the intake ports into the cylinder based on the timing of the multi-cylinder engine. After the ports are closed, combustion commences. Some of the pollutant formation and destruction reactions are intimately coupled with the primary fuel combustion process; others are only produced by the combustion environment and must be quantified separately. After combustion, the exhaust ports are opened and the combustion products exit the cylinder. The high energy combustion products flow through the exhaust runners and manifold to the turbocharger turbine and provide the thermo-mechanical and thermal energy to spin the turbocharger turbine. This flow of charge air and exhaust products through the engine air management system is shown in Figure 4.3. The turbine powers the turbocharger compressor providing the intake manifold with fresh charge air completing the cycle.

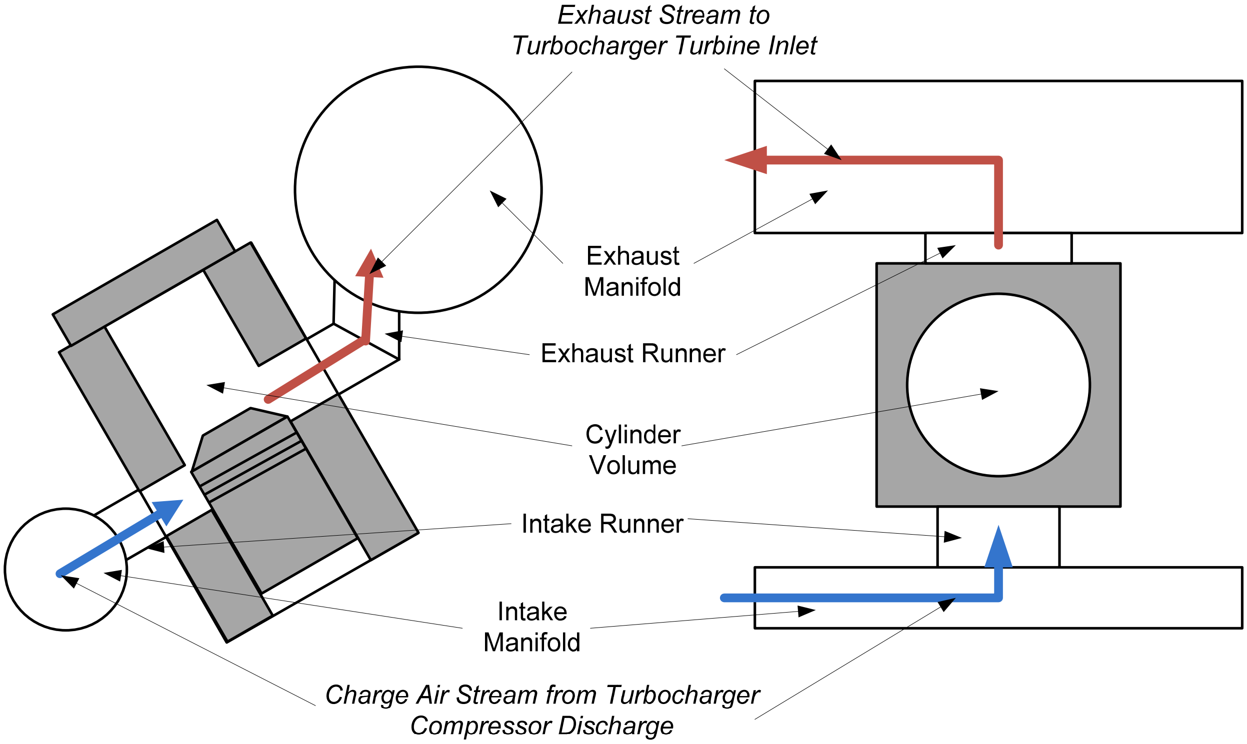

Figure 4.3: Engine air management system flow path

Charge Air Delivery

The air flows to each cylinder of a multi-cylinder engine, even under steady operating conditions, are not identical. This is due to differences in cylinder location and other geometric details of the flow path to each cylinder. The dynamics of the flow in multi-cylinder intake and exhaust systems can be modeled most completely using one-dimensional unsteady compressible flow equations. The selected method of solution of the governing equations is the finite implicit method. A thorough review of the development of the single-phase flow conservation equations identified previously in Chapter 3 can be found in Appendix A - Single-phase Flow Conservation Equations. The fully implicit method was used to descritise the continuity, momentum, and energy equations. The Newton-Raphson technique was then used to solve the set of nonlinear simultaneous algebraic equations at each time step.

As illustrated in Figure 4.4, the manifold in this study was treated as a pipe with a finite diameter of 12 in (0.3048 m) and length of 28 ft (8.5344 m) from the engine intercooler discharge to cylinder 5L. Connected to this pipe are the runners which were also modeled as pipe with a finite length and hydraulic diameter branching at 90° from the manifold. The cylinder runners are spaced 48 in (1.22 m) centerline to centerline. The illustration in Figure 4.4 is the left bank of the Cooper GMV intake manifold. Charge air is delivered to the intake manifold, of a given diameter (D_{inman}), at the compressor discharge pressure (p_{ca}). As the air travels down the intake manifold, experiencing a temporal and spatial distribution ($p_{inman} = funct(x, t)$), it is diverted to one of the intake runners (D_{run}), which are spaced every 48 in along the intake manifold. As the intake ports are opened to bring the charge air into the cylinder, the charge air interacts with the in-cylinder pressure ($p_{cyl} = funct(t)$), creating the intake manifold pulsation.

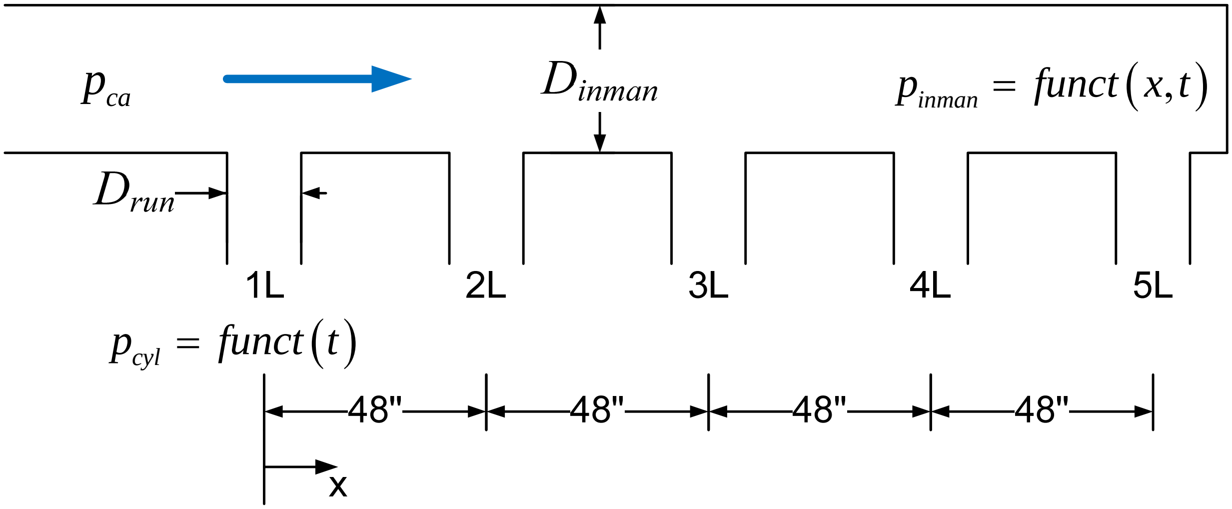

Figure 4.4: Cooper GMV left bank intake manifold schematic

The cross-section of the intake runners is 10 in by 5.5 in (0.25 m by 0.14 m), resulting in a calculated hydraulic diameter of 7.1 in (0.18 m).

The manifold model, when subjected to known engine operating conditions (p, T, and design $\dot{m}$) and the geometry shown in Figure 4.4, calculates the pressure distribution shown in Figure 4.5. The variables p, T, and design $\dot{m}$ are utilized as the boundary conditions for the model. Each circle represents the location of the intake runner for each cylinder relative to intake manifold.

For clarification, the pressures measured and calculated in this work are presented in the following English units: pounds per square inch absolute (psia), differential pounds per square inch gage (psig), inches of Mercury absolute (in HgA), and differential inches of Mercury gage (in Hg).

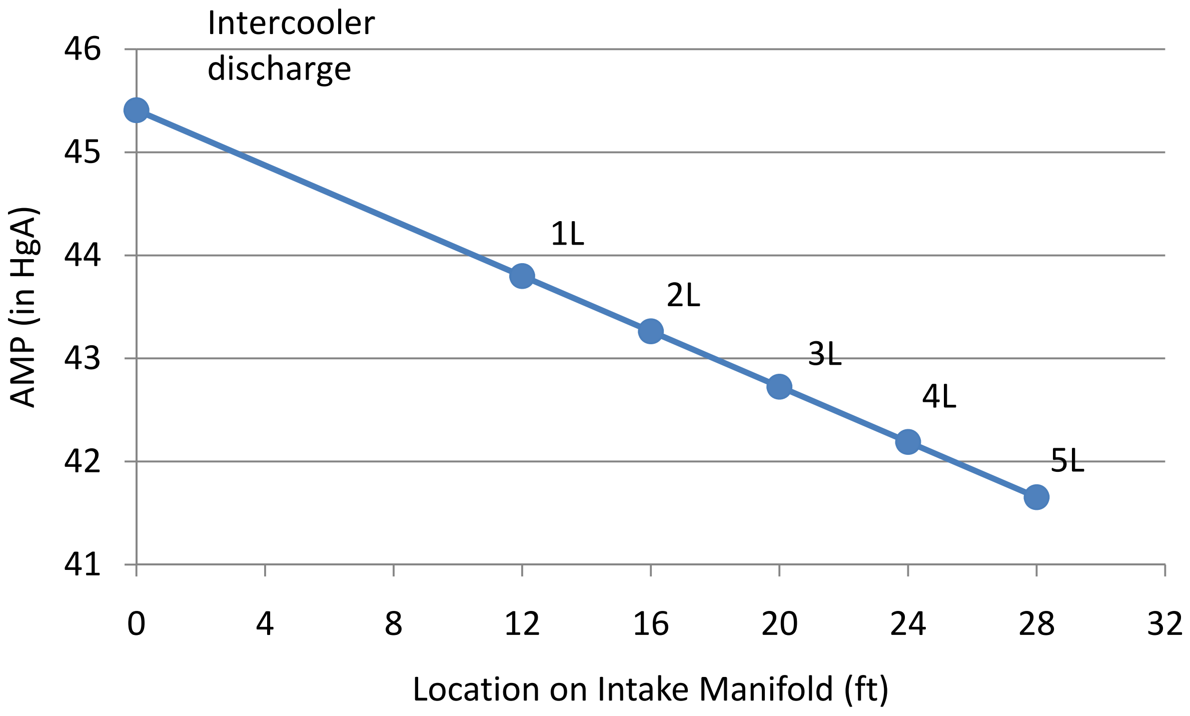

Figure 4.5: Steady-state Cooper GMV manifold pressure distribution

This data has been compared to and is consistent with current literature and field test data. *Abbaspour* (2004) also presents this comparison as included in the literature review in Chapter 2. This confirms that each cylinder is subjected to a different air manifold pressure due to the physics of the air delivery system.

To assess the impact of each cylinder on the air delivery system and overall engine operation, a single cylinder is initially modeled in a simplified manner. In order to model in-cylinder conditions, the previously developed T-RECS was integrated into the manifold flow model.

T-RECS is a design analysis tool that allows one to optimize the integration of the reciprocating engine and turbocharger air management system (Miyasato, 1997). T-RECS applies the first law of thermodynamic for an open system to the cylinder volume for the intake, compression, combustion, expansion, and exhaust process that in sequence make up the engines cooperating cycle, allowing for the calculation of the adiabatic flame temperature. During each process, sub models are used to describe geometric features, the thermodynamic properties of the unburned and burned gases, the mass and energy transfers across the system boundary, and the combustion process.

T-RECS uses a three-zone combustion model, one zone for each of the burned, unburned, and boundary zones. The burning rate can be simulated using either a Wiebe function or a user-entered range for the combustion process. T-RECS also uses the JANAF tables to simplify the calculation of equilibrium combustion constants. Specifically, the T-RECS program calculates the cycle-resolved in-cylinder temperature, pressure, and cylinder intake/exhaust flow rates of the turbocharged-engine system. The mathematical algorithms used to determine the pressure, temperature, and mass flow rate are based on fundamental engineering principles to provide the highest reliability in the calculated values (Chapman, 2000).

When coupled with the manifold model, the engine processor determines the crank angle-resolved pressure, temperature, burned and unburned mass fractions, and gas exchange rates for the cylinder. This in turn creates a transient description of the pressure and mass flow rates seen in the intake and exhaust ports (Miyasato 1997).

The T-RECS model operates with a forced mass and energy balance, using equations of state and chemical equilibrium. The intake runners and therefore the intake manifold are subject to the in-cylinder pressure variations modeled by T-RECS and illustrated in Figure 4.6. Figure 4.6 illustrates the in-cylinder pressure, and mass flows in and out of cylinder 1L of the candidate Cooper GMV engine when subjected to standard engine operating conditions.

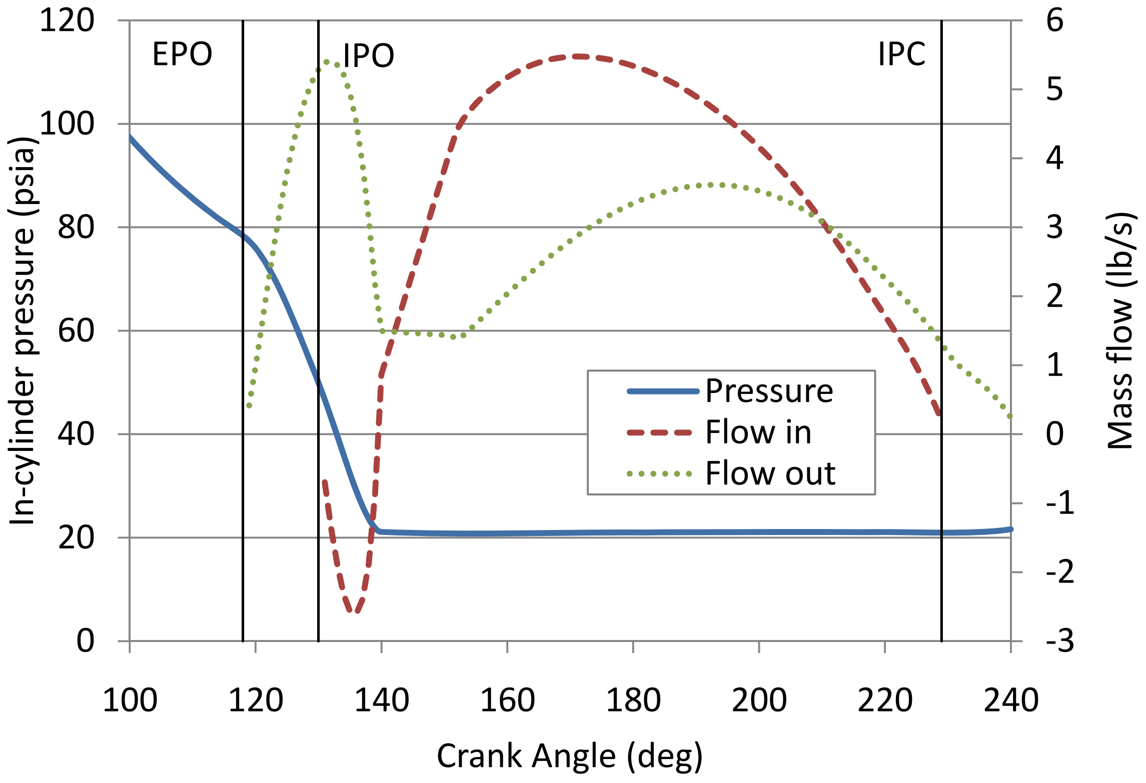

Figure 4.6: In-cylinder pressure and port flow rates

The in-cylinder pressure variation between intake port opening (IPO) and intake port closing (IPC) is the pressure wave that the intake manifold is subjected to during engine operation. This wave, in conjunction with the port activity, creates pulsation in the manifold.

The Charge Air Integrated Manifold Engine Numerical Simulation (CAIMENS) was developed from the coupling of the manifold model with the T-RECS engine process via the engine timing model and analysis of compressible flow through the ports. CAIMENS is a multi-cylinder engine algorithm that models the effects of charge air imbalance between cylinders using the physical relationships from Chapter 3. Figure 4.7 shows the block diagram of the CAIMENS algorithm. In order to begin calculations, engine operating parameters, including average air manifold temperature and pressure, design airflow rate, and manifold geometry must be known. These parameters are used to calculate first the steady state manifold pressure gradient from cylinder to cylinder due only to geometry and physics of flow through a pipe. This resultant pressure gradient, when fed into T-RECS allows the engine processor to calculate in-cylinder conditions for each individual cylinder. These in-cylinder pressure variations create pressure pulses in the air manifold when the piston uncovers the intake ports, which may disrupt airflow to the cylinders. A temporal and spatial variation of air manifold pressure, caused by the pressure pulses, is calculated as $AMP(x,t)$ in Figure 4.7.

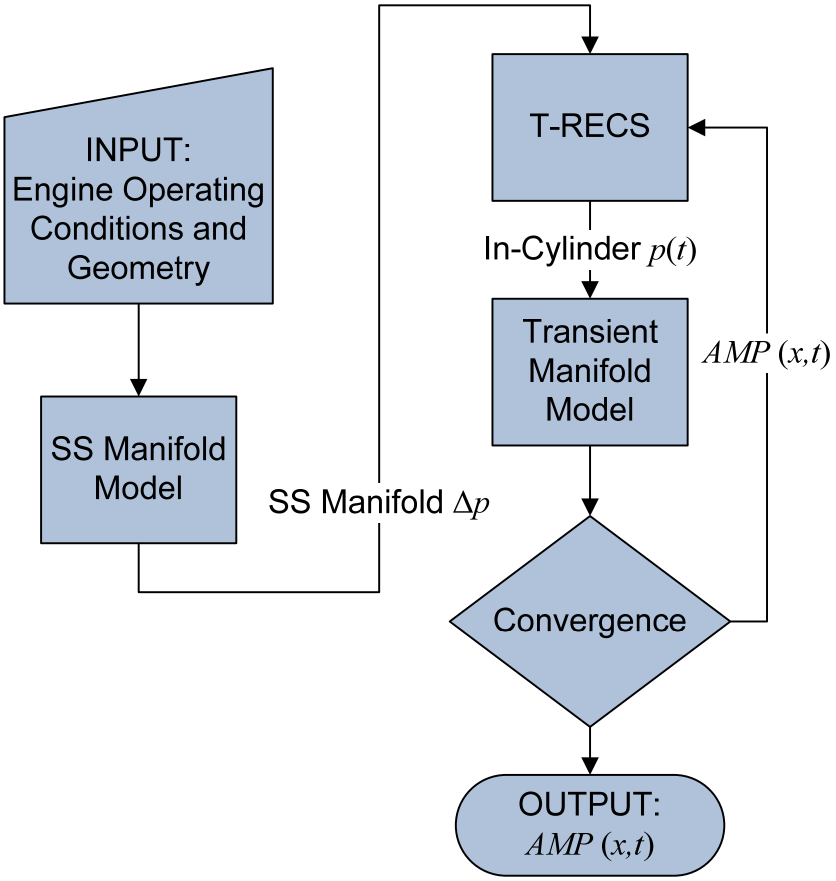

Figure 4.7: CAIMENS block diagram

The transient manifold model assess the resulting airflow by analyzing the in-cylinder pressure variations that impact the manifold when the ports are uncovered and also by understanding how the variation in the manifold pressure impacts in-cylinder conditions.

The in-cylinder pressure curve for cylinder 1L, generated by T-RECS in Figure 4.6 is reduced to the profile illustrated in Figure 4.8.

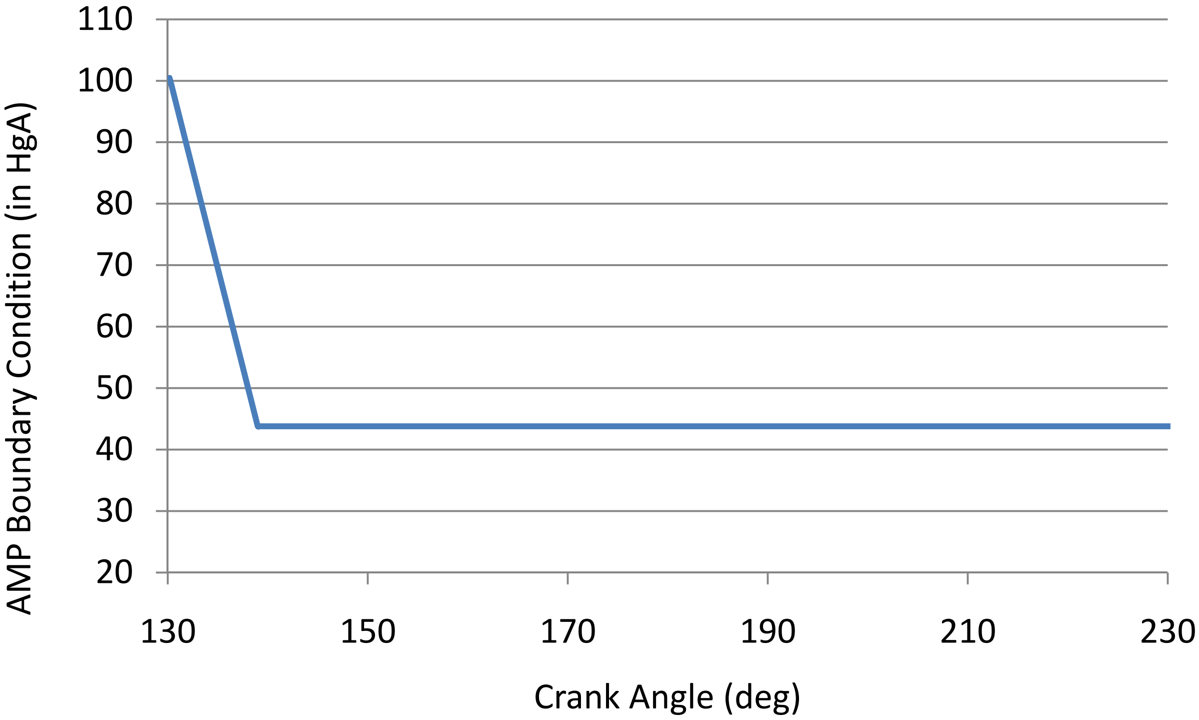

Figure 4.8: Simplified AMP boundary condition

This pressure profile is then input into the manifold model, which solves the pipe equations in conjunction with the boundary conditions discussed earlier (p, T, and design $\dot{m}$). The resultant pressure wave (Figure 4.9) is plotted over time at the location of each cylinder in the manifold. Intake port opening to intake port closing is a function of the speed of the engine. For this project, the speed of the engine is 300 revolutions per minute (rpm) resulting in an intake port uncovered to covered time of approximately 0.08 seconds.

If no other activity occurs in the manifold, the pressure wave from a cylinder will decrease to the steady state air manifold pressure at the time of the port closing. This decrease occurs as shown in Figure 4.9. The 1L local pressure wave (blue) closely mimics the in-cylinder pressure distribution from cylinder 1L. At every other cylinder, the results show that the pressure fluctuates with time before decreasing to the value of the steady state manifold pressure. This wave has been compared to and is consistent with candidate Cooper GMV data from an Enginuity, LLC pulsation study. The average amplitude of the manifold pulsation data is about 4 in Hg (13.5 kPa) which is consistent with the amplitude of the model pulse wave at each port opening (every 72° CA or 0.04 seconds).

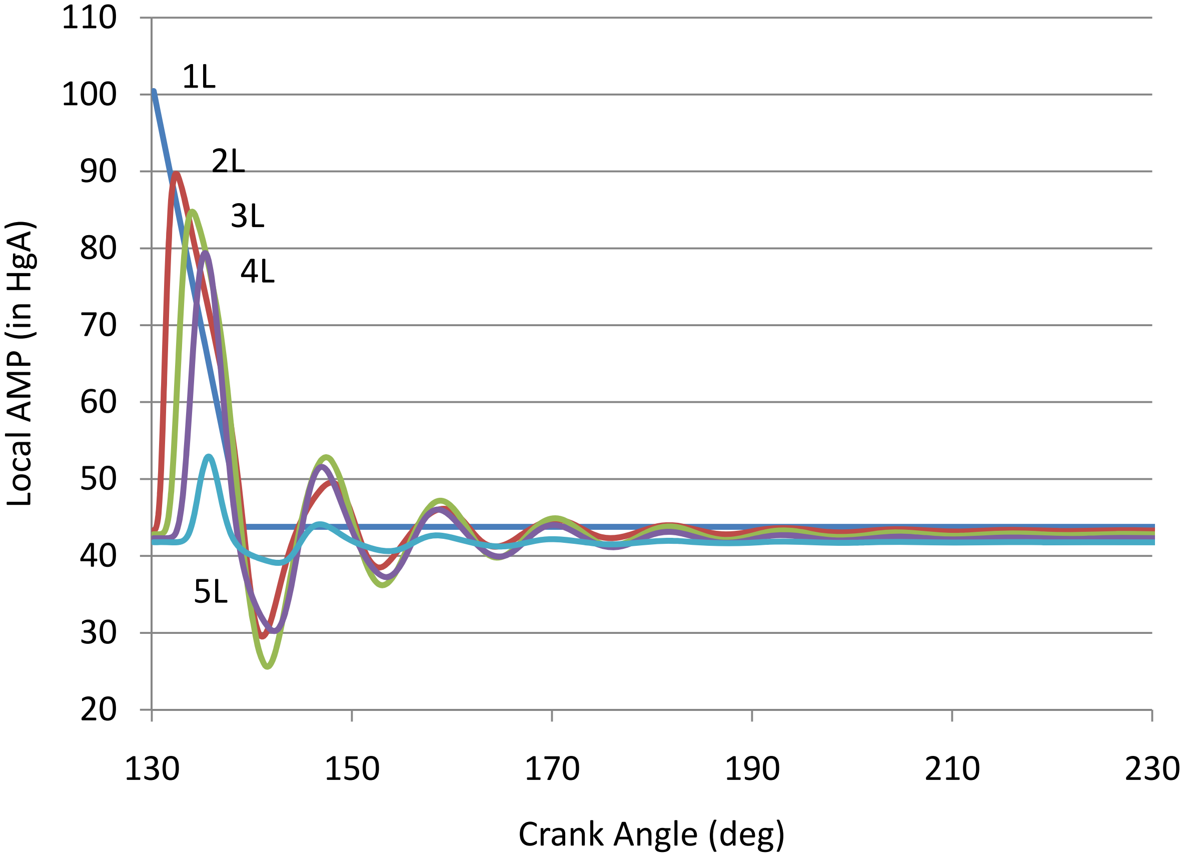

Figure 4.9: Cylinder 1L IPO manifold pressure distribution

As time progresses, the pressure wave created by cylinder 1L propagates down the length of the manifold. This proliferation is shown in Figure 4.10. As expected the pressure decreases with time and distance. Figure 4.10 shows the pressure distribution in the manifold plotted at times from 0.0001 seconds to 0.0050 seconds. From Figure 4.10, the intake port opening of cylinder 1L leads to a temporal and spatial pressure distribution throughout the manifold. Due to the nature of compressible fluids, the magnitude of the pressure wave is at times less than the steady state intake manifold pressure.

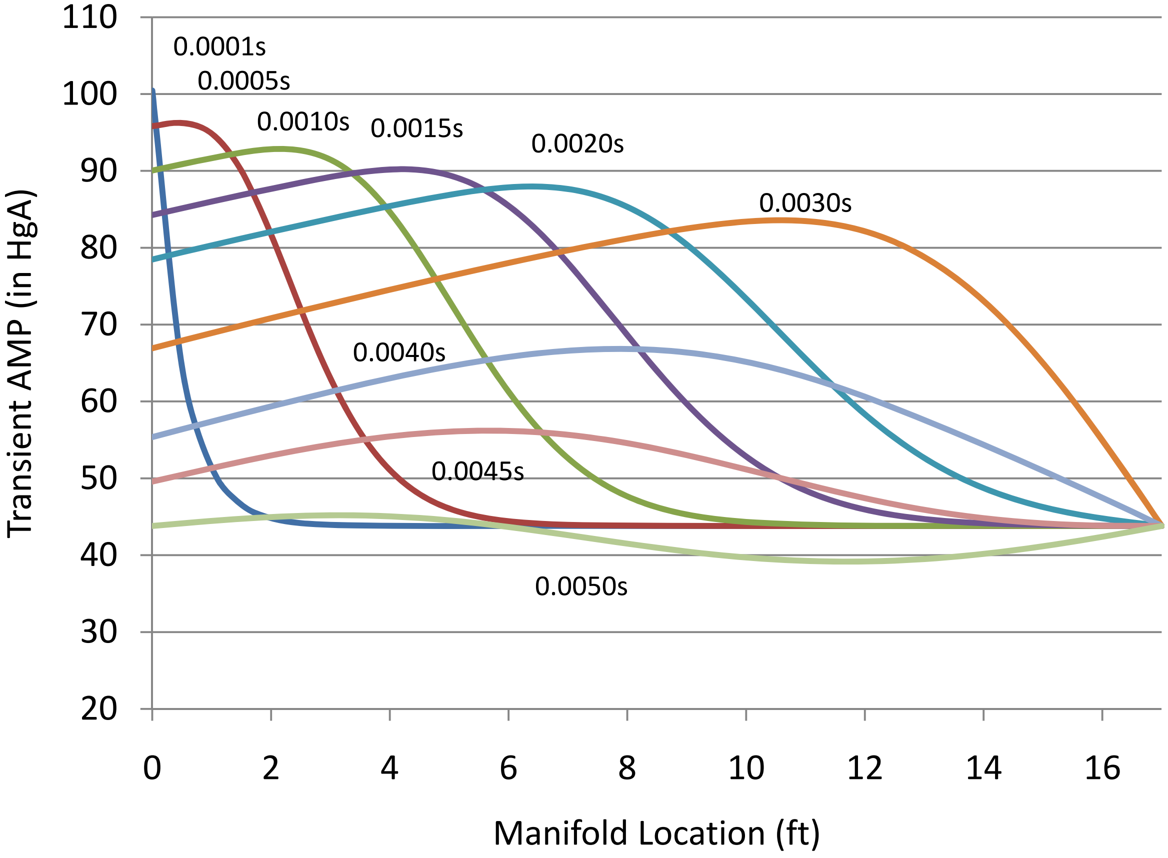

Figure 4.10: Cylinder 1L IPO intake manifold pressure wave propagation

The next step is to move to a multi-cylinder model to assess the impact of one cylinder on the next cylinder in the firing order and timing in the next section.

Engine Timing

The intake manifold and runners are coupled to the cylinders using the engine timing model. To describe the port activity and therefore the transient conditions created by the in-cylinder pressure, cylinder firing order must be known. The timing model for the Cooper GMV is diagramed in Figure 4.11 and Figure 4.12. Figure 4.11 illustrates both the left and right bank of cylinders as connected by the dual intake manifolds of the Cooper GMV engine. The cylinders are labeled according to the firing order of the engine. For example, cylinder 1L fires first followed by cylinder 1R. The firing order then continues to cylinders 4L and 4R.

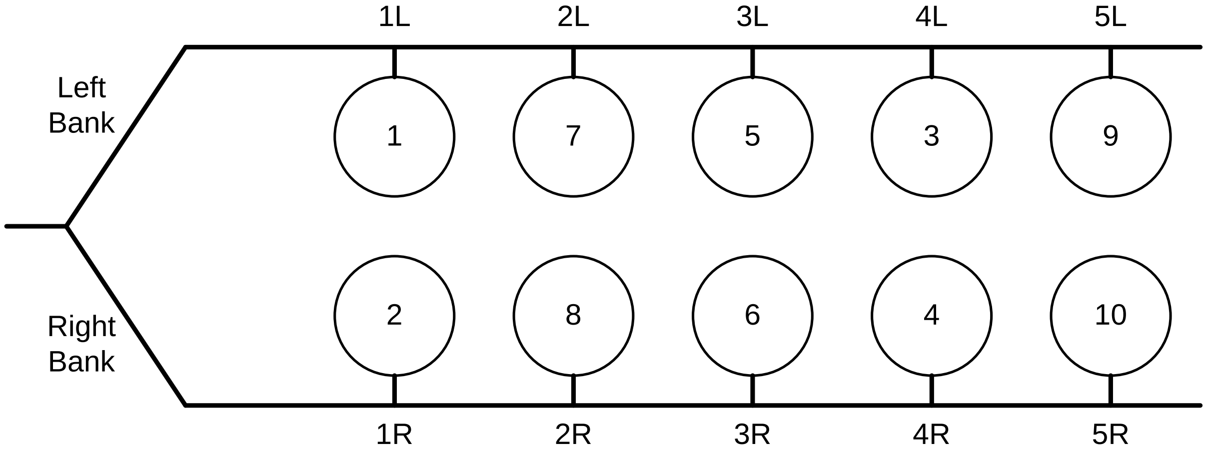

Figure 4.11: Firing order for 10-cylinder Cooper GMV

Figure 4.12 shows the left bank or master rod side of the Cooper GMV engine. The cylinders on a single manifold are timed to fire every 72°CA. For example, cylinder 1L reaches top dead center (TDC) at 0°CA. As the crank shaft rotates, cylinder 4L reaches TDC at 72°CA, cylinder 3L reaches TDC at 144°CA, and so forth.

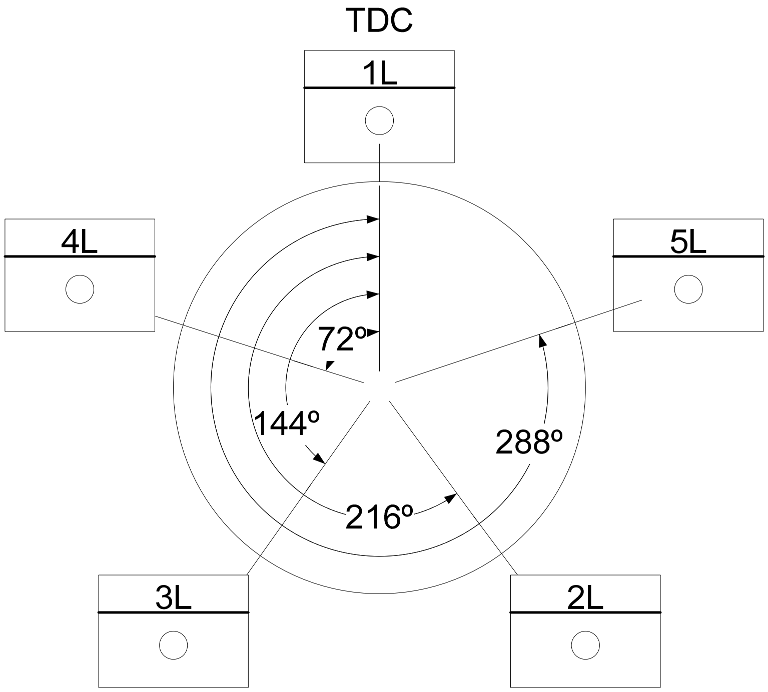

Figure 4.12: Cylinder timing– left bank of 10-cylinder Cooper GMV

This timing model is then used in combination with an instantaneous stroke calculation for each cylinder that allows for visualization of the port activity. For this study, the master rod side is considered. The instantaneous stroke (y), defined as the distance from the top of the cylinder, as described by *Heywood (1988)* is:

$$y = L_R + r - \left[(L_R^2 - r^2 \sin^2 \theta)^{\frac{1}{2}} + r \cos \theta \right] \tag{4.1}$$

The instantaneous stroke calculation verifies that at any time during a crank shaft revolution, there are only two cylinders open. As the cylinder 1L piston reaches bottom dead center, the cylinder 4L intake ports begin to uncover. The overlap of cylinders is the premise for 'cylinder cross-talk' and is illustrated in Figure 4.13. 'Cylinder cross-talk' is a phenomena resulting from the timing shown in Figure 4.12 and allowing for pressure pulsations from one cylinder intake port opening (IPO) to move down the intake manifold into another cylinder during that cylinder's scavenging process. This 'cylinder cross-talk' can change the flow of air into a cylinder. For example, cylinder 1L IPO will introduce pulsation to the intake manifold between IPO and bottom dead center (BDC). The residual waves will propagate down the manifold and into cylinder 4L during its IPO event.

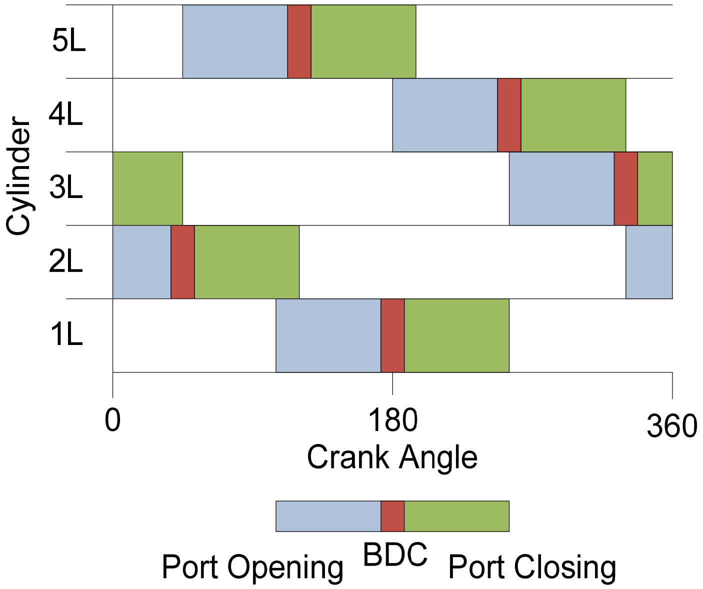

Figure 4.13: Port activity overlap

The next step is to move to a multi-cylinder model to assess the impact of one cylinder on the next cylinder in the firing order and timing illustrated in Figure 4.14.

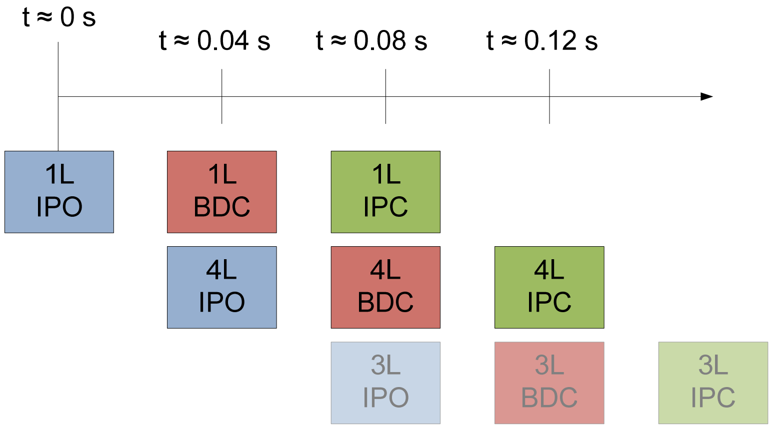

Figure 4.14: Timeline for port activity

The CAIMENS manifold flow calculations show that for a 12 in (0.3048 m) diameter manifold such as the one found on the candidate Cooper GMV engine, a pressure gradient on the order of 3.75 in Hg (12.71 kPa) occurs at steady state. Due to this pressure gradient, the in-cylinder pressure at cylinder 4L, which is the second cylinder to fire in the left bank, will be approximately 2 to 4 in Hg less than that of cylinder 1L, based on the pulsation shown in Figure 4.9.

This manifold pressure gradient translates into a significant change in peak pressure in the cylinder as shown by the T-RECS pressure traces in Figure 4.15 and Figure 4.16. The difference in peak pressure between cylinder 1L and cylinder 4L is 15 psig (104 kPa). It is important to note that cylinder 1L and cylinder 4L are actually offset by 72° of CA – they have been aligned in Figure 4.15 and Figure 4.16 in order to compare the relative peak pressures.

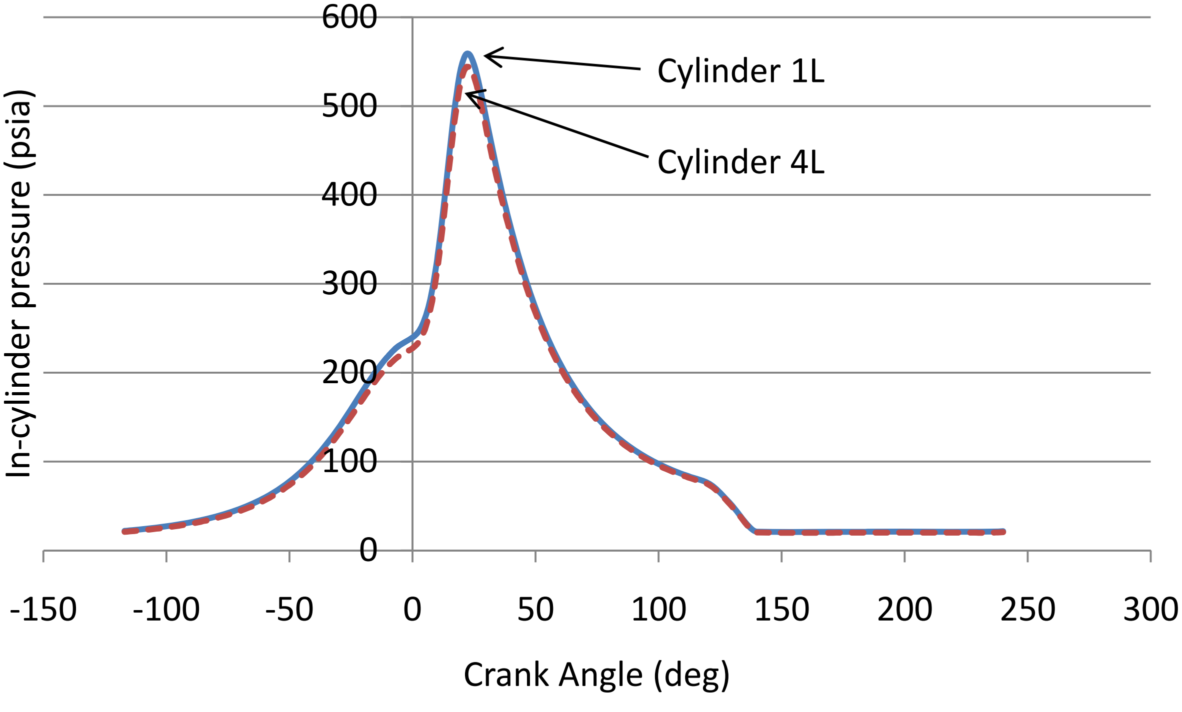

Figure 4.15: T-RECS cylinder 1L vs. cylinder 4L pressure trace

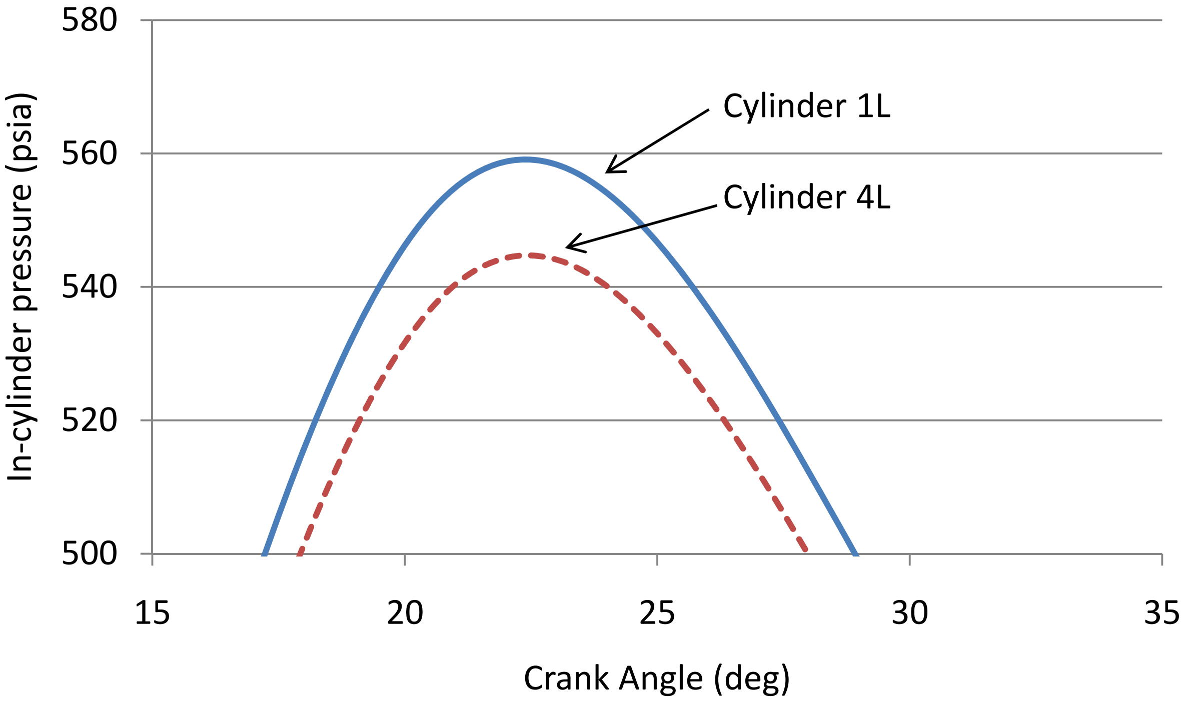

Figure 4.16: T-RECS cylinder 1L vs. cylinder 4L peak pressure

As discussed previously, the T-RECS pressure distributions for each cylinder are simplified and input into the manifold model creating a transient pressure wave. This wave is then plotted with respect to time at each cylinder location at cylinder 1L and cylinder 4L IPO activities. A comparison of cylinder 1L to cylinder 4L in-cylinder pressure variation when the intake ports are uncovered is shown in Figure 4.17. Figure 4.17 shows that a variation in manifold pressure of approximately 2 to 4 in Hg translates into a variation in peak combustion pressure of 14.45 psig (99.62 kPa) which finally translates into a difference in IPO pressure of 1.72 in Hg (5.82 kPa). Not only are cylinder 1L and cylinder 4L firing at different peak pressures, but they introduce different pressure pulse sizes into the intake manifold.

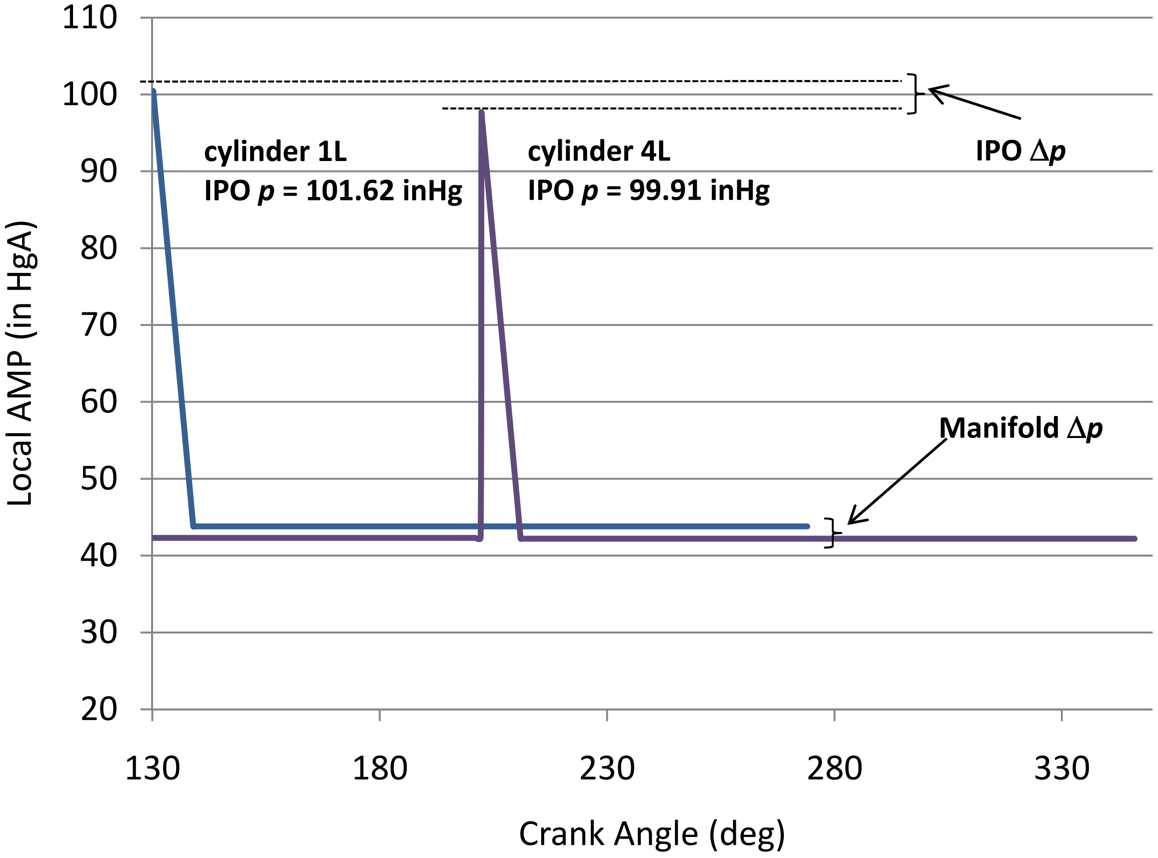

Figure 4.17: Cylinder 1L and cylinder 4L pressure

The wave propagation from cylinder 4L IPO is plotted with cylinder 1L in Figure 4.18. The intake ports for cylinder 4L are uncovered from 0.04 seconds to 0.12 seconds.

The port activity pressure pulse contribution to the manifold is fundamentally five separate pulse waves from each cylinder offset by 72°. This offset is due to the spacing of the cylinder IPO (Figure 4.14). Therefore, as cylinder 1L reaches bottom dead center, cylinder 4L intake ports open. There are always two cylinders open to the intake manifold. Because the intake ports are uncovered for 0.08 seconds and there is an overlap at bottom dead center, every 0.04 seconds two different cylinder parings remove air from the intake manifold. Also, as discussed earlier, the difference in manifold pressure due to pipe flow physics translates into a difference in cylinder peak pressure, which further translates into a difference in pressure at the ports. This is shown in Figure 4.18.

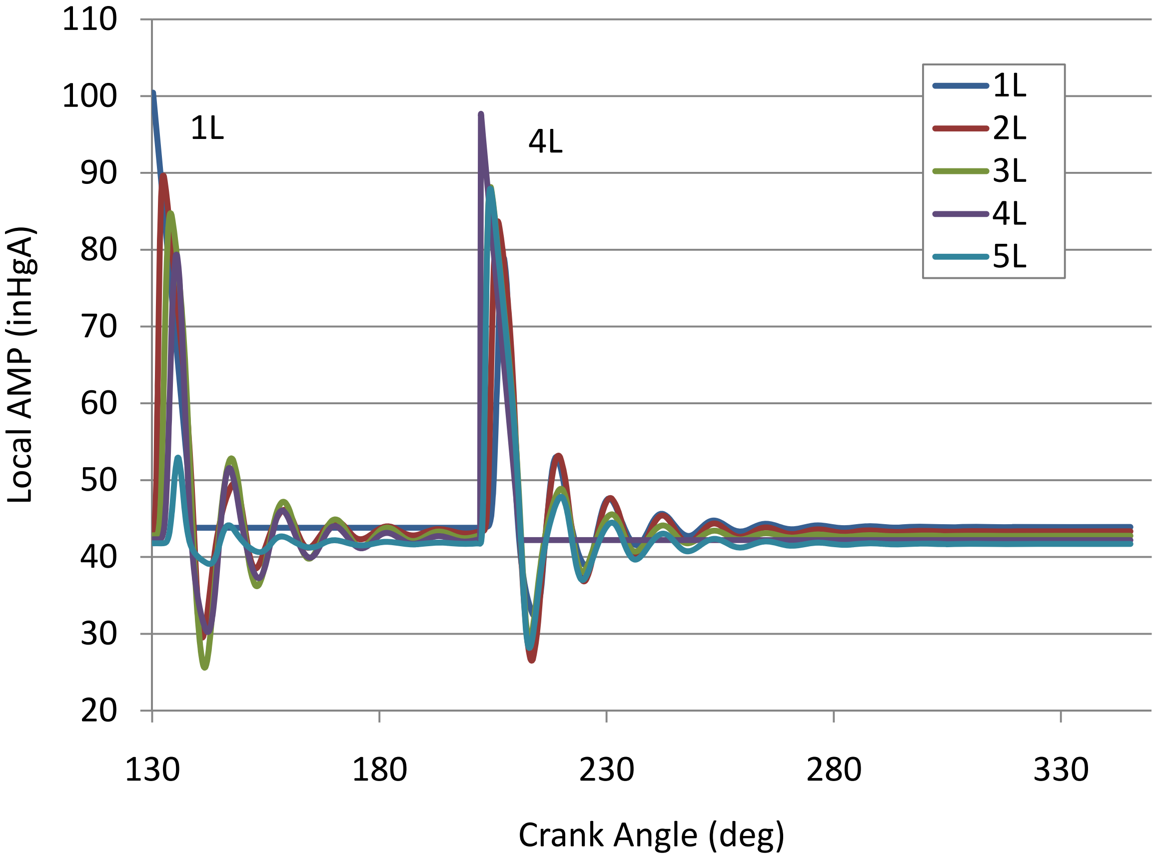

Figure 4.18: Cylinder 1L and 4L pressure propagation

As illustrated in Figure 4.18, the CAIMENS model computes the transient impact of one cylinder IPO on each successive cylinder. Because there are always two cylinders removing air from the intake manifold, there is a significant overlap in the pressure wave from one cylinder IPO event to the next cylinder in the IPO order. The pulsation model shows that not only does the manifold pressure gradient have a significant impact on the in-cylinder peak pressure, but it also has an impact on the pressure wave introduced to the intake manifold as the ports are opened. Also, each cylinder has a considerable impact on the airflow into each successive cylinder. CAIMENS provides the information necessary to quantify the impact of airflow imbalance, and allow for the visualization of the engine system before and after airflow correction.

Figure 4.18 illustrates the magnitude of the driving pressure that then leads to an air flow imbalance. The pressure gradients in Figure 4.18 quantify the air flow control that is needed to balance the cylinders of the Cooper GMV engine. The air flow correction should overcome a 3 to 5 in Hg gradient in intake manifold pressure. It should also be capable of compensating for the 1 to 2 in Hg magnitude residual wave propagating down the manifold from the previous cylinder IPO activity. In total, the air flow correction should be able to induce a 4 to 6 in Hg pressure drop.

An experimental analysis and development of a method to effectively distribute the charge air of large-bore 2SC engines is presented in Chapter 5 of this work. This experimental analysis is then used to validate the simple engineering model developed in this chapter.

In-Cylinder Kinetics

The intake manifold pressure gradient and cylinder “cross-talk” illustrated in Figure 4.18 quantifies the unbalanced distribution of charge air in the large-bore 2SC engine air management system. The CAIMENS model computes the transient impact of one cylinder IPO on each successive cylinder. The overlap in pulsation introduced to the intake system impacts the flow of charge air into each cylinder, directly impacting cylinder scavenging. Cylinder scavenging directly impacts the corrected trapped equivalence ratio, which in turn impacts each successive in-cylinder combustion event.

As discussed in Chapter 3, the corrected trapped equivalence ratio (φ_{se}), repeated here for reference, compares the actual fuel to air ratio to the stoichiometric fuel to air ratio, and is corrected by the scavenging efficiency (η_{se}):

$$\varphi_{se} = \frac{1}{\eta_{se}}\left[\frac{\left(\frac{\dot{m}_{fu}}{\dot{m}_{ca}}\right)_a}{\left(\frac{\dot{m}_{fu}}{\dot{m}_{ca}}\right)_{st}}\right] \tag{3.24}$$

where the scavenging efficiency (η_{se}), repeated here for reference, has been defined as (Chapman and Beshouri, 2000):

$$\eta_{se} = \kappa_2(1 - \kappa_1 e^{-\Lambda}) \tag{3.32}$$

The corrected trapped equivalence ratio, coupled with the ignition timing (IT) of the engine controls the temperature of the primary combustion reaction and therefore the temperature of the environment created by the combustion event. The burned mass fraction with respect to advancing crank angle is derived from a first law analysis of the pressure history actually measured on the engines. Such data is only valid for a particular engine and the operating condition from which the pressure history was obtained. The technique is utilized to establish a collection of heat release data for different engine operating conditions as well as different engine types (Heywood, 1988). For the engine simulation purpose, one method often used to represent this burned mass fraction is the Wiebe function, shown in Figure 4.19 (Annand and Roe, 1974):

$$x_b = 1 - exp\left[-\alpha\left(\frac{\theta - \theta_c}{\Delta\theta}\right)^{\nu+1}\right] \tag{4.2}$$

where, x_b is the burned mass fraction, θ is any given crank angle during combustion, θ_0 represents the beginning of combustion in crank angle, and $\Delta\theta$ is the total combustion duration. The constants α and ν are empirically acquired parameters used to fix the shape of the profile. The conservation equations of mass and energy for the open system are applied individually to the burned and unburned gas zones.

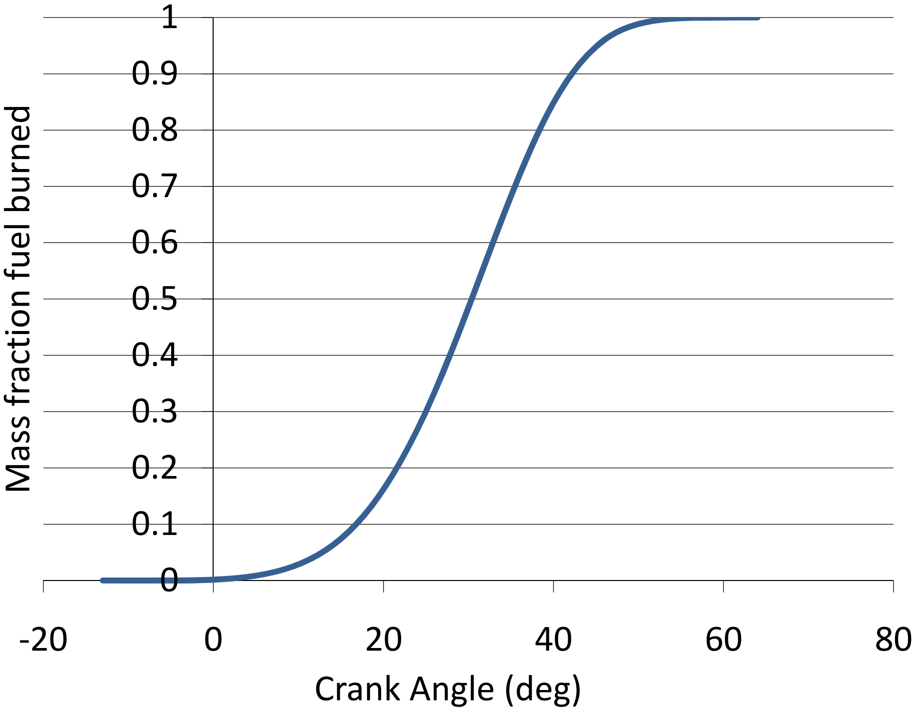

Figure 4.19: Wiebe function

For the purpose of this work, pollutant emission formation will be described by kinetic formation models for both NO_X and CO formation. As discussed in Chapter 3, a mechanism for NO_X formation has been defined in Chapter 3 as:

$$\frac{d[\mathrm{NO}]}{dt} = k_{f1}[\mathrm{O}][\mathrm{N_2}] - k_{r1}[\mathrm{NO}][\mathrm{N}] + k_{f2}[\mathrm{N}][\mathrm{O_2}] - k_{r2}[\mathrm{NO}][\mathrm{O}] + k_{f3}[\mathrm{N}][\mathrm{OH}] - k_{r3}[\mathrm{NO}][\mathrm{H}] \tag{3.33}$$

For very high temperature applications, such as the large-bore 2SC RICE, it can be assumed that the O, N, OH, and H remain in thermodynamic equilibrium in the post flame zone; therefore, their concentrations can be approximated as such. It can also be assumed that N remains at a steady-state concentration. Therefore, the net rate of change of N is very small and may be set equal to zero (Borman and Ragland, 1998). Introducing the afore-mentioned equilibrium assumption, and tuning the reaction rate constant defined in equation 3.26 to data collected from the candidate Cooper GMV engine result in a new NO formation rate:

$$\frac{d[\mathrm{NO}]}{dt} = \frac{8.2 \times 10^{16}}{T^{1/2}} \exp\left(\frac{-74000}{T}\right) [\mathrm{O_2}]^{1/2} [\mathrm{N_2}] \tag{4.3}$$

A comprehensive description of the development of this initial formation rate for NO is included in Appendix C - Nitrogen Oxide Formation Mechanism Development. The strong dependence of the NO formation rate on temperature is evident in both the pre-exponential factor and the exponential term. Both high temperatures and high oxygen concentrations can result in high NO formation rates, described previously by equation (3.25). The cycle-resolved NO concentration (solid line) and in-cylinder temperature (dashed line) are plotted in Figure 4.20. This cycle-resolved formation was created using the CAIMENS model for the candidate Cooper GMV operating at a corrected trapped equivalence ratio of 0.66.

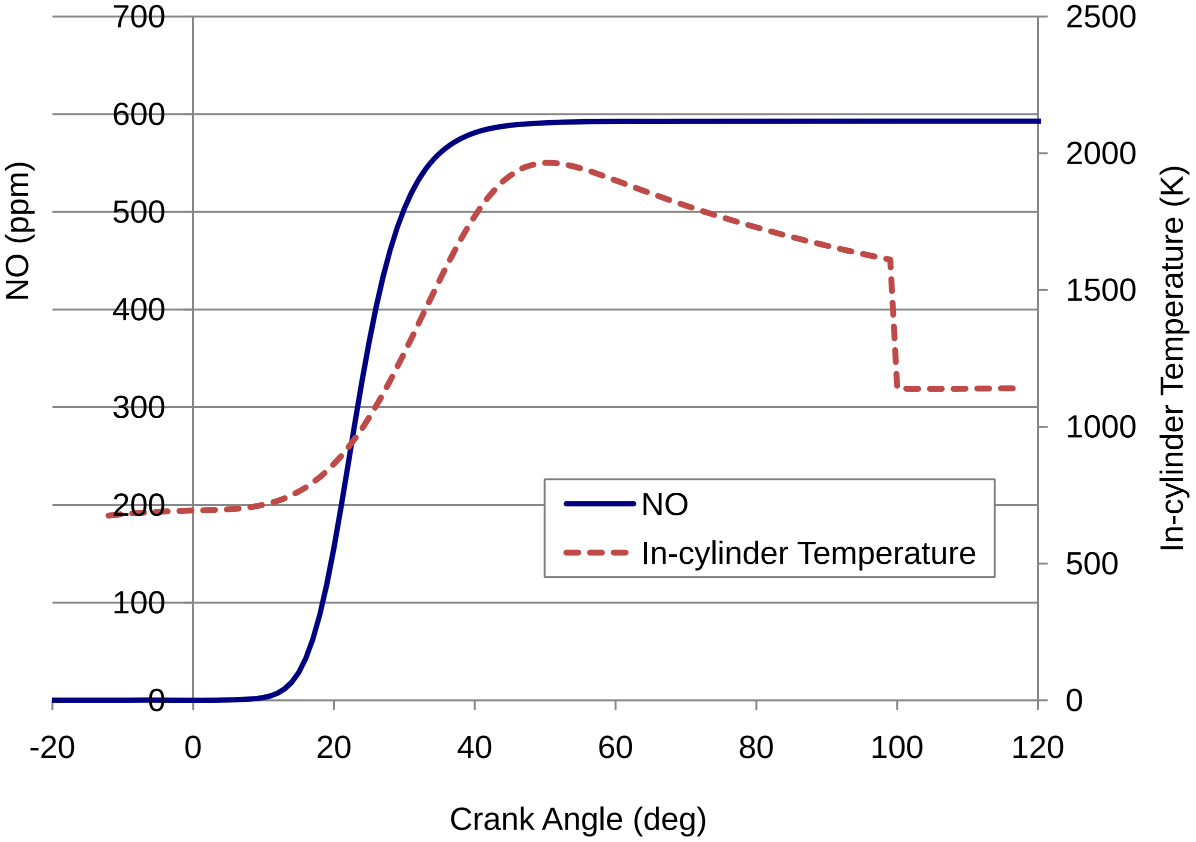

Figure 4.20: New cycle-resolved NO mechanism

The new NO Kinetic Model was then mapped over a range of corrected trapped equivalence ratios and compared to the candidate Cooper GMV engine data at an ignition timing of 10°CA BTDC. The new NO Kinetic Model, for a constant scavenging efficiency of 81.5%, is shown in Figure 4.21. This new model has been integrated into T-RECS.

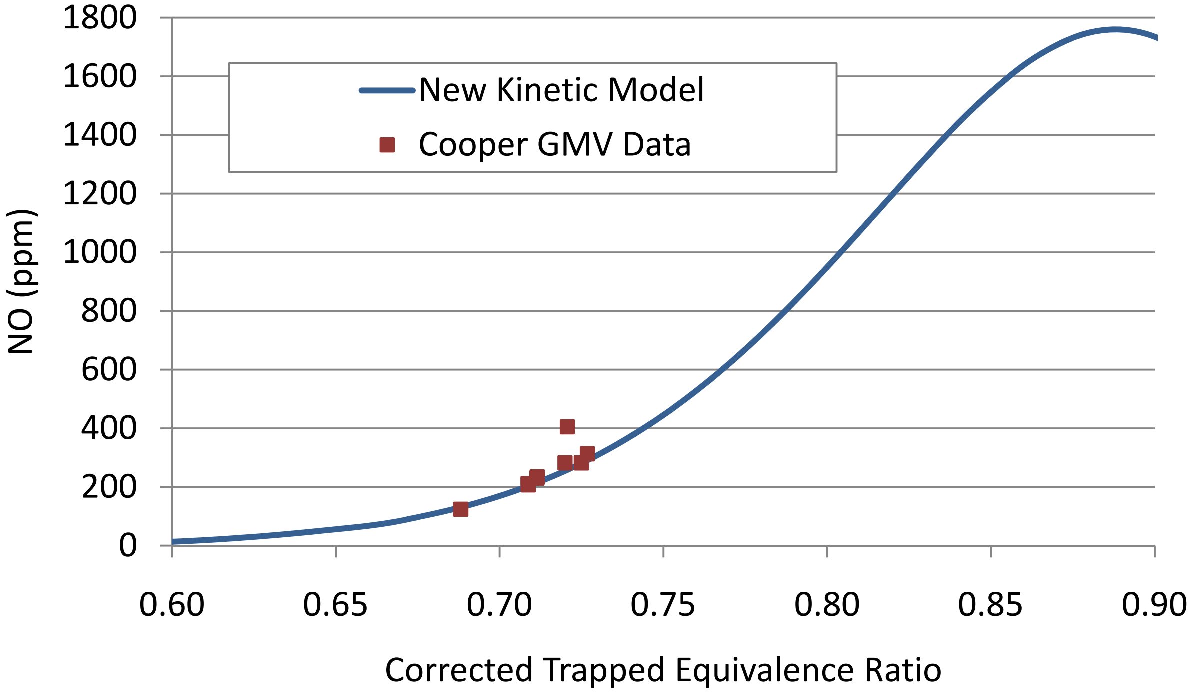

Figure 4.21: New NO Kinetic Model comparison to Cooper GMV data

The formation and destruction of CO is intimately coupled with the primary fuel combustion process; therefore, the CO exhaust concentration emission is primarily controlled by the corrected trapped equivalence ratio and the oxidation of a hydrocarbon fuel.

The burn rate function (equation 4.2) is used to define the mole fraction of fuel ($[CH_4]$) and oxygen ($[O_2]$) within the previously defined final kinetic mechanism, repeated here for reference:

$$\frac{d[\mathrm{CO}]}{dt} = k_f[\mathrm{CH_4}][\mathrm{O_2}]^{\frac{1}{2}} - k_{ox}[\mathrm{CO}][H_2O]^{\frac{1}{2}}[\mathrm{O_2}]^{\frac{1}{2}} \tag{3.31}$$

There are some limitations to the previously developed kinetic formation model. The reaction rate constant presented in equation (3.26) has been experimentally determined. Specifically, the pre-exponential term is a model tuning factor, as previously discussed with regard to the new NO Kinetic Model, and the specified reactions were conducted at constant pressure and temperature with ideal mixing (Hughes, 2001). However, during the combustion cycle of an internal combustion engine, the temperature and pressure are continuously changing as a function of crank angle. Also, the mixture of fuel and air entering the cylinder can be described via various mixing models, but is most certainly not complete, nor ideal. For example, using the rate constants in Table 2.2, but varying temperature with crank angle, gives the CO concentration in Figure 4.22.

Figure 4.22 illustrates the necessity of only applying kinetic mechanisms to the combustion environment for which they were developed. For example, at approximately 35 degrees of crank angle, the concentration of CO is negative, which is physically impossible. Therefore, it is appropriate to develop a new kinetic formation mechanism for CO, based on actual field data collected from the engine of interest.

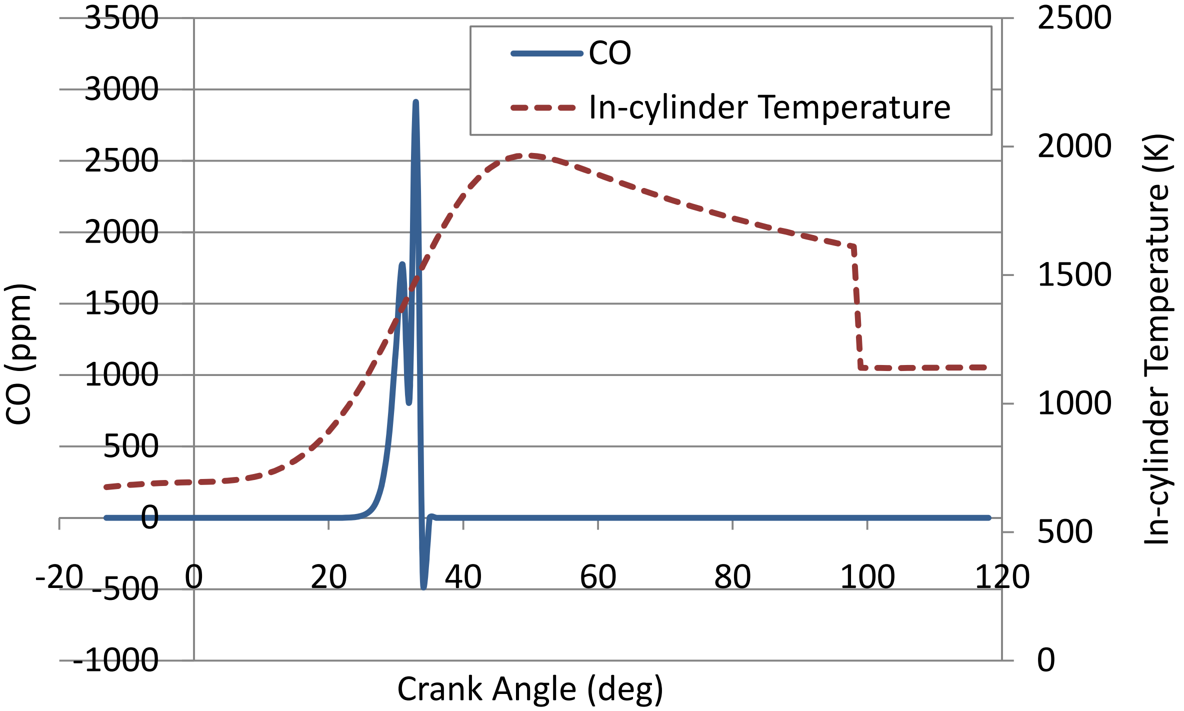

Figure 4.22: Previously developed mechanism with varied temperature

Alternately, using data collected from the candidate Cooper GMV engine, and applying the kinetic mechanism defined in Table 2.2 gives the cycle-resolved CO concentration illustrated in Figure 4.23. This application results in values that are significantly higher than the concentrations measured in the exhaust stream of the candidate Cooper GMV engine even before the engine reaches zero degrees of crank angle.

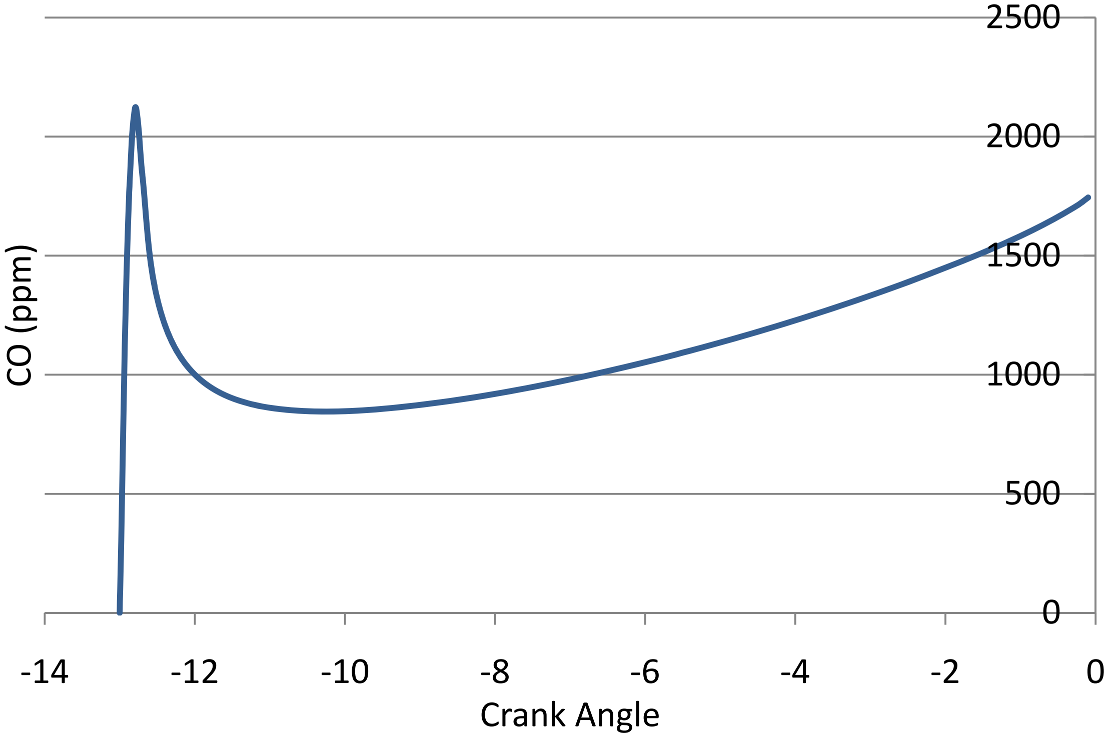

Figure 4.23: Previously developed mechanism applied to Cooper GMV field data

As previously discussed, the new kinetic algorithm for CO formation must integrate the effect of changing temperature and pressure in the cylinder and the updated reaction rate constants. Using the previously developed T-RECS algorithm, an output of the variation in temperature and pressure as a function of crank angle is found. This output is then integrated into equation 3.31 making the new model dependant on the in-cylinder combustion environment.

The reaction rate constants in equation (3.31) are then tuned to the Cooper GMV engine field data. Maintaining the previously defined activation energy:

$$\frac{d[\mathrm{CO}]}{dt} = 10^{12.8}\exp\left(\frac{-40000}{\hat{R}T}\right)[\mathrm{CH_4}][\mathrm{O_2}]^{\frac{1}{2}} - 2.7 \times 10^{5}\exp\left(\frac{-40000}{\hat{R}T}\right)[\mathrm{CO}][\mathrm{H_2O}]^{\frac{1}{2}}[\mathrm{O_2}]^{\frac{1}{2}} \tag{4.4}$$

The new CO cycle-resolved mechanism is illustrated in Figure 4.24. The data in Figure 4.24 shows that during in-cylinder combustion event, post ignition, the CH_4 is quickly oxidized to CO. After the CH_4 is consumed, the CO is subsequently oxidized to CO_2.

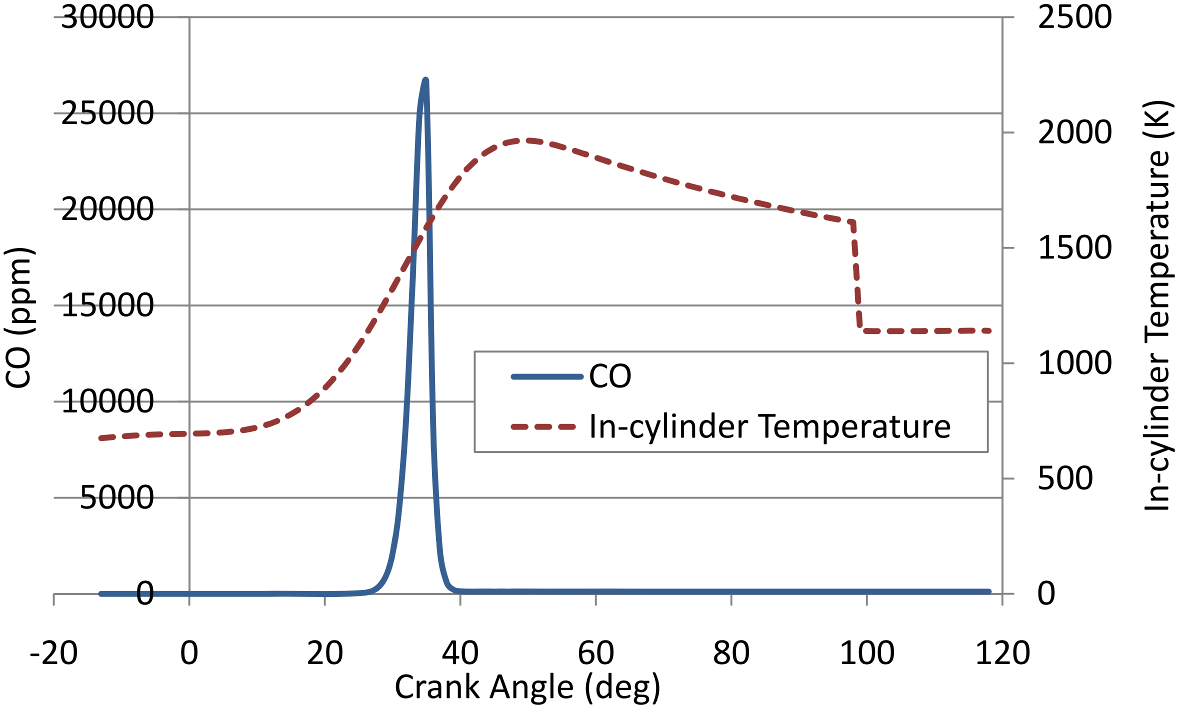

Figure 4.24: New cycle-resolved CO mechanism

A comparison of measured values of exhaust CO concentrations from the candidate Cooper GMV engine as a function of the engine corrected trapped equivalence ratio (equation 3.24) to the new kinetic model is shown in Figure 4.25. As shown, the new model, integrating cycle-resolved in-cylinder temperature and pressure, fits well with data collected from the candidate Cooper GMV data.

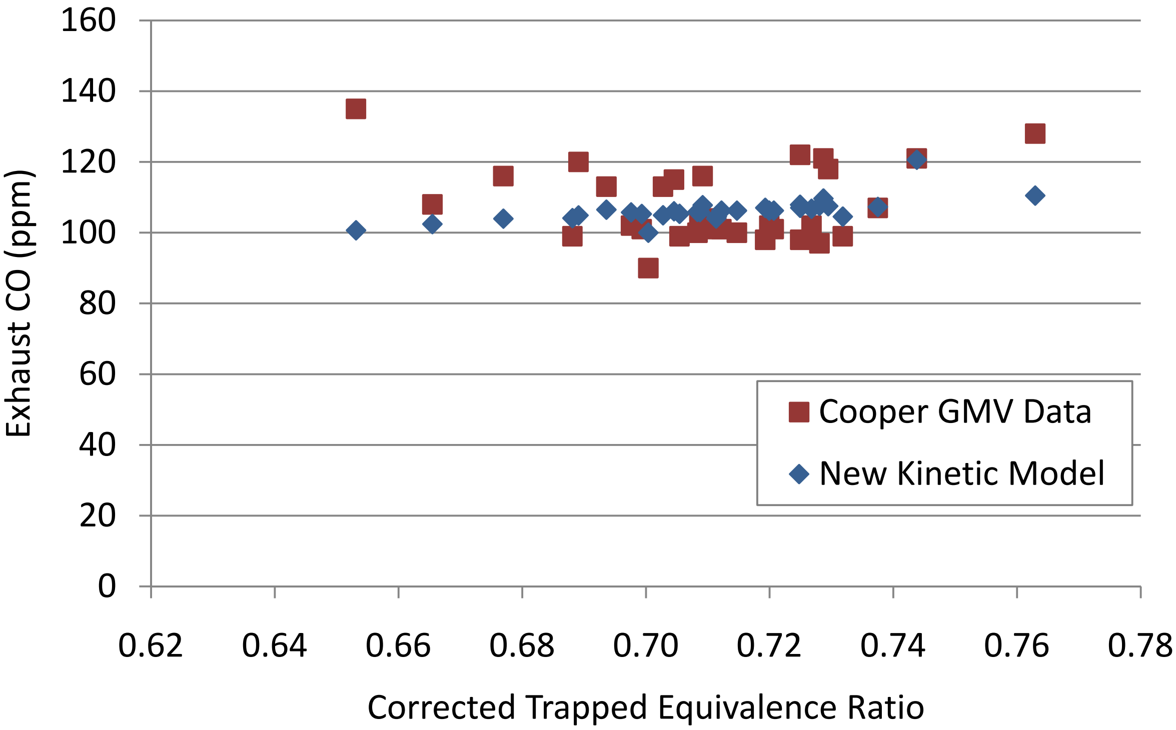

Figure 4.25: New CO Kinetic Model comparison to Cooper GMV Data

Both the new NO and CO kinetic mechanisms have been tuned and validated with data collected from the candidate Cooper GMV engine, and integrated into the T-RECS algorithm. This new T-RECS engine performance and emissions algorithm can be used to analyze the performance of the engine air management system. In addition to engine design applications, these formation mechanisms can be used to evaluate the effectiveness of current and future after-treatment technologies developed for large-bore 2SC RICE to ensure continuous regulatory compliance.

Exhaust Thermodynamic Analysis

The combustion environment and subsequent in-cylinder formation of NO and CO, discussed in the previous section, are controlled by the air delivery system. This air delivery system is controlled directly by the turbocharger compressor which is in turn powered by the turbocharger turbine. Therefore, the turbocharged-engine must be treated as an integrated system and the thermo- and fluid-dynamic interactions between the turbocharger turbine and compressor, and the other engine components must be well understood in order to increase operating flexibility while maintaining pollutant emissions within regulated limits. This cycle of fluid and mechanical energy transfer between the engine cylinder, turbocharger compressor, and turbocharger turbine is maintained by a delicate balance between each component's operating parameters. Analysis of the exhaust system includes physical geometry, gas exchange and blow-down processes, pulsation, and the relation between exhaust system performance and turbocharger operation.

Figure 4.26 illustrates the simplified turbocharged-engine system. To develop the requisite air flow rate, the turbocharger must operate at a relatively high efficiency, and the intake and exhaust system pressure losses must be minimized to optimize turbocharger operating flexibility.

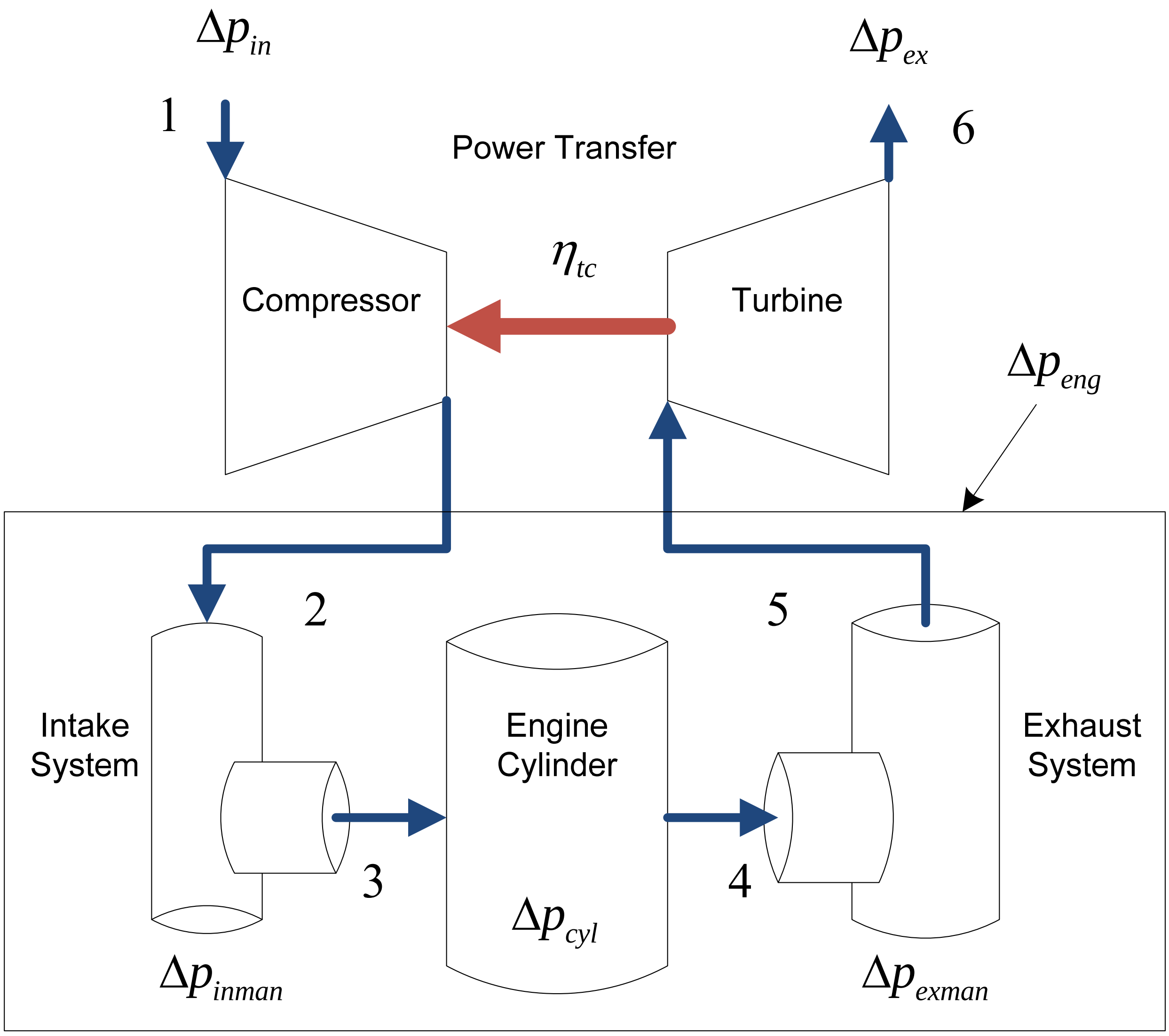

Figure 4.26: Simplified turbocharged-engine system with local pressure identification

The turbocharger turbine of a turbocharged-engine system must produce slightly more power than the turbocharger compressor consumes in order for the system to operate as intended. Otherwise, the turbocharger speed will decrease to a point where jet-assist is triggered. This power production is directly related to the turbine inlet temperature and pressure.

As the air flow rate through the engine is increased, as a result of many emissions-related upgrade projects, the turbocharged-engine experiences: 1) an increased pressure differential between the compressor discharge and turbine inlet, and 2) a reduction in the turbine inlet temperature. These two thermo-physical facts lead to a substantially decreased turbocharger operating range.

Consequently, to maintain turbocharger/engine operating flexibility as well as precise trapped equivalence ratio, the exhaust manifold must be designed in a way to: 1) minimize the differential pressure between the compressor discharge and turbine inlet, and 2) precisely control the scavenging efficiency such that the required trapped equivalence ratio is achieved over a wide operating range.

EMDS Development

In order to adequately characterize the dynamic pressure and temperature within the exhaust runners and manifold, the Charge Air Integrated Manifold Engine Numerical Simulation (CAIMENS) algorithm introduced in the previous sections was augmented. CAIMENS, developed for dynamic optimization of the intake system, was expanded to include the engine exhaust port, runner, and manifold flow path.

The exhaust stream of the large-bore 2SC RICE follows the flow path shown in Figure 4.27. Outside ambient air is brought in through the turbocharger compressor and delivered to the “log” style intake manifold via the compressor discharge. The compressed air then moves down the intake manifold and into one of multiple intake runners. Each intake runner delivers air to the corresponding cylinder. After combustion, the exhaust products are removed from the cylinder by the exhaust runners. The exhaust runners connect to a common “log” style exhaust manifold that delivers the exhaust products to the turbocharger turbine. Therefore, each cylinder experiences a dynamic intake and exhaust pressure and temperature.

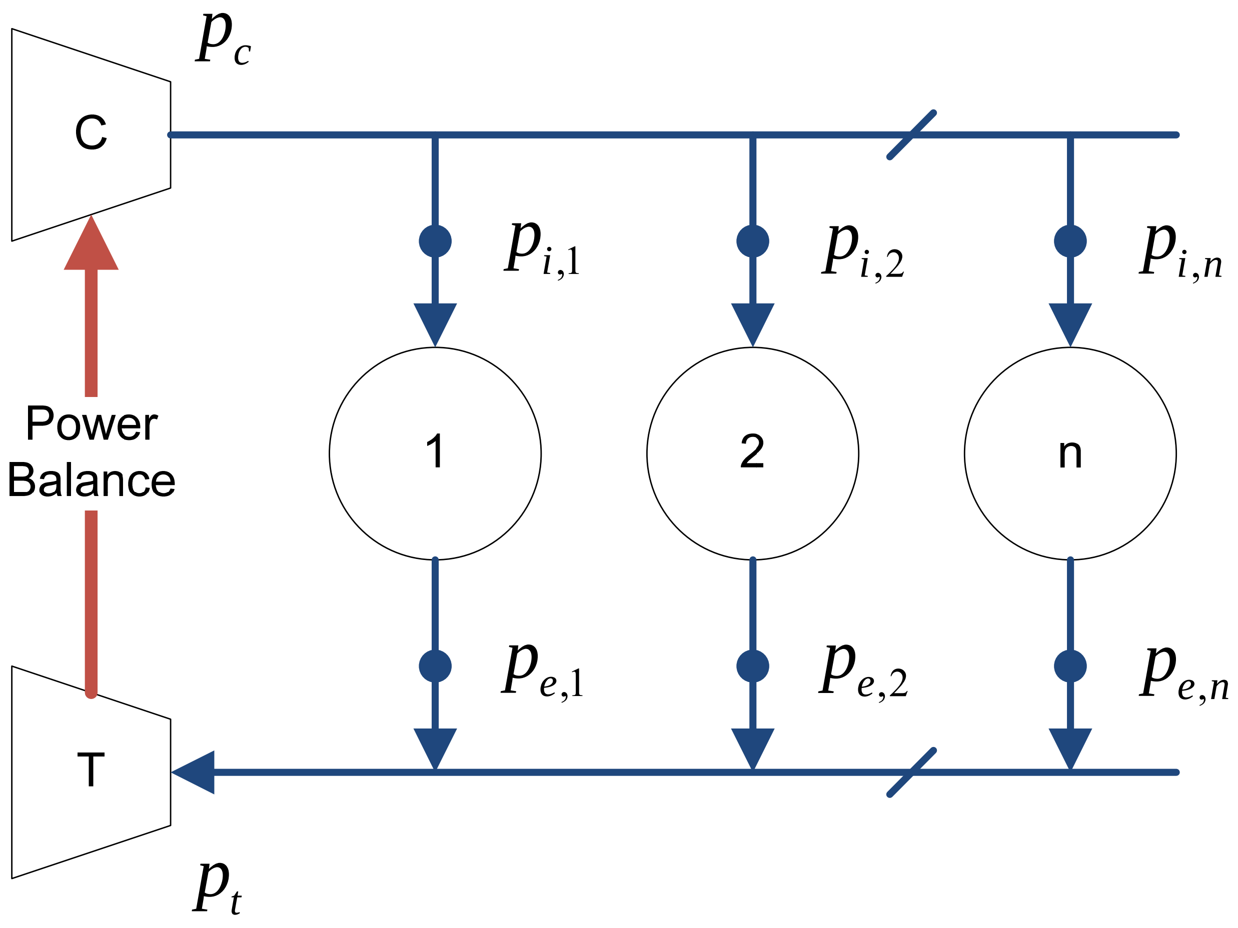

Figure 4.27: Engine intake and exhaust flow path

Expansion of the CAIMENS model required incorporation of the previously developed engine timing model for translation of the high pressure in-cylinder combustion products into exhaust port flow. The modified CAIMENS algorithm is illustrated in Figure 4.28. The author developed an exhaust port opening model (EPO), from the fundamentals of compressible flow described in Chapter 3, “Gas Exchange Processes and Port Flow,” as a method of conditioning the CAIMENS in-cylinder combustion algorithm, T-RECS. The conditioned CAIMENS model was used to develop the requisite boundary conditions for the exhaust manifold model (EMM), which was developed using the conservation fundamentals included in Chapter 3, “Continuity and Conservation in Pipe Matrices.” The EPO was also used as a tuning mechanism to validate the new model with field test data from the candidate Cooper GMV engine. Finally, CAIMENS was combined with the EPO and EMM in a closed-loop iterative algorithm to output instantaneous pressure data for the intake manifold and exhaust manifold at each of the cylinders, and the instantaneous pressure at the turbocharger turbine inlet. For simplicity, this new model has been named the Exhaust Manifold Design Software (EMDS), which integrates the previously developed algorithms and expanded fundamentals:

1. CAIMENS (Chapter 4, “Charge Air Delivery”),
2. Cooper GMV engine timing (Chapter 4, “Engine Timing”),
3. T-RECS NO Kinetic Mechanism (Chapter 4, “In-Cylinder Kinetics”),
4. T-RECS CO Kinetic Mechanism (Chapter 4, “In-Cylinder Kinetics”),
5. EPO (Chapter 3, “Gas Exchange Processes and Port Flow”), and
6. EMM (Chapter 3, “Continuity and Conservation in Pipe Matrices”).

The EMDS was created to predict fluid flow through the air delivery and exhaust removal systems of a large-bore 2SC RICE, to be used to develop a method to effectively and efficiently: 1) distribute charge air within the intake system, and 2) transfer exhaust products to the turbocharger turbine with minimal energy loss. The EMDS predicts pulsation and possible unbalanced air delivery and interference within the intake system and models energy release and pollutant emission formation during and just after the combustion event. Specifically, the EMDS outputs the transient pressure and temperature of the engine exhaust stream at the turbocharger turbine inlet.

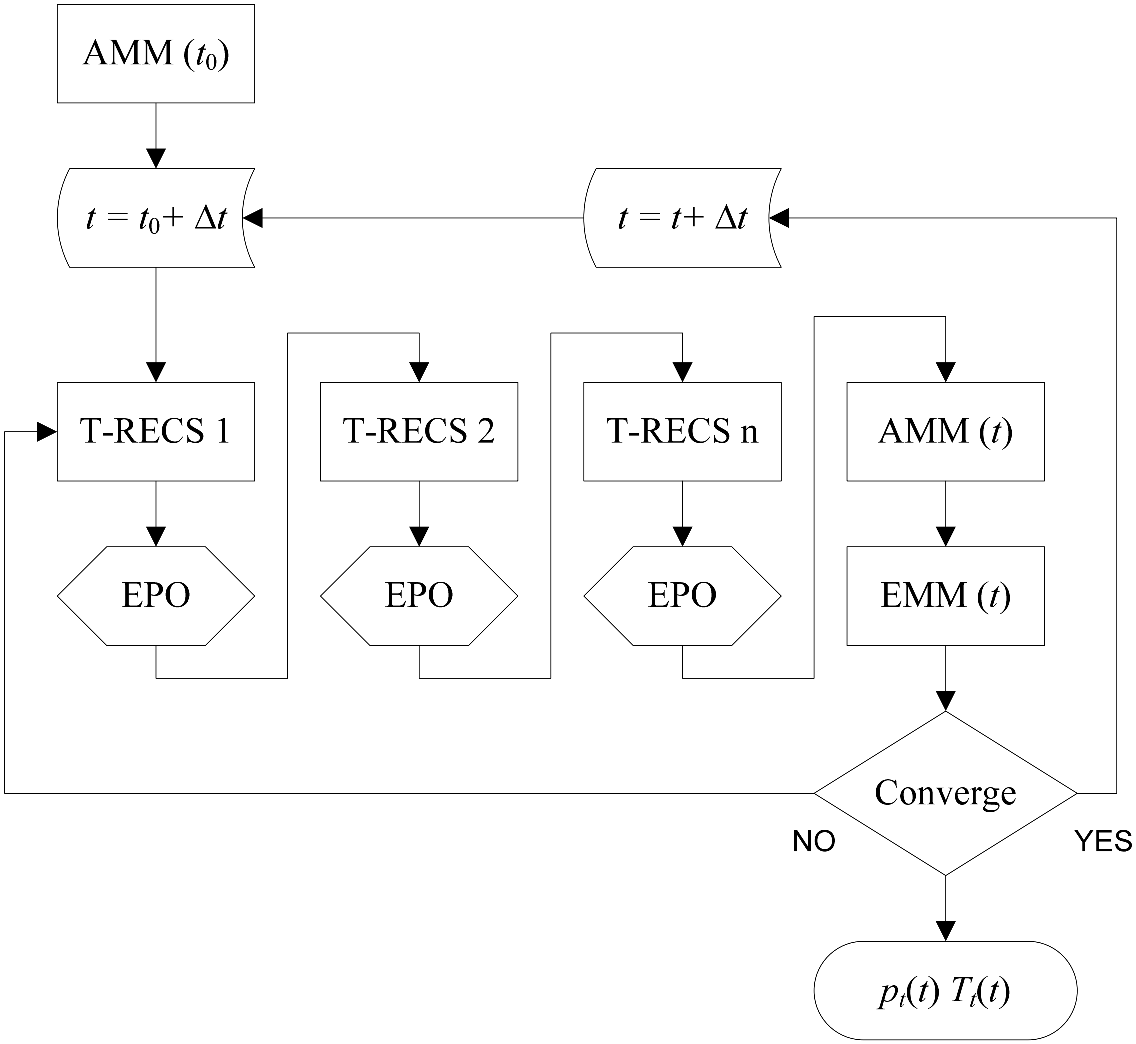

Figure 4.28: Exhaust Manifold Design Software (EMDS)

Hydraulic Loss

Work done during the development of the EMDS included development of a component based hydraulic analysis of the candidate Cooper GMV exhaust removal system to highlight the system's frictional and dynamic resistance to exhaust flow. This component based analysis allowed the author to breakdown and isolate geometrical components to analyze largest relative losses of available exhaust energy and therefore, the largest opportunity for recovery.

Borrowing from analysis of non-uniform flow in ducts, the author defined six hydraulic transitions within the standard exhaust geometry of the candidate engine (ASHRAE, 2005):

1. Exhaust port exit into the cylinder cavity;
2. Exhaust runner entrance from the cylinder cavity;
3. Flow of the exhaust products up exhaust runner (150 degree smooth radius elbow);
4. Exhaust runner transition into exhaust manifold, referred to as the RMT;
5. Flow of the exhaust products down the exhaust manifold; and
6. Flow through the 45 degree transition connecting the exhaust manifold to the turbocharger turbine inlet.

The hydraulic transitions encountered by the exhaust stream leaving a single cylinder are highlighted in Figure 4.29.

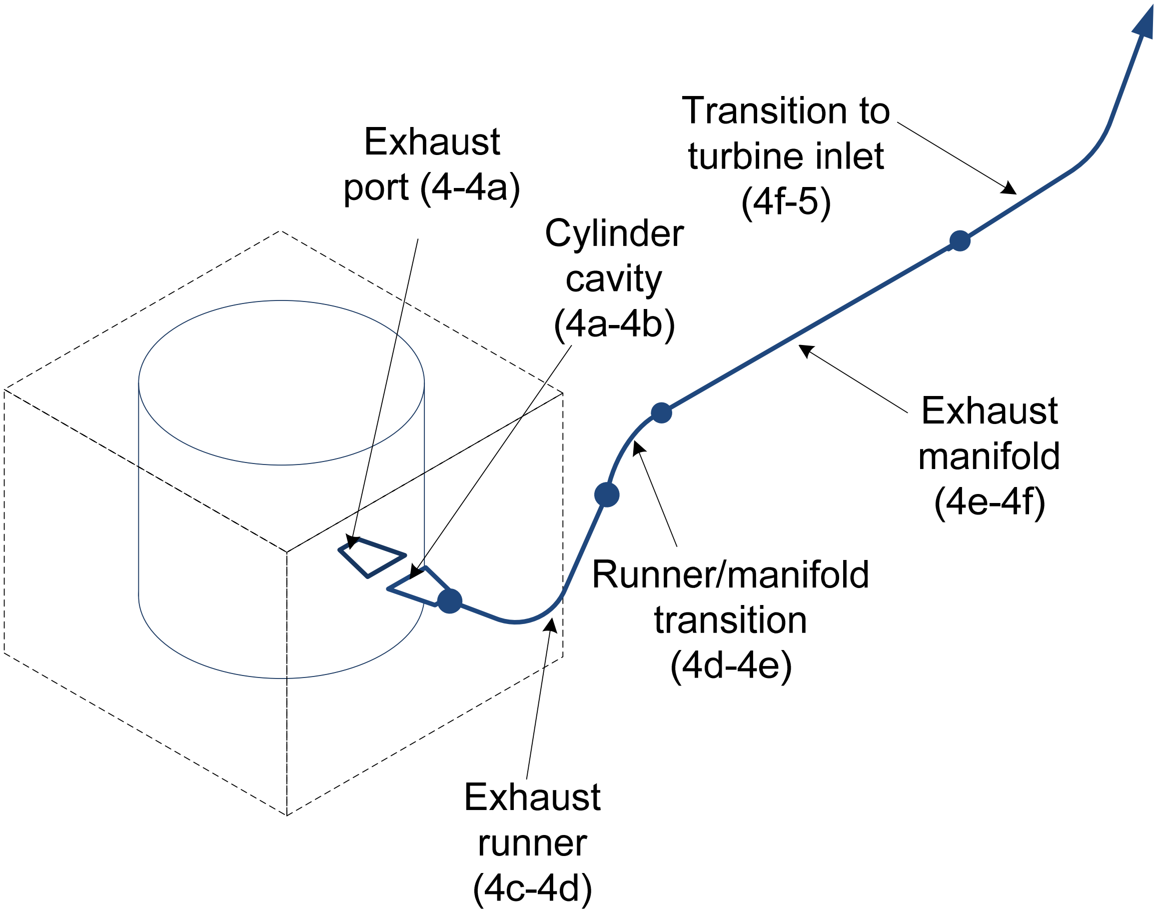

Figure 4.29: Exhaust path hydraulic transitions

As the exhaust stream exits the cylinder through one of 5 exhaust ports, it encounters an abrupt expansion into the rectangular cylinder cavity, shown in Figure 4.30. From the cylinder cavity, the stream encounters a gradual contraction into the rectangular exhaust runner. The stream then flows vertically through the 150° exhaust runner transition. The exhaust runner feeds the stream to the horizontal flow in the semi-circle shaped exhaust manifold. Finally, the exhaust manifold stream enters the turbocharger turbine inlet through a 45° elbow. The candidate Cooper GMV engine exhaust runner is a 17 in by 6.5 in (0.4318 m by 0.1651 m) rectangular duct, and the exhaust manifold is a 24 in (0.6096 m) circular conduit divided in half down the vertical centerline by a steel plate.

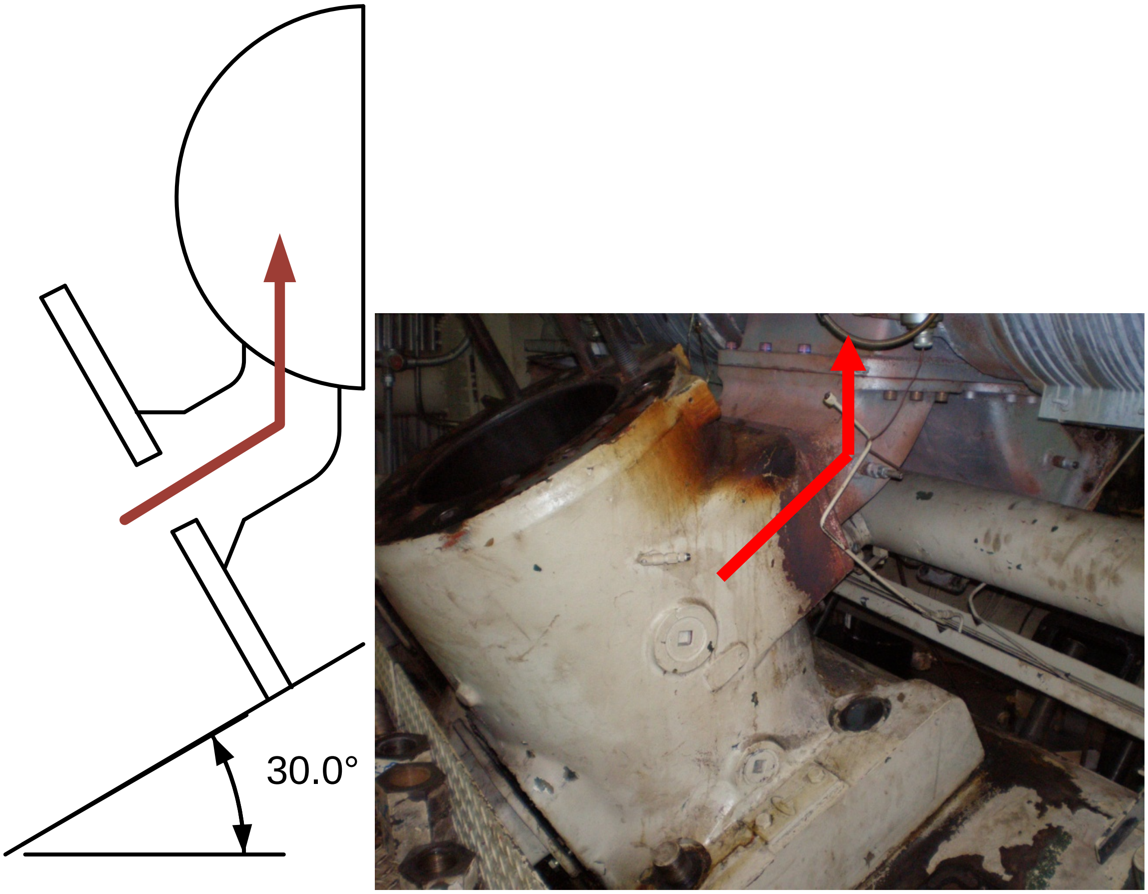

Figure 4.30: Exhaust flow path

Flow through each of the six identified components is governed by a local energy loss coefficient (*C*), used for fluid resistance, defined as the change in static pressure over the velocity pressure at the referenced cross section (ASHRAE, 2005):

$$C = \frac{\Delta p}{\left(\frac{\rho V^2}{2g}\right)} \tag{4.5}$$

Dynamic losses occur along a duct length, or in this work, a length of runner or manifold, and cannot be separated from fiction losses. The quality of the flow though the system is defined by the fluid resistance including frictional losses of the component as a function of the Reynolds number and the roughness factor. The friction factor, Reynolds number, and conduit diameter are related by the Colebrook-White equation included previously as equation (3.6). This quality is developed from conservation of momentum for a single-phase compressible fluid. Values for the calculation of the Reynolds number are determined by: 1) the Equation of State for a compressible fluid, 2) the Continuity Equation for compressible non-isothermal flow, and 3) the conduit diameter. The conduit diameter, if the conduit is non-circular can be calculated one of two ways: an equivalent diameter (D_e), if the duct is rectangular, or a hydraulic diameter (D_h), if the duct is neither circular nor rectangular.

$$D_e = \frac{1.30(HW)^{0.625}}{(H+W)^{0.250}} \tag{4.6}$$

$$D_h = \frac{4(HW)}{2H+2W} \tag{4.7}$$

The loss coefficient is used in the calculation of the hydraulic loss due to the component, defined by the Darcy-Weisbach equation (ASHRAE, 2005):

$$\Delta p = \left(\frac{12fL}{D_h} + C\right)\frac{\rho V^2}{2g} \tag{4.8}$$

The calculation and tuning of this hydraulic loss, via the magnitude of the loss coefficient, is integral to the optimization algorithm described previously. The magnitude of the loss coefficient is defined broadly in the literature, yet the calculation of hydraulic loss is very sensitive to the magnitude of the loss coefficient. Therefore, beginning with values published in the *ASHRAE Handbook: Fundamentals* (2005), the author considered a wide range of values for each of the six component loss coefficients, allowing for tuning of the optimization algorithm to the candidate engine components. A complete listing of loss coefficients used in the analysis of the candidate Cooper GMV exhaust system flow can be found in Appendix E -Loss Coefficients for Exhaust Flow.

In order to compare losses across each component, each component must be described as one of four hydraulic transitions using the corresponding hydraulic loss equation:

1. Expansion,
2. Contraction,
3. Change in flow direction, or
4. Length of circular/noncircular duct.

The six hydraulic losses were then combined in series, illustrated using the resistance diagram shown in Figure 4.31. These losses are a breakdown of Δp_{exman} (local pressure 4 to local pressure 5) identified previously in Figure 4.26 and Figure 4.29, and encompass all friction and dynamic losses in the exhaust removal system.

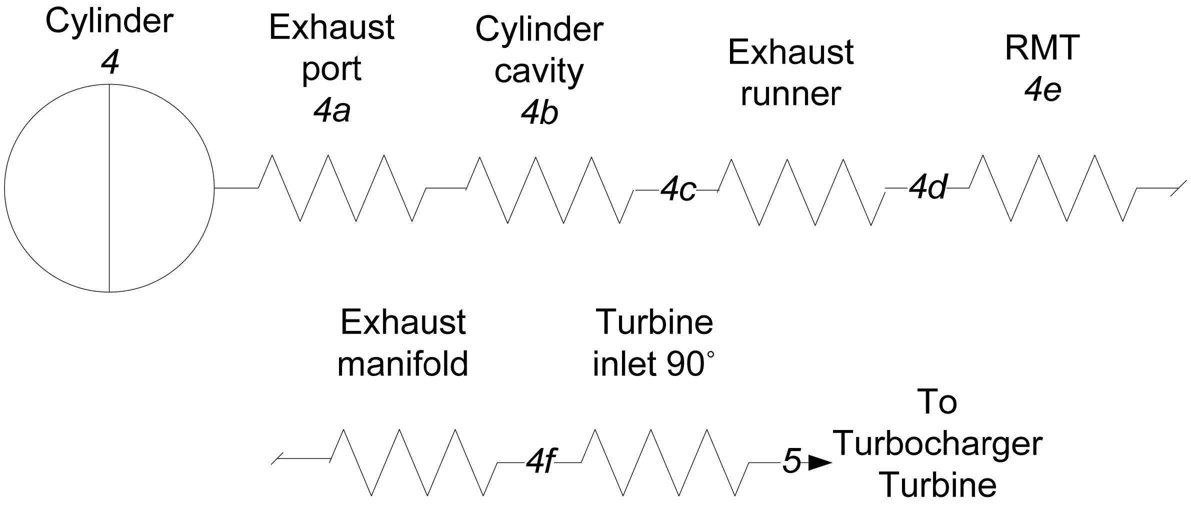

Figure 4.31: Resistance diagram of exhaust path losses

This series of components is mathematically described as a summation of the hydraulic loses in the system, or the hydraulic loss stream function:

$$\sum H_{4-5} = H_{4-4a} + H_{4a-4b} + H_{4b-4c} + H_{4c-4d} + H_{4d-4e} + H_{4e-4f} + H_{4f-5} \tag{4.9}$$

The hydraulic loss summation was used to tune relative component loss functions via the comparison of the optimization parameters to: 1) values of in-cylinder exhaust product pressure and temperature calculated by EMDS, and 2) high speed field data collected on the candidate Cooper GMV engine. The minimization of each component's hydraulic loss function was included as a method of optimization within the optimization software.

Radial Thermal Loss

The author then turned to thermal losses via radial heat transfer from the exhaust stream as the second category for optimization of the exhaust removal system. Thermal energy losses through insulation are governed primarily by the R-value or thermal conductivity (k) and thickness of the piping insulation as defined in Figure 4.32.

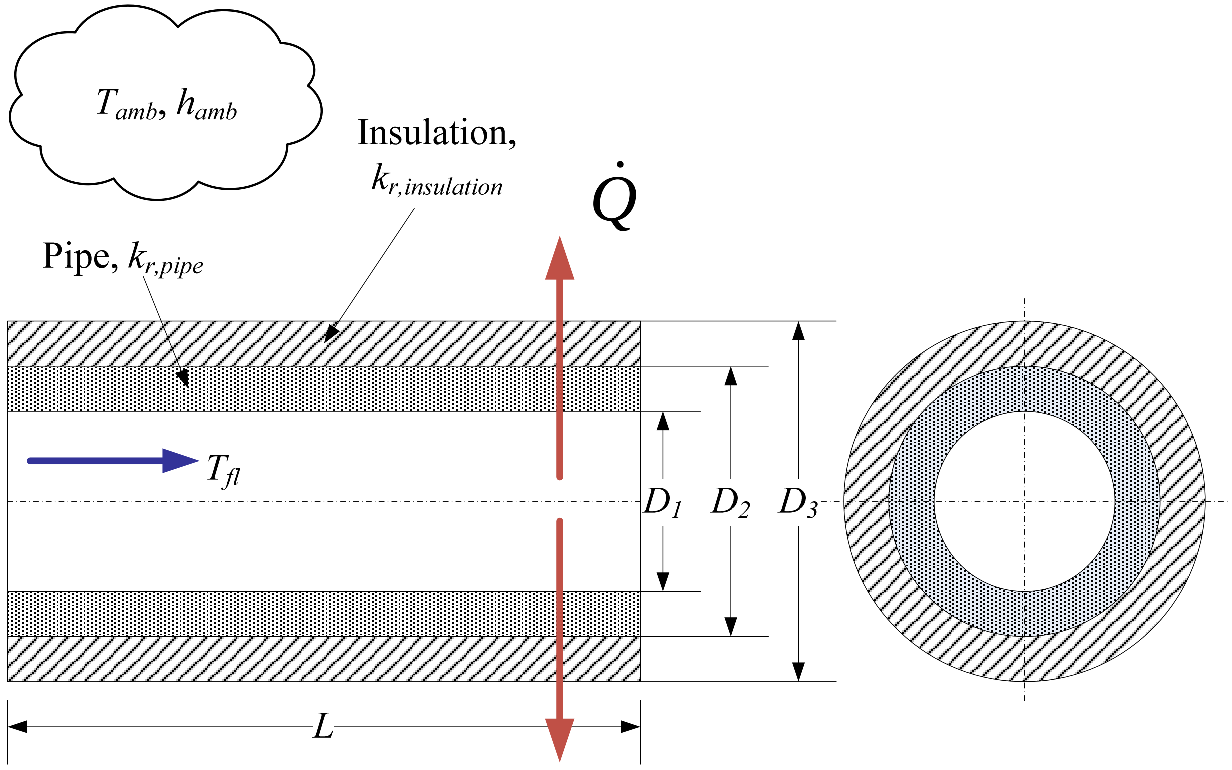

Figure 4.32: Heat loss through piping insulation

Heat transfer from a working fluid, the exhaust stream, out through the exhaust piping and subsequent insulation is defined as (Moran, 1998):

$$\dot{Q} = \frac{\pi L\left(T_{fl} - T_{amb}\right)}{\left[\frac{1}{2k_{r,pipe}}\left(\frac{D_2}{D_1}\right) + \frac{1}{2k_{r,insulation}}\left(\frac{D_3}{D_2}\right) + \frac{1}{h_{amb}D_3}\right]} \tag{4.10}$$

The fluid temperature (T_{fl}) is solved for using the EMDS algorithm and varies with the pressure pulsation in the exhaust manifold. The convective heat transfer coefficient reflects free convection of air at $T_{amb} = 38$ºC (100ºF).

Work done to identify the largest opportunities for mechanical and thermal available energy recovery allowed the author to specify a “test matrix” to characterize exhaust manifold performance. Exhaust manifold performance was broadly defined as the ability of the exhaust manifold to deliver the maximum amount of available energy from the engine to the turbocharger turbine inlet without disrupting scavenging efficiency.

The “test matrix” was defined as including: 1) manifold diameter, 2) manifold length, and 3) changes in the direction of fluid flow. These three variables were identified primarily due to their impact on the dissipation of mechanical and thermal energy. Each parameter contributes with varying significance to the energy loss as the exhaust stream exits the cylinder into the runner, transitions from the runner to the manifold, and travels down the manifold to the turbocharger.

EMDS Optimization

Several methods for optimization could be employed to enhance the performance of the exhaust manifold. The general goal of the optimizing procedure was to maximize/minimize one or more performance parameters while operating under a set of constraints and boundary conditions.

The optimization of the model had two goals: 1) limit the disruption of scavenging efficiency, and 2) maximize energy available to the turbocharger. Scavenging efficiency correlates directly to the pressure differential across the cylinder as well as turbocharger compressor flow rate. Similarly, maximum energy available at the turbocharger turbine, an integration of instantaneous thermal and mechanical (pressure) energy created by the engine and transferred down the exhaust manifold, also correlates to local pressure. Therefore, a schematic of the engine system was developed to identify local pressures, shown again for reference in Figure 4.33.

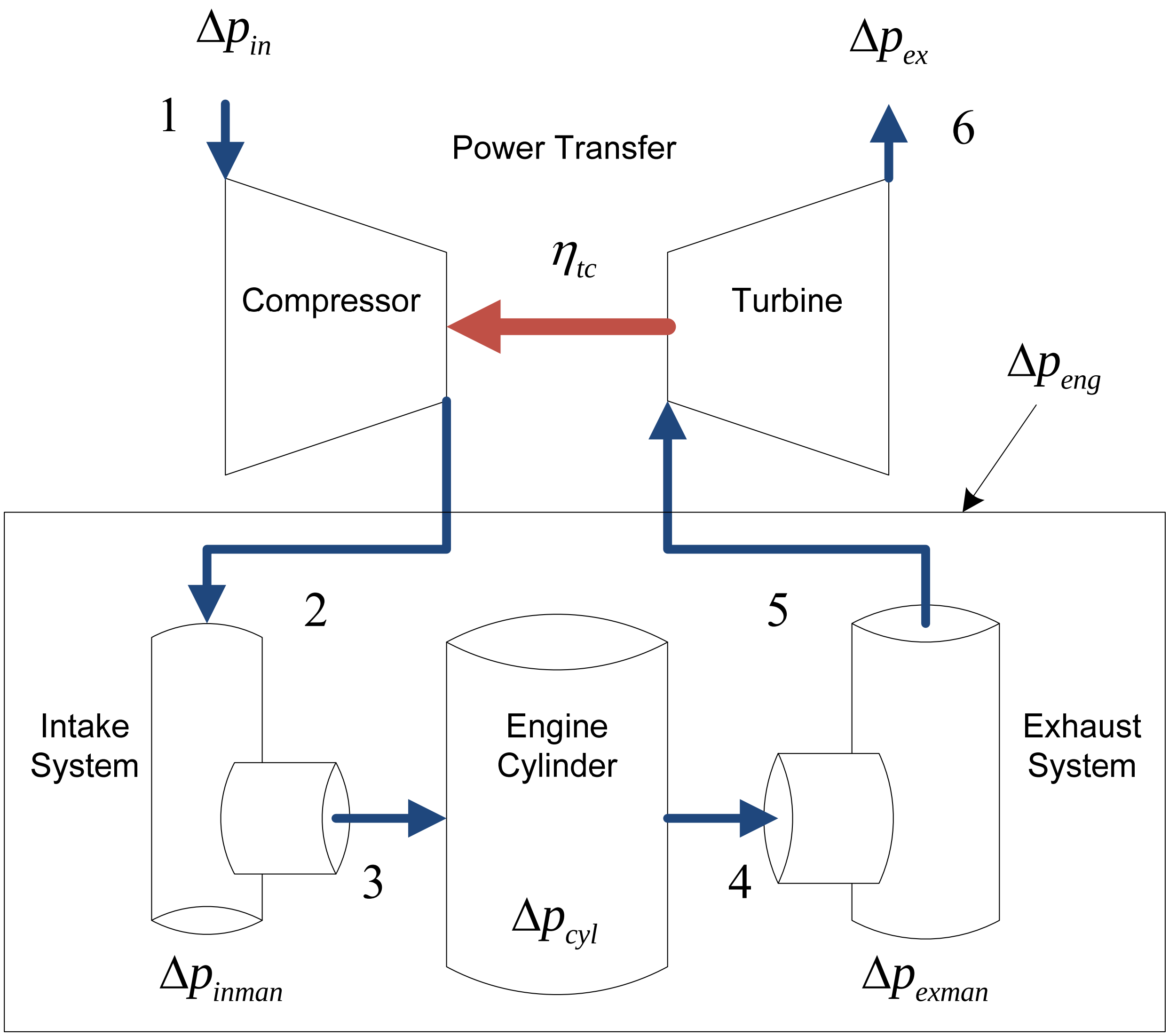

Figure 4.33: Local pressure identification

To develop the requisite turbocharger compressor air flow rate, the turbocharger must operate at a relatively high efficiency (η_{tc}). The system pressure losses (Δp_{eng}, Δp_{in}, and Δp_{ex}) must be minimized to optimize turbocharger operating flexibility. The terms Δp_{in} and Δp_{ex} are the pressure losses upstream and downstream of the turbocharger, and the term Δp_{eng} is the pressure differential between the compressor discharge and the turbine inlet. These parameters are summarized in Table 4.2.

Table 4.2: Turbocharger operating flexibility parameters

$\Delta p_{in} = p_{amb} - p_1$	$\Delta p_{ex} = p_6 - p_{amb}$	$\Delta p_{exman} = p_4 - p_5$
$\Delta p_{cyl} = p_3 - p_4$	$\Delta p_{inman} = p_2 - p_3$	$p_5 = \bar{p}_{turb}$
$\eta_{tc} = \eta_t \eta_c \eta_m$	$\Delta p_{eng} = \Delta p_{inman} + \Delta p_{cyl} + \Delta p_{exman}$	

The EMDS was then tuned and validated with field data collected on the candidate Cooper GMV engine. The Cooper GMV engine, when operating at full load and speed, and the compressor design air flow rate, creates the temporal and spatial distribution of exhaust pressure shown in Figure 4.34. As the exhaust ports of each cylinder are opened, determined by the engine firing order, an independent pulse of exhaust products is released into the exhaust removal system. Each pulse travels down the exhaust manifold toward the turbocharger turbine inlet. These pulses impact the operation of each successive cylinder. Therefore, the turbine inlet is subjected to a continuously changing dynamic pressure and temperature.

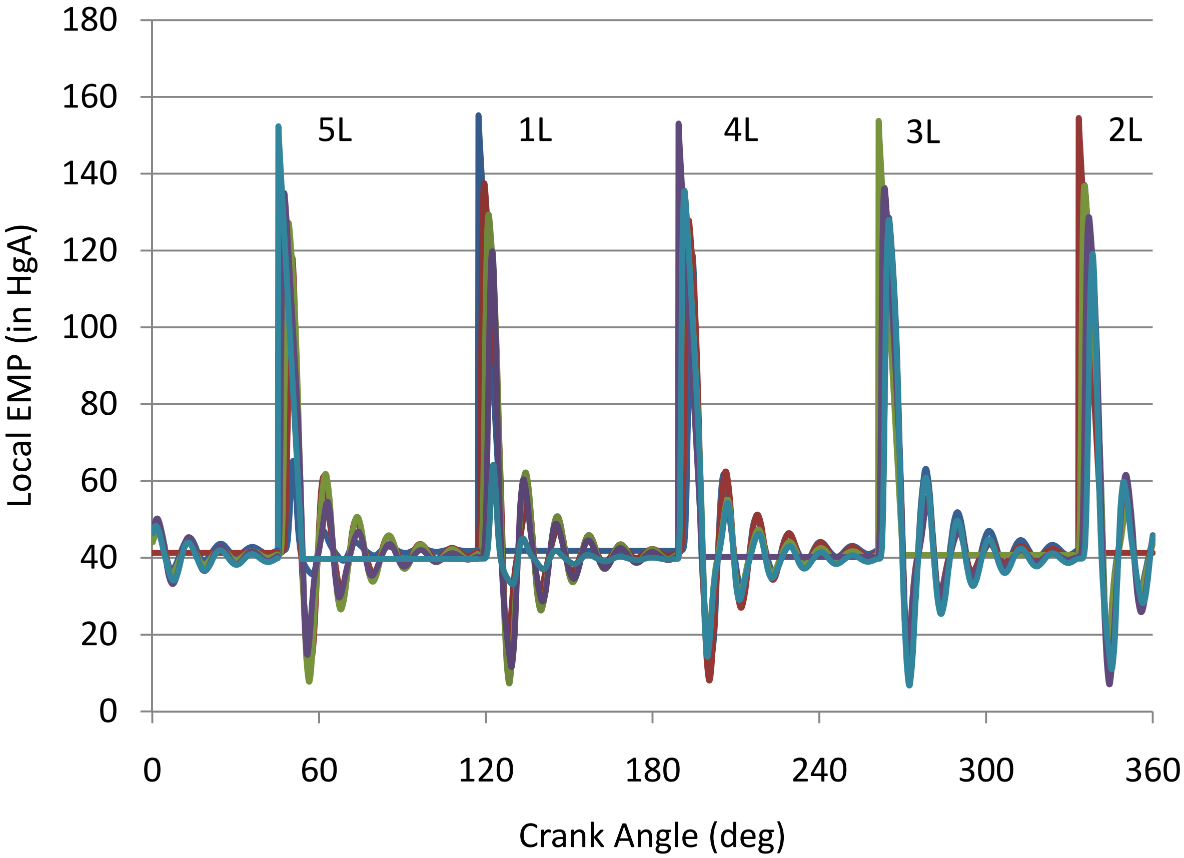

Figure 4.34: EMDS exhaust manifold pressure distribution

Scavenging Efficiency

For the EMDS, the focus was put on local pressures p_4 and p_5 in the Figure 4.33. Utilizing the exhaust side of the engine, scavenging efficiency, as a function of Δp_{cyl}, can be increased or decreased with p_4, which is the magnitude of the individual cylinder back pressure. Therefore, it is imperative that the pulsation in the exhaust stream be mapped, in order to minimize p_4 at the exhaust port opening event.

The mapped pulsation must highlight and subsequently prove or disprove the possibility of two phenomena: 1) standing waves in the exhaust system, and 2) high amplitude residual pulsation from previous cylinder exhaust port opening creating high back pressure at the exhaust port opening event of the next cylinder in the firing order.

The possibility of both phenomena has been extensively studied using the previously tuned EMDS, and the existence of both has been effectively disproved. With regard to standing waves in the exhaust system:

1. No standing wave could be created with the tuned EMDS in the exhaust system of the turbocharged candidate Cooper GMV engine.
2. The engine timing and firing order contributed only to wave destruction, not wave amplification, in the EMDS output.

With regard to high amplitude residual pulsation creating high back pressures at the exhaust port:

1. The engine timing and firing order prohibited the EMDS from placing a high amplitude wave at the exhaust port opening event of the active cylinder.
2. The abrupt exhaust runner to manifold junction significantly dampened the energy of the exhaust pulsation.

The number of cylinders on the existing Cooper GMV geometry was incrementally expanded in pursuit of a configuration that would allow for the high amplitude residual pulsation discussed previously. The increase in cylinders decreased the degree of crank angle and therefore, the timing between cylinder firing. The author concluded that in order to create an adverse effect on scavenging efficiency, the Cooper GMV would need an even number of at least 10, but no more than 14 cylinders on the left bank alone. With this expanded configuration, the EMDS was able to place a high amplitude residual wave from the previous cylinder exhaust port opening creating high back pressure at the exhaust port opening event of the next cylinder in the firing order. In conclusion, with reference to goal (1) of the optimization of the EMDS, the exhaust pulsation in the candidate Cooper GMV has minimal effect on its scavenging efficiency. Goal (2) will be addressed next.

Energy Available to Turbocharger

In order to highlight the local pressures, p_4 and p_5 (Figure 4.33), on the exhaust side of the system, parameters to minimize losses in the candidate Cooper GMV exhaust removal system illustrated in Figure 4.33 were investigated. These losses are grouped into two categories: 1) flow losses due fluid resistance in the flow path, and 2) thermal losses due to radial heat transfer.

In order to satisfy goal (2) of the optimization of the EMDS, the author defined a requisite turbocharger turbine inlet temperature to serve as the minimum exhaust fluid temperature for sustained turbocharger operation. The relationship between the various pressures and pressure losses throughout the turbocharged-engine system, the turbocharger overall efficiency, ambient conditions, and the required turbine inlet temperature for sustainability was derived from thermodynamic principles and is written as (subscript numbers refer to those in Figure 4.33):

$$T_5 = \frac{T_1}{\eta_{tc}(1+FA)}\frac{c_{p,a}}{c_{p,ex}}\left[1-\left(\frac{\Delta p_{eng}+p_5}{p_{amb}-\Delta p_{in}}\right)^{\frac{\gamma_{a-1}}{\gamma_a}}\right]\left[\left(\frac{p_{amb}+\Delta p_{exh}}{p_5}\right)^{\frac{\gamma_{a-1}}{\gamma_a}}-1\right]^{-1} \tag{4.11}$$

The turbine inlet temperature must be larger than T_5 and optimized by minimizing both the flow losses through and radial heat transfer out of the system to sustainably operate the turbocharger. Typical operating conditions for the candidate Cooper GMV engine to be used in equation 4.11 are listed in Table 4.3.

Table 4.3: Candidate Cooper GMV operating conditions

T_1	560 °R	Δp_{in}	5.0 in H_2O	p_2	22.3 psia	FA	0.03	η_{comp}	70%
p_{amb}	14.9 psia	Δp_{ex}	5.0 in H_2O	$c_{p,a}/c_{p,e}$	0.95	$\dot{m}_{ca}$	9.25 lb/s	η_{turb}	85%

Available Energy – Metric for Optimization

Available energy (av) is a function of both the mechanical (fluid resistance) and radial thermal losses across each component and is a function of the component local loss coefficient. Available energy, or availability, provided the metric by which the author could combine, analyze, and optimize losses in the candidate Cooper GMV engine exhaust removal system. This analysis can be completed on the system as a whole, or on a component basis. Each component hydraulic and thermal loss and the overall hydraulic and thermal loss of the system were used to calculate the total change in available energy. The change in available energy (Δav) across a component is defined as (Moran, 1998):

$$\Delta av_{4-5} = funct\left(\sum H_{4-5}, \sum \left(\frac{\dot{Q}}{\dot{m}_{exman}}\right)_{4-5}\right) \tag{4.12}$$

System available energy (av) at the turbocharger turbine inlet is a summation of the thermo-chemical flow energy available in the exhaust products and dynamic energy available in the stream due to its compressible characteristics. System available energy (av) is referenced to the dead state, p_0 = 1 atm and T_0 = 0°C, and defined as (Moran, 1998):

$$av = (h - h_0) + v(p_0 - p) - T_0(s - s_0) \tag{4.13}$$

As illustrated in Figure 4.35, system available energy was calculated using the EMDS integrated into the Optimization Software and inputting the turbocharger efficiency as an indicator of engine load.

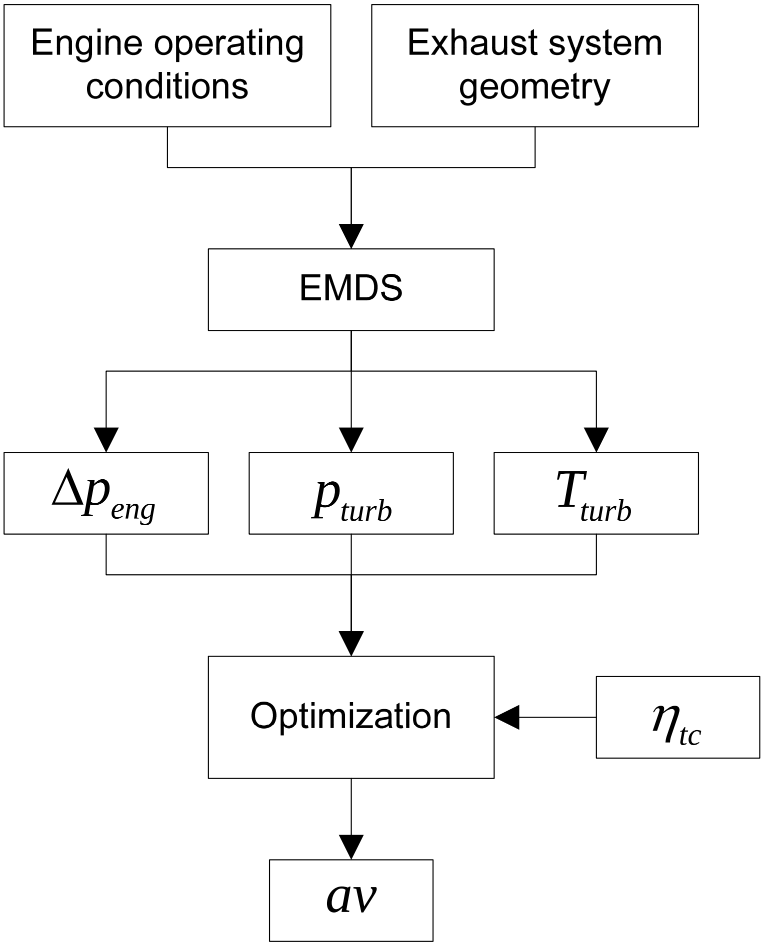

Figure 4.35: Available energy algorithm

The author plotted the requisite values versus engine differential pressure in Figure 4.36 to enhance visualization of the minimum required available energy for sustained turbocharger operation. As discussed previously, if the engine does not provide the minimum required available energy to the turbocharger turbine, jet-assist will be triggered. Conversely, if the engine is providing more energy than required, the waste-gate valve may be opened to essentially vent excess energy.

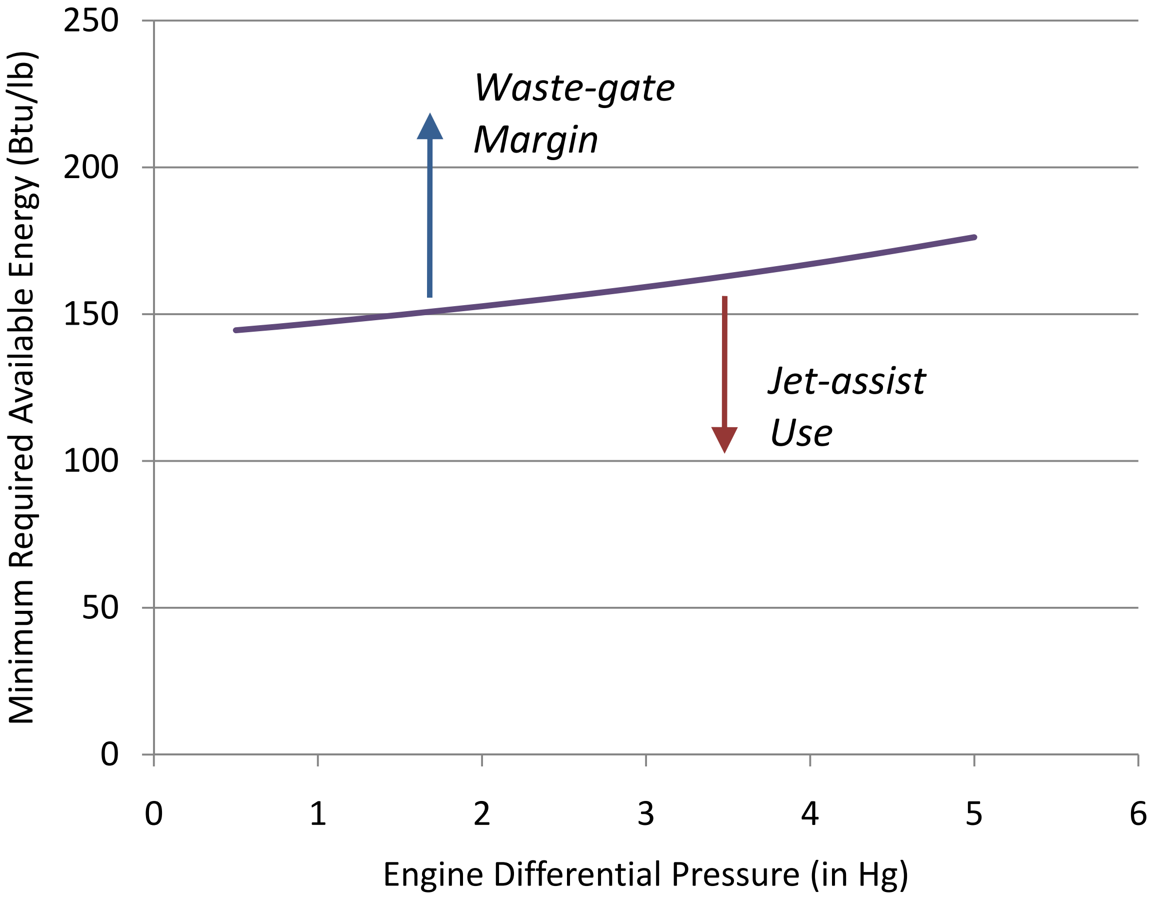

Figure 4.36: Available energy threshold

The implications of the available energy threshold are summarized below:

1. Any value of available energy calculated using engine exhaust system conditions that falls above the line of minimum required available energy is defined as "waste-gate margin," allowing for expanded engine operation.
2. "Waste-gate margin" is quantified by a percentage that compares maximum possible turbine output power to power consumed by the compressor. This is not to be interpreted as percent valve open due to the non-linearity of flow through a valve.
3. Any available energy value that falls below the minimum corresponds to the triggering of jet-assist to maintain turbocharger speed.

In order to translate available energy into expanded turbocharger operating range, the author developed a new metric, waste-gate margin (*wmg*), discussed previously. Waste-gate margin is defined as a percentage that compares the maximum possible turbine output to that consumed by the compressor, and is quantified by:

$$wmg(\%) = \frac{\dot{W}_{turb,max} - \dot{W}_{turb}}{\dot{W}_{turb}} \times 100 \tag{4.14}$$

where the maximum turbine power output ($\dot{W}_{turb,max}$) and power consumed by the compressor ($\dot{W}_{comp}$) are defined as:

$$\dot{W}_{turb,max} = \dot{m}_2(1 + FA)c_{p,5}\eta_t T_5 \left[1 - \left(\frac{p_6}{p_5}\right)^{\frac{\gamma-1}{\gamma}}\right] \tag{4.15}$$

$$\dot{W}_{turb} = -\dot{W}_{comp} = \frac{\dot{m}_2 c_{p,2} T_1}{\eta_c}\left[1 - \left(\frac{p_2}{p_1}\right)^{\frac{\gamma-1}{\gamma}}\right] \tag{4.16}$$

This previously undefined threshold for turbocharger operation allowed the author to satisfy goal (2) of the optimization and begin defining prerequisites for exhaust manifold design.

Component Based Analysis

In order to develop optimal exhaust manifold design parameters, a comprehensive component based analysis of the exhaust removal system, shown again in Figure 4.37 for reference, was completed.

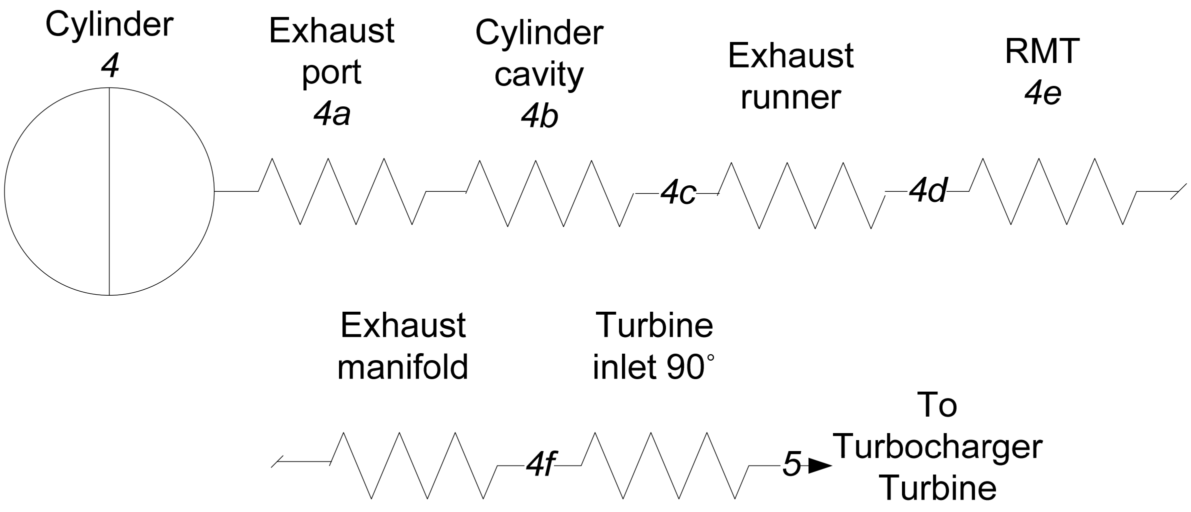

Figure 4.37: Resistance diagram of exhaust path losses

A summary of the results of the component based analysis of cylinder 1L is shown in and illustrated in Figure 4.38 outlines losses specific to heat hydraulic transition in the exhaust stream from cylinder 1L to the turbocharger turbine inlet. The total changes in available mechanical (due to fluid resistance) and available thermal energy (due to radial heat loss) are 19.91 Btu/lb and 1.75 Btu/lb, respectively. As referenced to the dead state (equation 4.13), there is 425.42 Btu/lb of available energy due to in-cylinder combustion, 21.65 Btu/lb of which is lost to the exhaust removal system, leaving 403.77 Btu/lb for the turbocharger turbine.

Table 4.4: Availability loss by component

Transition	Description	Δp (psig)	ΔT (°R)	Δav mech	Δav thermal	Δav total	av (Btu/lb)
4-4a	Contraction	0.288	3.617	0.706	0.062	0.768	425.417
4a-4b	Expansion	0.705	8.911	1.739	0.153	1.892	424.649
4b-4c	Contraction	2.680	34.434	6.711	0.588	7.299	422.757
4c-4d	Change in flow direction	3.266	43.250	8.410	0.736	9.146	415.458
4d-4e	RMT Junction	0.737	9.969	1.935	0.171	2.107	406.312
4e-4f	Circular duct	0.012	0.167	0.032	0.003	0.035	404.205
4f-5	Change in flow direction	0.141	1.917	0.372	0.033	0.405	404.170
4-5	Total	7.830	102.266	19.906	1.747	21.653	403.765

It is important to note the relative magnitudes of the availability loss across each component. Specifically, the 150° vertical turn of exhaust products within the exhaust runner is responsible for the largest loss of available energy in the exhaust removal system of each cylinder. The second largest loss of available energy is due to the contraction of the hot exhaust gases from the exhaust cylinder cavity into the exhaust runner, followed by the junction of the runner to manifold transition (RMT).

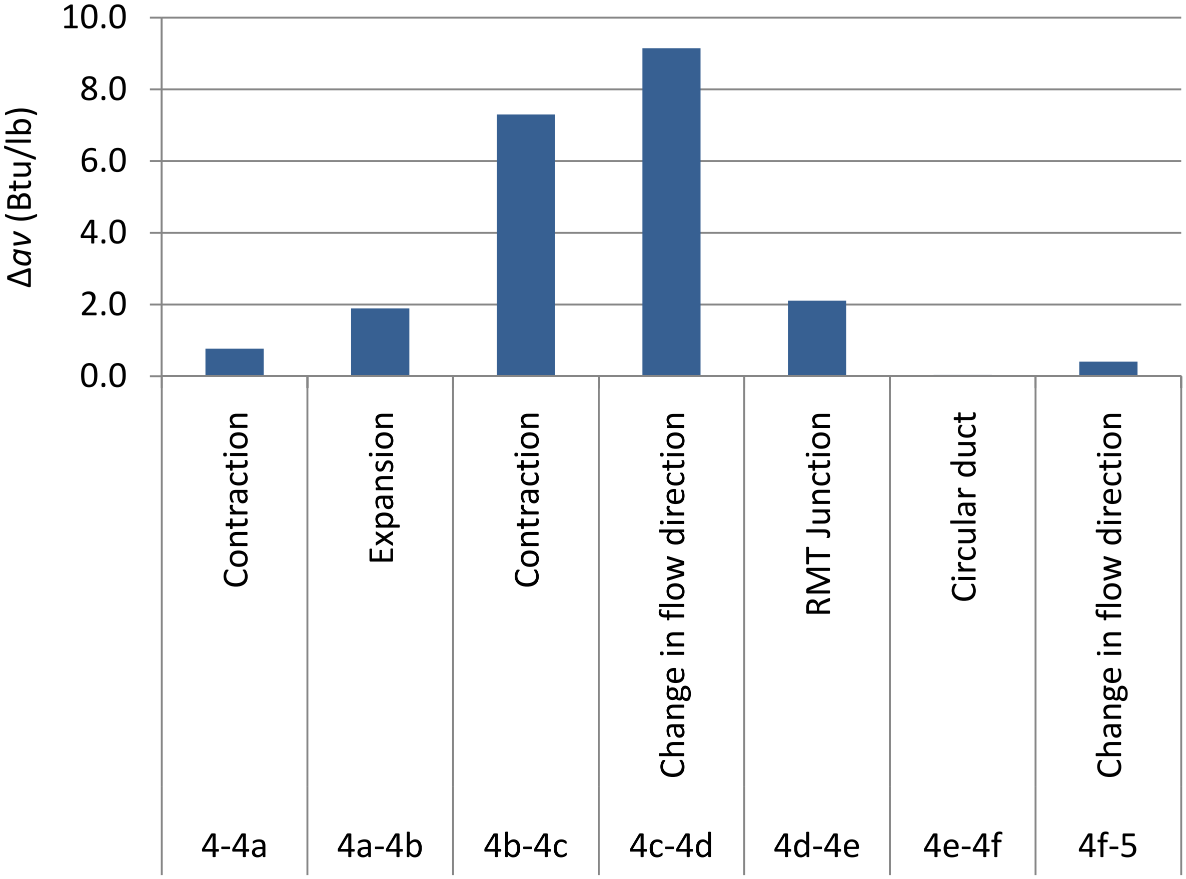

Figure 4.38: Single cylinder component availability losses

Each cylinder contributes to the overall mechanical and thermal energy loss of the engine via an average of all six cylinders, weighted by the mass flow rate of exhaust exiting the cylinder. As stated previously, each pulse of exhaust gas released into the removal system by the exhaust port opening event is integrated to identify the corresponding differential engine pressure. For the cylinder 1L analysis, engine differential pressure was 2.05 in Hg. For the candidate Cooper GMV engine, a component analysis is shown in Figure 4.39.

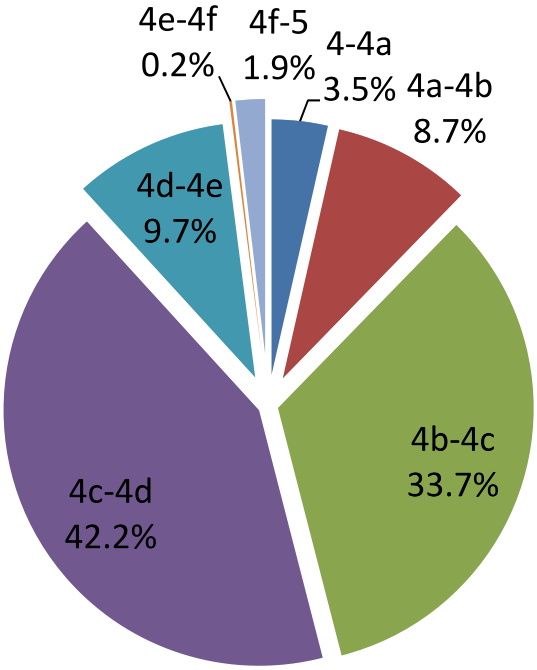

Figure 4.39: Engine component availability loss

This component based analysis of available energy as a metric for defining optimal exhaust manifold design parameters allowed for the: 1) investigation of energy losses in the candidate Cooper GMV exhaust removal system on a component basis, and 2) translation of the mitigation of these losses into a new metric – waste-gate margin – for expanded turbocharger operating range.

Summary

In summary, the thermodynamic analysis of the large-bore 2SC engine air management system has resulted in the development of new software for the purpose of analyzing: 1) the cylinder-to-cylinder distribution of charge air, 2) pollutant emission concentrations, and 3) energy availability to the turbocharger turbine. During the course of the thermodynamic analysis, four new algorithms were developed:

1. Charge Air Integrated Manifold Engine Numerical Simulation (CAIMENS),
2. T-RECS Kinetic NO Mechanism,
3. T-RECS Kinetic CO Mechanism, and
4. Exhaust Manifold Design Software (EMDS).

The CAIMENS model is a coupling of the previously developed T-RECS with a transient manifold flow model developed from fundamental engineering principles of continuity and conservation in pipe matrices. It is a multi-cylinder engine algorithm that models the effects of charge air imbalance between cylinders using the physical relationships summarized in Chapter 3.

In order to comprehensively analyze the candidate Cooper GMV exhaust removal system, the CAIMENS model required incorporation of the engine timing model, for translation of the high pressure in-cylinder combustion products into exhaust port flow, in addition to new kinetic mechanisms for in-cylinder NO and CO formation. For simplicity, this new model has been named the Exhaust Manifold Design Software (EMDS), which integrates the previously developed algorithms and expanded fundamentals.

The EMDS was created to predict fluid flow through the air delivery and exhaust removal systems of a large-bore 2SC RICE, to be used to develop a method to effectively and efficiently: 1) distribute charge air within the intake system, and 2) transfer exhaust products to the turbocharger turbine with minimal energy loss. The EMDS can predict pulsation and possible unbalanced air delivery and interference within the intake system and models energy release and pollutant emission formation during and just after the combustion event. Specifically, the EMDS outputs the transient pressure and temperature of the engine exhaust stream at the turbocharger turbine inlet.

CHAPTER 5 - Model Validation and Prototype Development

As discussed previously in Chapter 4, a simplified model can be developed to analyze the large-bore 2SC engine air management system. At present, it is not possible to construct models that predict engine operation from the basic governing equations alone. Due to the complexity of the engine process, empirical relations and a variety of tuning factors must be employed (Heywood, 1988). The simplified model previously developed is dependent on correct quantification of the air flow through the engine air management system.

The most significant airflow restriction in a 2SC engine is the flow through the intake and exhaust ports (Heywood, 1988). Typically, the minimum cross sectional area in the intake and exhaust system occurs at the ports. To account for the pressure reduction across the intake and exhaust ports, considerable success has been realized by modeling the gas flow as one-dimensional, quasi-steady, compressible flow (Heywood and Sher, 1999). The intake manifold and runner model coupled with the engine timing model creates a solution scheme that in turn provides the upstream pressure and gas temperature, or boundary conditions for quantifying flow through the intake and exhaust ports of the large-bore 2SC engine. The appropriate relationship is (Annand and Roe, 1974):

$$\dot{m}_R = \frac{C_D A_T p_0}{\sqrt{R T_0}} \left(\frac{p_T}{p_0}\right)^{\frac{1}{\gamma}} \left\{ \frac{2\gamma}{\gamma - 1} \left[1 - \left(\frac{p_T}{p_0}\right)^{\frac{\gamma-1}{\gamma}} \right] \right\}^{\frac{1}{2}} \tag{5.1}$$

The values C_D and A_T represent the discharge coefficient and the minimum area of the restriction. The subscript ‘0’ refers to the upstream stagnation point of the restriction. For flow into the cylinder via the intake or air delivery system, the stagnation conditions refer to local time-dependant conditions in the intake manifold. For exhaust flow out of the cylinder, the stagnation conditions refer to conditions in the cylinder. Alternately, the subscript 'T' refers to values at the restriction, or port in this case.

Ports located along the wall of the Cooper GMV cylinder are rectangular, maximizing the use of the cylinder wall and precisely controlling the timing of the port opening and closing. The corners of the ports are filleted to protect the piston rings from sharp edges. The crank angle at which the ports open, the size, number, geometry, and location of the ports around the cylinder circumference, and the direction and velocity of the jets issuing from the ports into the cylinder all affect the scavenging flow. This flow must be quantified in order to effectively simulate the engine air management system.

The discharge coefficient (C_D) included in the above equation for fluid flow through a restriction accounts for variables ignored by an idealized model such as friction. This coefficient is the ratio of the actual or real mass flow rate of the gas to the theoretical or ideal mass flow:

$$C_D = \frac{\dot{m}_a}{\dot{m}_{id}} \tag{5.2}$$

In order to evaluate the management of fluid flow into or out of the cylinder, the discharge coefficient (C_D) must be determined experimentally. To determine the C_D in a testing environment, the real mass flow through a restriction is measured and the ideal mass flow, based on the geometry of the restriction, local pressures and temperatures, is computed.

For any given restriction, the mass flow rate, upstream and downstream pressures, and temperature can be measured. With this data, the theoretical area of flow, referred to as the effective area (A_E), can be calculated. The effective area is defined as the cross-sectional area of the throat of a frictionless nozzle that allows identical mass flow to pass through with an identical pressure differential (Annand and Roe, 1974). For this same restriction, the minimum cross-sectional area encountered by the flow (A_T), or in this case, the cross-sectional area of the port, can also be measured. Therefore, the discharge coefficient can alternately be defined as a ratio of these areas (Heywood, 1988):

$$C_D = \frac{A_E}{A_T} \tag{5.3}$$

In order to effectively optimize the air management system of the large-bore 2SC engine, the charge air delivered to the log manifold must be equally distributed to each cylinder. This distribution is controlled by managing the effective flow area into each cylinder, illustrated by the integration of equations 5.2 and 5.3:

$$A_E = C_D \times A_T \Rightarrow \dot{m}_a \tag{5.4}$$

Impact on Pollutant Emission Reduction

As discussed previously in Chapter 3, NO_X is a function of corrected trapped equivalence ratio as illustrated in Figure 5.1.

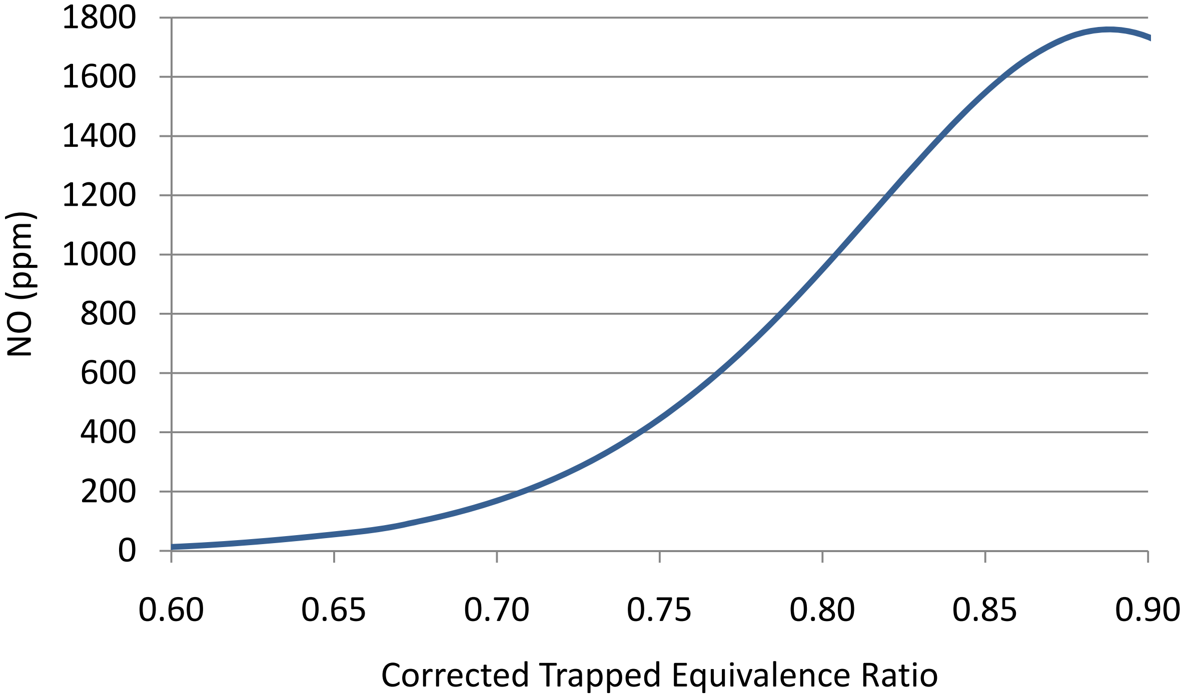

Figure 5.1: NO_X Production for varying discharge coefficients

The key to balancing NO_X production between cylinders is to ensure that, within a given engine frame, the fuel flow rate, air flow rate, and scavenging efficiency are the same for each cylinder, thereby achieving identical corrected trapped equivalence ratios in each. If this is not accomplished, then some cylinders operate leaner than average and some cylinders operate richer than average. Since NO_X production is a highly nonlinear function of corrected trapped equivalence ratio, the rich cylinders can produce disproportionately more NO_X than the all other cylinders.

For varying operating conditions, the CAIMENS model developed in Chapter 4 was used to investigate the variations in mass flow rate to each cylinder on the selected Cooper GMV engines. Performance test data, provided by El Paso Corporation, were used as input values for engine operating conditions of the CAIMENS model.

As discussed previously, NO_X production is a function of corrected trapped equivalence ratio, which is in turn a function of the real mass flow rate of air as shown by:

$$\varphi_{se} = \frac{1}{\eta_{se}}\left[\frac{\left(\frac{\dot{m}_{fu}}{\dot{m}_{ca}}\right)_a}{\left(\frac{\dot{m}_{fu}}{\dot{m}_{ca}}\right)_{st}}\right] \tag{5.5}$$

Therefore, changes in effective area directly impact mass flow rate which translates into a highly non-linear variation in NO_X production. The correlation is:

$$A_E \Rightarrow \dot{m}_a \Rightarrow \varphi_{se} \Rightarrow \mathrm{NO_X} \tag{5.6}$$

This correlation is illustrated by Figure 5.1. The correlation between corrected trapped equivalence ratio and NO_X production illustrates that a 10% variation in real mass flow rate between cylinders translates into a variation in NO_X production of up to 85% for the candidate Cooper GMV engine.

Air Management System Control

In order to balance the mass flow rate into each cylinder, for a given operating condition, flow control measures used by other comparable industries including the automotive industry were investigated. The automotive industry controls mass air flow rate into the engine by controlling the discharge coefficient (Azechi et al., 1992). Controlling the discharge coefficient is accomplished by adjusting or restricting the flow area using a throttling plate, shown in Figure 5.2 (Benson et al., 1974).

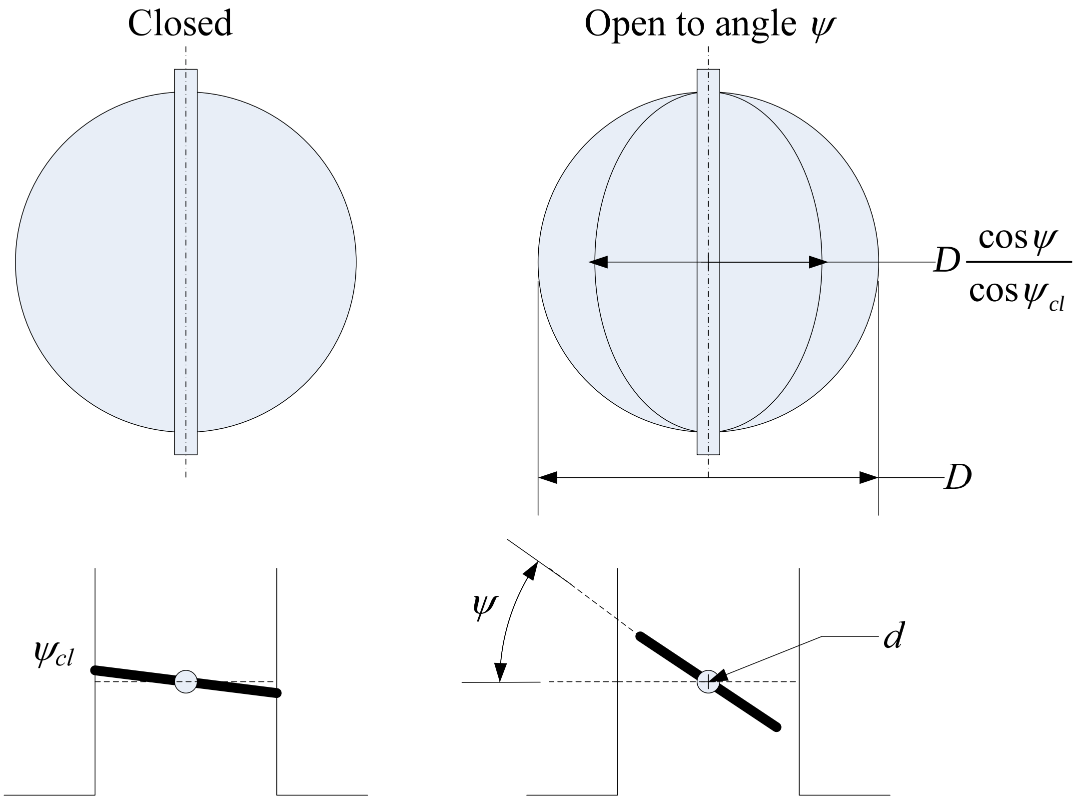

Figure 5.2: Conventional throttle plate

The throttle plate open area (A_{th}), as a function of the angle (ψ) for the conventional throttle plate geometry shown in Figure 5.2, is given by (Heywood, 1988):

$$\frac{4A_{th}}{\pi D} = \left(1-\frac{\cos\psi}{\cos\psi_{\mathrm{cl}}}\right) + \frac{2}{\pi}\left[\frac{D_d}{\cos\psi}(\cos^2\psi - D_d^2\cos^2\psi_{\mathrm{cl}})^{\frac{1}{2}} - \frac{\cos\psi}{\cos\psi_{\mathrm{cl}}}\sin^{-1}\left(\frac{D_d\cos\psi_{\mathrm{cl}}}{\cos\psi}\right) - D_d(1-D_d^2)^{\frac{1}{2}} + \sin^{-1}D_d\right] \tag{5.7}$$

The ratio of throttle plate open area (A_{th}) to the throttle bore diameter (D) is a function of the throttle plate angle when closed (ψ_{cl}), and the throttle ratio ($D_d = d/D$), a function of the throttle shaft diameter (d). When using in the compressible flow equation, the throttle plate open area (A_{th}), along with the cross-sectional area of the intake runner (A_{run}) is used in the reference area (A_T) calculation:

$$A_T = A_{run} - A_{th}(\psi) \tag{5.8}$$

The throttle area ($A_{th}(\psi)$), is calculated at some throttle plate angle between 0° (closed) and 90° (wide-open). This equation allows for analysis of the option that the maximum variation in discharge coefficient does not require a throttle plate that closes tightly against the cylinder intake runner wall.

This analysis of a throttle plate was incorporated into the CAIMENS model to optimize the effective area and therefore the mass flow rate into each cylinder, allowing an effective balance of the corrected trapped equivalence ratio and the NO_X production on a cylinder by cylinder basis for the selected Cooper GMV engine.

As discussed in Chapter 4, the CAIMENS model was used to quantify the impact of cylinder air flow imbalance by comparing NO_X production to mass flow rate of charge air and discharge coefficient. The model allowed the author to compute the a variation in charge air mass flow rate from 5% to 12% for the candidate engine based on the 4-6 in Hg pressure gradient between cylinder1L and cylinder 4L discussed in Chapter 4. This air mass flow rate variation translates into a variation of 65% to 92% in NO_X production. In order to overcome this imbalance, the discharge coefficient was altered by the introduction of an Air Flow Balancer (AFB) similar in design to that of a throttle plate used by the automotive industry (Benson et al., 1974).

Using the CAIMENS model, the author designed the AFB illustrated in Figure 5.3, for the Cooper GMV candidate engine geometry, to overcome the 4-6 in Hg pressure gradient identified during the development of the simplified model in Chapter 4.

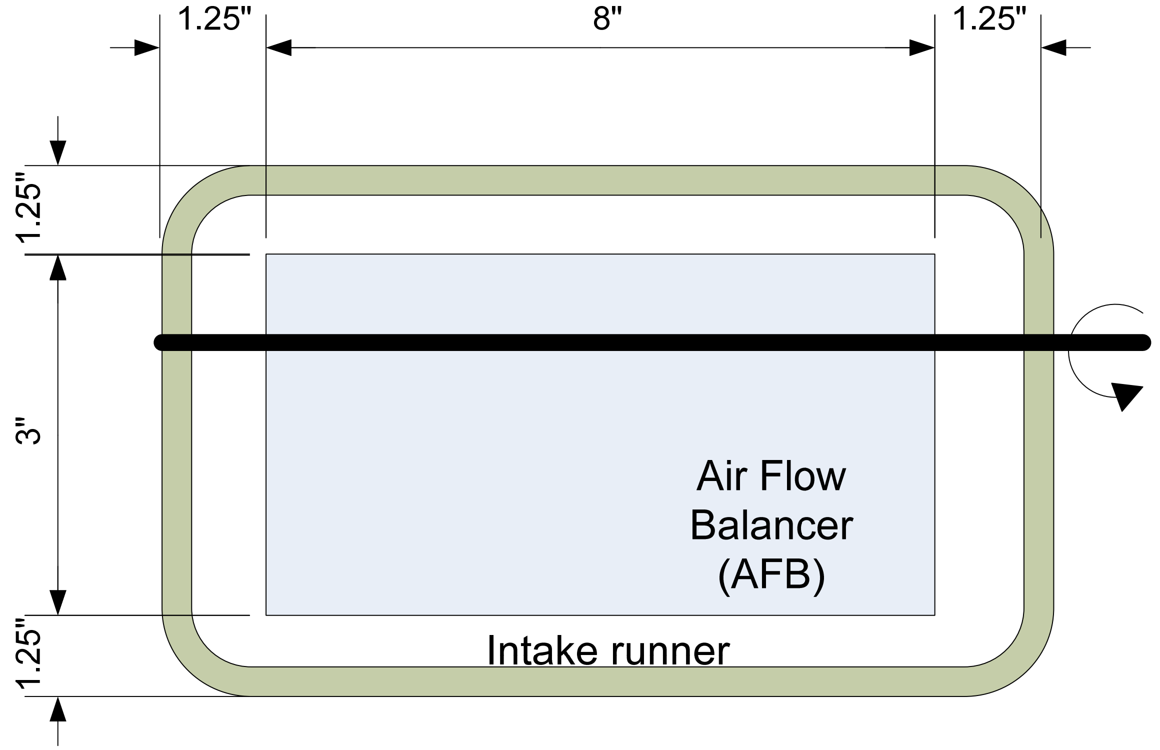

Figure 5.3: AFB geometry (not to scale)

After specifying the AFB geometry, the author investigated technologies for measuring mass air flow rate. The automotive industry uses a variety of air flow meters including, but not limited to hot wire anemometers, vane air flow meters, and Karmen vortex meters (Sullivan, 1998). Due to the space limitations created by the geometry of the intake system on the candidate engine, the hot wire anemometer was selected as a suitable instantaneous instrument for measuring mass air flow (MAF) rate. The selected hot wire anemometer was designated the MAF sensor. The completed Active Air Control (AAC) system concept is illustrated in Figure 5.4.

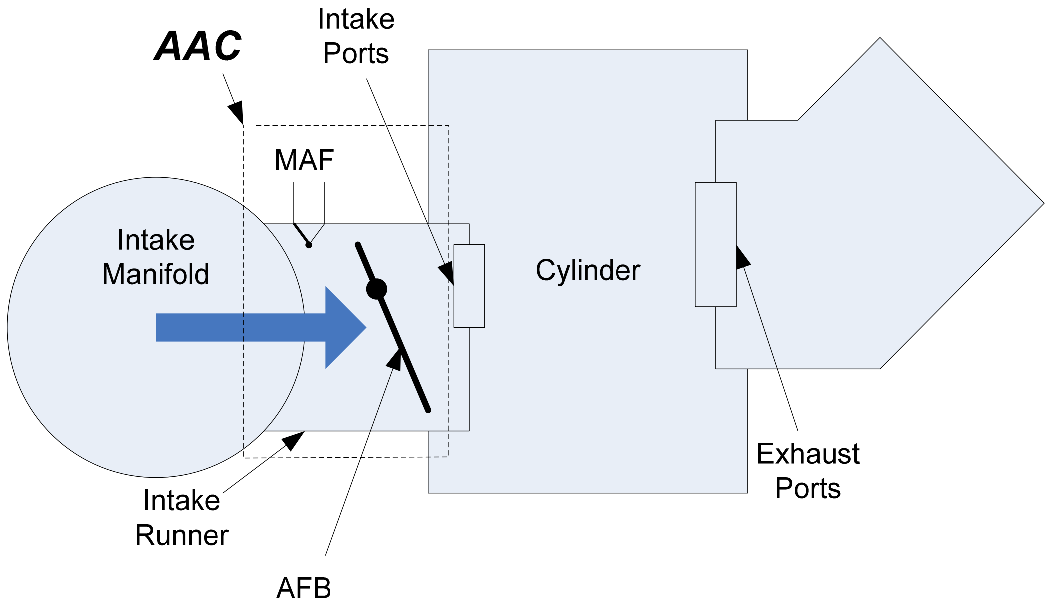

Figure 5.4: AAC system

Flow Bench Design

To sufficiently test the specified AAC system, the NGML steady-state air flow test bench was expanded from one cylinder to two cylinders, as shown in Figure 5.5. The purposes of the tests were to:

1. Experimentally determine the discharge coefficient of the AFB;
2. Verify the range of air flow imbalance that the AAC system was capable of correcting; and
3. Validate the simplified model developed in Chapter 4.

The two-cylinder flow bench includes pressure and temperature sensors installed on each intake runner and downstream valves to control and simulate the pressure differential between the intake runner and the cylinder. Test instrumentation includes two identical venturi flow meters selected due to their pressure recovery capability. Each venturi was capable of measuring flow in the range of 0-800 scfm. The venturi selected had a total permanent pressure loss of

0.7122 in H_2O. The venturis were instrumented with a static pressure transmitter, type K thermocouple, and differential pressure meter. Ambient pressure was measured through the use of a ±0.015% accurate 0-15 psia pressure transducer. All analog pressures and temperatures were first connected to an Opto 22 brick with accuracy of 16 μA, and then recorded on the computer by A/D conversion. The instrumentation used to collect data on the NGML flow bench is summarized in Table 5.1.

Table 5.1: Flow bench instrumentation

Measurement	Brand	Model	Range	Uncertainty
Pressure	Omega	PX725	0-25 psia	± 0.015%
Differential pressure	Omega	PX771A	0-100 in H_2O	± 0.1%
Temperature		Type K		± 0.5˚F (0.3˚C)
Venturi	Lambda Square	6”	0-800 scfm	0.7122 in H_2O
Air velocity	Dwyer	641-12-LED	0-2000 fpm	0.3% (0 to 150˚C)

An instrumentation diagram is shown in Figure 5.5.

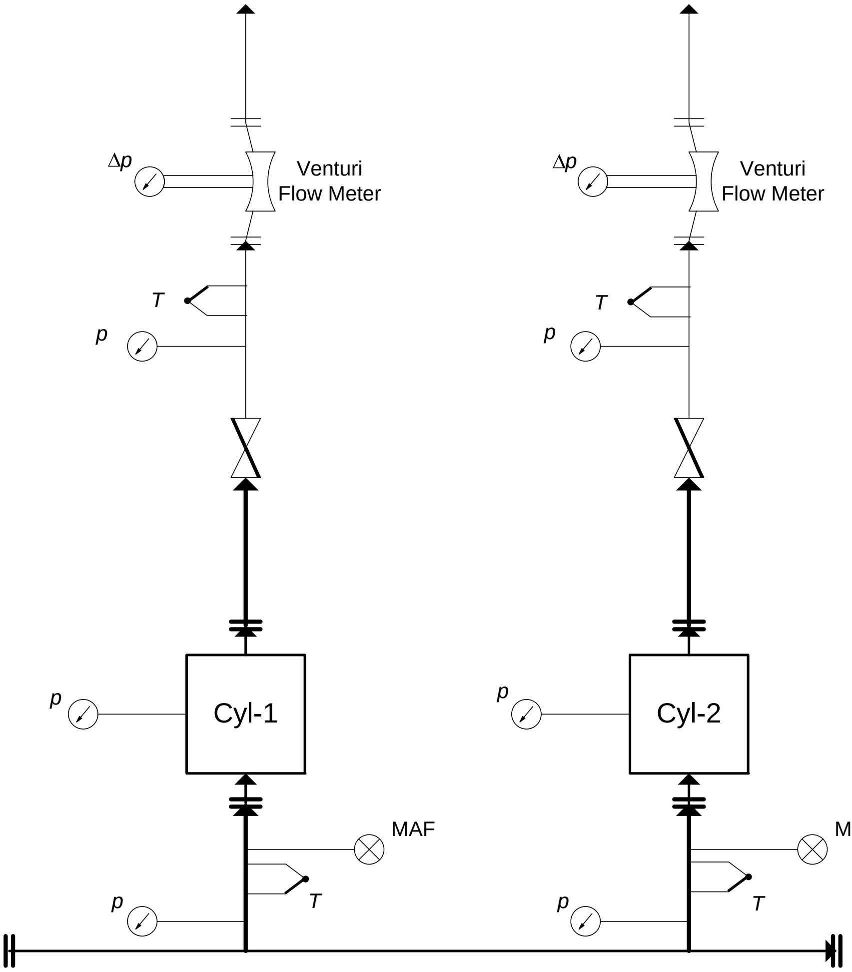

Figure 5.5: Multi-cylinder flow bench schematic

The flow bench design centered around two Cooper GMVA-10 engine cylinders. These cylinders were donated by El Paso Corporation. Arrow Industries also donated two Cooper GMV pistons, two piston hangers, and two piston pins. Including transportation, these donations totaled $18,720 toward the completion of this work. The flow bench assembly and instrumentation is illustrated in Figure 5.6 and Figure 5.7.

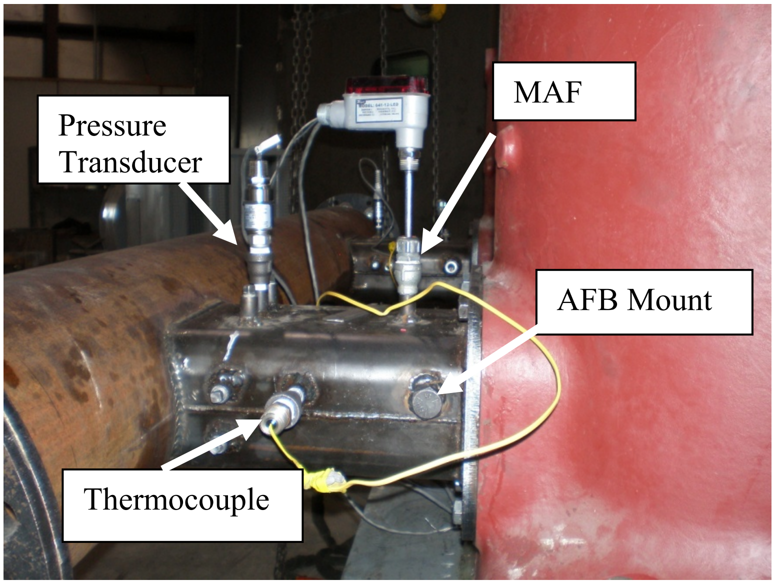

Figure 5.6: Flow bench intake runner instrumentation

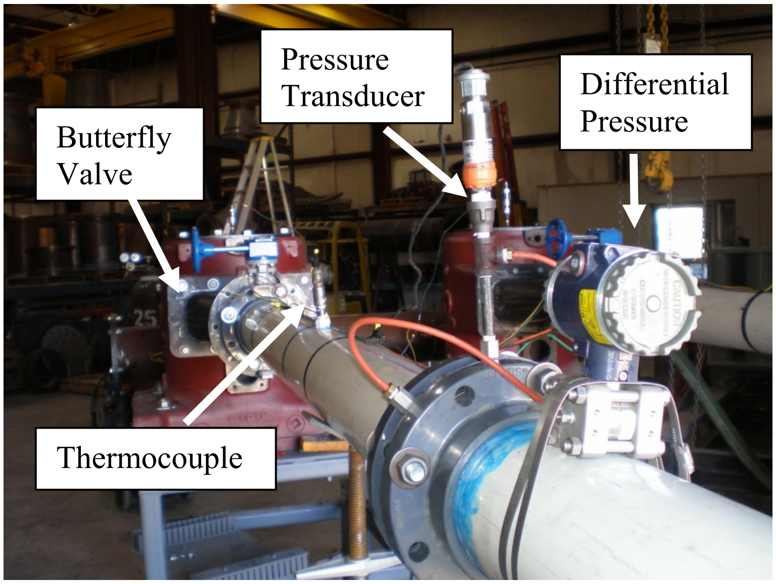

Figure 5.7: Flow bench exhaust instrumentation

Prototype Installation

The AAC system is shown as installed in each intake runner in Figure 5.8. The AFB consists of a 1/8 in thick, 3 in by 8 in plate welded to a 3/8 in rod. The AFB is mounted in the runner by drilling two holes in the sides of the runner just above the center line. The left side of the 3/8 in rod sits in a fitting welded to the outside of the runner while the right side, sealed by a gasket, protrudes 2 in from the side of the runner allowing for the mounting of an actuator. The MAF (not shown) is installed along the centerline of the top of the intake runner.

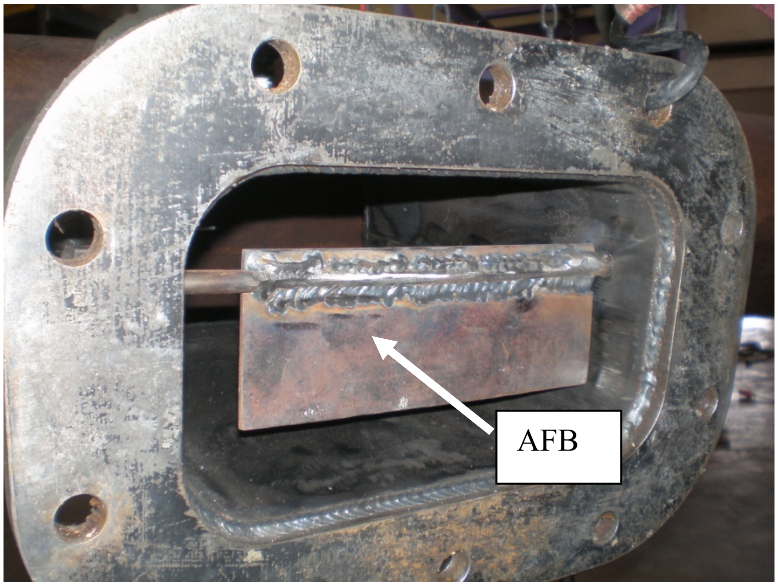

Figure 5.8: AAC system installation

Design of Experiment

The author first conducted a series of tests on a single cylinder. This allowed for the quantification of the discharge coefficient and the effective flow area as a function of AFB angle (ψ). The test matrix, created to simulate actual operating conditions for the Cooper GMV candidate engine, is shown in Table 5.2. According to test data supplied by El Paso Corporation, the candidate Cooper GMV engine operated over a range of intake manifold flow rates of 498-643 scfm and a range of AMP from 6.7 to 9.2 psig (El Paso, 2006).

Table 5.2: Flow bench test matrix

Flow (scfm)	500											
Pressure (psig)	7.0				8.0				9.0			
ψ (deg)	0	30	60	90	0	30	60	90	0	30	60	90
Flow (scfm)	550											
Pressure (psig)	7.0				8.0				9.0			
ψ (deg)	0	30	60	90	0	30	60	90	0	30	60	90
Flow (scfm)	600											
Pressure (psig)	7.0				8.0				9.0			
ψ (deg)	0	30	60	90	0	30	60	90	0	30	60	90

In order to transform the data collected on the airflow bench into useful information, the data must be used to determine the discharge coefficient as a function of the system geometry and the inlet pressure and temperature. This is accomplished by precisely measuring the actual airflow rate through the intake runner with a venturi, along with the necessary geometry.

The airflow rate through the system is determined by using the *ASME Nozzle Guidelines* (1971). Specifically, the airflow rate ($\dot{m}$) through the test system is based on (ASME, 1971):

$$\dot{m} = \frac{\pi C Y_a d^2}{4\sqrt{1-\delta^4}}\sqrt{2 g_c h_w \rho_{1v}} \tag{5.9}$$

The adiabatic expansion factor (Y_a) is calculated using the ratio ($PR = p_2/p_1$) of the upstream (p_1) and downstream (p_2) pressures:

$$Y_a = \left[PR^{\frac{2}{\gamma}} \left(\frac{\gamma}{\gamma - 1} \right) \left(\frac{1 - PR^{\frac{\gamma-1}{\gamma}}}{1 - PR} \right) \left(\frac{1 - \delta^4}{1 - \delta^4 PR^{\frac{2}{\gamma}}} \right) \right]^{\frac{1}{2}} \tag{5.10}$$

The mass flow rate through an ideal orifice can be found with equation 5.9. This equation can be equated with equation 5.1. Rearranging the compressible flow equation:

$$C_D = \frac{\dot{m}\sqrt{\gamma R T_0}}{A_T p_0 \gamma \left(\frac{p_T}{p_0} \right)^{\frac{1}{\gamma}} \sqrt{\frac{2}{\gamma - 1} \left(1 - \left(\frac{p_T}{p_0} \right)^{\frac{\gamma-1}{\gamma}} \right)}} \tag{5.11}$$

Equation 5.10 can be used to calculate the discharge coefficient from the reference area calculated from the AFB angle.

Experimental Uncertainty

In order to have confidence in the results obtained by experimental means, it is important to address the uncertainty band in the measured and calculated quantities. Determining the uncertainty of measurements and calculations before a system is constructed allows careful consideration of equipment, layout, and measurement effects.

The discharge coefficients for ports are measured as a function of airflow, port pressure ratio, and port geometry (Heywood, 1988). Therefore, the confidence bands of the determined discharge coefficient (C_D) are based on the uncertainty of equations 5.9 and 5.11.

Hosni et al. (1997) provide a means for determining the uncertainty (U_j) in a measurement. For the general relation where:

$$j = j(X_1, X_2, \ldots, X_i) \tag{5.12}$$

The uncertainty in the parameter of interest (j) is found by determining how much j changes with respect to each parameter on which j depends. In equation form, this total uncertainty is:

$$U_j = \sqrt{\left[\left(\frac{\partial j}{\partial X_1} U_{X_1}\right)^2 + \left(\frac{\partial j}{\partial X_2} U_{X_2}\right)^2 + \cdots + \left(\frac{\partial j}{\partial X_i} U_{X_i}\right)^2\right]} \tag{5.13}$$

As an example, from equation 5.11, the discharge coefficient depends on:

$$C_D = funct(\dot{m}, p_0, T_0, p_T, A_T, \gamma) \tag{5.14}$$

Applying equation 5.13 to the discharge coefficient and the parameters that the discharge coefficient is a function of results in:

$$U_{C_D} = \sqrt{\left(\frac{\partial C_D}{\partial \dot{m}} U_{\dot{m}}\right)^2 + \left(\frac{\partial C_D}{\partial p_0} U_{p_0}\right)^2 + \ldots} \tag{5.15}$$

$$U_{C_D}(\%) = \frac{U_{C_D}}{C_D} \times 100\% \tag{5.16}$$

Analysis of the uncertainty (U_{C_D}) with the instrumentation used in the air flow bench reveals an expected effective flow area uncertainty of ± 2.1% and an uncertainty in the measured flow ($U_{\dot{m}}$) of ± 1.7% Complete calculation of the uncertainty is included in Appendix F - Experimental Uncertainty Analysis.

Experimental Results and Discussion

For the test matrix show in Table 5.2, the author plotted the effective flow area, the product of the calculated discharge coefficient and the reference area, versus AFB angle, shown in Figure 5.9, Figure 5.10, and Figure 5.11. The data shows an inverse relationship between the

AFB angle and the effective area. Also, the calculated effective area behaves consistently over a range of intake manifold flow rates and pressures. These tests were repeated to confirm reliability of the results. Uncertainty is illustrated in the figures via the error bars.

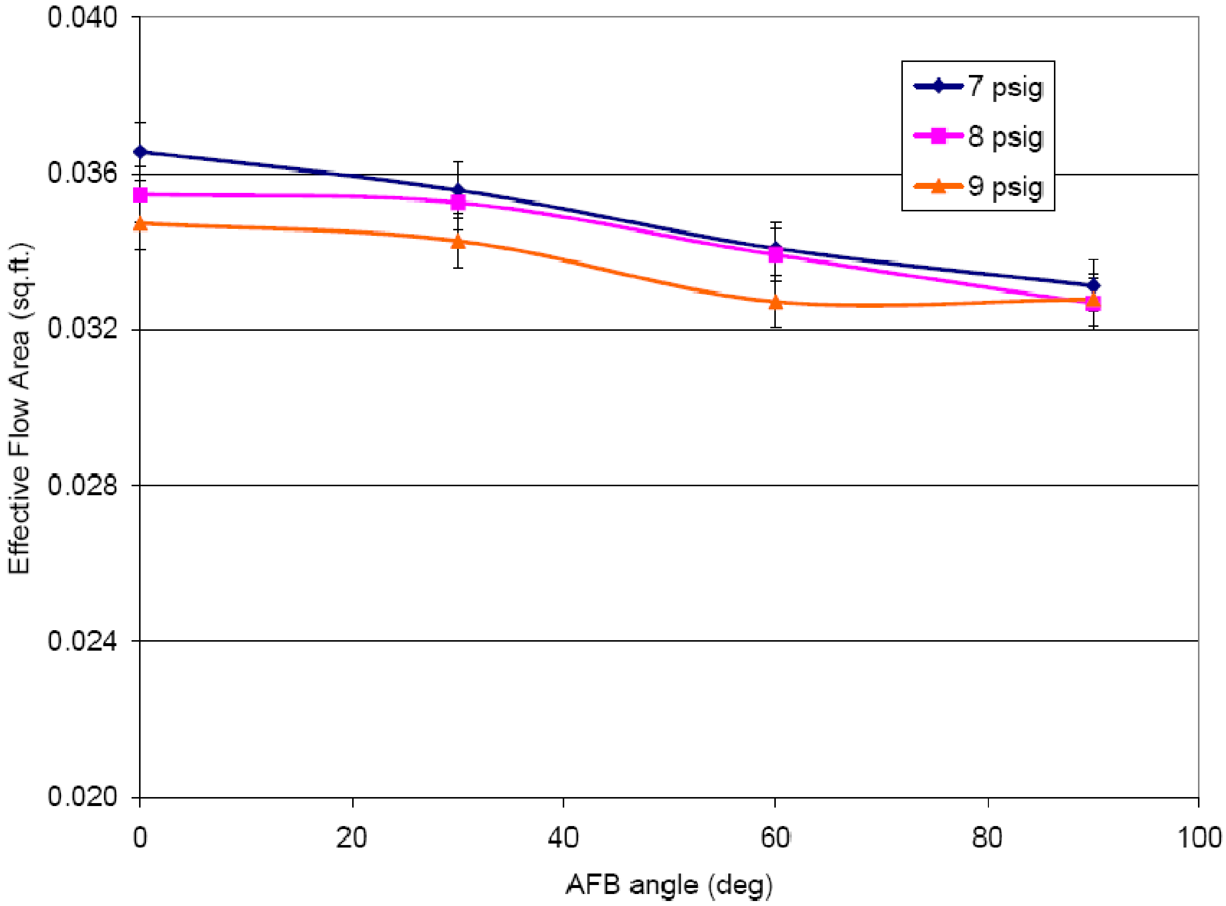

Figure 5.9: A_E vs. AFB angle at 500 scfm

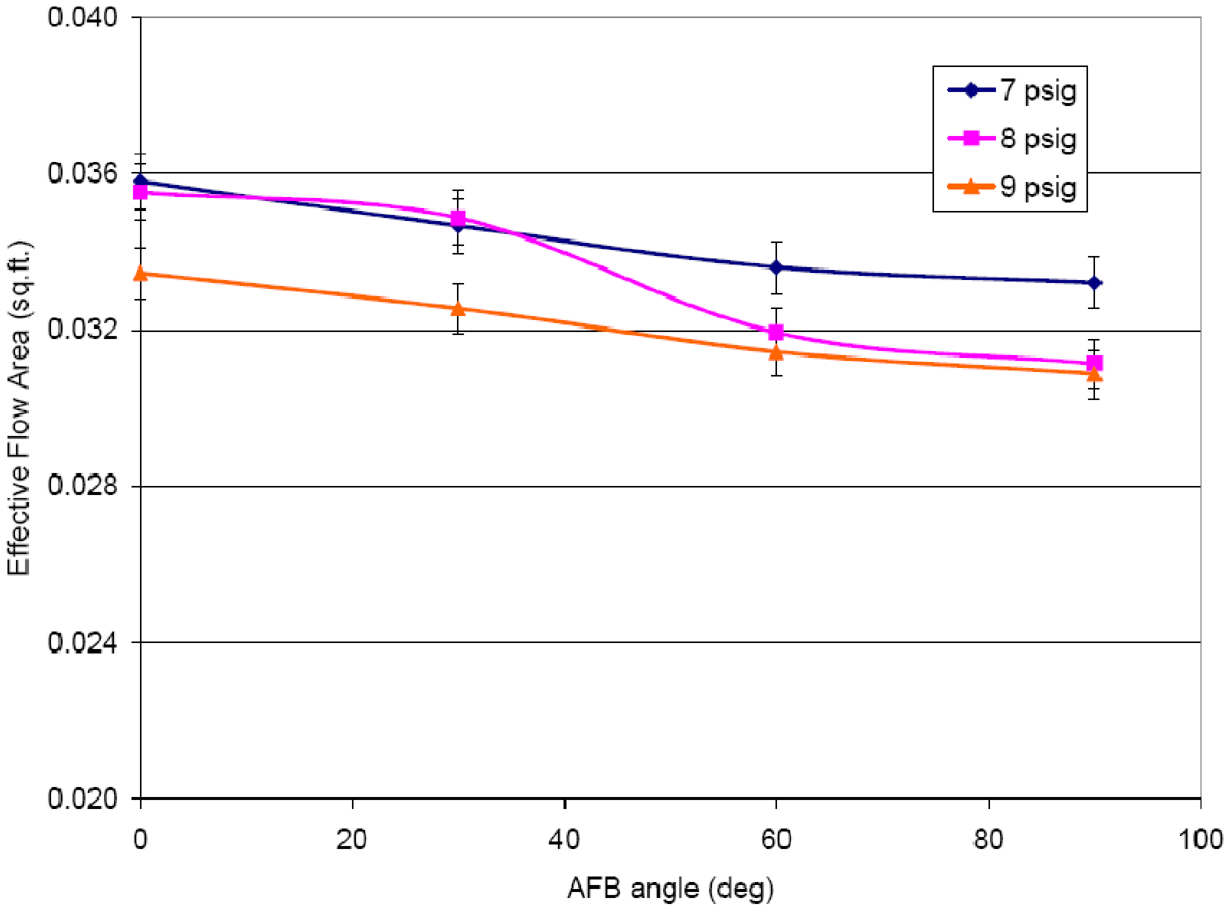

Figure 5.10: A_E **vs. AFB angle at 550 scfm**

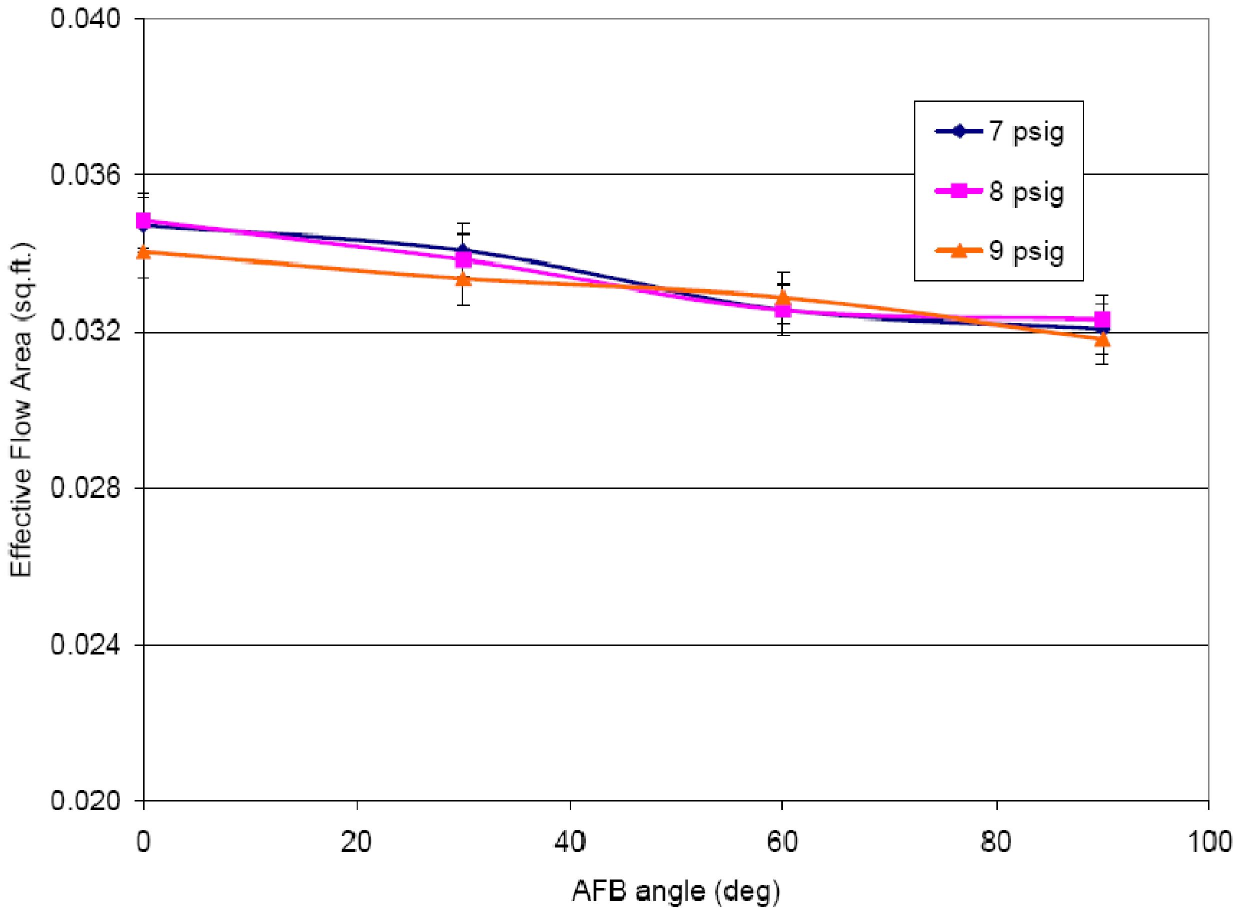

Figure 5.11: A_E vs. AFB angle at 600 scfm

Using a ratio of the max effective flow area to the minimum effective flow area, a percent change in effective flow area can be calculated (ΔA_E):

$$\Delta A_E(\%) = \frac{A_E(\psi) - A_E(\psi = 90°)}{A_E(\psi = 0°)} \times 100\% \tag{5.17}$$

The data shows that this AAC system, over a range of operating conditions from 7 to 9 psig and 500 to 600 scfm per cylinder, shows the same trend in effective flow area. Results are summarized in Table 5.3 below.

Table 5.3: Single cylinder A_E change

Flow Rate (scfm/cyl)	Pressure (psig)	Max A_E (ft^2)	Min A_E (ft^2)	Change (%)
500	7	0.0366	0.0331	9.4
	8	0.0355	0.0327	7.9
	9	0.0347	0.0328	5.6
550	7	0.0358	0.0332	7.2
	8	0.0355	0.0311	12.4
	9	0.0335	0.0309	7.7
600	7	0.0347	0.0321	7.6
	8	0.0349	0.0323	7.3
	9	0.0341	0.0318	6.6

For example, at 7 psig and 550 scfm per cylinder, when the AFB is re-positioned from an angle ψ of 0° to 90°, the effective area changes from a maximum of 0.0355 ft^2 to a minimum of 0.0311 ft^2. This change in effective area represents a reduction of 12.4%. The change in effective area correlates directly to mass flow rate thereby creating a minimum 5.6% to maximum 12.4% change in the mass flow rate to the cylinder. Analysis of the uncertainty, U_{C_D} with the instrumentation used in the air flow bench reveals an expected effective flow area uncertainty of ± 2.1% and an uncertainty in the measured flow, $U_{\dot{m}}$ of ± 1.7%.

After thoroughly characterizing the effective flow area of the AFB for a single cylinder over the test matrix above, the author focused on a multi-cylinder system. The author designed an experiment to determine the range of the AFB mass flow rate correction. The AFB would be adjusted to vary the mass flow rate of cylinder 1 to equal the mass flow rate of cylinder 2 for a given flow bench operating condition. Using the instantaneous stroke calculation presented in

Chapter 4, two cylinders on the candidate Cooper GMV engine that fire one after another and are positioned next to each other on the intake manifold were selected. To comply with these two requirements, the author selected cylinders 4L and 3L. Cylinder 3L and 4L piston height versus crank angle is presented in Figure 5.12.

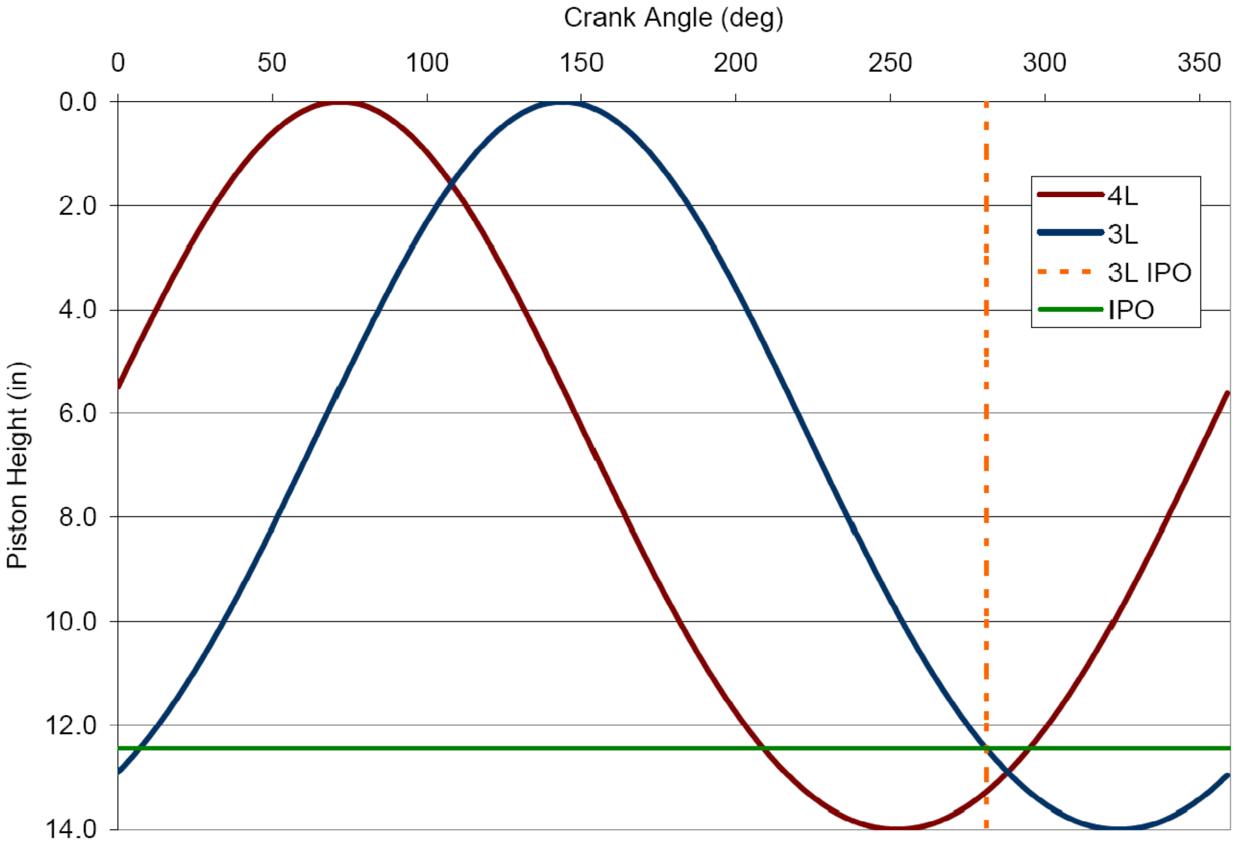

Figure 5.12: Cylinder 4L and 3L piston location

Figure 5.12 shows that:

1. Cylinder 3L trails cylinder 4L by 72°CA.
2. IPO is located at a piston height of 12.453 in when TDC is located at 0 in and BDC is located at 14 in.
3. Cylinder 3L IPO corresponds to a Cylinder 4L piston height of 13.290 in.

Using the information in Figure 5.12 and operating conditions for the candidate Cooper GMV previously used to characterize the effective flow area, the author designed the experiments outlined in Table 5.4. Cylinder 1 represents Cooper GMV engine cylinder 3L and cylinder 2 represents engine cylinder 4L.

Table 5.4: Multi-cylinder flow bench experiments

Multi-cylinder experiment #	Volumetric flow rate (scfm/cylinder)	AMP (psig)	Cylinder 1 piston location (in)	Cylinder 2 piston location (in)
1	500	7.5	12.453	13.290
2	600	8.5	12.453	13.290

Results from multi-cylinder experiment #1 and #2 are shown in Figure 5.13 and Figure 5.14, respectively. The data shown in Figure 5.13 and Figure 5.14 compare changing mass flow rates for each individual cylinder at varying AFB angles.

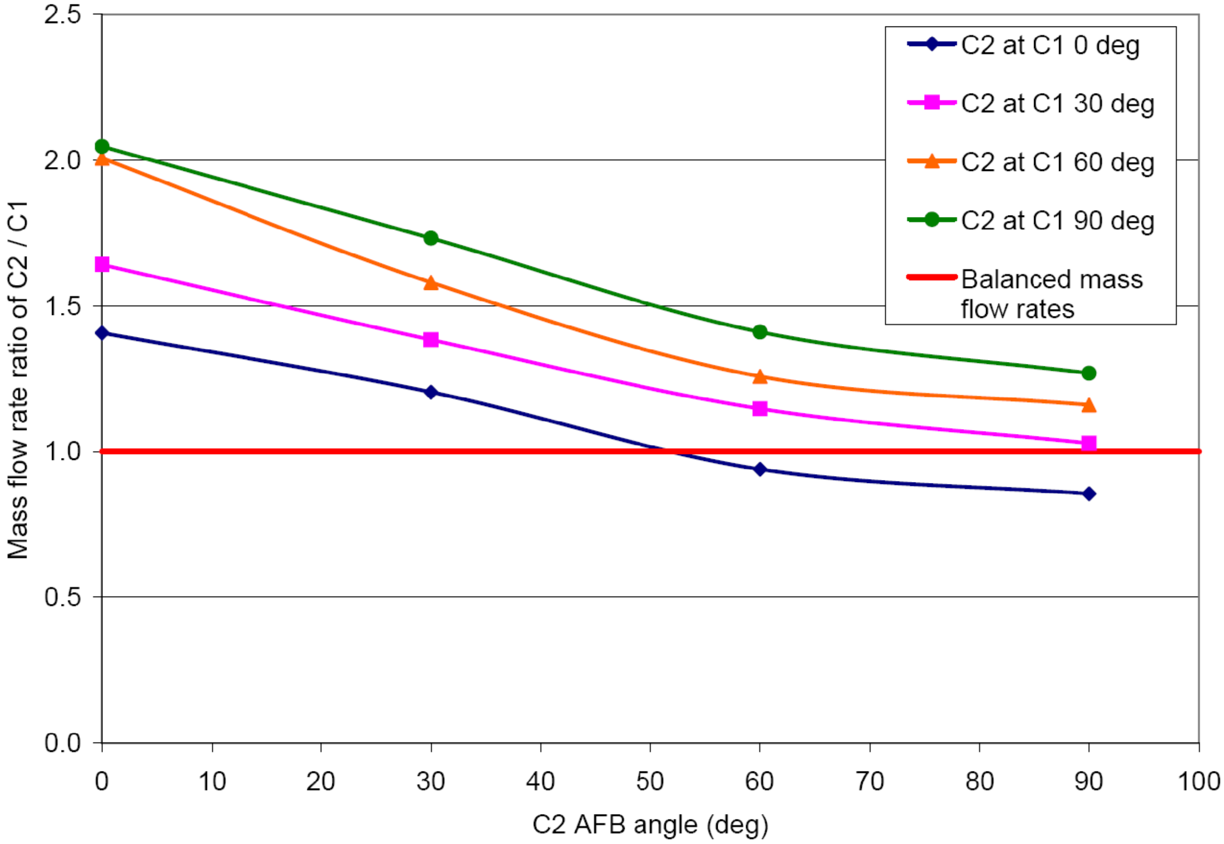

Figure 5.13: Ratio of mass flow rates vs. AFB angle at 7.5 psig and 500 scfm/cylinder

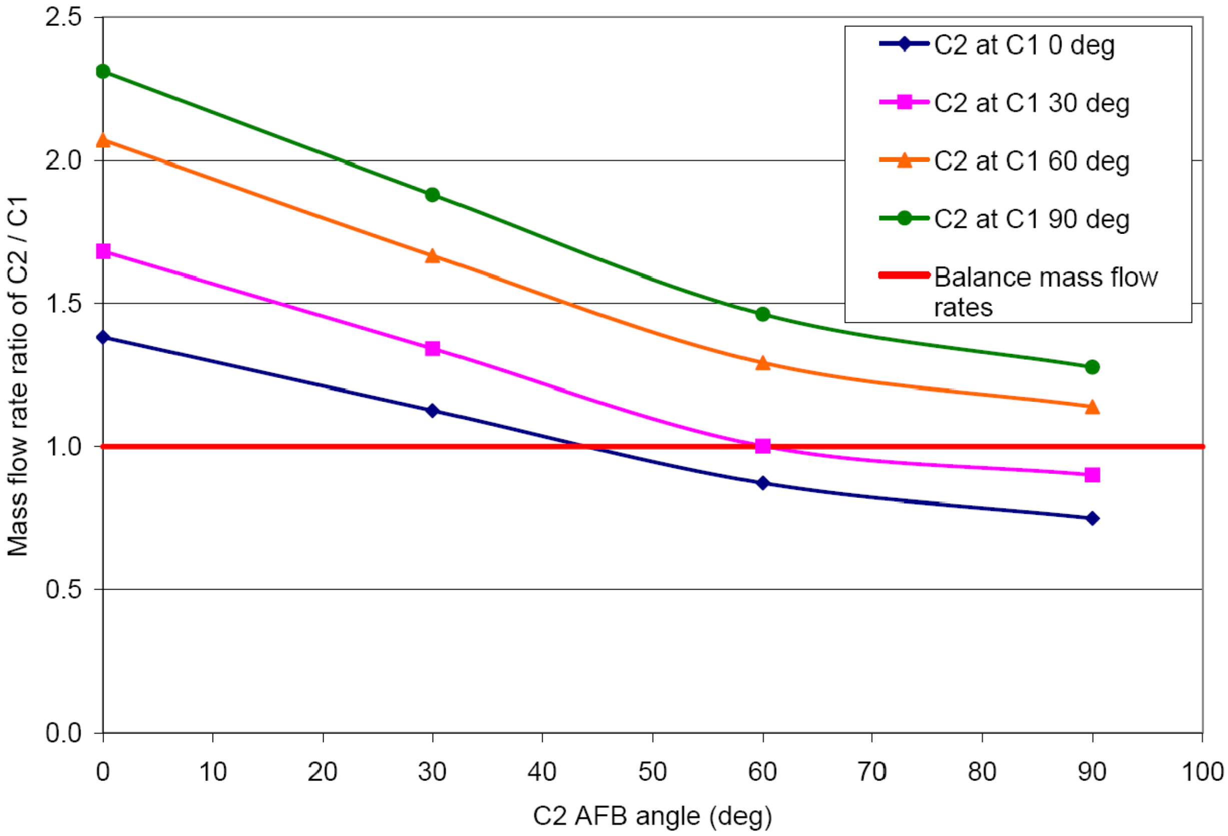

Figure 5.14: Ratio of mass flow rates vs. AFB angle at 8.5 psig and 600 scfm/cylinder

The data reported in Figure 5.13 and Figure 5.14 shows that:

1. The AAC system is capable of balancing mass flow rates in a multi-cylinder system;
2. At an operating condition of 7.5 psig AMP and 500 scfm/cylinder, the cylinder 1 AFB angle must be 0° while the cylinder 2 AFB angle must be 52°; and
3. At an operating condition of 8.5 psig and 600 scfm, the AAC system gives two options:
    a. The cylinder 1 AFB angle must be 0° while the cylinder 2 AFB angle must be 44°; or
    b. The cylinder 1 AFB angle must be 30° while the cylinder 2 AFB angle must be 61°.

This data allowed the author to relate the AFB angle to the mass flow rates of a multi-cylinder system. The effective flow rates for each cylinder allow for the calculation of not only the operating mass flow rates, but the AFB angle and mass flow rates needed to balance the engine air management system.

Summary

Due to the complexity of the engine process, empirical relations and a variety of tuning factors must be employed to construct and engine model (Heywood, 1988). The simplified model previously developed is dependent on correct quantification of the air flow through the engine air management system. In order to evaluate the management of fluid flow into or out of the cylinder, the discharge coefficient (C_D) was determined experimentally.

Beyond the quantification of the discharge coefficient, an air flow balancer (AFB) was designed using data from the CAIMENS algorithm developed in Chapter 4. This air flow balancer as part of an overall Active Air Control (AAC) system was used to balance the cylinder-to-cylinder distribution of air by the engine air management system.

CHAPTER 6 - Parametric Study

As identified in Chapter 1 of this work, the objective of the research can be decoupled into two goals:

1. Develop a mathematical model to predict fluid flow through the air delivery and exhaust removal systems of a large-bore 2SC engine; and
2. Use the model to develop a method to effectively and efficiently distribute charge air within the intake system, and transfer exhaust products to the turbocharger turbine with minimal energy loss.

The fulfillment of goal (1) of this objective has resulted in the development of four new algorithms, culminating in the Exhaust Manifold Design Software (EMDS). For review, the Charge Air Integrated Manifold Engine Numerical Simulation (CAIMENS) includes procedures to predict pulsation and possible unbalanced air delivery and interference within the intake system. The new T-RECS NO and CO Kinetic Mechanisms predict energy release and pollutant emission formation during and just after the combustion event. Finally, the EMDS itself includes a first and second law thermodynamic analysis of the exhaust stream to predict the availability of exhaust energy to the turbocharger turbine. The individual mathematical models were developed, tested, tuned with field data from the candidate Cooper GMV engine, and subsequently combined to form a comprehensive model of the engine air management. This development was comprehensively presented in Chapters 3-5 of this work.

In order to accomplish goal (2) of the objective of this work, a parametric investigation has been conducted to determine the effect of engine operating conditions and component geometry on the candidate Cooper GMV engine air management.

Charge Air Distribution

As discussed in Chapter 4, the CAIMENS model was used to quantify the impact of cylinder air flow imbalance by comparing NO_X production to mass flow rate of charge air and discharge coefficient. The model allowed the author to compute the a variation in charge air mass flow rate from 5% to 12% for the candidate engine based on the 4-6 in Hg pressure gradient between cylinder1L and cylinder 4L discussed in Chapter 4. This air mass flow rate variation translates into a variation of 65% to 92% in NO_X production. In order to overcome this imbalance, the discharge coefficient was altered by the introduction of an air flow balancer (AFB) similar in design to that of a throttle plate used by the automotive industry (Benson et al., 1974).

Using the CAIMENS model, the author designed the AFB in Chapter 5 for the candidate Cooper GMV engine geometry, to overcome the 4-6 in Hg pressure gradient identified during the development of the simplified model in Chapter 4. The AFB as part of an overall Active Air Control (AAC) system is used to balance the cylinder-to-cylinder distribution of air by the engine air management system by maintaining the same air manifold pressure at each cylinder on the intake manifold.

The effect of the installation of an AAC system on the cylinder 1L local AMP is shown in Figure 6.1. Figure 6.1 shows that the 43.6% decrease in effective area created by the AFB installation creates an 11.6% decrease in the AMP experienced by the intake ports while they are uncovered by the motion of the piston. The AFB in Figure 6.1 has been simulated at a 90° to the intake flow; therefore, if a higher local AMP is needed, the AFB angle may be decreased as discussed in Chapter 5.

It is important to note that due to the dynamic nature of the compressible flow in the intake system, the AAC system controls the AMP most effectively at high velocities (200-400 fpm) through the intake system. Therefore, in order for the AFB to be effective, it must be installed as close as physically possible to the intake ports.

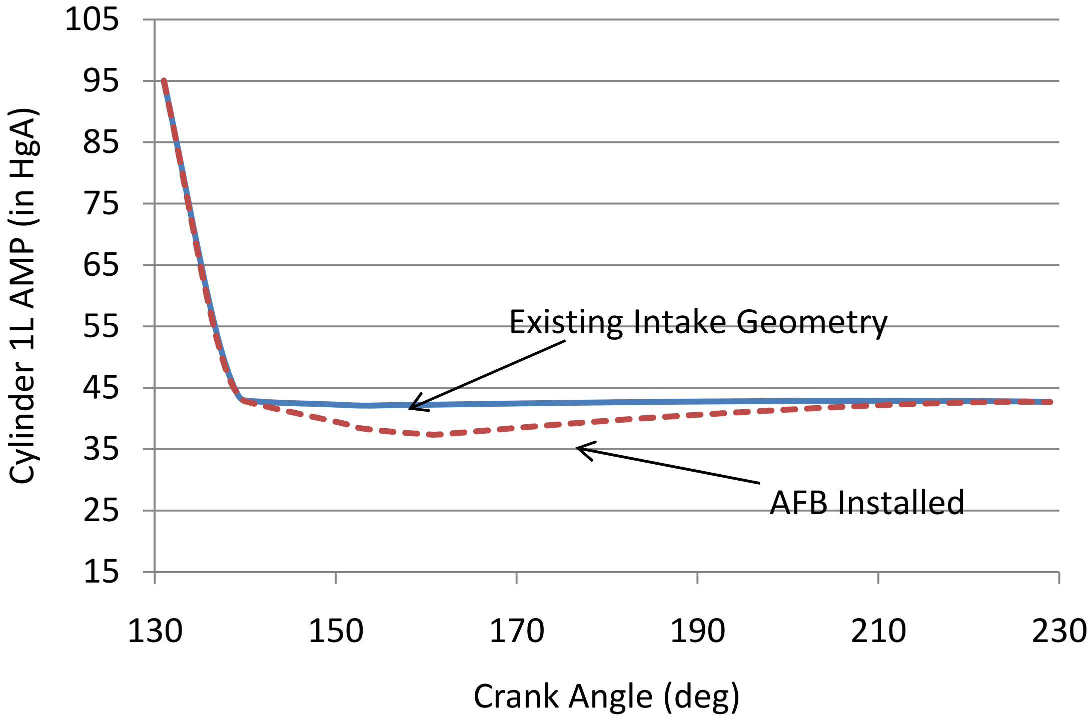

Figure 6.1: Cylinder 1L AMP with AFB

Installation of the AAC system has the capability to balance the charge air delivery to each cylinder of candidate Cooper GMV. Balancing of the engine charge air results in an effective balancing of engine corrected trapped equivalence ration and NO_X production on a cylinder by cylinder basis, shown in Figure 6.2. Total engine exhaust NO_X concentration is an average of the NO_X production of each cylinder; therefore, by installing the AAC system, the total engine NO_X is reduced by 50 ppm.

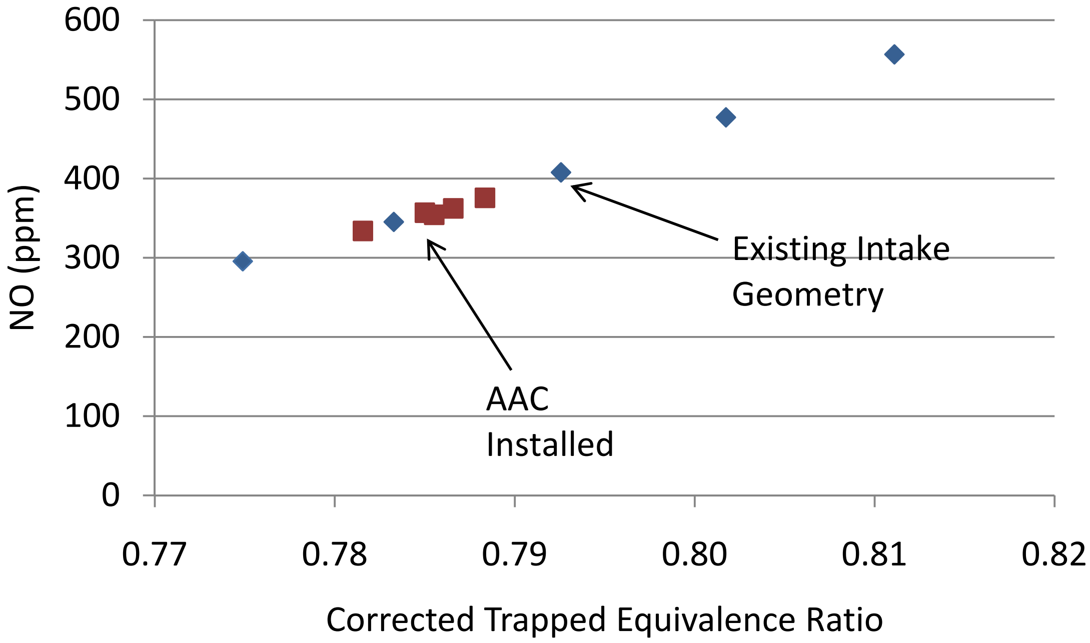

Figure 6.2: AAC system installation NO_X reduction

This analysis of the effect of AAC system installation on the candidate Cooper GMV engine satisfies the first part of goal (2) "use the model to develop a method to effectively and efficiently distribute charge air within the intake system" of the objective of this work. The investigation explores the impact of augmenting existing intake geometry on the candidate Cooper GMV engine air management.

Exhaust Energy Transfer

In order to satisfy the second part of goal (2) "use the model to develop a method to effectively and efficiently transfer exhaust products to the turbocharger turbine with minimal energy loss" of the objective of this work, the author defined losses in the exhaust system that could be partially recovered with minimal changes to the existing exhaust removal system.

The partially recoverable losses are due to: 1) the 150° vertical turn in the exhaust runner (4c-4d), 2) the 90° RMT junction (4d-4e), and 3) the exhaust manifold size (4e-4f). The removal or augmentation of these transitions in addition to the optimization of the exhaust manifold diameter allows for a significant recovery of available energy. The author also determined that the largest losses that could not be recovered are: 1) expansion into cylinder cavity (4a-4b), and 2) contraction from cylinder cavity into exhaust runner (4b-4c). These two hydraulic losses are a result of the cylinder design and casting process, and would require a significant investment in casting re-design to recover the energy loss. Component identification refers to the numbering in Figure 4.31, shown again for reference.

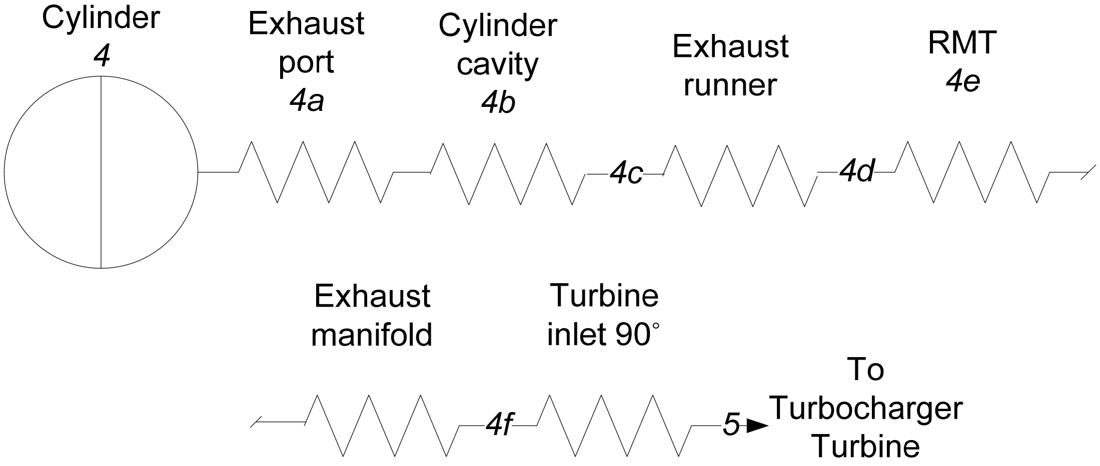

Figure 6.3: Resistance diagram of exhaust path losses

Focusing first on the 150° vertical turn in the exhaust runner (ERUN), the loss coefficient for a change in flow direction through a rectangular smooth radius elbow is a function of: 1) radius to width ratio, 2) height to width ratio, and 3) angle (ASHRAE, 2005). The height and width of the ERUN are fixed (result of the cylinder casting); therefore, only the elbow radius and angle may be changed. The available energy that may be recovered from optimizing the ERUN is shown in Figure 6.4. In order to minimize the available energy loss in the ERUN, the angle should be removed all together. Replacing the angled ERUN with a straight runner can recover up to 11.28 Btu/lb of exhaust energy, depending on the length of the elbow radius. The current design loses 31.7 times more energy than a straight runner. If this replacement is not realistic, the runner angle should be: 1) increased (straightened) as much as possible, or 2) augmented to the longest radius feasible.

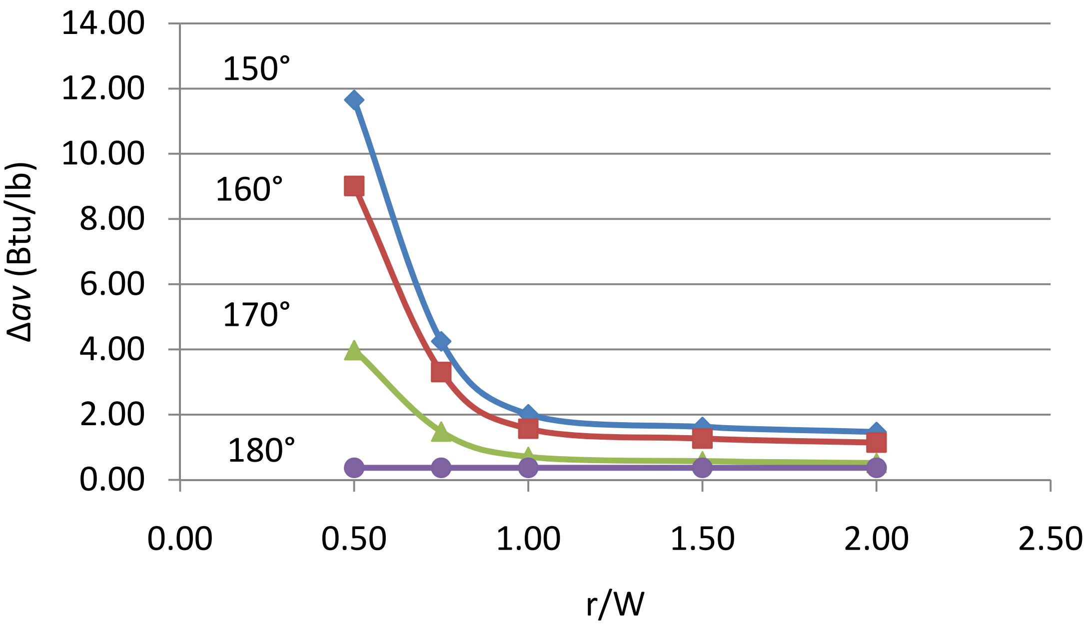

Figure 6.4: Variation in ERUN design

Moving downstream to the 90° RMT junction, the loss coefficient for a junction of this nature is a function of:

1. The upstream exhaust manifold diameter and flow velocity of the exhaust products (straight section);
2. The runner hydraulic diameter and the flow velocity of the single cylinder exhaust products (branch section); and
3. The downstream exhaust manifold diameter and the flow velocity of the total exhaust stream (common section).

Each section – straight, branch, and common – must be characterized individually; therefore, for simplicity, this characterization will focus on the junction of the cylinder 1L exhaust runner with the exhaust manifold just upstream of the turbocharger turbine inlet. The available energy that may be recovered from augmenting the RMT junction is shown in Figure 6.5. By directing the branch section flow relatively parallel to the straight section flow, the available energy can be increased by 7.84 Btu/lb. As much as 159.5% of the energy loss in the RMT junction can be recovered by decreasing the angle between the straight section and branch section streams.

It is important to note that the junction of two streams moving at different velocities is characterized by the turbulent mixing of the streams accompanied by pressure losses. In the course of mixing, an exchange of momentum takes place between the exhaust particles moving at different velocities, finally resulting in the equalization of the velocity distributions in the common stream. The jet with higher velocity (straight section) loses part of its kinetic energy by transmitting it to the slower moving jet. The energy stored in the lower velocity jet (branch section) increases as a result of mixing. As a result of this mixing, the total energy in the common section is a weighted average of the energy of each of the straight section and branch section streams. Therefore, the loss in total pressure and the local loss coefficient of the common section can have negative values (ASHRAE, 2005).

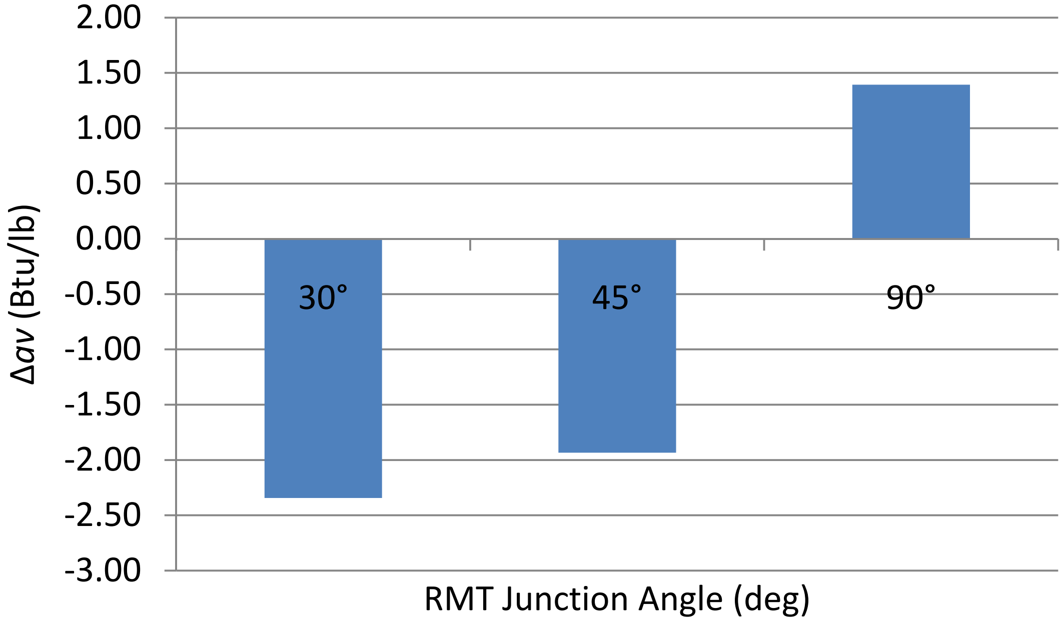

Figure 6.5: Variation in RMT junction angle

Continuing downstream through the exhaust diameter, the available energy loss is now a function of the length and diameter or hydraulic diameter of the conduit. Varying the diameter of the exhaust manifold creates another opportunity for recovery of available exhaust energy as shown in Figure 6.6. The existing exhaust manifold of the candidate Cooper GMV is divided down the vertical centerline by a plate, resulting in a calculated hydraulic diameter of 21.997 in. Removal of the vertical plate increases the manifold diameter to 36 in, recovering 30.9% of the energy loss in the exhaust manifold.

Limiting the surface area through which heat transfer can occur has been previously discussed as it increases the mechanical useable energy available to the turbocharger turbine inlet. Increasing the size of the exhaust manifold may seem as though it could provide limitless opportunity for energy recovery, but that opportunity is actually limited by the previously discussed RMT junction loss factor and radial heat transfer through the manifold surface. At 36 in in diameter, the manifold size augmentation has peaked and subsequent increases are overcome by the losses in thermal energy. As shown in Figure 6.6, a 36 in diameter manifold is the optimal diameter for the candidate Cooper GMV engine.

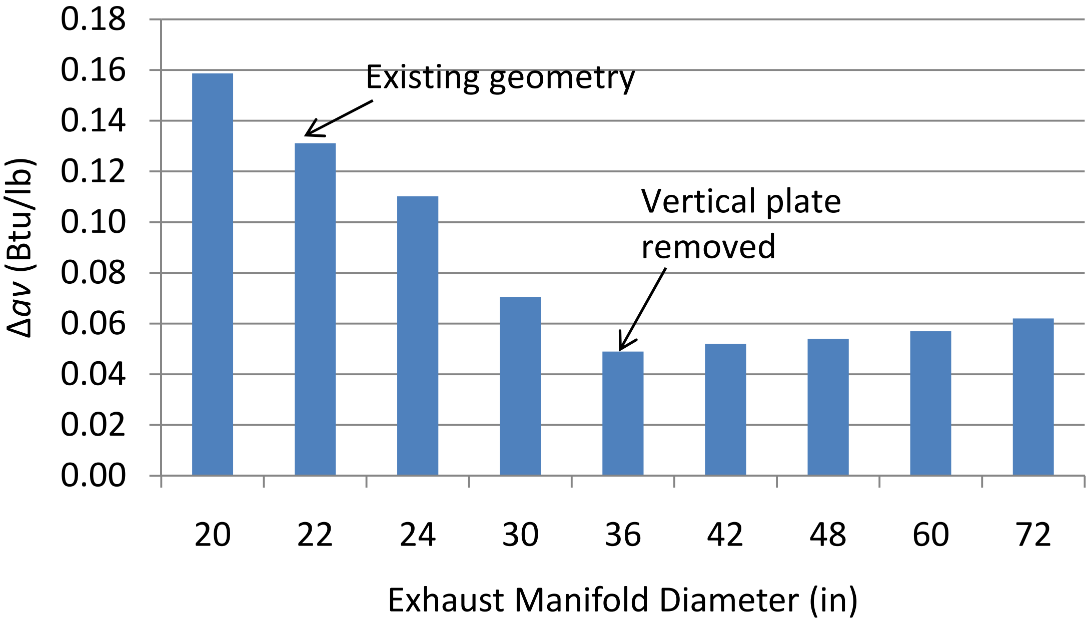

Figure 6.6: Variation in exhaust manifold diameter

Radial thermal energy losses through insulation are governed primarily by the R-value or thermal conductivity (k_r) and thickness of the piping insulation as defined previously in Figure 4.32. Thermal energy losses translate into an increase in the resistance of each of the components as shown previously. The loss of available energy as a function of the insulation thickness and thermal conductivity for various exhaust manifold diameters is plotted in Figure 6.7.

An investigation into various types of high-temperature, flame-resistant insulation that could be applied to exhaust manifolds resulted in multiple brands and designs varying in thermal conductivity from 0.25 to 0.75 Btu-in/ft^2-hr-ºF. Unfortunately, increasing insulation thickness is not a limitless opportunity for radial thermal energy recovery. Once the insulation thickness is greater than 3.0 in, the variation in lost available energy is less than 3% and effectively insignificant.

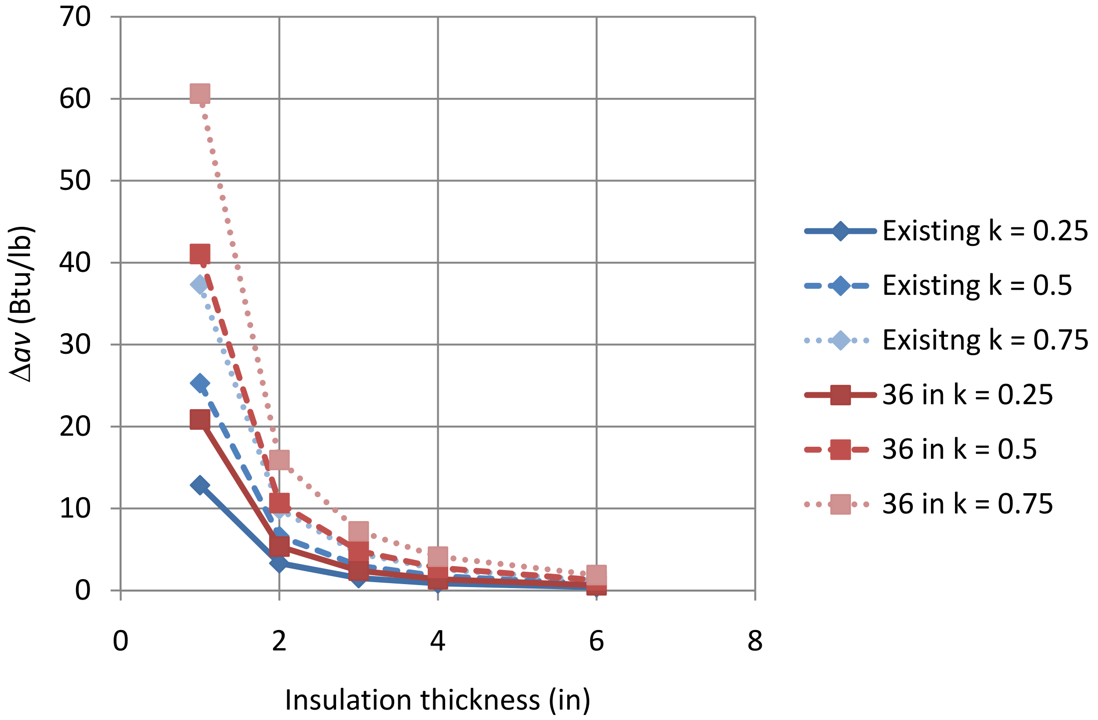

Figure 6.7: Variation in insulation thickness and thermal resistance

This component based analysis of available energy as a metric for defining optimal exhaust manifold design parameters allowed for the: 1) investigation of energy losses in the candidate Cooper GMV exhaust removal system on a component basis, and 2) translation of the mitigation of these losses into a new metric – waste-gate margin – for expanded turbocharger operating range.

Case Study

In order to adequately compare and contrast available energy gains due to augmenting the candidate Cooper GMV engine, the author developed a case study. The seven individual cases are described in Table 6.1. The “Base Line” case represents the typical geometry of the candidate engine. Cases 1 through 6 illustrate variations on designs that would recover available energy loss to components discussed previously in this chapter.

Table 6.1: Case descriptions

Case	AAC	ERUN (r/W = 1.5) angle (deg)	RMT Junction angle (deg)	Manifold Diameter (in)	Turbine Inlet angle (deg)
Base line	No	150	90	21.997	45
1	Yes	150	90	21.997	45
2	Yes	180	90	21.997	45
3	Yes	180	45	21.997	45
4	Yes	180	30	21.997	45
5	Yes	180	30	36	45
6	Yes	180	30	36	0

A breakdown of each of the seven cases by component is shown in Figure 6.8. Installing the AAC increases the energy available to the turbocharger turbine by 0.17 Btu/lb of exhaust gas. Augmenting the ERUN angle from a 150° vertical turn to a straight runner provides an extra 0.06 Btu/lb of exhaust gas to the turbocharger turbine. In addition to the augmentations in Cases 1 through 5, Case 6 accounts for relocating the turbocharger by removing the 45° elbow upstream of the turbocharger turbine inlet. Case 6 provides the turbocharger turbine with an extra 0.63 Btu/lb of exhaust gas over the Base line condition.

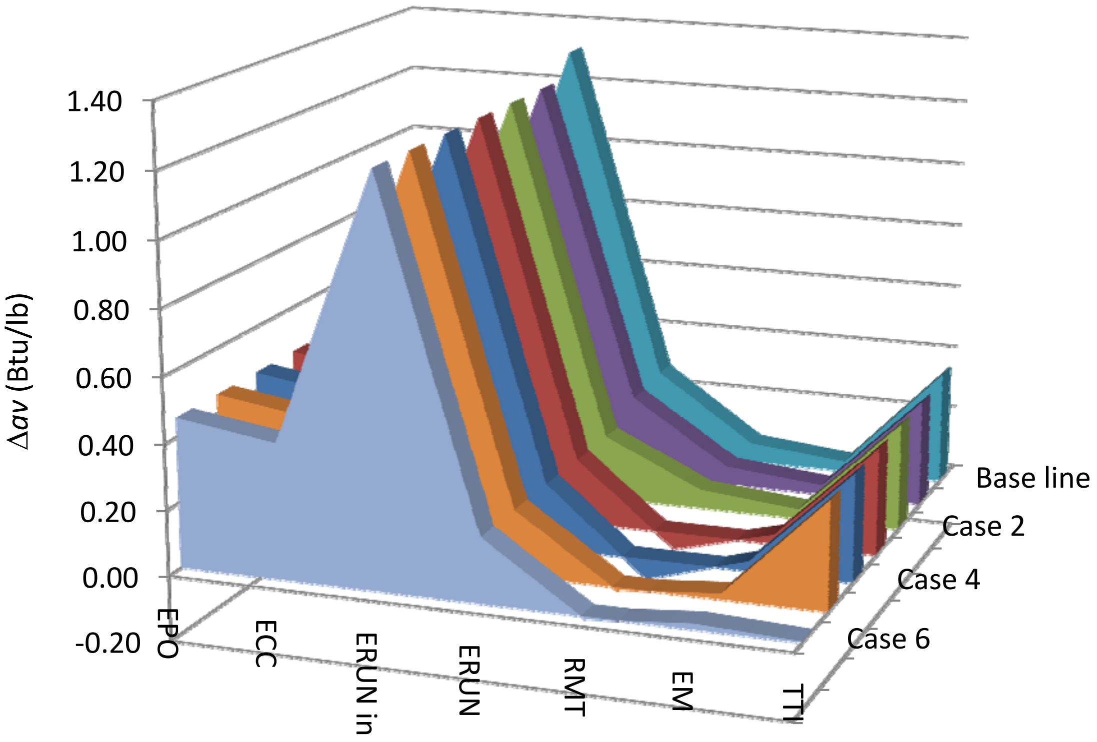

Figure 6.8: Change in available energy versus component by case

As shown in Figure 6.9, each case is incrementally better than the last, culminating in Case 6. Case 6 provides an increase in available energy to the turbocharger of over 1% when compared to the Base line condition.

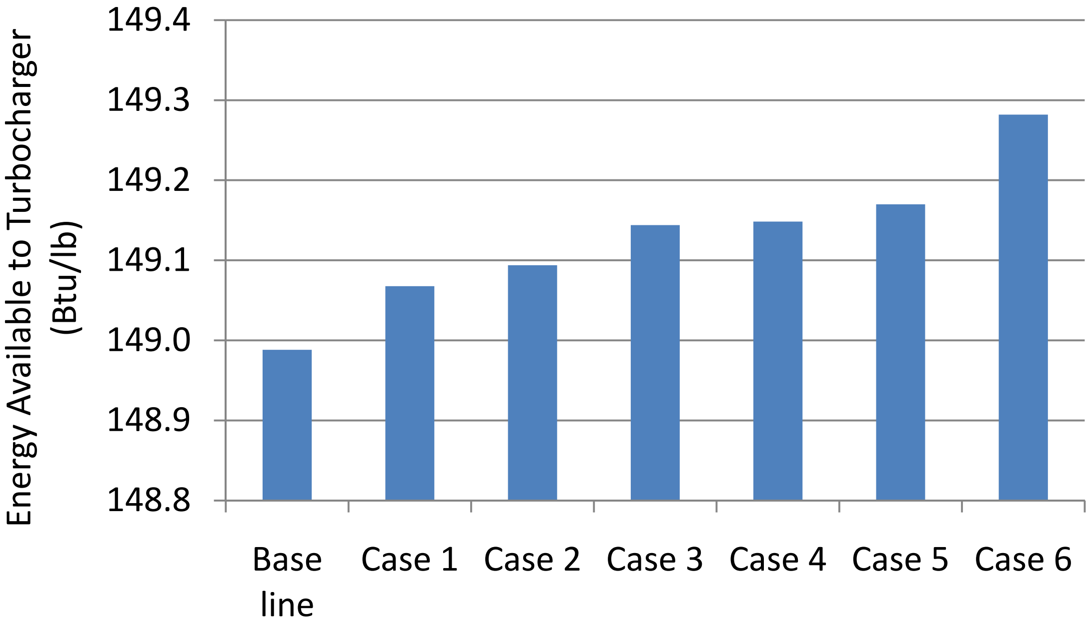

Figure 6.9: Energy available to turbocharger by case

Finally, each case is compared to the minimum required available energy, as described in Chapter 4 (Figure 4.36), in Figure 6.10. The difference between the case study and minimum values translates directly into waste-gate margin as described in Chapter 4.

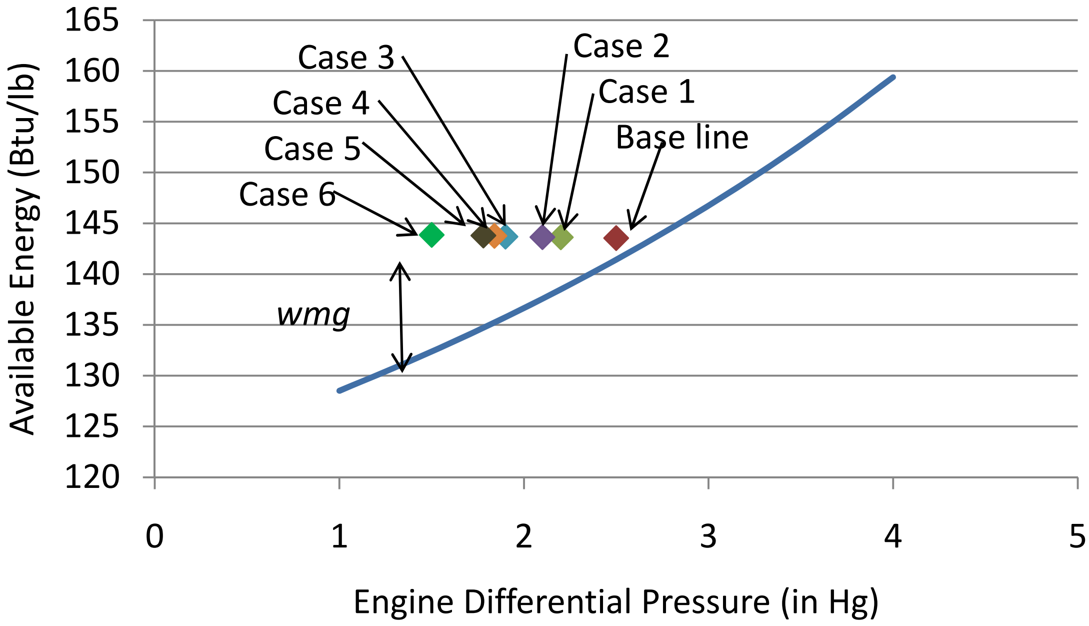

Figure 6.10: Available energy versus engine differential pressure

The results obtained via this case study provides a clear understanding of available energy as it relates to a component based design of the candidate Cooper GMV exhaust removal system. As per the case description in Table 6.1, the optimized exhaust removal system (Case 6) would include:

1. Installation of the AAC system;
2. Exhaust runners that would direct the exhaust flow to the turbocharger turbine via a straight run at a 30° angle to the exhaust manifold;
3. A 36 inch diameter "log" style exhaust manifold; and
4. A turbocharger mounted with the turbine inlet perpendicular to the exhaust manifold.

This exhaust removal configuration will provide the turbocharger turbine with 143.68 Btu/lb of available energy. In comparison to the Base line, the waste-gate margin can be increased from the Base line value of 1.50% to the Case 6 value of 8.75%, significantly expanding engine operating range.

CHAPTER 7 - Conclusions

The end product of this work is a thermodynamic analysis of the large-bore 2SC engine air management system resulting in the development of new software for the purpose of analyzing: 1) the cylinder-to-cylinder distribution of charge air, 2) pollutant emission concentrations, and 3) energy availability to the turbocharger turbine. During the course of the thermodynamic analysis, four new algorithms were developed:

1. Charge Air Integrated Manifold Engine Numerical Simulation (CAIMENS),
2. T-RECS NO Kinetic Mechanism,
3. T-RECS CO Kinetic Mechanism, and
4. Exhaust Manifold Design Software (EMDS).

The CAIMENS model is a coupling of the previously developed T-RECS with a transient manifold flow model developed from fundamental engineering principles of continuity and conservation in pipe matrices. It is a multi-cylinder engine algorithm that models the effects of charge air imbalance between cylinders using the physical relationships summarized in Chapter 3.

In order to comprehensively analyze the candidate Cooper GMV exhaust removal system, the CAIMENS model required incorporation of the engine timing model, for translation of the high pressure in-cylinder combustion products into exhaust port flow, in addition to new kinetic mechanisms for in-cylinder NO and CO formation. Both the new NO and CO kinetic mechanisms have been tuned and validate with data collected from the candidate Cooper GMV engine and integrated into the T-RECS algorithm. This new T-RECS engine performance and emissions algorithm can be used to analyze the performance of the engine air management system. In addition to engine design applications, these formation mechanisms can be used to evaluate the effectiveness of current and future after-treatment technologies developed for large-bore 2SC RICE to ensure continuous regulatory compliance.

The Exhaust Manifold Design Software (EMDS), which integrates the previously developed algorithms and expanded fundamentals, was created to predict fluid flow through the air delivery and exhaust removal systems of a large-bore 2SC RICE, to be used to develop a method to effectively and efficiently: 1) distribute charge air within the intake system, and 2) transfer exhaust products to the turbocharger turbine with minimal energy loss. The EMDS can predict pulsation and possible unbalanced air delivery and interference within the intake system and models energy release and pollutant emission formation during and just after the combustion event. Specifically, the EMDS outputs the transient pressure and temperature of the engine exhaust stream at the turbocharger turbine inlet.

Beyond the development of the four engine characterization algorithms, an air flow balancer (AFB) was designed using data from the CAIMENS algorithm developed in Chapter 4. This air flow balancer as part of an overall Active Air Control (AAC) system was used to balance the cylinder-to-cylinder distribution of air by the engine air management system.

The results obtained via this case study, included in Chapter 6, provide a clear understanding of available energy as it relates to a component based design of the candidate Cooper GMV exhaust removal system. As per the case study, the optimized exhaust removal system for the candidate Cooper GMV engine would include:

1. Installation of the AAC system;
2. Straight exhaust runners that would direct the exhaust flow toward the turbocharger turbine;
3. A “log” style exhaust manifold of optimal diameter; and

4. A turbocharger mounted with the turbine inlet perpendicular to the exhaust manifold.

As of 2007, over 1,200 compressor stations, a total 16.9 million installed horsepower, transmit over 881 billion cubic feet of natural gas per day through the U.S intra- and interstate transmission system (EIA, 2007). The natural gas transmission industry relies heavily on reciprocating large-bore two-stroke cycle (2SC) engines to power the prime mover compressors used to move the product through the pipeline. The majority of natural-gas-fired reciprocating engine-compressor units are at least 30 years old, employing technology that originated in the first half of the 20th century, prompting the use of the term “legacy” when referring to this technology. Over 70% of the total number of engines, and total horsepower within this system are large-bore 2SC turbocharged-engines fitted with “log” style intake and exhaust manifolds.

Legacy units are periodically retrofitted to include the newest technology to increase efficiency, safety, and reliability, with an emphasis on minimizing pollutant emissions. Current regulatory demands to reduce the environmental footprint of compressor stations have consistently increased the scale of station revitalization and retrofits with improved technology. The operating flexibility of the large-bore 2SC turbocharged-engine system is reduced by these upgrades. Specifically, turbocharger upgrades increase the flow rate of air through the system, increasing the engine differential pressure and decreasing combustion temperature, reducing the amount of energy available in the exhaust stream to operate the turbocharger turbine. This reduction in available energy significantly decreases engine operating flexibility. This flexibility can only be regained by reducing energy losses in the engine air management system. Losses in the air management can be recovered by utilizing the technology and techniques presented in this work.

Future Work

In order to complete step 5 of the *Chapman Research Strategy* (Chapman, 2008) discussed in Chapter 4, continued investigation of the developed AAC system should be conducted via a field test on either a Cooper or Clark make 2SC RICE.

Ideally, the AAC system would be installed and tested on an engine that has been used for other field tests, such as the Panhandle Energy engines in Olpe and Haven, Kansas. However, this is not mandatory as the cost-share partner will install the system.

Since the publication of the AAC system final report (Grauer and Chapman, 2008), a variety of other natural gas industry members, including the Advanced Engine Technology Corporation, have presented test results clearly documenting the impact of air flow imbalance on the cold compression trapped pressure in the cylinder. Furthermore, Southern California Natural Gas engine analysts have also observed and attempted to mitigate the impact of flow imbalance on some of their engines.

The AAC system laboratory analysis presented in this work was tailored specifically for the candidate Cooper GMV engine. However, the prototype is flexible, and with some modification and engineering effort can be scaled for any turbocharged-engine system.

Project objectives, tasks, and expected outcomes have been included in a proposal for field testing of the AAC system, submitted to PRCI.

References

Adair, J., Olsen, D., & Kirkpatrick, A. (2006). Exhaust tuning of large-bore, multi-cylinder, two-stroke, natural gas engines. *International Journal of Engine Research*, 7.

Abbaspour, M., Chapman, K.S., & Keshavarz, A. (2004). Non-isothermal transient gas pipeline simulation using fully implicit method. *Proceedings of the American Society of Mechanical Engineers International Pipeline Conference*.

Adriani, A. et al. (2005). Cost effective NO_X emission retrofit control technologies. *Proceedings of the Gas Machinery Conference*.

American Society of Heating, Refrigerating and Air-Conditioning Engineers, Inc. (2005). *ASHRAE Handbook: Fundamentals, Inch-Pound Edition*. Atlanta.

Annand, W.J.D. & Roe, G.E. (1974). Fundamentals of fluid flow. *Gas flow in the internal combustion engine: power, performance, emission control, and silencing*. Sparkford, CT: G.T. Foulis.

Azechi, M. et al. (1992). The development of new throttle valve actuation system for natural gas engine. *Proceedings of the Society of Automotive Engineers International Congress & Exposition*.

Bean, H. (Ed). (1971). *Fluid Meters Their Theory and Application* (6th ed). New York, NY: American Society of Mechanical Engineers.

Benedict, M., Webb, G.B., & Rubin, L.C. (1940). An empirical equation for thermodynamic properties of light hydrocarbons and their mixtures. *Journal of Chemical Physics*, 8, 344-345.

Benson, R.S., Baruah, P.C., & Sierens, R. (1974). Steady and non-steady flow in a simple carburetor. *Proceedings of the Institution of Mechanical Engineers*, 188, 537-548.

Beshouri, G. (1999). Carbon pollutant emissions and engine performance trade-offs vs. NO_X emissions for reciprocating internal combustion engines in gas transmission service. *Proceedings of the Gas Machinery Conference*.

Borman, G.L. &Ragland, K.W. (1998). Chemical kinetics of combustion. *Combustion Engineering*. Boston, MA: McGraw-Hill, 107-141.

Bourn, G., Phillips, F., Harris, R., & Raymer, R. (2005). Controlling engine air balance through manifold design – geometric analysis, simulation, and conceptual design." *Proceedings of the Gas Machinery Conference*.

Bowman, C.T. (1975). Kinetics of pollutant formation and destruction in combustion. *Progress in Energy and Combustion Science*, 33-45.

Chapman, K.S. et al. (2008). *Phase 2: Development of a gas turbine parametric emissions monitoring system* (PR-266-06203). Pipeline Research Council International, Inc.

Chapman, K.S. et al. (1997). *Enhanced monitoring guidelines for internal combustion engine parameter based compliance monitoring systems* (PR-239-9439). The Gas Research Institute.

Chapman, K.S., & Beshouri, G. (2000). Development of an air flow prediction algorithm through large-bore internal combustion engine for the purpose of engine-turbocharger matching. *Proceedings of the Gas Machinery Conference*.

Daily, J.W., & Harleman, D.R.F. (1966). Non-uniform flow in conduits. *Fluid Mechanics*. Reading, MA: Addison-Wesley, 309-368.

Deen, J.K., & Reintsema, S.R. (1983). "Modeling of high-rressure gas transmission lines. *Applied Mathematical Modeling*, 17, 268-273.

El Paso Corporation, (2006, March). *White Castle Station Unit #7 performance test data*.

Energy Information Administration (2009). *U.S. Natural Gas Pipelines*. Retrieved February 12, 2010. www.doe.eia.gov.

Environmental Protection Agency (1990). *Section 112: Maximum Achievable Control Technology*. Clean Air Act.

Environmental Protection Agency (2009). *National Emission Standards for Hazardous Air Pollutants for Reciprocating Internal Combustion Engines; Proposed Rule*. 40 CFR Part 63.

Environmental Protection Agency (2010, January 7). *Proposed National Ambient Air Quality Standards for Ozone*. 40 CFR Part 50.

Environmental Protection Agency (2010, February 9). *Proposed National Ambient Air Quality Standards for Nitrogen Dioxide*. 40 CFR Part 50.

Gad-el-Hak, M. (2000). *Flow control: Passive, active, and reactive flow management*. Cambridge, MA: Cambridge University Press.

Grauer, D., & Chapman, K.S., (2008). *Development of an active air control system: Final report* (PR-266-05208). Pipeline Research Council International, Inc.

Heywood, J.B., (1988). Modeling real engine flow and combustion processes. *Internal Combustion Engine Fundamentals*. New York, NY: McGraw Hill, 748-822.

Heywood, J.B., & Sher, E., (1999). Port, valve, intake, and exhaust system design. *The two-stroke cycle engine: Its development, operation, and design*. New York, NY: Taylor & Francis.

Hosni, M.H., Coleman, H.W., & Steele, W.G., (1999). *Application of MathCAD software in performing uncertainty analysis calculations to facilitate laboratory instruction*. Mathsoft.

Hughes, K.J. et al., (2001). Development and testing of a comprehensive chemical mechanism for the oxidation of methane. *International Journal of Chemical Kinetics*, 513-538.

Ingram, G.A., Franchek, M.A., & Balakrishnan, V. (2003). *Spark ignition engine mass air flow control for precise torque management* (2003-01-0624). Society of Automotive Engineers.

Issa, R.I., & Spalding, D.B., (1992). Unsteady one-dimensional compressible frictional flow with heat transfer. *Journal of Mechanical Engineering Science*, 14.6, 365-369.

Kenny, R.G., (1992). Developments in two-stroke cycle engine exhaust emissions. *Proceedings of the Institution of Mechanical Engineers*, 26, 93-106.

Lavoie, G.A., (1978). *Correlations of combustion data for SI engine calculations – laminar flame speed, quench distance, and global reaction rates* (940668). Society of Automotive Engineers.

Lawland, V.J., & Caton, J.A., (2009). A turbocharged, spark-ignition engine: Results from and engine cycle simulation including the second law of thermodynamics (ICES2009-76023). *Proceedings of American Society of Mechanical Engineers Internal Combustion Engine Division Spring Technical Conference*.

Li, J. et al., (2007). A comprehensive kinetic mechanism for CO, CH_2O, and CH_3OH combustion. *International Journal of Chemical Kinetics*, 109-136.

Li, Y., (2003). *Airflow through ports of large-bore reciprocating engines*. Doctoral dissertation, Kansas State University.

Macian, V., Lujan, J.M., Bermudez, V., & Guardiola, C., (2004). Exhaust pressure pulsation observation from turbocharger instantaneous speed measurement. *Journal of Measurement and Science Technology*, 15, 1185-1194.

Miyasato, F., (1997). *Development of air flow prediction algorithm through large-bore internal combustion engines*. Doctoral dissertation, Kansas State University.

Moran, M.J., (1989). *Availability analysis: A guide to efficient energy use* (Rev. ed.). New York, NY: Prentice Hall/ASME.

Moran, M.J., & Shapiro, H.N., (2008). *Fundamentals of Engineering Thermodynamics* (6th ed.). Hoboken, NJ: John Wiley & Sons, Inc.

Olsen, D. et al., (2003). *Evaluation of CO or THC emissions control technologies for control of organic hazardous air pollutant emissions from natural gas fired engines: Final technical report* (535508). Gas Research Institute.

Osiadacz, A.J., & Chaczykowski, M. (2001). Simulation of non-isothermal transient gas flow in a pipeline. *Archives of Thermodynamics*, 22, 51-70.

Ouyang, L., & Aziz, K., (1996). Steady-state gas flow in pipes. *Journal of Petroleum Science and Engineering*, 14, 137-158.

Paulus, Jr. D.M., Gaggioli, R.A., & Dunbar, W.R., (2001). Entropy production as a predictive performance measure for turbomachinery. *Journal of Engineering for Gas Turbines and Power*, 123, 17-21.

Pipeline Research Council International, Inc. (2005). *Pipeline engine emissions control roadmap: Technology pathways to cost-effective year 2010 reciprocating engine emissions compliance*.

Price, G.R, McBrien, R.K., Rizopoulos, S.N., & Golshan, H., (1996). Evaluating the effective friction factor and overall heat transfer coefficient during unsteady pipeline operation. *Proceedings of the American Society of Mechanical Engineers International Pipeline Conference*, 2, 1175-1182.

Rakopoulos, C.D., & Giakoumis, E.G., (2006). Second-law analyses applied to internal combustion engines operation. *Progress in Energy and Combustion Science*, 32, 2-47.

RTI International, (2009). *Regulatory impact analysis (RIA) for existing stationary reciprocating internal combustion engines (RICE) NESHAP: Final report*.

South Coast Air Quality Management District, (2005). *Rule 1110.2 – Emission from gaseous- and liquid-fueled engines*.

Sayin, C., Hosoz, M., Canakci, M., & Kilicaslan, I., (2007). Energy and exergy analyses of a gasoline engine. *International Journal of Energy Research*, 31, 259-273.

Scherer, M., Arndt, C., & Loffeld, O., (1997). Influence of manifold pressure pulsation to mean value models in air fuel ratio control (MP4-3). *Proceedings of the 5th IEEE Mediterranean Conference on Control and Automation*.

Sengupta, J., Abbaspour, M., & Chapman, K.S., (2006). Assessing the impact of pressure pulses in exhaust manifolds during blow-down process on in-cylinder distribution using T-RECS (ICEF2006-1527). *Proceedings of the American Society of Mechanical Engineers Internal Combustion Engine Division Fall Technical Conference*.

Sezer, I., & Bilgin, A., (2008). Mathematical analysis of spark ignition engine operation via the combination of the fires and second law of thermodynamics. *Proceedings of the Royal Society*, 464, 3107-3128.

Sullivan, K., (1998). *Sensors #4 - Air flow sensors*. Autoshop101: Automotive Training and Resource Site for Automotive Electronics, Toyota Motor Sales, U.S.A. http://www. autoshop101. com/forms/h34.pdf.

Thorley, A.R.D., & Tiley, C.H., (1987). Unsteady and transient flow of compressible fluids in pipelines – A review of theoretical and some experimental studies. *Journal of Heat and Fluid Flow*, 8.1, 3-15.

Woods, W.A., & Goh, G.K., (1979). Compressible flow through a butterfly throttle valve in a pipe. *Proceedings of the Institution of Mechanical Engineers*, 193, 23.

Yoshida, S., & Yamato, H., (2005). Exergy analysis of a diesel engine cycle and its performance improvement. *International Journal of Exergy*, 2, 284-298.

Zervas, E. et al., (2003). Emissions of regulated pollutant from a spark ignition engine: Influence of fuel and air/fuel equivalence ratio. *Journal of Environmental Science and Technology*, 37(14), 3232-3238.

Appendix A - Single-phase Flow Conservation Equations

The non-isothermal flow of fluid in pipes is governed by the time-dependant continuity, momentum, and energy equations, coupled with an equation of state for homogeneous, one-dimensional flow, adapted from *Abbaspour* (2004).

Continuity Equation

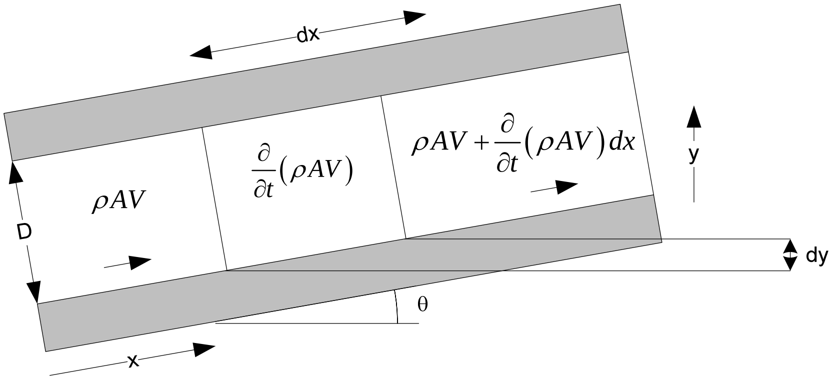

Figure A.1: Control volume for continuity equation

The conservation of mass for the control volume shown in Figure A.1 is:

$$\rho AV - \rho AV - \frac{\partial}{\partial t}(\rho AV)dx = \frac{\partial}{\partial t}(\rho AV) \tag{A1}$$

Combining terms:

$$\frac{\partial}{\partial t}(\rho AV)dx + \frac{\partial}{\partial t}(\rho AV) = 0 \tag{A2}$$

Finally:

$$\frac{\partial \rho}{\partial t} + \frac{\partial}{\partial x}(\rho V) = 0 \tag{A3}$$

Conservation of Momentum

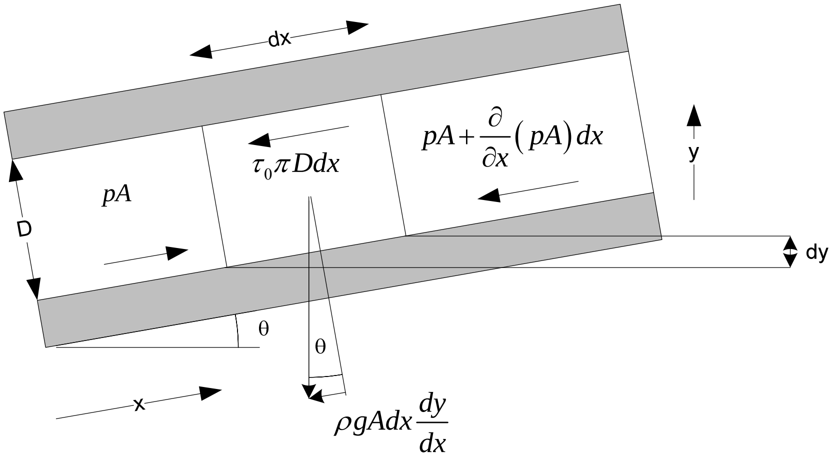

Figure A.2: Control volume for conservation of momentum

The conservation of momentum for the control volume shown in Figure A.2 is:

$$pA - pA - \frac{\partial}{\partial x}(pA)dx - \tau_0 \pi D dx - \rho g A dx \frac{dy}{dx} = (\rho A dx)\left(V\frac{\partial V}{\partial x} + \frac{\partial V}{\partial t}\right) \quad \text{(A4)}$$

Combining terms:

$$-A\frac{\partial p}{\partial x} - \tau_0 \pi D - \rho g A \frac{dy}{dx} = (\rho A)\left(V\frac{\partial V}{\partial x} + \frac{\partial V}{\partial t}\right) \quad \text{(A5)}$$

The shear stress at the pipe wall (τ_0) is a function of the Darcy friction factor (f):

$$\tau_0 = \frac{f\rho V|V|}{8} \quad \text{(A6)}$$

Defining $\sin\theta = \frac{dy}{dx}$:

$$-A\frac{\partial p}{\partial x} - \frac{f\rho V|V|}{8}\pi D - \rho g A \sin\theta = (\rho A)\left(V\frac{\partial V}{\partial x} + \frac{\partial V}{\partial t}\right) \quad \text{(A7)}$$

Finally, renaming the friction factor term (w) and rearranging:

$$\rho\frac{\partial V}{\partial t} + \rho V\frac{\partial V}{\partial x} + \frac{\partial p}{\partial x} = -\frac{w}{A} - \rho g A \sin\theta \quad \text{(A8)}$$

Conservation of Energy

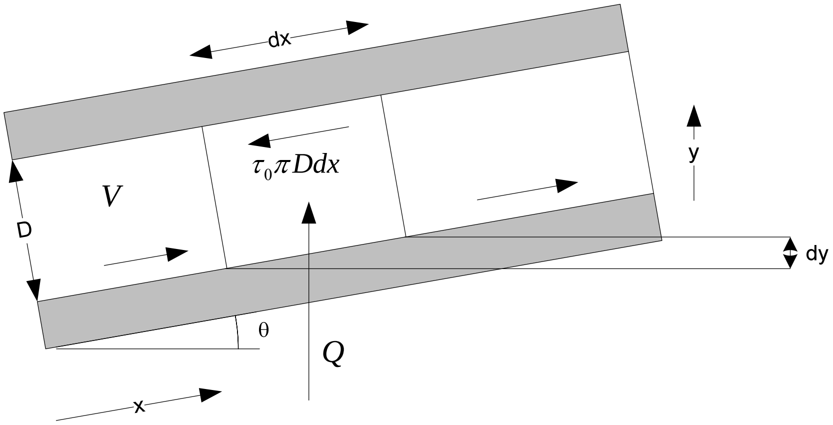

Figure A.3: Control volume for conservation of energy

The conservation of energy from the first law of thermodynamics for the control volume shown in Figure A.3 is:

$$Q = q\rho A dx = \frac{\partial}{\partial t}\left(\rho A dx\left(u + \frac{V^2}{2} + gy\right)\right) + \frac{\partial}{\partial x}\left(\rho V A\left(u + \frac{V^2}{2} + gy + \frac{p}{\rho}\right)\right) dx \tag{A9}$$

The heat transferred (Q) is a function of the heat addition per unit mass per unit time (q) and the internal energy of the fluid (u).

Separating the last term, introducing the continuity equation previously defined, and dividing by $\rho A dx$, the energy equation reduces to:

$$q = \frac{\partial}{\partial t}\left(u + \frac{V^2}{2} + gy\right) + \frac{V}{\rho}\frac{\partial p}{\partial x} + \frac{p}{\rho A}\frac{\partial (VA)}{dx} \tag{A10}$$

Using the previously defined momentum equation and dividing by the velocity (V):

$$\frac{V}{\rho}\frac{\partial p}{\partial x} = -V\frac{\partial V}{\partial t} - \frac{wV}{\rho A} - gV\sin\theta \tag{A11}$$

Incorporating the previously defined equation for continuity:

$$q = \frac{\partial}{\partial t}\left(u + \frac{V^2}{2} + gy\right) - V\frac{\partial V}{\partial t} - \frac{wV}{\rho A} - gV\sin\theta - \frac{p}{\rho^2}\frac{\partial \rho}{dt} \tag{A12}$$

Combining terms and utilizing the definition of enthalpy ($h \equiv u + \frac{p}{\rho}$), the energy equation reduces to:

$$q + \frac{wV}{\rho A} = \frac{\partial h}{\partial t} - \frac{1}{\rho}\frac{\partial p}{dt} \tag{A13}$$

Finally, defining a heat transfer term ($\Omega = q\rho A$):

$$\rho\frac{\partial h}{\partial t} + \rho V\frac{\partial h}{\partial x} - \frac{\partial p}{dt} - V\frac{\partial p}{dx} = \frac{\Omega + wV}{A} \tag{A14}$$

Incorporating an Equation of State

The previously defined equations for continuity (A3), conservation of momentum (A8), and conservation of energy (A14) are not a suitable set of equations for simultaneous solution. Therefore, they must be rewritten with pressure (p), velocity (V), and temperature (T) as the dependant variables using an equation of state, which must be a function of the fluid compressibility factor (Z):

$$\rho = \frac{p}{ZRT} \tag{A15}$$

Written in logarithmic form and then converted to a differential with respect to time:

$$\frac{1}{\rho}\frac{\partial \rho}{\partial t} = \frac{1}{p}\frac{\partial p}{\partial t} - \frac{1}{Z}\frac{\partial Z}{\partial t} - \frac{1}{R}\frac{\partial R}{\partial t} - \frac{1}{T}\frac{\partial T}{\partial t} \tag{A16}$$

Defining the fluid compressibility factor (Z) as a function of both pressure (p) and temperature (T), and substituting into the continuity equation (A3):

$$\left(\frac{1}{p} - \frac{1}{Z}\left(\frac{\partial Z}{\partial p}\right)_T\right)\frac{\partial p}{\partial t} - \left(\frac{1}{T} - \frac{1}{Z}\left(\frac{\partial Z}{\partial T}\right)_p\right)\frac{\partial T}{\partial t} + \frac{\partial V}{\partial x} = 0 \tag{A17}$$

In order to obtain the gas enthalpy (h), *Zemansky* (1968) described the thermodynamic identity:

$$dh = c_p dT - c_p \eta_J dP \tag{A18}$$

The Joule-Thompson coefficient (η_J) is defined as:

$$\eta_J = \left(\frac{\partial T}{\partial p}\right)_h \tag{A19}$$

Rearranging equation (A18) and equating to (A19), dividing both sides by dt, and substituting into the conservation of energy (A14):

$$\rho c_p \frac{\partial T}{\partial t} + \left(\frac{T}{\rho}\left(\frac{\partial \rho}{\partial T}\right)_p\right)\frac{\partial p}{dt} = \frac{\Omega + wV}{A} \tag{A20}$$

Combining equations (A17) and (A20) to find dp/dt and evaluating the previously defined equation of state (A15) at constant pressure:

$$\frac{\rho}{p}\left[\left(1 - \frac{p}{Z}\left(\frac{\partial Z}{\partial p}\right)_T\right) - \frac{p}{\rho c_p T}\left(1 + \frac{T}{Z}\left(\frac{\partial Z}{\partial T}\right)_p\right)^2\right]\frac{\partial p}{dt} + \rho\frac{\partial V}{\partial x} \tag{A21}$$

$$= \frac{1}{c_p T}\left(1 + \frac{T}{Z}\left(\frac{\partial Z}{\partial T}\right)_p\right)\frac{\Omega + wV}{A}$$

Combining equations (A20) and (A21) to find dT/dt:

$$\rho c_p\left(\frac{1}{p} - \frac{1}{Z}\left(\frac{\partial Z}{\partial p}\right)_T\right)\frac{\partial T}{\partial t} + \frac{T}{p}\left(\frac{1}{T} + \frac{1}{Z}\left(\frac{\partial Z}{\partial T}\right)_p\right)\left(\frac{\partial \rho}{\partial T}\right)_p\frac{\partial T}{\partial t} \tag{A22}$$

$$= \frac{T}{p}\left(\frac{\partial \rho}{\partial T}\right)_p\frac{\partial V}{\partial x} + \left(\frac{1}{p} - \frac{1}{Z}\left(\frac{\partial Z}{\partial p}\right)_T\right)\frac{\Omega + wV}{A}$$

Dividing by c_p evaluating the previously defined equation of state (A15) at constant pressure as before:

$$\frac{\rho}{p}\left[\left(1 - \frac{p}{Z}\left(\frac{\partial Z}{\partial p}\right)_T\right) - \frac{p}{\rho c_p T}\left(1 + \frac{T}{Z}\left(\frac{\partial Z}{\partial T}\right)_p\right)^2\right] + \frac{1}{c_p}\left(1 + \frac{T}{Z}\left(\frac{\partial Z}{\partial T}\right)_p\frac{\partial V}{\partial x}\right) \tag{A23}$$

$$= \frac{1}{c_p T}\left(1 - \frac{p}{Z}\left(\frac{\partial Z}{\partial p}\right)_T\right)\frac{\Omega + wV}{A}$$

Numerical Formulation using the Fully Implicit Method

The fully implicit method allows for the transformation of partial differential equations into algebraic equations using finite difference approximations for partial derivatives. Figure A.4 shows the mesh used in the translation of the spatial and geometric partial derivative terms to finite difference approximations for the three independent variables pressure, temperature, and mass flow rate (Abbaspour, 2004).

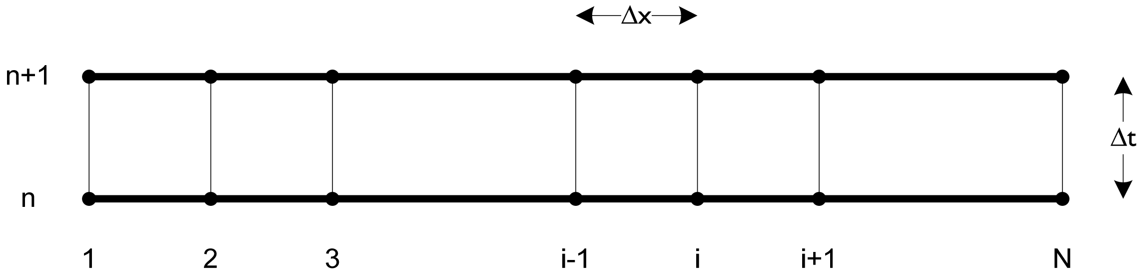

Figure A.4: Spatial-geometric grid for finite difference approximation

Spatial partial derivative approximations (Kuichi, 1994):

$$\frac{\partial P}{\partial t} = \frac{(P_{i+1}^{n+1} + P_{i}^{n+1} - P_{i+1}^{n} - P_{i}^{n+1})}{2\Delta t} \tag{A24}$$

$$\frac{\partial \dot{m}}{\partial t} = \frac{(\dot{m}_{i+1}^{n+1} + \dot{m}_{i}^{n+1} - \dot{m}_{i+1}^{n} - \dot{m}_{i}^{n+1})}{2\Delta t} \tag{A25}$$

$$\frac{\partial T}{\partial t} = \frac{(T_{i+1}^{n+1} + T_{i}^{n+1} - T_{i+1}^{n} - T_{i}^{n+1})}{2\Delta t} \tag{A26}$$

Geometric partial derivative approximations (Kuichi, 1994):

$$\frac{\partial P}{\partial x} = \frac{P_{i+1}^{n+1} - P_{i}^{n+1}}{\Delta x} \tag{A27}$$

$$\frac{\partial \dot{m}}{\partial x} = \frac{\dot{m}_{i+1}^{n+1} - \dot{m}_{i}^{n+1}}{\Delta x} \tag{A28}$$

$$\frac{\partial T}{\partial x} = \frac{T_{i+1}^{n+1} - T_{i}^{n+1}}{\Delta x} \tag{A29}$$

Nodal interface approximations (Kuichi, 1994):

$$P = \frac{P_{i+1}^{n+1} + P_i^{n+1}}{2} \tag{A30}$$

$$\dot{m} = \frac{\dot{m}_{i+1}^{n+1} + \dot{m}_i^{n+1}}{2} \tag{A31}$$

$$T = \frac{T_{i+1}^{n+1} + T_i^{n+1}}{2} \tag{A32}$$

Appendix B - Compressible Flow through a Restriction

A mathematical model for a gas flow through a restriction can be derived from the mass flow equation for compressible ideal flow (Annand and Roe, 1974). Ideal flow is assumed to be frictionless, steady, adiabatic, and reversible. This development is dimensionless and well suited for experimental tests due to the relatively easily measured variables and computational simplicity. The mass flow rate ($\dot{m}$), as a function of the effective flow area (A_E), density of the gas (ρ), and velocity (V) is defined as:

$$\dot{m} = \rho A_E V \tag{B1}$$

The ideal gas equation states that the density of a gas (ρ) is a function of the real gas constant divided by the molar mass ($R = \hat{R}/M$), static gas pressure (p), and gas temperature (T):

$$\rho = \frac{p}{RT} \tag{B2}$$

To obtain a dimensionless equation, a dimensionless coefficient is defined which contains the mass flow rate ($\dot{m}$), stagnation pressure (p_t), stagnation temperature (T_t), specific heat ratio (γ), total mass (m), and length (L) (Annand and Roe, 1974):

$$\frac{\dot{m}\sqrt{\gamma R T_t}}{A_E p_t} = \frac{[mT^{-1}][LT^{-1}]}{[L^2][mL^{-1}T^{-2}]} \tag{B3}$$

By combining the mass flow equation (B1) with the ideal gas equation (B2), and multiplying both sides by $\sqrt{\gamma R T_t}/A_E p_t$, a dimensionless form of the mass flow equation is created:

$$\frac{\dot{m}\sqrt{\gamma R T_t}}{A_E p_t} = \frac{pV}{RT}\frac{\sqrt{\gamma R T_t}}{p_t} = \left(\frac{\gamma}{RT}\right)^{\frac{1}{2}} V \left(\frac{p}{p_t}\right)\left(\frac{T_t}{T}\right)^{\frac{1}{2}} \tag{B4}$$

Equation (B4) relates the pressure and temperature ratios across the restriction. These are easily measured variables. The velocity on the other hand is not. To eliminate the velocity variable, a series of manipulations are performed using thermodynamic definitions of specific heats (B5, B6), enthalpy (B7, B8), and the Mach number (B9).

Given the definitions:

$$\gamma = \frac{c_p}{c_v} \qquad \text{(B5)} \qquad\qquad R = c_p - c_v \qquad \text{(B6)}$$

$$h_t = h + \frac{V^2}{2} \qquad \text{(B7)} \qquad\qquad h = c_p T \qquad \text{(B8)}$$

$$Ma = \frac{V}{c} = \frac{V}{\sqrt{\gamma R T}} \qquad \text{(B9)} \qquad\qquad \frac{p_t}{p} = \left(\frac{T_t}{T}\right)^{\frac{\gamma}{\gamma-1}} \qquad \text{(B10)}$$

Manipulations can be made:

$$h_t - h = c_p(T_t - T) = \frac{V^2}{2}$$

$$T_t = T + \frac{V^2}{2c_p} = T + \frac{V^2}{2\frac{\gamma R}{\gamma - 1}} = T + \frac{\left(M\sqrt{\gamma R T}\right)^2}{2\frac{\gamma R}{\gamma - 1}}$$

Resulting in:

$$T_t = T\left(1 + \frac{\gamma - 1}{2}M^2\right) \qquad \text{(B11)}$$

With definition (B10):

$$p_t = p\left(1 + \frac{\gamma - 1}{2}M^2\right)^{\frac{\gamma}{\gamma-1}} \qquad \text{(B12)}$$

Using equations (B9), (B11), and (B12), equation (B4) can be written as:

$$\frac{\dot{m}\sqrt{\gamma R T_0}}{A_E p_0} = \gamma Ma\left(1 + \frac{\gamma - 1}{2}Ma^2\right)^{\frac{-(\gamma+1)}{2(\gamma-1)}} \qquad \text{(B13)}$$

Solving equation (B12) for the positive value of Mach number (Ma), and substituting it into equation (B13) (Annand and Roe, 1974):

$$\frac{\dot{m}\sqrt{\gamma R T_t}}{A_E p_t} = \gamma \left(\frac{p}{p_t}\right)^{\frac{1}{\gamma}} \sqrt{\frac{2}{\gamma - 1}\left(1 - \left(\frac{p}{p_t}\right)^{\frac{\gamma-1}{\gamma}}\right)} \tag{B14}$$

Equation (B14) is used extensively in experimental studies to determine discharge coefficients. Variables used in this equation are included in the table of nomenclature below.

Table 7.1: Nomenclature for compressible flow equation

p	Downstream static pressure
p_t	Upstream stagnation or total pressure
T_t	Upstream stagnation or total temperature
$\dot{m}$	Mass flow rate
A_E	Effective flow area
R	Gas constant divided by the molar mass of the gas ($R = \hat{R}/M$)
γ	Ratio of specific heats

Appendix C - Nitrogen Oxide Formation Mechanism Development

The mechanism of NO formation from atmospheric nitrogen has been studied extensively. Principal reactions governing the formation and destruction of NO from molecular nitrogen are (Heywood, 1988):

$$\mathrm{O} + \mathrm{N_2} \overset{1}{\leftrightarrow} \mathrm{NO} + \mathrm{N}$$

$$\mathrm{N} + \mathrm{O_2} \overset{2}{\leftrightarrow} \mathrm{NO} + \mathrm{O}$$

$$\mathrm{N} + \mathrm{OH} \overset{3}{\leftrightarrow} \mathrm{NO} + \mathrm{H}$$

As discussed in Chapter 3, a mechanism for NO_X formation has been defined as (Heywood, 1988):

$$\frac{d[\mathrm{NO}]}{dt} = k_{f1}[\mathrm{O}][\mathrm{N_2}] - k_{r1}[\mathrm{NO}][\mathrm{N}] + k_{f2}[\mathrm{N}][\mathrm{O_2}] - k_{r2}[\mathrm{NO}][\mathrm{O}] + k_{f3}[\mathrm{N}][\mathrm{OH}] - k_{r3}[\mathrm{NO}][\mathrm{H}] \tag{C1}$$

For very high temperature applications, such as the large-bore 2SC RICE, it can be assumed that the O, N, OH, and H remain in thermodynamic equilibrium in the post flame zone; therefore, their concentrations can be approximated as such. It may also be assumed that the N remains at steady state concentration:

$$\frac{d[\mathrm{N}]}{dt} = k_{f1}[\mathrm{O}][\mathrm{N_2}] - k_{r1}[\mathrm{NO}][\mathrm{N}] - k_{f2}[\mathrm{N}][\mathrm{O_2}] + k_{r2}[\mathrm{NO}][\mathrm{O}] - k_{f3}[\mathrm{N}][\mathrm{OH}] + k_{r3}[\mathrm{NO}][\mathrm{H}] = 0 \tag{C2}$$

Solving for N at steady state (Borman and Ragland, 1998):

$$[\mathrm{N}] = \frac{k_{f1}[\mathrm{O}][\mathrm{N_2}]+k_{r2}[\mathrm{NO}][\mathrm{O}] + k_{r3}[\mathrm{NO}][\mathrm{H}]}{k_{r1}[\mathrm{NO}] + k_{f2}[\mathrm{O_2}] + k_{f3}[\mathrm{OH}]} \tag{C3}$$

Using equation (C3) to eliminate [N], the NO formation rate then becomes:

$$\frac{d[\mathrm{NO}]}{dt} = 2k_{f1}[\mathrm{O}][\mathrm{N_2}]\frac{1-\dfrac{[\mathrm{NO}]^2}{K_{fb}[\mathrm{O_2}][\mathrm{N_2}]}}{1+\dfrac{k_{r1}[\mathrm{NO}]}{k_{f2}[\mathrm{O_2}]+k_{f3}[\mathrm{OH}]}} \tag{C4}$$

$$K_{fb} = \left(\frac{k_{f1}}{k_{r1}}\right)\left(\frac{k_{f2}}{k_{r2}}\right) \tag{C5}$$

The main source of nitrogen oxides emissions in combustion are oxidation of molecular nitrogen in the post-flame zone (thermal NO), formation of in the flame zone (prompt NO) , and oxidation of nitrogen-containing compounds in the fuel (fuel-bound NO). For adiabatic combustion with excess oxygen in the post-flame zone, thermal NO formation is the main source of NO emissions. Introducing the aforementioned equilibrium assumption for very high-temperature applications, such as internal combustion engines (Heywood, 1988):

$$R_1 = k_{f1}[\mathrm{O}]_\mathrm{e}[\mathrm{N_2}]_\mathrm{e} = k_{r1}[\mathrm{NO}]_\mathrm{e}[\mathrm{N}]_\mathrm{e} \tag{C6}$$

$$R_2 = k_{f2}[\mathrm{N}]_\mathrm{e}[\mathrm{O_2}]_\mathrm{e} = k_{r2}[\mathrm{NO}]_\mathrm{e}[\mathrm{O}]_\mathrm{e} \tag{C7}$$

$$R_2 = k_{f3}[\mathrm{N}]_e[\mathrm{OH}]_\mathrm{e} = k_{r3}[\mathrm{NO}]_\mathrm{e}[\mathrm{H}]_\mathrm{e} \tag{C8}$$

Typical values for the one-way equilibrium rate constants for equations (C6), (C7), and (C8) are readily found in the literature (Borman and Ragland, 1998). Equilibrium values for O, N, OH, and H are calculated using the EMDS, shown in Figure C.1.

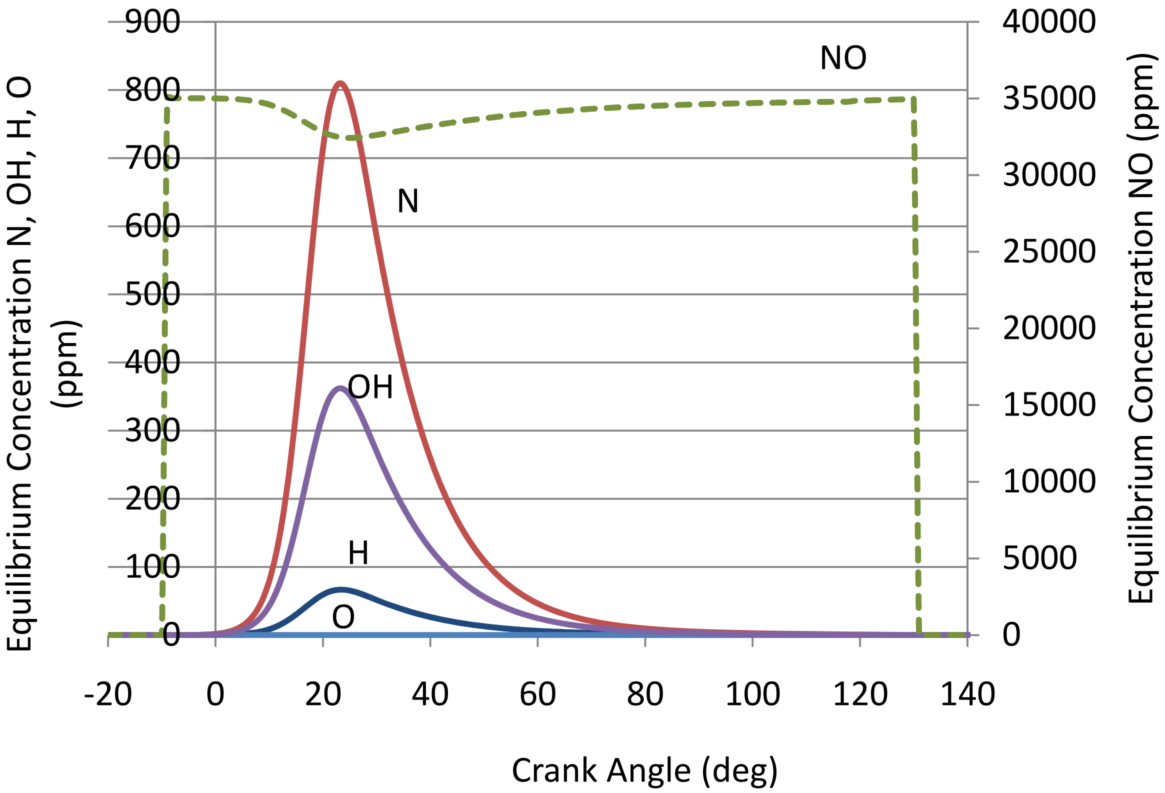

Figure C.1: EMDS Equilibrium Combustion Concentrations

Substituting equations (C7), (C8), and (C9) into equation (C6):

$$\frac{d[\mathrm{NO}]}{dt} = \frac{2\mathrm{R}_1\left\{1 - \left(\frac{[\mathrm{NO}]}{[\mathrm{NO}]_\mathrm{e}}\right)^2\right\}}{1 + \left(\frac{[\mathrm{NO}]}{[\mathrm{NO}]_\mathrm{e}}\right)\frac{\mathrm{R}_1}{(\mathrm{R}_2 + \mathrm{R}_3)}} \tag{C9}$$

The strong temperature dependence of the NO formation rate can be demonstrated by considering the initial value of $\frac{d[\mathrm{NO}]}{dt}$ when $\frac{[\mathrm{NO}]}{[\mathrm{NO}]_e} \ll 1$, from equation (C6) and (C9):

$$\frac{d[\mathrm{NO}]}{dt} = 2\mathrm{R}_1 = 2k_{f1}[\mathrm{O}]_\mathrm{e}[\mathrm{N}_2]_\mathrm{e} \tag{C10}$$

The equilibrium oxygen atom concentration can be found from:

$$[\mathrm{O}]_{\mathrm{e}} = \frac{K_{p(\mathrm{O})}[\mathrm{O}_2]_{\mathrm{e}}^{1/2}}{\left(\hat{R}T\right)^{1/2}} \tag{C11}$$

Where $K_{p(\mathrm{O})}$ is the equilibrium constant for the dissociation of O_2 to elemental oxygen (O) and is found using the procedure documented in Appendix D -Chemical Kinetic Reaction Mechanism Development. The initial NO formation rate is then written by combining equations (C10) and (C11), and tuning the pre-exponential factor and activation energy with values from the literature and exhaust data from the candidate Cooper GMV engine:

$$\frac{d[\mathrm{NO}]}{dt} = \frac{8.2 \times 10^{16}}{T^{1/2}} \exp\left(\frac{-74000}{T}\right) [\mathrm{O}]_{\mathrm{e}}^{1/2}[\mathrm{N}_2]_{\mathrm{e}} \tag{C12}$$

Appendix D - Chemical Kinetic Reaction Mechanism Development

This methodology for development of a general chemical kinetic reaction mechanism used in this work for evaluating the formation and destruction of CO in a large-bore 2SC engines is modified from *Borman and Ragland* (1998).

For a balanced reaction of the generic form:

$$a\text{A} + b\text{B} \rightarrow c\text{C} + d\text{D} \tag{D1}$$

Lower case values (a, b, c, d) are stoichiometric coefficients and molar concentrations are identified using square brackets [ ]. The rate of destruction of the reactants A and B, and the rate of formation of the products C and D are given by:

$$\frac{d[\text{A}]}{dt} = -ak_f[\text{A}]^a[\text{B}]^b \tag{D2}$$

$$\frac{d[\text{B}]}{dt} = -bk_f[\text{A}]^a[\text{B}]^b \tag{D3}$$

$$\frac{d[\text{C}]}{dt} = ck_f[\text{A}]^a[\text{B}]^b \tag{D4}$$

$$\frac{d[\text{D}]}{dt} = dk_f[\text{A}]^a[\text{B}]^b \tag{D5}$$

Elementary reactions are reversible; therefore, the backward reaction is:

$$c\text{C} + d\text{D} \rightarrow a\text{A} + b\text{B} \tag{D6}$$

For example, the backward reaction rate of A is:

$$\frac{d[\text{A}]}{dt} = ak_b[\text{C}]^c[\text{D}]^d \tag{D7}$$

Combining the forward and backward reaction rates, equation (D2) and (D7), respectively:

$$\frac{d[\text{A}]}{dt} = a\left(k_b[\text{C}]^c[\text{D}]^d - k_f[\text{A}]^a[\text{B}]^b\right) \tag{D8}$$

At, equilibrium, $d[\mathrm{A}]/dt = 0$, therefore the ratio of the forward to backward kinetic rate constant equals the thermodynamic equilibrium constant based on the reactant and product molar concentrations:

$$\frac{k_f}{k_b} = \frac{[C]^c[D]^d}{[\mathrm{A}]^a[\mathrm{B}]^b} = K_c \tag{D9}$$

$$K_c = K_p\left(\hat{R}T\right)^{a+b-c-d} \tag{D10}$$

The equilibrium constant (K_p) is evaluated using normalized values of the Gibbs free energy, enthalpy, and entropy of the combustion species. Therefore, if only one rate constant is known, equation (D9) can be used to obtain the other rate constant (Borman and Ragland, 1998).

Appendix E - Loss Coefficients for Exhaust Flow

The "Exhaust Thermodynamic Analysis" included in CHAPTER 4 - Solution Method and Development of the Air Management Model included a hydraulic loss stream function developed using well documented analysis of experimentally determined port flow by *Li* (2000) and duct flow included in the *ASHRAE Handbook: Fundamentals* (2005). The developed resistance diagram:

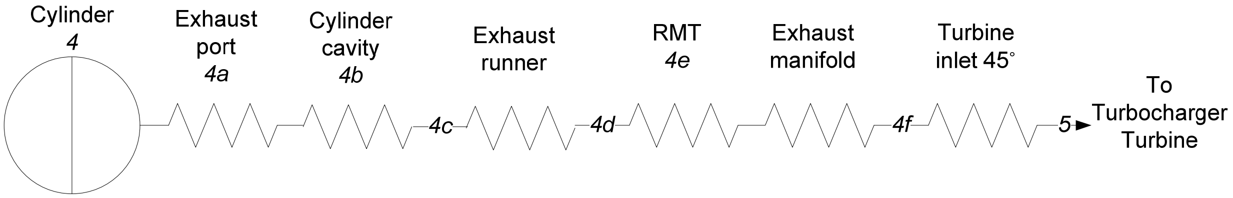

Figure E.1: Resistance diagram of exhaust path losses

and corresponding hydraulic loss stream function are included here for reference:

$$\sum H_{4-5} = H_{4-4a} + H_{4a-4b} + H_{4b-4c} + H_{4c-4d} + H_{4d-4e} + H_{4e-4f} + H_{4f-5} \tag{4.17}$$

Each of the component hydraulic losses is a function of the dynamic loss coefficient (*C*). The development or documentation of each of the dynamic loss coefficients used by the author is included here for reference.

Exhaust Port Flow (4-4a)

An experimental determination of port discharge coefficients for a Cooper GMV cylinder, as well as for Clark HBA and Worthington UTC cylinder, can be found in *Li* (2000). The evaluation of coefficients of discharge as a function of port opening fraction for large bore piston-controlled ports was completed by curve-fitting experimental data with polynomials. The general mathematical expression can be written as (Li, 2000):

$$C = \sum_{i=0}^{n} \alpha_i (fr) \tag{E1}$$

where the discharge coefficient is a function of the coefficients of the curve-fit (α), the port open fraction (*fr*), and the highest degree of the polynomial (*n*). Therefore, the experimentally determined curve-fit for the candidate Cooper GMV exhaust port flow is:

$$C = 0.3761 + 1.7325(fr) - 3.2569(fr)^2 + 3.3329(fr)^3 - 1.4927(fr)^4 \tag{E2}$$

When the exhaust port is 100% open or $fr = 1.00$, $C_D = 0.692$.

Exhaust Port to Exhaust Cylinder Cavity to Exhaust Runner (4a-4b-4c)

The *ASHRAE Handbook: Fundamentals* (2005) includes coefficients for round to rectangular expanding transitions (Table ED4-2). The expansion from the upstream hydraulic area (A_0) to the downstream hydraulic area (A_1) takes place at an angle (θ):

Table 7.2: Loss coefficient for round to rectangular transitions (ASHRAE ED4-2)

	C				
A_0/A_1	60°	90°	120°	150°	180°
0.06	0.88	0.95	0.98	0.98	0.93
0.10	0.84	0.89	0.91	0.91	0.88
0.25	0.62	0.64	0.64	0.64	0.64
0.50	0.33	0.33	0.32	0.31	0.30
1.00	0.00	0.00	0.00	0.00	0.00
2.00	0.24	0.49	0.73	0.97	1.04
4.00	1.12	2.72	4.33	5.62	6.58
6.00	2.52	6.51	10.14	13.05	15.14
10.00	8.05	19.06	29.07	37.08	43.05

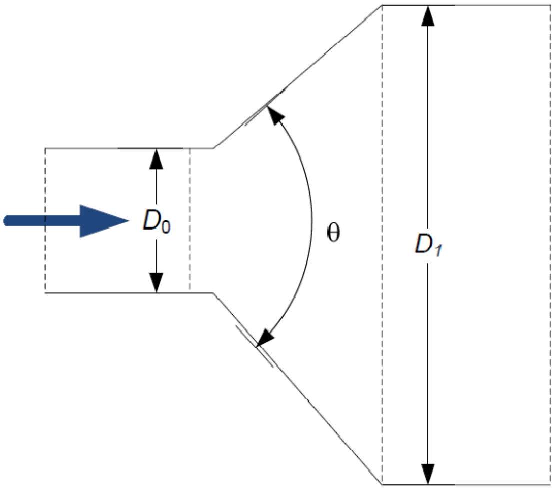

In order to identify the loss coefficient for the expansion of the exhaust products from the exhaust ports (EPO) to the exhaust cylinder cavity (ECC), upstream and downstream areas must be identified. The hydraulic diameter of the five, 4.125 inch by 2.5 inch, exhaust ports is 15.556 inches; therefore, the hydraulic area is $A_{EPO} = 12.226 \text{ in}^2$. The area of the 22 inch by 11 inch exhaust cylinder cavity is $A_{ECC} = 242.0 \text{ in}^2$. Therefore, $\frac{A_0}{A_1} = \frac{A_{EPO}}{A_{ECC}} = 0.051$ at an angle of $\theta = 180°$; extrapolating in Table 7.2, $C = 0.889$.

Following the same analysis for the contraction of the exhaust products from the ECC to the exhaust runner (ERUN), the downstream area of the 17 inch by 6.5 inch exhaust runner is $A_{ERUN} = 110.50 \text{ in}^2$. Therefore, $\frac{A_0}{A_1} = \frac{A_{ECC}}{A_{ERUN}} = 2.91$, at a calculated angle of $\theta = 79.6°$; interpolating in Table 7.2, $C = 0.571$.

Exhaust Runner (4c-4d)

Once the exhaust stream enters the ERUN, it experiences a change in direction equivalent to a 150 degree vertical turn through a constant area rectangular fitting. The loss coefficient is calculated by multiplying an angle factor (*K*) by a wetted perimeter factor (C_p) (AHSRAE, 2005):

$$C = K \times C_p \tag{E3}$$

The loss coefficient for ERUN is calculated by extrapolating values in Table 7.3.

Table 7.3: Loss coefficient for smooth radius rectangular elbow (ASHRAE CR3-1)

C_p					
	H/W				
r/W	0.25	0.50	0.75	1.00	1.50
0.50	1.53	1.38	1.29	1.18	1.06
0.75	0.57	0.52	0.48	0.44	0.40
1.00	0.27	0.25	0.23	0.21	0.19
1.50	0.22	0.20	0.19	0.17	0.15
2.00	0.2	0.18	0.16	0.15	0.14
K					
θ	90	110	130	150	180
K	1.00	1.13	1.20	1.28	1.40

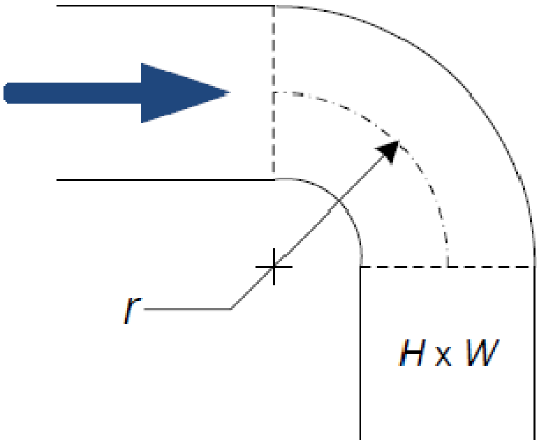

Interpolating in Table 7.3 for the 17 inch by 6.5 inch exhaust runner, $\frac{H}{W} = 0.382$, $C_p = 0.544$. Therefore, at a transition angle of 150 degrees, $C = 0.696$.

Exhaust Runner to Exhaust Manifold Transition (4d-4e)

The combining of the exhaust products of one cylinder to that of the products moving down the exhaust manifold (RMT) can be analyzed as a junction or converging tee (ASHRAE, 2005). In order to analyze this transition, the hydraulic diameter and area of the half-circle shaped manifold (EM) must be calculated. Using the hydraulic calculation included in "Hydraulic Loss" in CHAPTER 4 - Solution Method and Development of the Air Management Model, the manifold hydraulic area and diameter are $A_{EM} = 380.01 \text{ in}^2$ and $D_{EM} = 21.997$ in, respectively.

In order to evaluate the local loss of a junction, the components of the junction must be identified as:

1. The branch section (b) – the exhaust runner,

2. The straight section (s) – the manifold upstream of the exhaust runner, or
3. The common section (c) – the manifold downstream of the exhaust runner.

Each of the three components have their own hydraulic area (A_i), volumetric flow rate ($\dot{\forall}$), and loss coefficient (C). In order to evaluate the total loss of the junction, each loss coefficient must be referenced to the common section using the individual component's local velocity:

$$C_i = \frac{C_{c,i}}{(V_i/V_c)^2} \tag{E4}$$

where the subscript i indicates either the branch section (b) or the straight section (s).

An exhaustive analysis of the flow of engine exhaust products from each cylinder using the EMDS and data from the candidate Cooper GMV engine revealed that the mass flow rate itself varies from cylinder to cylinder by $\pm 5\%$ to $\pm 10\%$. Therefore, as an example, the subsequent analysis of the RMT will focus on the delivery of exhaust products to the exhaust manifold by cylinder 1L of the candidate Cooper GMV engine.

The volumetric flow rate ($\dot{\forall}$) of the cylinder 1L exhaust products may be calculated using the mass flow rate ($\dot{m}$) and the density (ρ), both of which are output by the EMDS, by:

$$\dot{\forall}= \dot{m}\rho \tag{E5}$$

Using the calculated volumetric flow rates and hydraulic area for each of the branch and straight sections, in addition to local loss coefficient values (C_b, C_s) from interpolation and extrapolation of Table 7.4, to total loss for the junction can be calculated:

$$C = \sum_i C_{c,i} \tag{E6}$$

Table 7.4: Loss coefficient for converging tee (AHSRAE ED5-3)

C_b				
		$\dot{\forall}_b/\dot{\forall}_c$		
A_s/A_c	A_b/A_c	0.4	0.5	0.6
1	0.2	0.87	0.92	0.95
	0.3	0.83	0.90	0.94
	0.4	0.85	0.93	0.97
C_s				
		$\dot{\forall}_s/\dot{\forall}_c$		
A_s/A_c	A_b/A_c	0.4	0.5	0.6
1	0.2	2.40	1.58	0.98
	0.3	2.65	1.69	1.03
	0.4	3.04	1.86	1.11

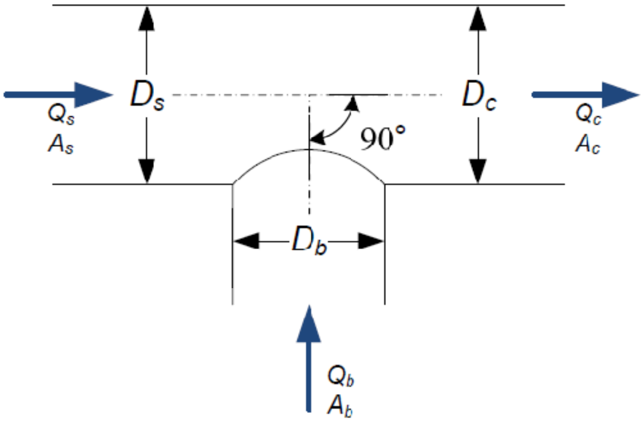

Identifying a conservative variation in each cylinder exhaust mass flow rate (2L, 3L, 4L, and 5L) of $\pm 10\%$ from the cylinder 1L exhaust mass flow rate, the local loss coefficient for the for the branch and straight section are $C_b = 0.8887$ and $C_s = 1.1806$. Therefore, the total local loss coefficient for the junction of the cylinder 1L exhaust runner and the exhaust manifold is $C_c = 4.704$.

It is important to note that the junction of two streams moving at different velocities is characterized by the turbulent mixing of the streams accompanied by pressure losses. In the course of mixing, an exchange of momentum takes place between the exhaust particles moving at different velocities, finally resulting in the equalization of the velocity distributions in the common stream. The jet with higher velocity (exhaust manifold or straight section) loses part of its kinetic energy by transmitting it to the slower moving jet. The loss in total pressure before and after mixing is always large and positive for the higher velocity jet and increases with an increase in the amount of energy transmitted to the lower velocity jet. Consequently the local loss coefficient (C_s), defined by equation 4.5, will always be positive. The energy stored in the lower velocity jet (exhaust runner or branch section) increases as a result of mixing. The loss in total pressure and the local loss coefficient (C_b) can, therefore, also have negative values for the lower velocity jet (ASHRAE, 2005).

Exhaust Manifold (4e-4f)

Analysis of the exhaust manifold is accomplished using the Darcy Equation to find the friction loss as a function of the friction factor (*f*), geometry of the manifold, and the local velocity pressure:

$$\Delta p = \frac{12fL}{D_h}\left(\frac{\rho V^2}{2g_c}\right) \tag{E7}$$

The friction factor is calculated for turbulent flow in rough pipes using the modified Colebrook-White equation, repeated here for reference (Ouyang and Azziz, 1996):

$$f^{-0.5} = 3.48 - 4\log\left(\frac{2\epsilon}{D} + \frac{9.35}{f^{0.5}\mathrm{Re}}\right) \tag{E8}$$

Turbine Inlet Transition (4f-5)

Finally, the exhaust products encounter a 45 degree elbow before entering the turbocharger turbine inlet. The local loss coefficient is a function of the diameter of the conduit and the radius of the elbow.

Table 7.5: Loss coefficient for 45° elbow (ASHRAE CD3-3)

C			
	D (in)		
r/D	4.0	5.0	6.0
1.00	0.10	0.08	0.05
1.50	0.13	0.10	0.08
2.00	0.25	0.21	0.18

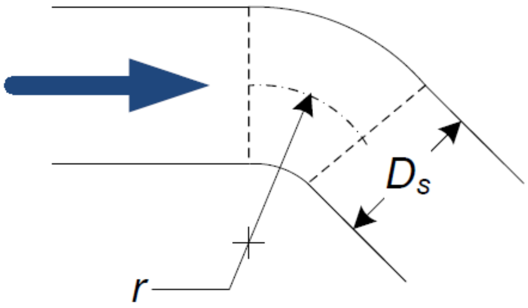

For the purpose of characterizing the exhaust manifold to turbocharger turbine inlet transition, the author selected a radius to diameter ratio of $r/D = 1.5$ at a hydraulic diameter of $D_{EM} = 5.499$ in. The local loss coefficient for the 45 degree turbine inlet transition, from interpolation in Table 7.5, is $C = 0.90$.

Appendix F - Experimental Uncertainty Analysis

Uncertainty Analysis Calculations For Flow Bench Tests:

Pressure Uncertainty:

Uncertainty of single system (*Pressure Transmitter* (FS=16mA, Cal_range = 15psi) and *Opto brick*):

$FS := 16mA \quad Cal\_Range := 15psi$

Individual Uncertainty:

Omega PX725 Transmitter -- $U_{ot} := .015\% \cdot Cal\_Range$

Opto22 Brick -- $U_o := 16\mu A$

$U_o = 1.6 \times 10^{-5} A$

$$U_p := \sqrt{\left(U_o \cdot \frac{Cal\_Range}{FS}\right)^2 + U_{ot}^{\,2}}$$

$U_p = 0.0152psi$

Temperature Uncertainty:

Uncertainty of single system (Thermocouple (Range=140R), Transmitter (FS=16mA) and *Opto brick*):

$FS := 16mA$

Individual Uncertainty:

Cold Junction Error -- $U_{CJ} := 0.05K \cdot 15$ $\quad U_{CJ} = 0.75K$

Thermocouple -- $U_{Therm} := .18R$

Transmitter -- $U_{Trans} := U_{CJ}$

$$U_T := \sqrt{\left(U_{Therm}\right)^2 + U_{Trans}^{\,2}}$$

$U_T = 1.3619\,R$

System of 2 Thermocouples:

$$U_{2T} := \sqrt{2 \cdot \left(U_T\right)^2}$$

$U_{2T} = 1.9261\,R$

Mass flow rate:

The following data was given or collected.

$\beta := 0.4419 \qquad d := 2.6801\,\mathrm{in} \quad C := 0.9950 \quad Y := 0.9696 \quad F := 1.0$

Venturi Uncertainty:

Uncertainty of venturi tube: $U_t := 0.7122\,\mathrm{in}$

Uncertainty of dP meter: $U_m := 0.001\,\mathrm{in}$

Uncertainty of system: $U_v := \sqrt{U_t^{\,2} + U_m^{\,2}}$

$U_v = 0.7122\,\mathrm{in}$

Density Uncertainty:

$$r := \left(\frac{1545}{28.97}\right)\cdot\frac{\mathrm{ft\cdot lbf}}{\mathrm{R\cdot lb}} \qquad r = 53.331\,\frac{\mathrm{ft\cdot lbf}}{\mathrm{R\cdot lb}}$$

$p_a := 14.24\,\mathrm{psi} \qquad \Delta p := 21.03\,\mathrm{in} \qquad t := (459.7 + 68.31)\mathrm{R} \qquad t = 528.01\,\mathrm{R}$

$$\rho = \frac{\left(p_a - \frac{\Delta p}{27.4}\right)}{r\cdot t}$$

$$\rho := \frac{\left(p_a - \frac{\Delta p}{27.4\cdot\frac{\mathrm{in}}{\mathrm{psi}}}\right)}{r\cdot t} \qquad \rho = 0.0689\,\frac{\mathrm{lb}}{\mathrm{ft}^3}$$

$$\rho_{partp} := \frac{d}{dp_a}\frac{\left(p_a - \frac{\Delta p}{27.4\cdot\frac{\mathrm{in}}{\mathrm{psi}}}\right)}{r\cdot t} \qquad \rho_{part\Delta p} := \frac{d}{d\Delta p}\frac{\left(p_a - \frac{\Delta p}{27.4\cdot\frac{\mathrm{in}}{\mathrm{psi}}}\right)}{r\cdot t} \qquad \rho_{partt} := \frac{d}{dt}\frac{\left(p_a - \frac{\Delta p}{27.4\cdot\frac{\mathrm{in}}{\mathrm{psi}}}\right)}{r\cdot t}$$

$$\rho_{partp} = 3.5512\times 10^{-5}\,\frac{\mathrm{lb}}{\mathrm{ft\cdot lbf}} \qquad \rho_{part\Delta p} = -0.3518\,\frac{\mathrm{kg}}{\mathrm{m}^2\cdot\mathrm{s}^2}\,\frac{\mathrm{lb}}{\mathrm{ft\cdot lbf}} \qquad \rho_{partt} = -1.3048\times 10^{-4}\,\frac{\mathrm{lb}}{\mathrm{R\cdot ft}^3}$$

$$U_\rho := \sqrt{\left(\rho_{partp}\cdot U_p\right)^2 + \left(\rho_{part\Delta p}\cdot U_m\right)^2 + \left(\rho_{partt}\cdot U_{2T}\right)^2}$$

$$U_{\rho\%} := \frac{U_\rho}{\rho}$$

$U_\rho = 2.6301\times 10^{-4}\,\frac{\mathrm{lb}}{\mathrm{ft}^3}$

$U_{\rho\%} = 0.3818\,\%$

Uncertainty of Discharge Coefficients:

Given data:

$m_r = 0.8531 \frac{lb}{s}$ $r = 53.331\,ft \cdot \frac{lbf}{R \cdot lb}$ $T_0 := 530.26R$ $P_0 := 21.36psi$ $P := 21.227psi$

$A_{ref} := 0.401 \cdot ft^2$ $k := 1.4$

Individual Uncertainties:

Pressure Uncertainty: $U_p = 0.0152\,psi$

Temperature Uncertainties:

One Thermocouple: $U_T = 1.3619\,R$

Two Thermocouples: $U_{2T} = 1.9261\,R$

Uncertainty of Measured Mass Flow Rate:

$U_{mr} = 0.0145 \frac{lb}{s}$

Uncertainty of Area:

$U_A := 0.001 \cdot A_{ref}$ $U_A = 0.0577\,in^2$

For simplity, assume uncertainties of total pressure and total temperature are the same as those of static pressure and static temperature.

Define :

$$C_d = \frac{m_r \cdot \sqrt{r \cdot T_0}}{\left(A_{ref} \cdot P_0\right) \cdot \left(\frac{P}{P_0}\right)^{\frac{1}{k}} \left[\left(2 \cdot \frac{k}{k-1}\right) \cdot \left[1 - \left(\frac{P}{P_0}\right)^{\frac{(k-1)}{k}}\right]\right]^{0.5}}$$

Partial Derivatives:

mr: $$C_{dpartmr} := \frac{d}{dm_r} \frac{m_r \cdot \sqrt{r \cdot T_0}}{\left(A_{ref} \cdot P_0\right) \cdot \left(\frac{P}{P_0}\right)^{\frac{1}{k}} \left[\left(2 \cdot \frac{k}{k-1}\right) \cdot \left[1 - \left(\frac{P}{P_0}\right)^{\frac{(k-1)}{k}}\right]\right]^{0.5}}$$

T0:

$$C_{dpartT0} := \frac{d}{dT_0}\frac{m_r\cdot\sqrt{r\cdot T_0}}{(A_{ref}\cdot P_0)\cdot\left(\frac{P}{P_0}\right)^{\frac{1}{k}}\left[\left(2\cdot\frac{k}{k-1}\right)\cdot\left[1-\left(\frac{P}{P_0}\right)^{\frac{(k-1)}{k}}\right]\right]^{0.5}}$$

P0:

$$C_{dpartP0} := \frac{d}{dP_0}\frac{m_r\cdot\sqrt{r\cdot T_0}}{(A_{ref}\cdot P_0)\cdot\left(\frac{P}{P_0}\right)^{\frac{1}{k}}\left[\left(2\cdot\frac{k}{k-1}\right)\cdot\left[1-\left(\frac{P}{P_0}\right)^{\frac{(k-1)}{k}}\right]\right]^{0.5}}$$

P:

$$C_{dpartP} := \frac{d}{dP}\frac{m_r\cdot\sqrt{r\cdot T_0}}{(A_{ref}\cdot P_0)\cdot\left(\frac{P}{P_0}\right)^{\frac{1}{k}}\left[\left(2\cdot\frac{k}{k-1}\right)\cdot\left[1-\left(\frac{P}{P_0}\right)^{\frac{(k-1)}{k}}\right]\right]^{0.5}}$$

Aref:

$$C_{dpartAref} := \frac{d}{dA_{ref}}\frac{m_r\cdot\sqrt{r\cdot T_0}}{(A_{ref}\cdot P_0)\cdot\left(\frac{P}{P_0}\right)^{\frac{1}{k}}\left[\left(2\cdot\frac{k}{k-1}\right)\cdot\left[1-\left(\frac{P}{P_0}\right)^{\frac{(k-1)}{k}}\right]\right]^{0.5}}$$

Calculate Cd:

$$C_d := \frac{m_r\cdot\sqrt{r\cdot T_0}}{(A_{ref}\cdot P_0)\cdot\left(\frac{P}{P_0}\right)^{\frac{1}{k}}\left[\left(2\cdot\frac{k}{k-1}\right)\cdot\left[1-\left(\frac{P}{P_0}\right)^{\frac{(k-1)}{k}}\right]\right]^{0.5}}$$

$$C_d = 0.1834$$

Uncertainty:

$$U_{Cd} := \sqrt{(C_{dpartmr}\cdot U_{mr})^2 + (C_{dpartT0}\cdot U_{2T})^2 + (C_{dpartP0}\cdot U_p)^2 + (C_{dpartP}\cdot U_p)^2 + (C_{dpartAref}\cdot U_A)^2}$$

$$U_{Cd} = 3.83\times 10^{-3}$$

$$U_{Cd\%} := \frac{U_{Cd}}{C_d}$$

$$U_{Cd\%} = 2.0881\cdot\%$$

Uncertainty of Effective Flow Area:

Given data:

$A_{ref} = 0.401 \cdot ft^2$ $C_d = 0.1834$

Individual Uncertainties:

Uncertainty of Discharge Coefficient: $U_{Cd} = 3.83 \times 10^{-3}$

Uncertainty of Area: $U_A = 5.7744 \times 10^{-3} \cdot in^2$

Define:

$A_E \equiv C_d \cdot A_{ref}$

Partial Derivatives:

$$A_{EpartCd} := \frac{d}{dC_d}\left(C_d \cdot A_{ref}\right)$$

$$A_{EpartAref} := \frac{d}{dA_{ref}}\left(C_d \cdot A_{ref}\right)$$

Calculate Effective Flow Area:

$A_E := C_d \cdot A_{ref}$ $A_E = 6.8333 \times 10^{-3}\, m^2$

Uncertainty:

$$U_{AE} := \sqrt{\left(A_{EpartCd} \cdot U_{Cd}\right)^2 + \left(A_{EpartAref} \cdot U_A\right)^2}$$

$U_{AE} = 1.4268 \times 10^{-4}\, m^2$

$$U_{AE\%} := \frac{U_{AE}}{A_E}$$

$U_{AE\%} = 2.0881 \cdot \%$